

# Rocking Revisited 1

## Rocking of a Single Cube on a Breakwater Slope

Master's Thesis, final report

Author: T.N. Le

Date: June 12, 2016



Picture cover page:  
Broken armour units on breakwater.  
Picture courtesy Royal HaskoningDHV

# ROCKING REVISITED 1

ROCKING OF A SINGLE CUBE ON A BREAKWATER SLOPE

by

**T.N. Le**

Student ID: 4088395

in partial fulfillment of the requirements for the degree of

**Master of Science**

in Civil Engineering

at Delft University of Technology

Date: June 12, 2016

Graduation committee:	prof. dr. ir. W.S.J. Uijtewaal,	Delft University of Technology
	dr. ir. B. Hofland,	Delft University of Technology / Deltares
	ir. J.P. van den Bos,	Delft University of Technology
	ir. J.C. van der Lem,	Royal HaskoningDHV
	dr. ir. M.R.A. van Gent,	Deltares

An electronic version of this thesis is available at <http://repository.tudelft.nl/>.

The use of trademarks in any publication of Delft University of Technology does not imply any endorsement or disapproval of this product by the university.



# PREFACE

This Master's thesis report presents my work in partial fulfilment of the requirements for the degree Master of Science in Hydraulic Engineering at Delft University of Technology. I have researched the rocking behaviour of a single cube on a breakwater slope. This research has been carried out in cooperation with Royal HaskoningDHV and Deltares.

First of all, I would like to thank my graduation committee consisting of Wim Uijtewaal (TU Delft), Cock van der Lem (Royal HaskoningDHV), Bas Hofland (TU Delft/ Deltares), Jeroen van den Bos (TU Delft) and Marcel van Gent (Deltares) for their input and guidance during my Master's thesis. Many thanks to Paul Meijs and Wim Taal (Deltares) for their generosity in providing accelerometers for the experiments and for their advice regarding the measurement equipment. Furthermore, I would like to thank Sander de Vree, Hans Tas, Frank Kalkman and Jaap van Duin (TU Delft) for their support during the experiments. I am also very thankful to all colleagues at Royal HaskoningDHV for making my time as graduate intern enjoyable. Last but not least, I would like to thank my family, friends and girlfriend for their encouragements and unconditional support.

Tuan Nam Le  
*Delft, June 2016*

# EXECUTIVE SUMMARY

After several breakwater failures in the late 1970's and early 1980's it was realized that, with the growing size of double layer armour units, the strength of the units became a critical factor. To incorporate the strength of the armour unit in the breakwater design procedure, a joint industry research program was initiated under the coordination of the Centre for Civil Engineering Research and Codes workgroup C70 (CUR C70). The research program covered an analysis on damage cases, an inventory of available knowledge, physical model tests on rocking behaviour, force-time behaviour during collision of concrete units and the development of a design procedure and practical applications (CUR, 1990a). A result from the research program is a numerical application known as "Rocking" (CUR, 1990b). "Rocking" computes whether double layer armour units break for given hydraulic and geometric conditions in a statistical manner.

Nowadays, it is observed that breakage also occurs for single layer armour units. However, it is not possible to apply "Rocking" directly for single layer armour units, since the movement mechanism under wave attack is different for each type of armour unit. Therefore, the main objective of the current research project is to *obtain knowledge on, and measurements of the rocking behaviour and failure mode of single layer armour units*. To achieve this objective, an analysis of previous research is conducted and furthermore, wave flume experiments are conducted on a single cube.

An analysis of previous research conducted by CUR C70 reveals a number of important weak points. The first point is the assumption for the fixed number of 3 collisions per moving unit. This assumption was not verified with research. The second point is the deployment of a unidirectional accelerometer. During the tests, movements occurred in multiple directions. Consequently, the impacts, which occurred in different directions relative to the orientation of the accelerometer, were not captured accurately. The third point is the exclusion of the wave steepness during tests for impact velocities. Hence, it is unclear whether the wave steepness is of influence for the magnitude of impact. The outcome of the calculation in "Rocking" is largely dependent on the mentioned points. Therefore, it is chosen to take those points into account in the current research.

To understand the movements of armour units, a theoretical assessment is conducted for an exposed cube, which rotates around a hinge. To account for wave loading, an equation based on Morison, O'Brien, Johnson & Schaaf (1950) is applied. For plunging breakers, an additional impact force based on Goda et al. (as cited in Chella, Torum & Myrhaug (2012)) is added. The magnitude of movement is expressed with Newton's second law, in which the acceleration is calculated as a function of the sum of forces and mass of the element. The resulting velocity of the cube is estimated by integration of the acceleration over time.

Wave flume tests are conducted, in which a similar set-up as in the theoretical analysis is applied. This is chosen to have a better insight in the physical processes. The tested parameters are: degree of exposure of cube, wave height, wave steepness and position on slope in relation to the water level. Instead of measuring accelerations due to the mechanical impacts (Sokolewicz, 1986), the accelerations due to movement are measured. This allows the usage of cheaper measurement equipment and also a more direct methodology to determine the velocities of the cube before impact. A three-axis accelerometer, which is placed in the cube's center, is applied during this Master's Thesis.

Data processing shows that crosstalk occurs in two accelerometer axes. Therefore, only the accelerometer z-axis is processed. To come to the desired impact velocities, a synthetic model is used, which takes the time period of movement and the angle of the cube before and after movement as input values. With an iteratively fitted tangential acceleration of the cube in time, the measured signal in the accelerometer is approximated. The resulting approximations for tangential and normal acceleration are imposed in the equation of motion for the rotating cube. Subsequently, the output is the angle of the cube in time. Differentiation of the angle in time results in the angular velocities, in which the impact velocity is taken to be equal to the occurring velocity before collision. The outcome of this methodology appears to be largely dependent on the noise in the data signals and therefore, interpretation has to be done with caution. Only datasets with a large number of data points are interpreted.

Analysing the data shows that the number of collisions is dependent on the wave height, wave steepness, position on the slope and degree of exposure of the cube. Hence, an assumption for a fixed number of 3 collisions by CUR C70 is proven to be inaccurate. Therefore, it is recommended that in future research, the amount of collisions of a moving unit is regarded as a function that has dependencies on hydraulic and geometric conditions. For multiple conditions the number of collisions is observed to become very large and hence, concrete fatigue becomes important.

Consequently, it is recommended to incorporate fatigue in the calculation procedure of "Rocking". Furthermore, it is clearly observed that the probability to exceed a certain impact velocity changes with changing wave steepness. It is concluded that the wave steepness is of influence for the probability distribution functions and hence, the exclusion of the wave steepness by CUR C70 is proven to be incorrect. The wave steepness should be included as a variable parameter in the probability distribution function for impact velocities. In addition, it is observed that the data is described best with a Weibull distribution, which is different from the exponential distribution obtained by CUR C70. However, the two distribution types are from the same family of distributions and hence, the differences between the distribution functions remain small. Further statistical analysis is recommended for more reliability in the type of distribution. Next, it is clearly observed that the probability distribution is dependent on the type of movement and therefore, it is advised to consider multiple types of movement to find the governing impacts. Lastly, analysis shows that the analytical model overestimates the impact velocities and therefore, is too conservative. The assumptions made for the analytical model should be further investigated to derive a more accurate calculation method.

This Master's thesis creates excellent opportunities for further research on the rocking behaviour of single layer armour units. In terms of design, an updated version of "Rocking" for single layer armour units is preferred. The first step towards that purpose is to conduct similar impact tests in a representative model breakwater. With such a set-up, more modes of movement will be encountered. Hence, it is recommended to develop a wireless device that contains an accelerometer and a gyroscope, to capture and process the armour unit movements, that occur in various directions, successfully. Furthermore, it is advised to be aware of crosstalk in future wave flume experiments.

# CONTENTS

<b>Nomenclature</b>	<b>ix</b>
<b>List of Figures</b>	<b>x</b>
<b>List of Tables</b>	<b>xi</b>
<b>1 Introduction</b>	<b>1</b>
1.1 Breakwaters . . . . .	1
1.2 The Strength of Concrete Armour Units . . . . .	2
1.3 Problem Description . . . . .	2
1.4 Objective . . . . .	3
1.5 Methodology . . . . .	3
<b>2 Analysis Previously Conducted Research</b>	<b>4</b>
2.1 Analysis Research CUR C70 . . . . .	4
2.1.1 Overview . . . . .	4
2.1.2 Number of Moved Units and Collisions . . . . .	5
2.1.3 Impacts . . . . .	7
2.1.4 Load-Time Relation . . . . .	9
2.1.5 Stresses . . . . .	11
2.1.6 Strength . . . . .	12
2.1.7 Computer Application “Rocking” . . . . .	13
2.2 Alternative Methodology . . . . .	14
2.3 Additional Literature . . . . .	14
<b>3 Analytical Model</b>	<b>16</b>
3.1 Overview . . . . .	16
3.2 Wave Loading . . . . .	17
3.3 Moment of Force . . . . .	19
3.4 Analysis and Expectations . . . . .	21
<b>4 Set-up and Execution Experiments</b>	<b>23</b>
4.1 Overview . . . . .	23
4.1.1 Experimental Set-up . . . . .	23
4.1.2 Limitations . . . . .	26
4.1.3 Wave Flume . . . . .	26
4.2 Scaling . . . . .	26
4.2.1 Dimensionless Relationships . . . . .	26
4.2.2 Dimensions Model and Hydraulic Conditions . . . . .	27
4.3 Measurement Equipment . . . . .	27
4.3.1 Accelerometer . . . . .	28
4.3.2 Pressure Sensor . . . . .	31
4.3.3 Cameras . . . . .	31
4.3.4 Wave Gauges . . . . .	31
4.4 Test Program . . . . .	32
4.5 Expectations . . . . .	35
4.6 Visual Observations . . . . .	35
<b>5 Data Processing</b>	<b>36</b>
5.1 Interpretation . . . . .	36
5.2 Velocities Before Collision . . . . .	37
5.2.1 Equations of Motion . . . . .	37
5.2.2 Synthetic Model . . . . .	39

5.2.3	Signal Processing and Filtering. . . . .	41
5.3	Number of Collisions . . . . .	41
5.4	Start of Collisions . . . . .	42
5.5	Detection of Collisions . . . . .	42
<b>6</b>	<b>Analysis Results</b>	<b>44</b>
6.1	Analytical Model versus Measurements . . . . .	44
6.2	Analysis Number of Collisions . . . . .	44
6.3	Analysis Start of Collisions . . . . .	48
6.4	Analysis Velocities before Collision . . . . .	49
6.4.1	Probability Distribution . . . . .	49
6.4.2	Significant Wave Height Dependencies . . . . .	49
6.4.3	Wave Steepness Dependencies. . . . .	50
6.4.4	Slope Position Dependencies . . . . .	51
6.4.5	Upward versus Downward Movement . . . . .	51
6.4.6	Embedded Cube . . . . .	51
6.5	General Distribution Function for Velocities before Collision . . . . .	51
6.5.1	Probability Distribution . . . . .	52
6.5.2	Significant Wave Height Dependencies . . . . .	52
6.5.3	Wave Steepness Dependencies. . . . .	53
6.5.4	Slope Position Dependencies . . . . .	53
6.5.5	Embedded Cube . . . . .	54
6.6	Analysis Magnitude of Maximum Impact Velocities. . . . .	54
6.6.1	Comparison with CUR C70. . . . .	55
6.6.2	Dependencies Magnitude Maximum Impact Velocities . . . . .	55
6.7	Additional Aspects . . . . .	55
<b>7</b>	<b>Conclusions</b>	<b>58</b>
7.1	Number of Collisions . . . . .	58
7.2	Influence Wave Steepness on Impact Velocities . . . . .	58
7.3	Weibull Distribution Function for impact Velocities. . . . .	58
7.4	Type of Movement . . . . .	59
7.5	Additional Conclusions . . . . .	59
<b>8</b>	<b>Recommendations</b>	<b>60</b>
8.1	Opportunities for Current Research. . . . .	60
8.1.1	Laboratory Experiments . . . . .	60
8.1.2	Data Processing . . . . .	61
8.1.3	Analysis . . . . .	63
8.2	Applicability Accelerometer ADXL335. . . . .	63
8.3	Action Plan Rocking. . . . .	63
8.4	Additional Opportunities . . . . .	65
	<b>Bibliography</b>	<b>66</b>
<b>A</b>	<b>Structure Scheme “Rocking”</b>	<b>68</b>
<b>B</b>	<b>Matlab Routine “Rocking”</b>	<b>72</b>
<b>C</b>	<b>Implementation Test Set-Up in Wave Flume</b>	<b>76</b>
<b>D</b>	<b>Market Study Accelerometers</b>	<b>79</b>
<b>E</b>	<b>Validation Accelerometer</b>	<b>81</b>
<b>F</b>	<b>Approach Differential Equation Using Numerical Methods</b>	<b>86</b>
<b>G</b>	<b>Matlab Routine for Data Processing</b>	<b>89</b>
<b>H</b>	<b>Results Velocities before Collision</b>	<b>95</b>
<b>I</b>	<b>Hexapod</b>	<b>150</b>

# NOMENCLATURE

## Concrete

$\sigma$	Stresses	$[kN/m^2]$
$arm_s$	Position of critical stresses in leg armour unit relative to the rotational point	$[m]$
$f_c$	Tensile strength with all reduction factors combined	$[N/mm^2]$
$f_{c0}$	Axial tensile strength	$[N/mm^2]$
$K_S$	Coefficient for the effect of the duration of the collision on concrete's tensile strength	$[-]$
$K_t$	Coefficient for the temperature effect on concrete's tensile strength	$[-]$
$K_v$	Coefficient for the volume effect on concrete's tensile strength	$[-]$
$S$	Actual duration of collision	$[N/mm^2.s]$
$S_0$	Reference duration of collision	$[N/mm^2.s]$
$V$	Volume of part of armour unit in which critical stresses occur	$[mm^3]$
$V_0$	Volume of cylinder with height of 600 mm and diameter of 150 mm	$[mm^3]$

## Generic Symbols

$[Y/D_n]_p$	Position of the cube relative to the water level found after processing of data	$[-]$
$\alpha$	Slope angle	$[rad]$
$\Delta$	Relative mass density of $\rho_s$ and $\rho_w$	$[-]$
$\rho_s$	Density of armour unit	$[kg/m^3]$
$\rho_w$	Density of water	$[kg/m^3]$
$\xi$	Iribarren number for $H$ and $T$	$[-]$
$\xi_m$	Iribarren number for $H_s$ and $T_m$	$[-]$
$D_n$	Nominal diameter	$[m]$
$g$	Gravitational acceleration	$[m/s^2]$
$H$	Wave height	$[m]$
$H_s$	Significant wave height from wave record	$[m]$
$H_{m0}$	Significant wave height from wave energy spectrum	$[m]$
$L$	Wave length	$[m]$
$L_0$	Deep water wave length	$[m]$
$M$	Mass armour unit	$[kg]$
$N$	Number of waves	$[-]$
$p$	Probability of exceedance distribution function	$[-]$
$s$	Fictitious wave steepness based on $H$ and $T$	$[-]$
$s_m$	Fictitious wave steepness based on $H_s$ and $T_m$	$[-]$
$s_{m-1.0}$	Fictitious wave steepness based on $H_{m0}$ and $T_{m-1.0}$	$[-]$

$T$	Wave period	[s]
$T_m$	Mean wave period from wave record	[s]
$T_{m-1.0}$	Wave period based on the ratio of the wave energy spectral moments $m_{-1}$ and $m_0$ .	[s]
$Y/D_n$	Position of the cube relative to the water level	[-]
<b>Impacts</b>		
$\alpha$	Effective mass	[kg]
$\omega$	Angular velocity	[rad/s]
$\phi_g$	Initial angle between gravitation and the accelerometer z-axis	[rad]
$\phi_T$	Angle between the tangential direction of rotation and the orientation of accelerometer z-axis	[rad]
$\theta$	Turning angle relative to orientation of breakwater slope	[°]
$\theta_m$	Turning angle derived from the synthetic model relative to orientation of breakwater slope	[rad]
$a$	Acceleration armour unit during collision	[m/s <sup>2</sup> ]
$a_g$	Acceleration exerted by gravity	[m/s <sup>2</sup> ]
$a_n$	Acceleration in normal direction in plane of rotation	[m/s <sup>2</sup> ]
$a_T$	Acceleration in tangential direction in plane of rotation	[m/s <sup>2</sup> ]
$a_z$	Acceleration measured by the accelerometer z-axis	[m/s <sup>2</sup> ]
$Ar m_r$	Distance between place of collision and center of rotation	[m]
$B$	Probability of exceedance distribution coefficient describing the position of the function	[-]
$C$	Probability exceedance distribution coefficient describing the lower limit of the function	[-]
$C_{nm}$	Coefficient derived from the synthetic model describing the normal acceleration in relation to the measurements in the z-axis	[m/s <sup>2</sup> ]
$C_{tm}$	Coefficient derived from the synthetic model describing the tangential acceleration in relation to the measurements in the z-axis	[m/s <sup>2</sup> ]
$F$	Force acting on armour unit	[N]
$H$	Height armour unit	[m]
$I_0$	Moment of inertia around rotational point	[kg.m <sup>3</sup> ]
$I_{gs}$	Moment of inertia around center armour unit	[kg.m <sup>3</sup> ]
$l$	Lever contributing to the torque around the rotational point	[m]
$M_1$	Mass of the active unit causing the collision	[kg]
$M_2$	Mass of the passive unit undergoing the collision plus an added mass from clamping forces	[kg]
$r$	Distance from center of cube to rotational point	[m]
$V$	Velocity center of armour unit before collision	[m/s]
$V_{collision}$	Velocity of collision of the part of the armour unit that collides	[m/s]
<b>Load-Time</b>		
$A1$	Area underneath rising zone	[kN.s]
$A2$	Area underneath descending zone	[kN.s]
$d$	Diameter outer end of armour unit leg	[mm]
$K_{e1}$	Contact stiffness parameter for the rising zone	[kN/mm <sup>3/2</sup> ]
$K_{e2}$	Contact stiffness parameter for descending zone	[kN/mm <sup>3/2</sup> ]

$K_p$	Contact stiffness parameter for plastic zone	[kN]
$P_m$	Maximum force of all zones combined	[kN]
$P_{e2}$	Real maximum force descending zone	[kN]
$P_{max,1}$	Maximum theoretical force rising zone	[kN]
$P_{max,2}$	Maximum theoretical force descending zone	[kN]
$T_m$	Time span in which the maximum force of all zones combined is developed	[s]
$T_p$	Time span of plastic zone	[s]
$T_{e2}$	Time span in which the real maximum force is developed of the descending zone	[s]
$T_{max,1}$	Time span in which the maximum theoretical force is developed in the rising zone	[s]
$T_{max,2}$	Time span in which the maximum theoretical force is developed in the descending zone	[s]

### Number of Collisions

$a$	Coefficient taking into account the probabilistic spreading of stability formulas 2.5 and 2.6	[-]
$N_{broken}$	Number of broken armour units on breakwater slope	[-]
$N_{o<0.5D}$	Number of units that was moved over a distance of less than 0.5 times the diameter in cross-section with a width of 1 $D_n$	[-]
$N_{o>0.5D}$	Number of units that was moved over a distance of more than 0.5 times the diameter in a cross-section with a width of 1 $D_n$	[-]
$N_{od}$	Number of displaced units in cross-section with a width of 1 $D_n$	[-]
$N_{otot}$	Number of moved units in cross-section with a width of 1 $D_n$ including $N_{od}$ , $N_{o>0.5D}$ and $N_{o<0.5D}$	[-]

### Scaling

$\nu$	Viscosity	[kg/(s.m)]
$\sigma$	Surface tension	[N/m]
$Fr$	Froude number	[-]
$N_s$	Stability number	[-]
$Re$	Reynolds number	[-]
$St$	Strouhal number	[-]
$We$	Weber number	[-]

### Wave Loading

$\gamma_f$	Correction factor for slope roughness	[-]
$c_1$	Empirical constant for the run-up relationships	[-]
$C_a$	Inertia coefficient	[-]
$C_b$	Breaking wave celerity	[m/s]
$C_D$	Drag coefficient	[-]
$c_u$	Empirically fitted constant for the run-up velocity relationship	[-]
$D$	Diameter unit	[m]
$F$	Inertia and drag forcing	[kN]
$F_I$	Wave impact force	[kN]
$F_z$	Gravitational force	[kN]
$r$	Freeboard	[m]

---

$R_u$	Run-up height	[ $m$ ]
$R_{u_{2\%}}$	2% exceedance run-up height	[ $m$ ]
$u$	Wave run-up velocity	[ $m/s$ ]
$V$	Total volume armour unit	[ $m^3$ ]
$V_w$	Volume unit over which the forcing acts	[ $m^3$ ]

# LIST OF FIGURES

1.1	Cross section breakwater design (Gijsman, Haan, Koning, Le & Steeneken , 2015) . . . . .	1
1.2	Application of single layer cubes (Deltares , 2014) . . . . .	2
1.3	Broken Armour Units on breakwater (picture courtesy Royal HaskoningDHV) . . . . .	2
2.1	Calculation Procedure (CUR , 1990a) . . . . .	5
2.2	Force-Time relationship (CUR , 1990a) . . . . .	9
2.3	Structure Computer Application Rocking . . . . .	13
2.4	The determination of the Dolosse dimensions from design graphs (Burcharth , 1992) . . . . .	15
3.1	Wave run-up on slope with protruding element . . . . .	16
3.2	Rotations of the armour unit . . . . .	19
4.1	Illustration experimental setup - side view . . . . .	23
4.2	Position cube relative to mean water level - side view . . . . .	24
4.3	Illustration experimental set-up - top view perpendicular to slope . . . . .	24
4.4	Regular placement single layer cubes (Van Gent & Luis , 2013) - top view of physical model . . . . .	25
4.5	Illustration experimental set-up with embedded cube - top view perpendicular to slope . . . . .	25
4.6	Detailed illustration of embedded cube near cube . . . . .	25
4.7	Differences in measurements of this Master's thesis in comparison with Sokolewicz (1986) . . . . .	28
4.8	Accelerometer ADXL335 (Adafruit , n.d.) . . . . .	29
4.9	Orientation accelerometer inside cube . . . . .	30
4.10	Placement of cube measuring pressure (upper cube) and cube measuring accelerations (lower cube) . . . . .	30
4.11	Overview set-up wave flume . . . . .	31
5.1	Raw data signals from measurements, in Voltage . . . . .	38
5.2	Decomposition acceleration signal for cube moving upward . . . . .	39
5.3	Comparison synthetic model with measured signal for surging breakers . . . . .	40
5.4	Comparison synthetic model with measured signal for collapsing breakers, extreme case . . . . .	40
5.5	Indication upward and downward movement in accelerometer data . . . . .	41
5.6	Velocity signal in time, showing the influence of noise . . . . .	42
6.1	Comparison impact velocities from analytical model with regular waves, upward rotation . . . . .	45
6.2	Number of collisions for position on slope $Y/D_n = -2$ . . . . .	46
6.3	Number of collisions for position on slope $Y/D_n = 0$ . . . . .	46
6.4	Number of collisions for position on slope $Y/D_n = 2$ . . . . .	46
6.5	Number of collisions for steepness $s_{m-1,0} = 0.04$ . . . . .	47
6.6	Number of collisions for steepness $s_{m-1,0} = 0.02$ . . . . .	47
6.7	Comparison magnitude of impact velocities . . . . .	54
6.8	Comparison time lag between wave impact and start of movement . . . . .	56
6.9	Comparison of the signals of upward movement under surging and collapsing breaker conditions . . . . .	56
6.10	More foam during collapsing breaker conditions . . . . .	57
8.1	Alignment accelerometer axes parallel to the tangential and normal acceleration . . . . .	62

# LIST OF TABLES

3.1	Velocities before collision from analytical model, $s = 0.02$ , upward rotation . . . . .	21
3.2	Velocities before collision from analytical model, $s = 0.08$ , upward rotation . . . . .	21
4.1	Measurement errors in accelerometer (Analog Devices , 2009) . . . . .	29
4.2	Test program for regular waves . . . . .	33
4.3	Test program for irregular waves . . . . .	34

# 1

## INTRODUCTION

### 1.1. BREAKWATERS

The classic rubble mound breakwater has been widely used to prevent the coasts and ports from wave attack for centuries. This breakwater consists of a core of fine quarry material with heavy armour stones or concrete blocks on top. Those armour units and concrete blocks got their stability against wave attack from their own weight.

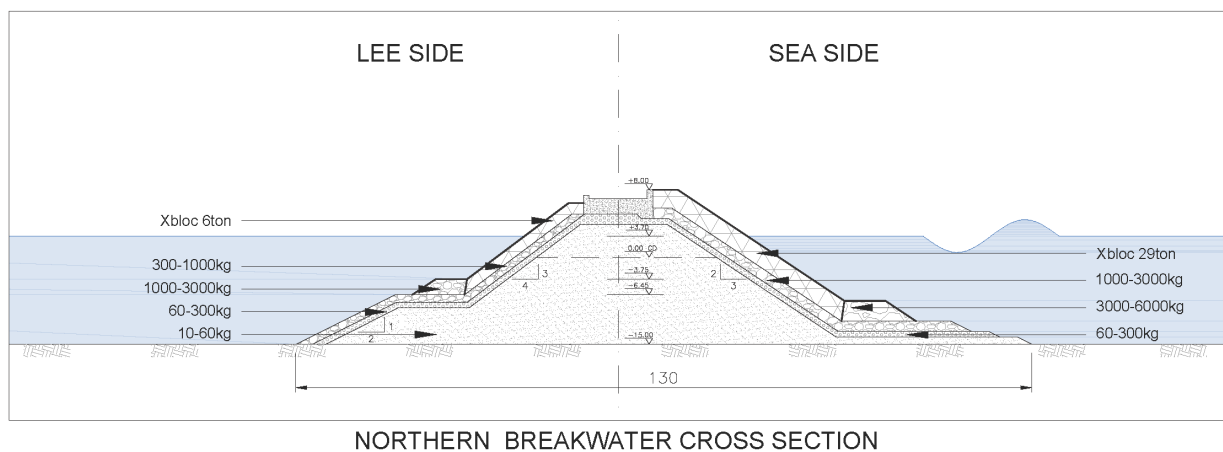


Figure 1.1: Cross section breakwater design (Gijssman, Haan, Koning, Le & Steeneken , 2015)

The introduction of slender armour units began approximately half a century ago. These units were used as replacement for the armour stones and concrete blocks. The speciality of these slender armour units was the interlocking character because it increased the stability against wave attack, while required less weight from the units. This saved a considerable amount of concrete and costs.

The first generation armour units (e.g. Dolosse, Tetrapodes, cubes) were applied in a double layer. Recently, armour units such as Accropode, Coreloc, Xbloc and single layer cubes have been developed and have the advantage that they can be applied in a single layer. Consequently, the amount of concrete is saved in comparison to the first generation units. The design of single layer armour units on a rubble mound breakwater are shown in Figure 1.1. An application in practice is shown in Figure 1.2.



Figure 1.2: Application of single layer cubes (Deltares, 2014)

## 1.2. THE STRENGTH OF CONCRETE ARMOUR UNITS

After several breakwater failures in the late 1970's and early 1980's, it was realized that, with the growing sizes of slender armour units, the strength of the units in a double layer became a critical factor. Analysis showed that mechanical failure of the units was the cause for the final collapse of a breakwater in most cases. To incorporate the strength of the armour unit in the breakwater design procedure, an extensive joint industry research program was initiated under the coordination of the Centre for Civil Engineering Research and Codes (CUR) in the 1980's. The research program covered an analysis on damage cases, an inventory of available knowledge, physical model tests on rocking behaviour, force-time behaviour during collision of concrete units and the development of a design procedure and practical applications. The program had the purpose to investigate the strength of Tetrapodes and cubes both typically applied in a double armour layer.

One of the results of the research program was the establishment of computer application "Rocking". Rocking computes whether armour units break for given hydraulic and geometric conditions in a statistical way.

## 1.3. PROBLEM DESCRIPTION

Nowadays, the majority of rubble mound breakwaters requiring armour units are provided with single layer armour units. For the past couple of years, it is observed that breakage also occurs for these units, see Figure 1.3.



Figure 1.3: Broken Armour Units on breakwater (picture courtesy Royal HaskoningDHV)

Since the shape, mass, placement style and breakwater conditions are different for each armour unit, the rocking mechanism under wave attack is different for each armour unit. It is therefore not possible to use "Rocking" for modern single layer armour units. Since knowledge on the rocking behaviour of single layer armour units is limited, it is of paramount importance that research is conducted on the latter.

## 1.4. OBJECTIVE

The objective for the entire research program follows from the problem discussed in Section 1.3:

Obtaining knowledge on, and measurements of the rocking behaviour and failure mode of single layer armour units

## 1.5. METHODOLOGY

The objective in Section 1.4 could be reached by:

1. Analysing previously conducted research and application "Rocking".
2. Obtaining knowledge on the impacts and amount of collisions.
3. Obtaining knowledge on the number of colliding units in relation to the hydraulic conditions.
4. Obtaining knowledge on the type of movements and collisions.
5. Obtaining knowledge on the force-time relationships for specific armour unit concrete characteristics.
6. Obtaining knowledge on the stresses for specific armour unit characteristics.
7. Obtaining knowledge on the strength of the armour unit.
8. An update of numerical application "Rocking".

To achieve those indicated steps, either the method of conducting laboratory tests or applying numerical models can be used. To be consistent with the research by CUR C70, it is chosen to conduct laboratory tests in the current research project. In addition, the steps shown above are applicable for all types of single layer armour units. This Master's thesis is only focussed on the investigation of the rocking behaviour of a single cube on a schematised breakwater slope. More specifically, the following aspects are addressed:

1. An analysis of previously conducted research and application "Rocking".
2. The set-up of a theoretical model to understand the rocking behaviour of a single cube, rotating around a hinge, on a simplified breakwater slope, without roughness and porosity.
3. The measurements of the rocking behaviour of a single cube, rotating around a hinge, on a simplified breakwater slope, without roughness and porosity. The single cube is subjected to varying wave height, wave steepness, position relative to the water level and degree of exposure regarding wave attack. The measurements are conducted with an accelerometer, placed in the center of the cube, that measures the movements of the cube.
4. An analysis of the data from the experiments, on the number of collisions and velocities of the cube before impact.
5. A comparison of the results from the current research project with the results from previously conducted research.

# 2

## ANALYSIS PREVIOUSLY CONDUCTED RESEARCH

In the 1980's and 1990's, interest grew in the development of knowledge regarding the prediction of armour unit breakage. This was a result of several breakwater failure cases. Therefore, research was performed on the strength of concrete armour units. This chapter gives a thorough description and analysis of a Dutch joint industry research program. Additionally, a research program with an alternative measurement approach is described. Lastly, additional literature regarding measurement techniques and numerical modelling are mentioned.

### 2.1. ANALYSIS RESEARCH CUR C70

After several breakwater failures in the late 1970's and early 1980's it was realized that, with the growing sizes of slender armour units, the strength of the units became a critical factor. Analysis showed that mechanical failure of the units was the cause for the final collapse of a breakwater in most cases. To incorporate the strength of the armour unit in the breakwater design procedure, an extensive joint industry research program was initiated. This program was coordinated by the Centre for Civil Engineering Research and Codes (CUR) and was conducted in the 1980's.

#### 2.1.1. OVERVIEW

The research program covered an analysis on damage cases, an inventory of available knowledge, physical model tests on rocking behaviour, force-time behaviour during collision of concrete units and the development of a design procedure and practical applications. The program had the purpose to investigate the strength of Tetrapodes and cubes, both typically applied in a double layer.

The resulting calculation procedure provided an estimation of the probability of breakage of an armour unit. This probability of breakage was related to the wave height and position of the armour unit on the breakwater slope. Based on an estimation of the number of moved units, number of collisions and probability of breakage, the number of failed units on the breakwater was calculated. Additionally a numerical application, known as "Rocking", was developed in which the calculation procedure was conducted as a Monte Carlo simulation.

Application "Rocking" executed the computation as shown in Figure 2.1. From the hydraulic conditions and breakwater geometry (box 1) the number of displaced units out of the armour layer was calculated (box 2) with formulas from breakwater stability tests. An adjustment to those formulas was necessary (box 3) to represent the range of armour layer movement in which collisions between units play a role. Consequently, the number of displaced units were changed to the total number of moved units, which included both small movements and displaced units.

Measurements from model tests with accelerometers placed inside armour units form the basis for relationships of the impact velocity and momentum during collision (box 4). Research in the load-time relationship during concrete to concrete impact (box 5) together with the momentum of collision, provide an estimation of the maximum stresses inside an armour unit (box 6). An armour unit was considered to be broken in case the maximum stresses exceed the strength in the critical part of the armour unit. The total number of broken units on a slope was estimated with

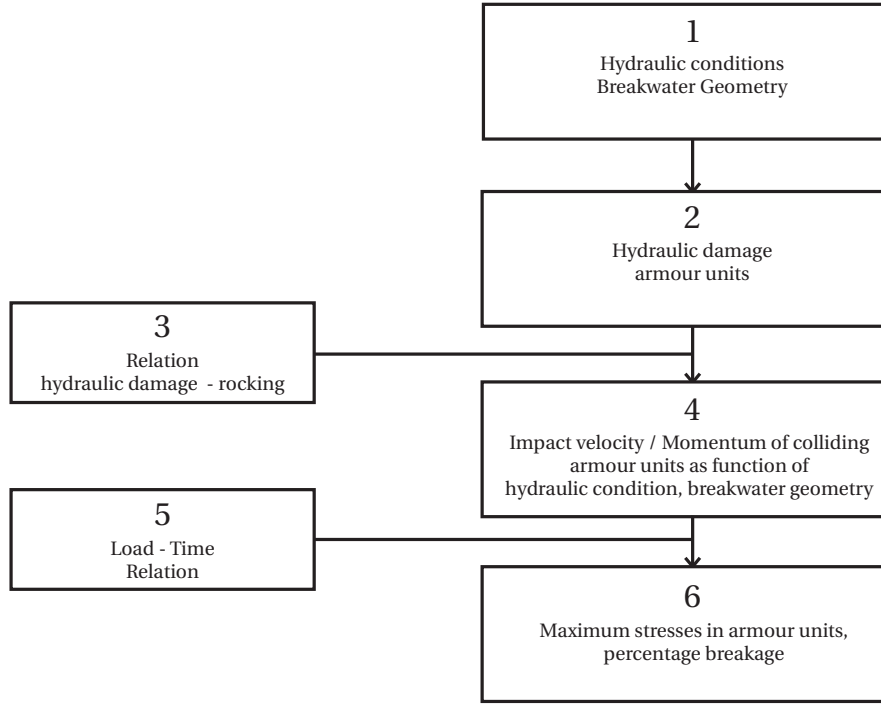


Figure 2.1: Calculation Procedure (CUR , 1990a)

input from the number of moved units (box 3), the average number of collisions per moved unit and the probability of breakage (box 6).

It should be mentioned that the parameter notation is not consistent in both literature (CUR , 1989), the “Rocking” manual (“Handleiding Rocking” , 1990) and the computer script. In this chapter, the same notations as in the “Rocking” manual are used. It was however necessary to change a few parameter notations for clarity. In Appendix A and B the original notations are shown.

### 2.1.2. NUMBER OF MOVED UNITS AND COLLISIONS

With the aim to develop insight in the total number of armour units subjected to collisions, stability model tests were performed. Armour unit stability formulas by Van der Meer (1988) were taken as a starting point, shown in Equations 2.1 and 2.2. Van der Meer (1988) derived the following stability formula for cubes in a double layer:

$$\frac{H_s}{\Delta D_n} = \left( 6.7 \frac{N_{od}^{0.4}}{N^{0.3}} + 1 \right) s_m^{-0.1} \quad (2.1)$$

Additionally, the stability formula for Tetrapodes was described as following (Van der Meer , 1988):

$$\frac{H_s}{\Delta D_n} = \left( 3.75 \frac{N_{od}^{0.5}}{N^{0.25}} + 0.85 \right) s_m^{-0.2} \quad (2.2)$$

With the formulas, relations were created between the number of displaced units ( $N_{od}$  [-]), the armour unit size ( $D_n$  [m]), wave height ( $H_s$  [m]) and wave steepness ( $s_m$  [-]). The number of collisions between elements was however not considered. Therefore new stability tests were performed on the total number of moved units ( $N_{tot}$  [-]). This implied taking into account the number of displaced units ( $N_{od}$  [-]), the number of units moved more than 0.5 times the diameter ( $N_{o>0.5D}$  [-]) and the number of units moved less than 0.5 times the diameter ( $N_{o<0.5D}$  [-]). From data analysis it was concluded that a reduction of  $\frac{H_s}{\Delta D_n} = 0.5$  [-] in Equations 2.1 and 2.2 gave a satisfactory representation for the total number of moved units.

Consequently, the relationship for the total number of moved cubes in a double layer became:

$$\frac{H_s}{\Delta D_n} = \left( 6.7 \frac{N_{tot}^{0.4}}{N^{0.3}} + 1 \right) s_m^{-0.1-0.5} \quad (2.3)$$

Additionally, the relationship for the total number of moved Tetrapodes was described as following:

$$\frac{H_s}{\Delta D_n} = \left( 3.75 \frac{N_{tot}^{0.5}}{N^{0.25}} + 0.85 \right) s_m^{-0.2} - 0.5 \quad (2.4)$$

To estimate the number of broken armour units, the average number of collisions per moving unit was investigated. For this purpose, video images from armour unit impact tests were analysed. The elaboration of the impact tests is shown in Section 2.1.3. The armour units were marked as moved one time and moved more than once. It was concluded that on average 40% of the moved units collided once. However, the number of collisions of the other 60% of the moved armour units could not be deducted from the analysis. Therefore, the amount of collisions per moving units was estimated to be more or less equal to an average of 3, based on rough assumptions.

#### ANALYSIS

Stability tests are known for the large spreading in results. Therefore, in Van der Meer (1988) the parameter  $a$  was introduced, having a mean of 1.0 and a standard deviation of 0.10:

$$\frac{H_s}{\Delta D_n} = a * f(N_{od}, N, s_m) \quad (2.5)$$

The same values were applied for the relationship of the total number of moved units, as a first estimation by CUR C70:

$$\frac{H_s}{\Delta D_n} = a * f(N_{tot}, N, s_m) \quad (2.6)$$

This parameter  $a$  [-] was however not taken into account in the calculation procedure of application “Rocking”. The total number of moved units was calculated deterministically, before the start of the Monte Carlo simulation (see Appendix B). For higher accuracy of results it is therefore advised to include parameter  $a$  in the Monte Carlo simulation.

Next to that, parameter  $N_{tot}$  did not take into account rocking. It is conceivable that rocking also results in collisions with neighbouring armour units and under layer. Therefore, it is probably the case that the number of colliding units was underestimated. On the other hand, it is imaginable that it was difficult to observe rocking with the techniques used in the research. With rocking, the unit has the possibility to rotate and fall back to its original position. Therefore, an analysis of changes in the unit's position before and after the test does not give satisfactory results.

In addition, significant differences in results were observed between the stability tests for cubes in a double layer of Van der Meer (1988) and CUR C70 (CUR, 1989). The tests done by CUR C70 appeared to be more stable. The documentation by CUR C70 named two reasons for the differences. The first reason was that many units were subjected to substantial settlement during the tests by CUR C70. If those movements were assumed to be similar to the displacement of out the armour layer, then a higher correlation between the results was achieved between the two tests. The second reason was the difference in material usage and with that, the friction between units was different. Due to a proportionality with the angle of internal friction the stability increased with an increase of material friction.

For application of the provided relationships in the current research it is necessary to have knowledge about the armour unit type dependencies. Obviously, the relationships are among others dependent on the shape of the unit, placement and packing density. Therefore, a direct relation for single layer armour units cannot be assumed. Analysis of stability research for each armour unit type is necessary.

Lastly, the average number of collisions was a very rough assumption, since the results from video analysis did not provide any proof. For a correct representation clearly extra research needs to be conducted. In addition, a video analysis of the impact tests may have led to an incorrect representation of the collisions in the stability test, since the packing of the instrumented units was different (see Section 2.1.3).

### 2.1.3. IMPACTS

To estimate whether a unit breaks, the loads on an armour unit during collision were determined. This was done according to an indirect measurement methodology: First, accelerations of units during collision were measured. Integration of these accelerations resulted in the mechanical impact velocity. Next, the momentum during collision was calculated together with input from the impact velocity and the type of movement. Ultimately, the resulting information was used for the determination of the stresses inside the armour unit, as shown in Section 2.1.5.

The accelerations were measured with an accelerometer placed in the center of the armour unit. For the purpose of measuring impacts, unidirectional piezoelectric accelerometers from Bruël and Kjaer were applied. With a frequency range up to 120 kHz and acceleration range over more than 65 g (600 m/s<sup>2</sup>), the accelerometer specifications were sufficient for measurements of impacts with duration of +/- 10 kHz and maximum accelerations of 55 g. The tests were conducted for both regular and irregular waves with a wave height range from 0.04 m up to 0.18 m. The Iribarren number  $\xi_0$  was kept at a fixed rate of 3. The instrumented units were placed in such a way that movement was likely to occur. Furthermore, the position of the armour unit on the slope was varied.

Only the results of irregular waves were processed, since insufficient movements were observed during the tests with regular waves. It was chosen to process only the acceleration peaks larger than one third of the maximum peak value. Instead of integrating the acceleration signal over time, a relation between the hydraulic conditions and acceleration peaks was established:

$$p(a/g) = \exp[-((a/g - c)/B)]^Y \quad (2.7)$$

$$c = 10 \exp(-0.4|y/D_n|) \quad (2.8)$$

$$B = 5 \exp(-0.4|y/D_n|) H_s/\Delta D_n \quad (2.9)$$

In Equation 2.7 parameter  $a$  [m/s<sup>2</sup>] is the acceleration during impact and  $B$  and  $c$  are dimensionless coefficients in which the magnitude is determined by the position of the unit on the slope and significant wave height. Thereafter, an analysis of the acceleration peak form factor as a function of time was conducted, to establish a relationship between accelerations and velocities. A linear relation was deduced for cubes in a double layer:

$$V/\sqrt{gD_n} = 0.0049(a/g) \quad (2.10)$$

Here, parameter  $V$  is the velocity from the impulse of impact in m/s. For Tetrapodes the following relationship was found:

$$V/\sqrt{gD_n} = 0.0081(a/g)^{0.7} \quad (2.11)$$

To account for the large scatter, the coefficients 0.0049 and 0.0081 in Equations 2.10 and 2.11 were taken into account stochastically with standard deviations of 0.001 and 0.0016 respectively. The distribution of velocities followed from the substitution of the relationship accelerations - velocities and the distribution of accelerations. For cubes in a double layer, the following relationships were established:

$$p(V/\sqrt{gD_n}) = \exp[-(((V/\sqrt{gD_n}) - c)/B)] \quad (2.12)$$

$$c = 0.049 \exp(-0.4|y/D_n|) \quad (2.13)$$

$$B = 0.025 \exp(-0.4|y/D_n|) H_s/\Delta D_n \quad (2.14)$$

The distribution relationships for Tetrapodes were established as following:

$$p(V/\sqrt{gD_n}) = \exp[-(((V/\sqrt{gD_n})^{1.43} - c)/B)] \quad (2.15)$$

$$c = 0.0103 \exp(-0.4|y/D_n|) \quad (2.16)$$

$$B = 0.0051 \exp(-0.4|y/D_n|) H_s/\Delta D_n \quad (2.17)$$

A summary of some important conclusions from the tests (Sokolewicz , 1986):

1. The maximum accelerations were found near the waterline and have a magnitude of 55 g with a small probability of occurrence.
2. Higher significant wave heights resulted in larger accelerations, provided that the rocking mode of an armour unit did not change.
3. Movements of the armour unit were dependent on the choice of regular or irregular waves.
4. The breaker type had significant influence on the movement of an armour unit. The highest degree of movement was observed with a collapsing breaker.
5. Collisions against the edge of an armour unit lead to higher loads.

The impact velocity was used together with the rocking mode to calculate the momentum. The rocking mode (translation or rotation) determined the type of calculation. It was assumed that in 50% of the cases the Tetrapodes rotate and in the remaining percentage the Tetrapodes translate. In addition, only translations were assumed for cubes in a double layer. Since the accelerations were measured in the center of the unit, it was necessary to translate those to the velocity of the position in the unit where collision was considered. The relationships for the velocity of collision and momentum ( $V_{collision}$ ) of the translating unit were applied as follows (CUR , 1990b):

$$Momentum = MV \quad (2.18)$$

$$V_{collision} = V \quad (2.19)$$

The momentum during translation was calculated with the mass ( $M [kg]$ ) and velocity from the impulse of impact ( $V [m/s]$ ) of the armour unit. In case of a translation the velocity before impact  $V_{collision}$  was equal to the velocity in the center of the unit. For rotation the following relationships were applied (CUR , 1990b):

$$Momentum = I_0 \omega / Arm_r \quad (2.20)$$

$$\omega = V / 0.65h \quad (2.21)$$

$$V_{collision} = Momentum / M \quad (2.22)$$

In which velocity ( $V [m/s]$ ) was a known parameter from previously established relations. Ultimately, the velocity of collision was derived. In addition, the momentum was considered to be a function of the moments of inertia  $I_0 [kgm^2]$ , the angular velocity  $\omega [rad/s]$  and the distance between the place of collision and the center of rotation  $Arm_r [m]$ . The place of collision was chosen to be variable because of the random armour unit placement. Consequently  $Arm_r [m]$  was taken into account as a variable. In the procedure it was assumed that 50% of the collisions occurred at the outer end of the Tetrapode's leg. The other 50% of the collisions was assumed to be uniformly distributed over the leg.

The behaviour of the (passive) armour units that were hit determined the magnitude of forcing in the units. Therefore an effective mass  $\alpha [kg]$  was introduced, which was dependent on the degree of movement of the passive unit. The added mass was assumed to be uniformly distributed from  $0.5M$  to  $M$ . A higher effective mass resulted in higher forces since the passive unit was less willing to move. Parameter  $\alpha$  was included in the calculation as following (CUR , 1990b):

$$\alpha = \frac{M_1 * M_2}{M_1 + M_2} \quad (2.23)$$

$M_1$  represented the mass of the active unit causing the collision. Furthermore,  $M_2$  represented the mass of the passive unit plus the added mass from clamping forces. Parameter  $M_2$  was equal to the mass of an armour unit in case the unit was not clamped in between other units and reached infinity if the unit was fully clamped. Consequently, the added mass had a range from  $0.5M_1$  to  $M_1$ .

## ANALYSIS

The CUR C70 methodology determined the mechanical forces indirectly by measuring accelerations. This was done by using a unidirectional, wired accelerometer. With this the first disadvantage is that only movements in one direction were captured, resulting in possible measurement inconsistencies. The accelerations are only captured accurately

when they occur in the direction of the installed accelerometer. The second disadvantage is the wiring: influence of the wires to the test results cannot be excluded, especially when keeping in mind that the units have potential to move in all degrees of freedom. It is reasonable to assume that the wires influenced the movement of an armour unit in at least one degree of freedom.

Furthermore, the wired armour units were packed in such a way that movement was likely to occur. It is the question whether the measurements were also representative for an armour unit packed in a breakwater stability test. To answer this, a test could be considered in which a larger amount of armour units is equipped with accelerometers, with a packing similar to a stability test.

The analysis of the acceleration peaks results in relationships with velocities that only have an empirical basis. However, a large scatter, resulting in a large deviation of 20%, makes the chosen trends empirically weak. Therefore, with respect to accuracy, it is advised to apply numerical integration.

In addition, the accelerometer tests were conducted without a variation of the wave steepness. Therefore the accelerations were only related to the wave height. Consequently, it is not known whether the wave period has influence on the magnitude of accelerations.

The relationships from the research deducted by CUR C70 show that there are differences between the movements of the cube compared to the Tetrapode. Consequently, it is not possible to apply the relationships directly to other types of armour units.

Considering the momentum, it is striking that the modes of movement were restricted to only rotation or translation. Combinations of translations and rotations were excluded with this choice. These modes of movement were based on theoretical analysis and simplistic user observations during the wave flume tests. However, specific research to this matter was not conducted and therefore the scientific strength is still low. Furthermore, the percentage of Tetrapodes that translated and rotated was not verified by research. The same applies for the place of collision on an armour unit and the effective mass.

#### 2.1.4. LOAD-TIME RELATION

For the determination of the stresses in an armour unit, the next step was to establish a relation between the momentum and forces. Therefore, as a function of the velocity of collision, momentum and the material contact stiffness, the force-time relationship during collision was obtained. The applied force-time model is shown in Figure 2.2. This diagram is established based on the theory of Hertz (Mier & Lenos, 1991). The maximum force  $P_m$  in the armour unit was obtained from this diagram by deriving the maximum value.

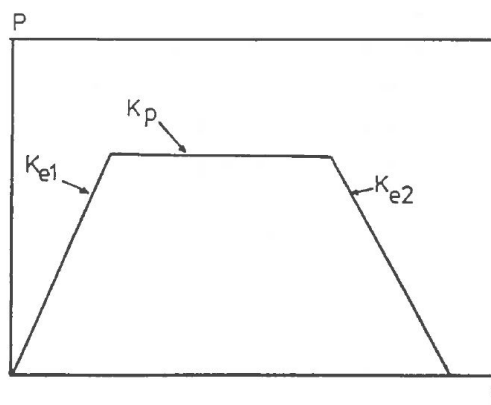


Figure 2.2: Force-Time relationship (CUR, 1990a)

The parameters  $K_{e1}$  [ $N/mm^{1.5}$ ],  $K_{e2}$  [ $N/mm^{1.5}$ ] and  $K_p$  [ $N$ ] shown in Figure 2.2 are concrete contact stiffness parameters and were applied for a specific part of the force-time diagram in Figure 2.2. The upward trend took into account the elastic deformation in concrete. The horizontal trend was the plastic deformation and the downward trend represented the restitution of force. Theoretically, the area underneath the diagram represented the momentum of the colliding unit.

Depending on the magnitude of mass or velocity (combination of the two resulted in momentum) the collision could

be either elastic or plastic. In case an elastic collision occurred, Figure 2.2 turned into a profile without horizontal trend. To determine whether a collision was plastic or elastic parameter  $K_p$  [N] was applied (CUR , 1990b):

$$K_p = \left( \frac{d}{420} \right)^2 90^2 \frac{\pi}{4} \frac{B}{45} \quad (2.24)$$

Parameter  $d$  [mm] represented the diameter of the leg of the armour unit and parameter  $B$  [N/mm<sup>2</sup>] represented the compressive strength. In CUR C70, this equation was used as a starting point for determination of the maximum force during collision. Parameter  $K_p$  [N] was compared to the maximum theoretical force ( $P_{max,2}$  [N]) developed over time ( $T_{max,2}$  [s]) in the descending branch (CUR , 1990b):

$$P_{max,2} = (1.25 \alpha V^2 K_{e2}^{0.65})^{0.6} \quad (2.25)$$

$$T_{max,2} = 1.47 (1.25 \alpha / (V^{0.5} K_{e2}))^{0.4} \quad (2.26)$$

Parameter  $V$  [m/s] was the velocity before collision ( $V_{collision}$ ) calculated in Subsection 2.1.3. In case  $P_{max,2}$  was larger than  $K_p$  the collision was plastic, otherwise the collision was considered to be elastic. Please note that a plastic collision was not defined for the cube, since during the tests only elastic behaviour was observed. In case an elastic collision occurs, the following relationships were applied for the descending branch (CUR , 1990b):

$$T_{e2} = \frac{T_{max,2}}{\pi/2} \arccos \left( \frac{P_{max,2} T_{max,2} - (0.5MV) 0.5\pi}{P_{max,2} T_{max,2}} \right) \quad (2.27)$$

$$P_{e2} = P_{max,2} \sin \left( \frac{T_{e2} \pi/2}{T_{max,2}} \right) \quad (2.28)$$

In case of a plastic collision, the following relations were applied for the descending branch (CUR , 1990b):

$$T_{e2} = \frac{T_{max,2}}{\pi/2} \arcsin \left( \frac{K_p}{P_{max,2}} \right) \quad (2.29)$$

$$P_{e2} = K_p \quad (2.30)$$

Subsequently, the rising branch was characterized (CUR , 1990b):

$$P_{max,1} = (1.25 \alpha V^2 K_{e1}^{0.65})^{0.6} \quad (2.31)$$

$$T_{max,1} = 1.47 * (1.25 \alpha / (V^{0.5} K_{e1}))^{0.4} \quad (2.32)$$

$$T_{e1} = \frac{T_{max,1}}{\pi/2} \arcsin \left( \frac{P_{e2}}{P_{max,1}} \right) \quad (2.33)$$

The surface area ( $A1$  [kgm/s]) underneath the rising branch was calculated as follows (CUR , 1990b):

$$A1 = \frac{P_{max,1} T_{max,1}}{\pi/2} \left( 1 - \cos \left( \frac{T_{e1}}{T_{max,1}} \pi/2 \right) \right) \quad (2.34)$$

In case of an elastic deformation, the surface area underneath the descending branch was (CUR , 1990b):

$$A2 = 0.5MV \quad (2.35)$$

For a plastic collision, the following relationship for the surface area underneath the descending branch was applied (CUR , 1990b):

$$A2 = \frac{P_{max,2} T_{max,2}}{\pi/2} \left( 1 - \cos \left( \frac{T_{e2}}{T_{max,2}} \pi/2 \right) \right) \quad (2.36)$$

After construction of the force-time relationship, the maximum force ( $P_m$ ) was determined. Parameter  $P_m$  [N] was considered to be equal to  $P_{e2}$  [N]. In addition, the time span in which the maximum force was built up ( $T_m$  [s]) was equal to  $T_{e1}$  [s]. For a plastic collision the following relations were applied for the time span (CUR , 1990b):

$$T_p = \frac{MV - (A1 + A2)}{P_{e2}} \quad (2.37)$$

$$T_m = T_{e1} + T_p \quad (2.38)$$

#### ANALYSIS

The force from plastic deformation was always assumed to be constant. In practice this does not have to be the case, since hardening or softening of the material can occur during the loading (Mier & Lenos , 1991).

In addition, the force-time diagram was verified with experiments. The behaviour of a concrete cube was observed by slamming it into a concrete cone. Consequently, it was concluded that the theory represents the situations in practice. It was therefore assumed that the concrete armour unit behaviour represents the test set-up.

Lastly, the surface area of the diagram was assumed to be equal to momentum. In reality however, due to crushing and deflection under collision the values may be slightly different.

#### 2.1.5. STRESSES

The stresses in the armour unit followed from the maximum force and the theoretically determined failure mode and critical cross section of the unit. For Tetrapodes breakage was most likely caused by the bending moment. The critical section was at the beginning of the leg (Horden , 1986). In the design procedure it was chosen to keep the position of critical stresses variable by introducing parameter  $arm_S$  [-]. This parameter represented the relative distance from the rotational point to the position where the critical stresses were considered. The governing stresses ( $\sigma$  [N/mm<sup>2</sup>]) for Tetrapodes were calculated as follows:

$$\sigma = arm_S 22.3 P_m / D_n^2 \quad (2.39)$$

For the cube it was determined that the tensile stresses perpendicular to the plane (in Dutch: spltjsterkte) were governing. The following relation was used to calculate the stresses:

$$\sigma = 0.64 P_m / D_n^2 \quad (2.40)$$

#### ANALYSIS

The shown relations show minor differences with derived relationships from theory. Since the approach is only explained shortly (CUR , 1989), it is unclear what is causing these differences.

In addition, the analytically determined critical stresses were assumed to represent reality in order of magnitude and failure mode. Since a very simple linear elastic approach was followed, it is recommended to use more accurate models for higher accuracy in results. Another important point is that the stresses were assumed to be independent from the duration of the collision.

In terms of armour unit type dependencies, attention should be given to the type of collisions and governing type of stresses in the critical cross-section. Therefore an independent assessment is necessary for each type of armour unit.

### 2.1.6. STRENGTH

The actual concrete strength was needed to conclude whether an armour unit fails. The strength was compared with the stresses calculated in Subsection 2.1.5. A calculation was done by multiplying the characteristic axial tensile strength of a cylinder with diameter of 150 *mm* and height of 600 *mm* with the following correction factors for (CUR, 1989):

1. Volume
2. Temperature
3. Duration of collision

Correction factors for fatigue were not taken into account, since these effects only play an important role after 10 collisions. It was assumed that not many elements collide more than 10 times. A reduction of the tensile strength was considered for a larger volume than the considered cylinder (parameter  $K_v$  [-]). According to Equation 2.41, parameter  $V_0$  was the volume of the considered cylinder and  $V$  was the volume of the part of the armour unit under the governing tension. Assumed was that for Tetrapodes this volume is equal to 1/10 of the total volume of the armour unit.

$$K_v = \left( \frac{V}{V_0} \right)^{0.04} \quad (2.41)$$

Equation 2.41 was rewritten as function of the nominal diameter  $D_n$  for Tetrapodes:

$$K_v = 0.94D_n^{-0.12} \quad (2.42)$$

For cubes in a double layer, the total volume of the armour unit was taken into account:

$$K_v = 0.80D_n^{-0.12} \quad (2.43)$$

Residual stresses in concrete occur due to the unequal distribution of heat production during hardening. This results in tensile stresses in the core and compressive stresses in the outer part of the armour unit. Therefore a reduction of tensile strength was taken into account, which was based on the following conditions: a temperature of the surroundings of 15 degrees Celsius, an initial armour unit temperature of 25 degrees Celsius and a blast furnace 'A' cement composition with an amount of 325 *kg/m*<sup>3</sup>. The derived reduction for the tensile strength ( $K_t$  [-]) is shown in Equation 2.44 for Tetrapodes. For cubes in a double layer, Equation 2.45 was used.

$$K_t = 0.84D_n^{-0.20} \quad (2.44)$$

$$K_t = 0.74D_n^{-0.20} \quad (2.45)$$

The effect of the duration of the collision on the strength of concrete was given as a correction factor  $K_S$  [-] in Equation 2.46. Parameter  $S$  represented the actual collision duration in *N/mm*<sup>2</sup>*s* in which the duration was taken from the rising and horizontal branch of the force-time relationship, representing the time for development of the maximum force. Parameter  $S_0$  was considered to be the reference duration of 0.1 *N/mm*<sup>2</sup>*s*.

$$K_S = (S/S_0)^{0.42} \quad (2.46)$$

A combination of the correctional factors resulted in a relationship for the Tetrapode's strength ( $f_c$  [*N/mm*<sup>2</sup>]):

$$f_c = 0.94D_n^{-0.12} 0.84D_n^{-0.20} (S/S_0)^{0.42} f_{c0} \quad (2.47)$$

The total strength for cubes in a double layer was calculated as following:

$$f_c = 0.80D_n^{-0.12} 0.74D_n^{-0.20} (S/S_0)^{0.42} f_{c0} \quad (2.48)$$

## ANALYSIS

An expression is given in literature for the concrete strength taking into account the volume and temperature factors (CUR , 1989). This expression is however different from the derivation shown in Equations 2.47 and 2.48. Since only a short derivation is shown in literature (CUR , 1989), the reason behind the differences remains unclear.

### 2.1.7. COMPUTER APPLICATION “ROCKING”

The design procedure and probabilistic method were incorporated in a computer program called “Rocking”. In summary, the estimation of the probability of breakage was done with a Monte Carlo simulation. This probability of breakage was consequently multiplied with the calculated number of moved units. As a result, the number of broken units was displayed. The layout of the computer program is shown in Figure 2.3.

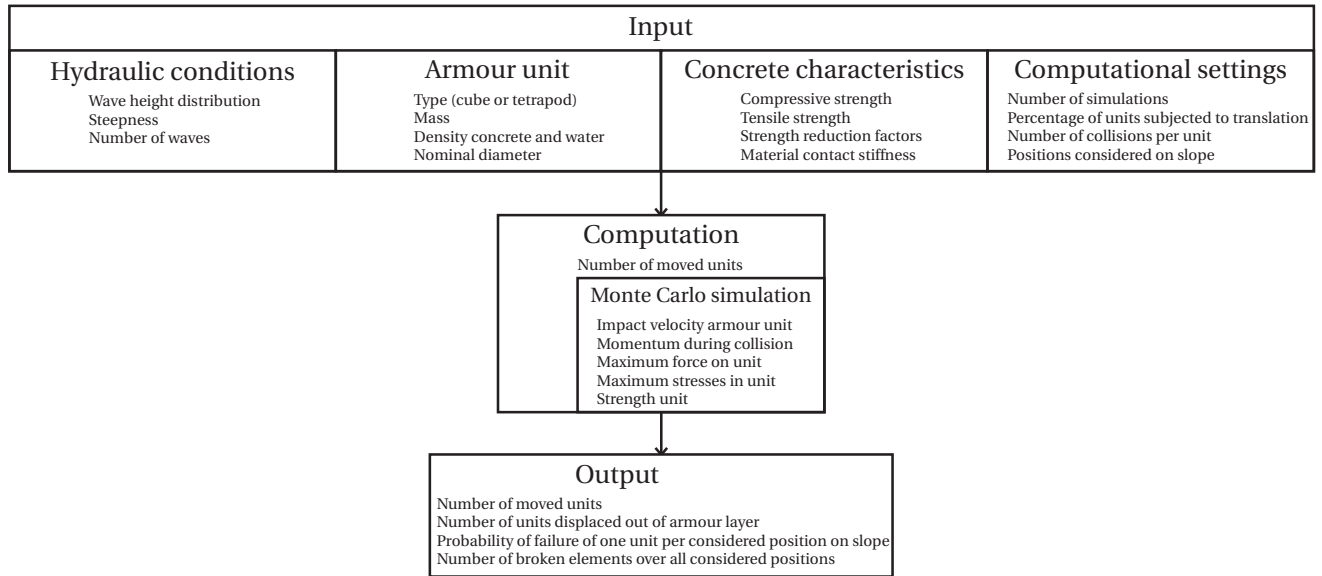


Figure 2.3: Structure Computer Application Rocking

As shown in Figure 2.3 the computer model asked the user to submit generic details about the wave conditions, armour units, concrete and computational settings. Consequently, the program computed the probability of breakage of an armour unit according to a Monte Carlo simulation, excluding the calculation of the number of moved units. The armour unit is considered to be broken if the stresses exceed the strength:

$$\sigma > f_c \quad (2.49)$$

The probability of failure was calculated as following:

$$P(\text{Failure one element}) = \frac{\text{Number of simulations resulting in failure}}{\text{Total number of simulations}} \quad (2.50)$$

Subsequently, the program gave an output with the number of moved units and number of displaced units. The number of broken elements on the breakwater slope was calculated as a function of the probability of breakage and the number of moved units:

$$N_{broken} = f(N_{otot} P(\text{Failure one element})) \quad (2.51)$$

A chart of all processes can be found in Appendix A and a script of the numerical model can be found in Appendix B.

## ANALYSIS

It has to be kept in mind that the input value for wave steepness was only used in the relation of the number of moved units, see Equations 2.3 and 2.4. The relationships for impact velocities were independent from the wave steepness (Equations 2.12 and 2.15).

An error in the script is found in the velocity distribution. In "Handleiding Rocking" (1990) the constants  $B$  and  $C$  in Equation 7 were erroneously interchanged. Parameter  $C$  is supposed to represent the lower limit of the distribution. Parameter  $B$  represents the position of the distribution. The parameters are shown correctly in literature (CUR, 1989). Therefore, it is recommended to adjust the script to literature.

In addition, it is recommended to perform a FORM analysis after one is certain of the quality of the script. With the FORM analysis, an understanding of the influence of the inserted parameters can be found, or in other words, the sensitivity of the parameters is found. This allows the developer to see which parameters influence the outcome most and with that, the developer knows which parameters to fine tune to come to a reliable result. Furthermore, a more detailed analysis of the deterministic input parameters is recommended, to determine that they are actually non-variable.

## 2.2. ALTERNATIVE METHODOLOGY

An alternative research was done by multiple European institutes. This research with Aalborg University as leading institute (up to 1995) was set up to contribute to the development of rational methods for the design of rubble mound breakwaters (Burcharth & Zhou, 1995) and was structured in three main tasks:

1. Structural integrity of concrete armour units
2. Displacement failure modes
3. Design guidelines

Under the first task research was done, among other topics, on stresses in Tetrapodes and Dolosses. The difference between the CUR C70 methodology was that the stresses were measured directly using a sensitive strain gauge load-cell technique (Scott, Turcke & Baird, 1986). An advantage of this direct method was that less calculations were needed to come to the desired results. A disadvantage of this method was that the armour unit consists of different material, which may have an influence on the impact loads. Furthermore, the elasto-plastic effect and the force-time behaviour of concrete armour units were not taken into account. From the experiments the maximum tensile stresses were directly related to the wave height for Dolosse. One of the applications of this relationship is shown in Figure 2.4 (Burcharth, 1992). From the design graphs in Figure 2.4, the Dolosse waist ratio could be estimated with a given failure probability of 1 percent, a concrete tensile strength, a Dolosse mass and a significant wave height.

Also an analysis for Tetrapodes was done for the number of impacts, location of impacts and impact stresses (Nes, 1994). The goal was to derive probabilistic parameters from the results. However, because of the large variations in results, it was recommended to do more research to establish a probabilistic relation.

Furthermore, research was done on concrete fatigue. From the research results it was concluded that fatigue plays an important role, if the number of collisions of an armour unit is above 10. This implies that more impacts will result in a significant higher probability of failure.

## 2.3. ADDITIONAL LITERATURE

### DEBRIS LOCATION TRACKING

Natural disasters can cause on-land water flows, which lead to potential displacement of debris and potential impacts of the debris into structures. In Goseberg, Nistor & Stolle (2015) a measurement system was developed, named as "smart debris", to determine these impacts. A rectangular, waterproof box was equipped with an accelerometer, magnetometer and gyroscope. The box represented a scale model of the debris and had the purpose to simulate and capture the movements and orientation of debris. The data was stored using internal memory in the box. In addition, the device was equipped with a real-time locating system that used a wireless position sensor. A similar device can be used to measure movements and impacts of armour units on a breakwater slope. Issues such as size, sampling frequency and synchronization between sensors have to be kept in mind during development.

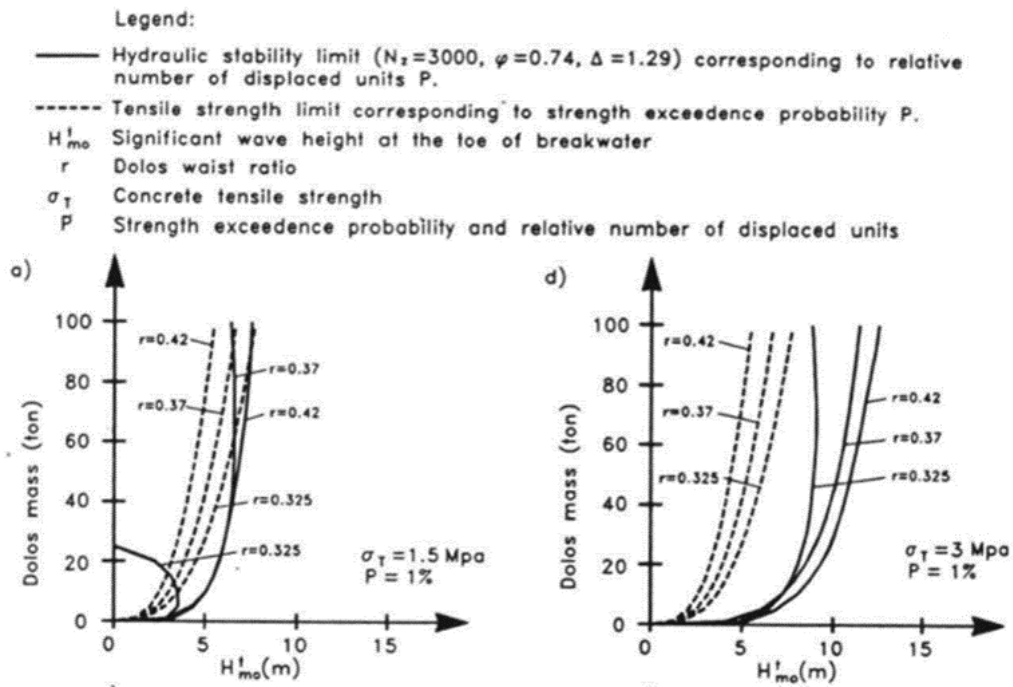


Figure 2.4: The determination of the Dolosse dimensions from design graphs (Burcharth , 1992)

#### NUMERICAL MODELLING OF FORCES, STRESSES AND BREAKAGES OF CONCRETE ARMOUR UNITS

To provide virtual breakwater design tools, as replacement for physical models, a numerical model, known as FEM-DEM (combined finite-discrete element method) is under development (Latham et al. , 2014). This model can potentially determine the stresses inside armour units as a function of wave parameters and the strength of armour units. However, it has to be kept in mind that currently, many processes are simplified and require more development. Furthermore, the model is computationally expensive and needs to be optimised (Latham et al. , 2014).

# 3

## ANALYTICAL MODEL

The movements of armour units are reassessed. In this chapter detailed information is given for the wave forcing on and the resulting movements of the armour units. In analogy with the results of Section 2.1.3 the movements are expressed in terms of accelerations and velocities.

Hofland (2005) measured turbulence induced motions of flow over a rock bed and observed mostly rotation under moving stones. Armour units are expected to behave similarly and therefore a rotational mode of movement is considered. An armour unit rotates around a point at the upper end of the unit, see Figure 3.1. The movement is stopped after collision with the base or with another armour unit. As a result, the moment of force of the moving unit is transferred into the object of collision. If it is assumed that all moment of force is transferred, the moment of force produced by movement must be equal to the moment of force on the object of collision.

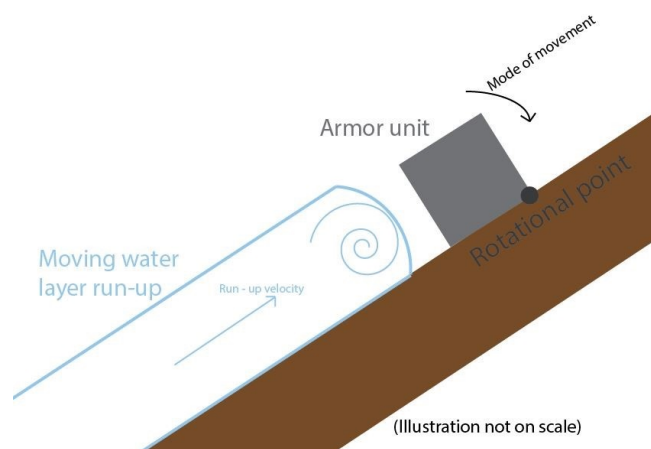


Figure 3.1: Wave run-up on slope with protruding element

A number of assumptions are made in the analytical procedure. Therefore, the calculations cannot replace wave flume tests. The analytical procedure has the purpose to provide a general physical understanding of the movements of an armour unit on a breakwater slope. All assumptions are discussed in Section 3.4.

### 3.1. OVERVIEW

The magnitude of the loads acting on the armour units is influenced by the ocean wave characteristics and the wave-structure interaction. To include all relevant physical processes, a derivation from the equation by Morison, O'Brien, Johnson & Schaaf (1950) is used. This equation consists of a wave forcing which is dependent on the drag, inertia and added mass. For plunging breakers, an additional impact force based on Goda et al. (as cited in Chella, Torum & Myrhaug (2012)) is added to the Morison Equation. The magnitude of the forcing is, among others, dependent on the run-up and run-down velocity and acceleration. This velocity on a slope can be estimated with a relation proposed

by Van Gent (2002) and Schuttrumpf & Oumeraci (2005). Furthermore, the inertia term in the equation derived from Morison, O'Brien, Johnson & Schaaf (1950) is taken to be equal to the change of the wave velocity of a sinusoidal wave.

With these assumptions, the movements are initiated in case the torque by a wave load exceeds the resisting torque by gravity. The magnitude of movement is expressed with Newton's second law, in which the acceleration is calculated as a function of the sum of forces and mass of the element. The resulting velocity before collision is calculated with the distance over which the unit rotates.

### 3.2. WAVE LOADING

The water movement during run-up is shown in Figure 3.1. The armour unit undergoes a sudden forcing of the wave during run-up. The order of magnitude of forcing is different for different breaker types. Plunging breakers are observed to have breaking jets that contribute to the forcing of the armour unit. This impact force, derived by Goda et al. (as cited in Chella, Torum & Myrhaug (2012)), is taken into account in Equation 3.3. After the first impact, drag and inertia forces dominate as a consequence of the water flow during run-up and run-down. Equation 3.2 is derived from Morison, O'Brien, Johnson & Schaaf (1950) to determine the drag and inertia forces on an armour unit. It is assumed that the unit is totally under water. The resisting force against movement is the gravitational force, see Equation 3.1. A detailed explanation of the various parameters in the Morison equation and impact force is given in this section.

$$F_z = (\rho_s - \rho_w)gV \quad (3.1)$$

$$F = \frac{1}{2}\rho_w AC_D(u - u_p)^2 + (1 + C_a)\rho_w V_w \frac{D(u - u_p)}{Dt} - \rho_w C_a V_w \frac{Du}{Dt} \quad (3.2)$$

$$F_I = \frac{1}{2}\rho_w C_s DC_b^2 h \quad (3.3)$$

$\rho_s$  = Density of armour unit [ $kg/m^3$ ]

$\rho_w$  = Density of water [ $kg/m^3$ ]

$A$  = Surface area of wave forcing [ $m^2$ ]

$u$  = Velocity of water [ $m/s$ ]

$u_p$  = Velocity of unit [ $m/s$ ]

$V$  = Total volume armour unit [ $m^3$ ]

$V_w$  = Volume over which the wave forcing acts [ $m^3$ ]

$C_D$  = Drag coefficient [-]

$C_a$  = Inertia coefficient [-]

$C_s$  = Slamming force factor [-]

$C_b$  = Breaking wave celerity [ $m/s$ ]

$D$  = Diameter unit [ $m$ ]

$h$  = Height unit [ $m$ ]

Equation 3.2 can be divided in three terms. The first term represents the drag force, the second term the inertia and the last term the added mass. The impact force shown in Equation 3.3 is added to the Morison Equation in case plunging breakers are considered.

Equation 3.3 is derived from a relation for round, slender structures. The following equation by Goda et al. (as cited in Chella, Torum & Myrhaug (2012)) is used as starting point:  $F_I = \frac{1}{2}\rho_w C_s DC_b^2 \lambda \eta_b$ . Here,  $F_I$  is the slamming force,  $C_s$  is the slamming force factor equal to  $2\pi$ ,  $C_b$  is the breaking wave celerity,  $\lambda$  is the curling factor which indicates the percentage of active forcing in the wave crest. Lastly  $\eta_b$  indicates the surface elevation. This equation is modified for usage on the schematised breakwater slope. The armour unit is assumed to be under the category of slender structures ( $D \ll L$ ), which corresponds to the cases used in Goda et al. (as cited in Chella, Torum & Myrhaug (2012)). In addition, the forcing is assumed to work over the entire front surface area of the armour unit, as the schematised slope does not give any shelter from wave run-up against the unit. Besides, the wave height, which results in a similar

water layer thickness during run-up, is assumed to be larger than the height of the cube. Therefore, the total height of the cube is exposed to wave attack. Consequently, the terms  $\lambda\eta_b$  are replaced by  $h$ , see Equation 3.3. Furthermore, the different dynamic response of the cubic armour unit, in relation to the round structures, which lead to different rising time and different maximum impact forces, are not taken into account.

The  $C_D$  and  $C_a$  coefficients are empirically determined constants and are dependent on the Reynolds number, shape, size and roughness of the unit, wave height and period (Journée, Massie, 2001). Typical values for the  $C_D$  coefficient are ranging between 0.5 and 2. A typical drag coefficient of 1.05 in turbulent flow applies for cubes (Sadraey, 2012). The  $C_a$  coefficient has typically a value between 0 and 1. This coefficient is equal to 0.6 for cubes (Sarpkaya, 2010).

The acceleration of the water in Equation 3.2 is assumed to be equal to the change in velocity profile with time span equal to a quarter of the wave period. This applies for a sinusoidal velocity profile in time, provided that the run-up and run-down period approximates the wave period.

A method to determine the wave run-up velocities is provided by Van Gent (2002) and Schüttrumpf & Oumeraci (2005). The researchers based the expression on a uniform flow with a certain layer thickness and on measurements on top of a dike crest. The derived relationship is shown in Equation 3.4. In this representation the equation can be applied for regular waves. However, the equation is suited for both regular and irregular waves, according to the research conducted by Schüttrumpf (as cited in Schüttrumpf & Oumeraci (2005)). For irregular waves values with a probability of exceedance of 2% apply for the velocity and run-up. In addition, a significant wave height  $H_s$  is used. By changing the freeboard for the position of the calculated armour unit, a first estimation of the velocity is obtained. It is assumed that the run-up velocity is higher than the run-down velocity in case of an impermeable slope, without friction and overtopping. This is based on the expression for run-down in the Rock Manual (CIRIA, CUR & CETMEF, 2007), which gives lower values than the run-up. To quantify the run-down, the run-down velocity is taken into account with the same value as the run-up velocity, to be conservative. The parameters of Equation 3.4 are explained in more detail below.

$$u = \sqrt{Hg} c_u \sqrt{\frac{Ru - r}{\gamma_f H}} \quad (3.4)$$

$H$  or  $H_s$  = Significant wave height [m]

$g$  = Gravitational constant [ $m/s^2$ ]

$c_u$  = Empirically fitted constant [-]

$Ru$  or  $Ru_{2\%}$  = Run-up height [m]

$r$  = Freeboard [m]

$\gamma_f$  = Correction factor for slope roughness [-]

Parameter  $c_u$  is an empirically determined constant equal to 1.37 (Schüttrumpf & Oumeraci, 2005). Furthermore, a slope correction factor equal to 1 is used, since a smooth slope is considered. For the run-up height, the expression provided by Hunt (as cited in Battjes (1969)) is applied. For regular waves the used expression is shown in Equation 3.5. For irregular waves (See Equation 3.6), the 2% probability of exceedance is used for the run-up expression, together with the wave height  $H_s$  and indirectly the mean wave period  $T_m$ .

$$R_u = c_1 H \frac{\tan(\alpha)}{\sqrt{H/L_0}} \quad (3.5)$$

$$R_{u_{2\%}} = c_1 H_s \frac{\tan(\alpha)}{\sqrt{H_s/L_0}} \quad (3.6)$$

In which constant  $c_1$  is for regular waves equal to 1.0 and for irregular waves 1.5. For surging breakers ( $\xi$  and  $\xi_m < 1.8$ ) the run-up is limited to  $R_u/H = 3.0$  and  $R_{u_{2\%}}/H_s = 3.0$ . The Iribarren numbers  $\xi$  and  $\xi_m$  are defined as following:

$$\xi = \frac{\tan(\alpha)}{\sqrt{H/L_0}} \quad (3.7)$$

$$\xi_m = \frac{\tan(\alpha)}{\sqrt{H_s/L_0}} \quad (3.8)$$

$$(3.9)$$

In which  $L_0 = (g * T^2)/(2\pi)$  for regular waves and  $L_0 = (g * T_m^2)/(2\pi)$  for irregular waves.

From the expressions given in this section, it is concluded that the breakwater configuration has an important role in the magnitude of the forcing. Furthermore, the wave characteristic that play an important role are the wave height and period.

### 3.3. MOMENT OF FORCE

The estimated wave forcing can be used to determine the initiation and magnitude of movement in terms of accelerations and velocities. The way a unit moves is assumed to be majorly rotations, based on the measurements by Hofland (2005). Newton's second law is used to come with the desired results ( $F = Ma$ ). This law is rewritten in terms of rotation, as shown in Equation 3.10.

$$\Sigma[F l] = I_0 \alpha_u \quad (3.10)$$

The expression on the left hand side in Equation 3.10 is the summation of the forces multiplied by their lever  $l$  [m] contributing to the torque around the rotational point. Parameter  $I_0$  [ $kgm^2$ ] represents the moment of inertia of the armour unit around the rotational point. The angular acceleration  $\alpha_u$  [ $rad/s^2$ ] is estimated after the determination of the other parameters in the expression. The acceleration of the center of an armour unit is finally obtained after multiplying the angular acceleration with the distance from rotational center to the center of mass.

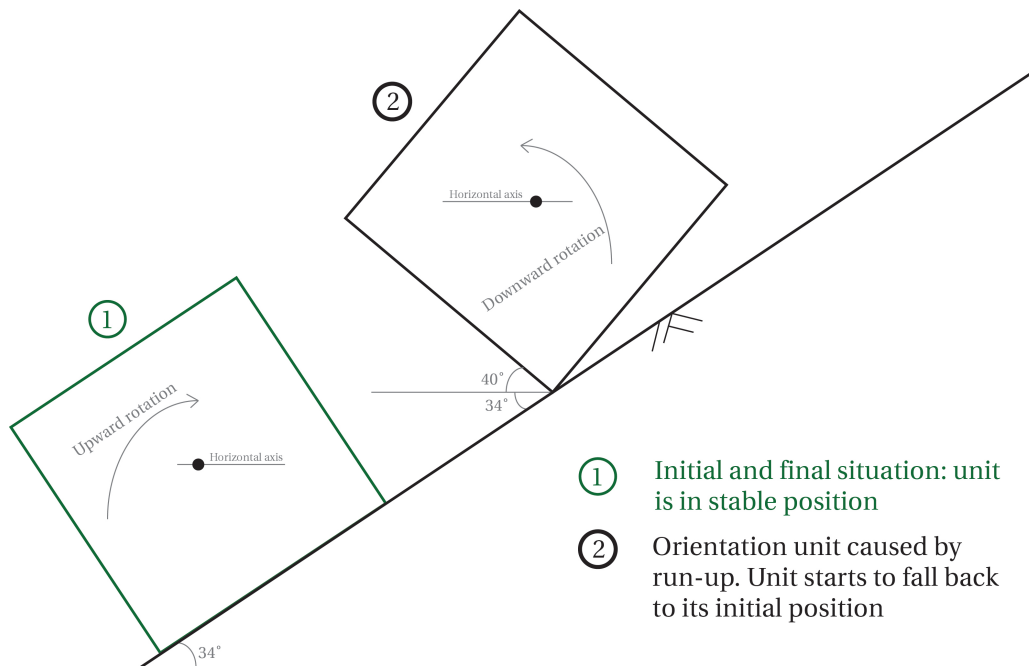


Figure 3.2: Rotations of the armour unit

A visualization of the movement of an armour unit is shown in Figure 3.2. Two types of accelerations can be distinguished: The first type includes the accelerations from the initiation of movement. The second type includes accelerations from a unit in an unstable position, falling back to the initial state. The wave run-up applies for the first type and the wave run-down applies for the second type. The magnitude of acceleration of the two types differs, since the

direction and angle of the forces relative of the orientation of the slope is different. Moreover, impact forces are not taken into account in the run-down.

An application is conducted for the situation during wave run up, as described in Figure 3.1. First, the gravitational force on the x and y axis parallel and perpendicular to the slope is determined as following:

$$F_{z_{y1}} = (\rho_s \cos(\alpha) - \rho_w) g V \quad (3.11)$$

$$F_{z_{x1}} = \rho_s g V \cos(90 - \alpha) \quad (3.12)$$

Next, the lever of the forcing around the rotational point is described for run-up as following:

$$l_{F_{z_{y1}}} = l_{F_{z_{x1}}} = l_{F_1} = 0.5 D \quad (3.13)$$

This results in the torque around the rotational point during run-up in which F is calculated with Equation 3.2 (and Equation 3.3 dependent on the breaker type):

$$\Sigma[F l] = l_{F_{z_{y1}}} F_{z_{y1}} + l_{F_{z_{x1}}} F_{z_{x1}} - F l_{F_1} \quad (3.14)$$

For run-down the following relations apply, in which  $\theta$  represents the turning angle equal to 40 degrees relative to the slope:

$$F_{z_{y2}} = (\rho_s \cos(90 - \alpha - \theta) - \rho_w) g V \quad (3.15)$$

$$F_{z_{x2}} = \rho_s g V \cos(\alpha + \theta) \quad (3.16)$$

$$l_{F_{z_{y2}}} = 0.5 D \cos(90 - \alpha - \theta) \quad (3.17)$$

$$l_{F_{z_{x2}}} = 0.5 D (\tan(45) + \sin(90 - \alpha - \theta)) \quad (3.18)$$

$$l_{F_2} = 0.5 D \cos(\theta) \quad (3.19)$$

$$\Sigma[F l] = -l_{F_{z_{y2}}} F_{z_{y2}} + l_{F_{z_{x2}}} F_{z_{x2}} + F l_{F_2} \quad (3.20)$$

To work to a solution for the angular acceleration, the moment of inertia is calculated. First the moment of inertia of the cubes' center is calculated:

$$I_{gs} = \frac{1}{6} \rho_s D^5 \quad (3.21)$$

Next, the moment of inertia around the rotational point is established:

$$I_0 = I_{gs} + (0.5D)^2 M \quad (3.22)$$

With Equation 3.10 the angular acceleration is determined. The acceleration in the center of the armour unit is obtained with:

$$\alpha = \alpha_u \sqrt{(1.5 D)^2 + (0.5 D)^2} \quad (3.23)$$

The timespan in which the unit accelerates is calculated with the relation  $s = 0.5at^2$ . The distance is taken to be equal to the vertical distance that the leg of the unit travels over the rotational angle. Subsequently the maximum velocity during movement is estimated with  $V = at$ .

To determine whether the analytical model represents the velocities before collision in a realistic manner, the outcome of the analytical model is compared with the velocities before collision from the wave flume tests with regular waves. Tables 3.1 and 3.2 show the results of surging and collapsing breakers respectively. It is chosen to compare the velocities before collision from upward movement, as Equation 3.4 is derived for upward movement only. Therefore,

the results from the analytical model for upward movement are assumed to be more representative. Furthermore, the velocities before collision are presented in  $[rad/s]$  because the results of the wave flume tests are in  $[rad/s]$ , see Chapter 5.

Table 3.1: Velocities before collision from analytical model,  $s = 0.02$ , upward rotation

Wave height $H$ [m]	Velocity before collision $\omega$ [rad/s]
0.11	68
0.14	76
0.16	83
0.19	90
0.21	96

Table 3.2: Velocities before collision from analytical model,  $s = 0.08$ , upward rotation

Wave height $H$ [m]	Velocity before collision $\omega$ [rad/s]
0.11	128
0.14	143
0.16	156
0.19	169
0.21	180

### 3.4. ANALYSIS AND EXPECTATIONS

To determine the accelerations and velocities analytically, it is inevitable to make simplifications. These simplifications lead to deviations with the results obtained in for instance wave flume tests. A summation of the assumptions and an explanation of the possible deviations in results are shown in the following paragraphs.

The first assumption is made for the flow surface area. It is assumed that the drag works over the entire front area of the cube. It is imaginable that this is different in practice. For instance, there is a possibility that the layer thickness of the wave run-up is smaller than the height of the cube, which implies that the flow surface area becomes smaller. Next to that, the wave impact might not be right on the front surface of the cube, or might not work over the entire front surface. This results in a smaller surface area subjected to the breaker. The second assumption is regarding the usage of the relation for impact velocities by Goda et al. (as cited in Chella, Torum & Myrhaug (2012)) on an armour unit. The relation was derived for slender piles in deep water and hence, the physical behaviour of the water differs from the situation on the breakwater slope. Furthermore, the different dynamic response of the cubic armour unit, in relation to the round structures, which lead to different rising time and different maximum impact forces, are neglected. The third assumption is related to the velocity of the water. The velocity of the water on the slope varies over the flow depth and fluctuations in the form of vortexes might play an important role in the initiation of movement of an armour unit. The expression by Van Gent (2002) and Schuttrumpf & Oumeraci (2005) neglects these phenomena. The fourth assumption is regarding the wave run-down. It is assumed that the same water velocities occur with wave run-down in comparison with wave run-up. However, the expression by Van Gent (2002) and Schuttrumpf & Oumeraci (2005) was only derived for wave run-up. The fifth assumption is a constant acceleration of the water in time. The acceleration profile in reality can deviate from a constant relationship due to changes in flow pattern, flow velocity, magnitude and direction of forcing.

In terms of the magnitude of measurements it is expected that the velocities of the cube are generally lower in case of plunging breakers, since the wave impact contribution works over a short time span. It is also expected that the contribution of drag is smaller in case of plunging breakers. Drag is expected to be of influence later in time in relation to wave impact and hence, the influence to the movements of the cube is smaller, as movement is likely to be initiated by wave impact. Furthermore, it is questionable whether Equation 3.3 can be applied directly on a breakwater slope, as the equation is only verified for slender offshore structures.

The last assumption is regarding the accelerations of the cube with initiation of movement. The analytical method only takes into account accelerations at the start of movement. During movement the relative velocity in the Morison expression changes to the second order and the impact force of wave breaking is diminished. Therefore, it is expected that the magnitude of the accelerations differs. On the contrary, the surface area taken into account also changes since

the orientation, drag inertia and orientation of gravitational force changes. Therefore, it is hard to predict a value for the accelerations during movement and hence, the accelerations of the cube during movement are assumed to be equal to the start of movement.

Differences between the acceleration profiles are also found as a consequence of the exclusion of the measurement of the normal (centripetal) acceleration and the gravitational acceleration. Measured data of accelerations consist of three components. The first component gives information about the orientation of the unit and the second and third component are linked to movements. The analytical model only provides the accelerations in tangential direction of movement. It necessary to separate the three components in the measurement signal to come to a correct comparison of accelerations and velocities between the analytical model and the measurements.

# 4

## SET-UP AND EXECUTION EXPERIMENTS

The wave flume experiments have the purpose to review and update the results from computer application “Rocking”. This chapter discusses the important parameters, the test set-up and limitations of the test set-up. Furthermore, the scaling parameters are elaborated and information is given on the test equipment. In addition, the execution of the wave flume tests is discussed.

### 4.1. OVERVIEW

Chapter 3 shows that the determination of the wave forcing on an armour unit is a complicated process. Many parameters influence the movement of the armour unit. For the wave flume tests it is chosen to select the most important parameters as variables. From the equations for the run-up and run-up velocity (Equations 3.4 and 3.5) it is seen that these parameters are the wave height and wave period. Furthermore Sokolewicz (1986) showed that the position on the slope determines to great extend the magnitude of movement. Therefore the position on the slope is also taken into account as a variable. The test set-up is kept as simple as possible, similar to the analytical model in Chapter 3, to create reliable reference data for potential research in CFD-modelling. This implies a continuous smooth slope where overtopping does not play a role. To take into account the wave run-up, the slope is extended beyond the height of the flume. Additional tests are done with a more representative configuration for breakwaters using an embedded cube.

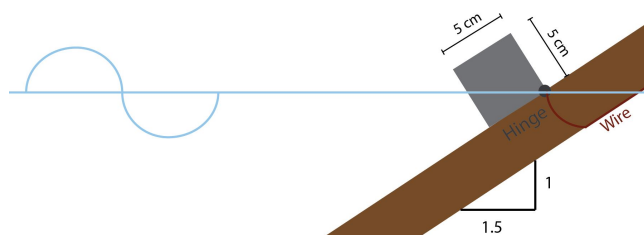


Figure 4.1: Illustration experimental setup - side view

#### 4.1.1. EXPERIMENTAL SET-UP

The set-up of the wave flume model is shown in Figure 4.1. A cube with a width and height of 5 cm is placed on a smooth, continuous slope (wooden base) of 1/1.5. The cube is attached to the slope with a hinge, allowing the cube to rotate in one direction. During sufficient wave run-up, the cube starts to move and collides eventually with the slope at a rotation angle of  $90^\circ$ . The cube falls back to its original position during run-down. The positioning of the cube relative to the water level is based on Sokolewicz (1986). In that research, the instrumented units were placed at four positions on the slope: at  $2D_n$  above mean water level, at mean water level,  $2D_n$  and  $4D_n$  below mean water level. With respect to time restrictions in the current research, the cube is placed at 3 positions relative to the water level:  $Y/D_n = -2$ ,  $Y/D_n = 0$ , and  $Y/D_n = 2$ . Parameter  $Y$  represents the position of the cube and  $D_n$  the nominal diameter. Consequently, the cube positions correspond to the first three positions used in Sokolewicz (1986). A visualisation of

the position of the cube is shown in Figure 4.2. Please note that the exact position of  $Y/D_n = 0$  is defined at the hinge. The positions were not defined exactly by Sokolewicz (1986). Furthermore, the hydraulic conditions are varied over the wave height, wave steepness and wave type.

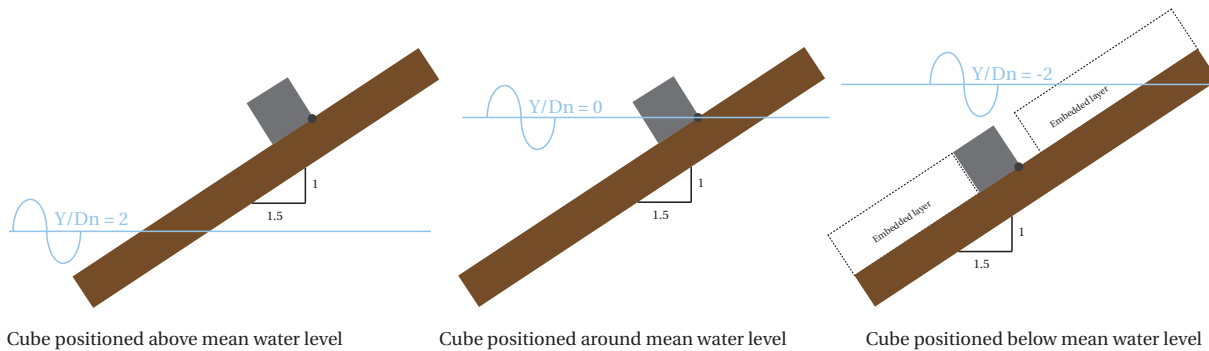


Figure 4.2: Position cube relative to mean water level - side view

Figure 4.3 illustrates a top view perpendicular to the wooden board. A second non-rotating cube is attached at a center to center distance of 25 cm from the rotating cube. This cube is equipped to measure the water pressure, with the purpose to provide reference data for CFD-modelling. The center to center distance is assumed to have negligible influence on the hydraulic forcing (Huis, Stuip, Walther & Van Westen, 1987). In addition, measurements of the wave run-up velocity are conducted. For this purpose it is necessary to allow an undisturbed run-up and run-down in one part of the base. Extra spacing is created on the left side of Figure 4.3.

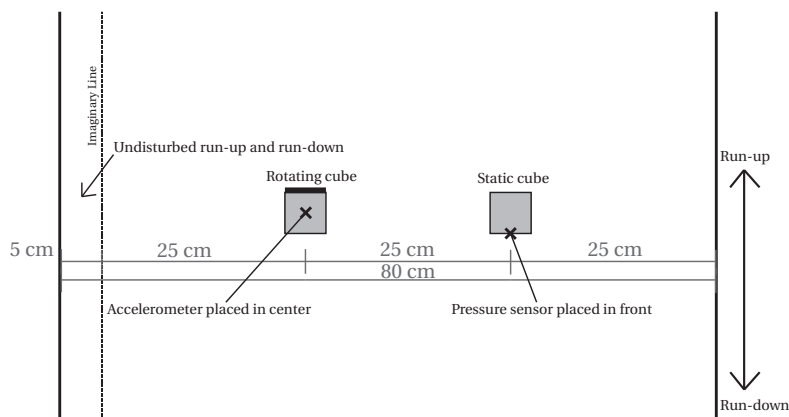


Figure 4.3: Illustration experimental set-up - top view perpendicular to slope

The second series of experimental runs consist of a slope configuration with the cubes surrounded by a representation of other breakwater cubes (embedded cube). The layer is designed such that it represents a single layer cube placed in the upper row of the slope, right below the transition with the crest. Due to the transitional gap between slope and crest in a prototype breakwater, a relatively high chance of movement is expected at that location. The other dimensions are based on a prototype single layer cube breakwater. For instance, the horizontal gap between the cube and wooden elevation represents a packing density of 25%. In vertical direction the cubes are piled up on top of each other, in which the center of the cube is vertically (parallel to slope) aligned with the gap in between two cubes in the row below, see Figure 4.4. The schematisation used in the experiments is shown in Figure 4.5, and in detail in Figure 4.6. In addition, to avoid entrapment of water in the trench, holes in the wooden base are necessary (Figure 4.6). Additional pictures showing the implementation of the test set-up in the wave flume are shown in Appendix C. The embedded cube is tested with a cube position relative to the water level of  $Y/D_n = -2$ , see Figure 4.2 for an illustration and Section 4.4 for more information.



Figure 4.4: Regular placement single layer cubes (Van Gent & Luis , 2013) - top view of physical model

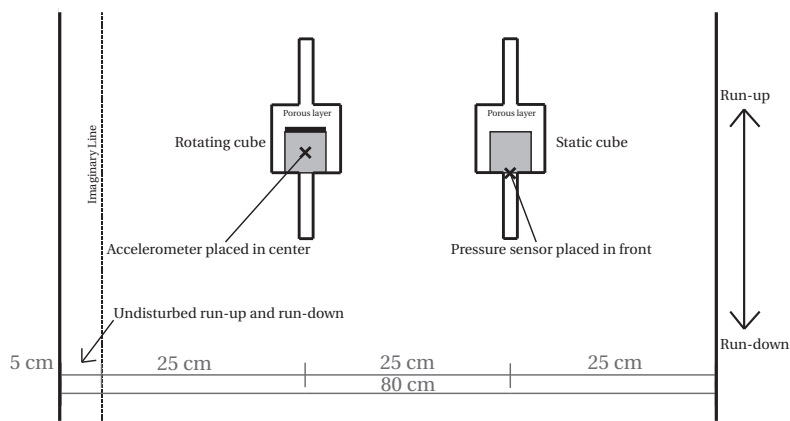


Figure 4.5: Illustration experimental set-up with embedded cube - top view perpendicular to slope

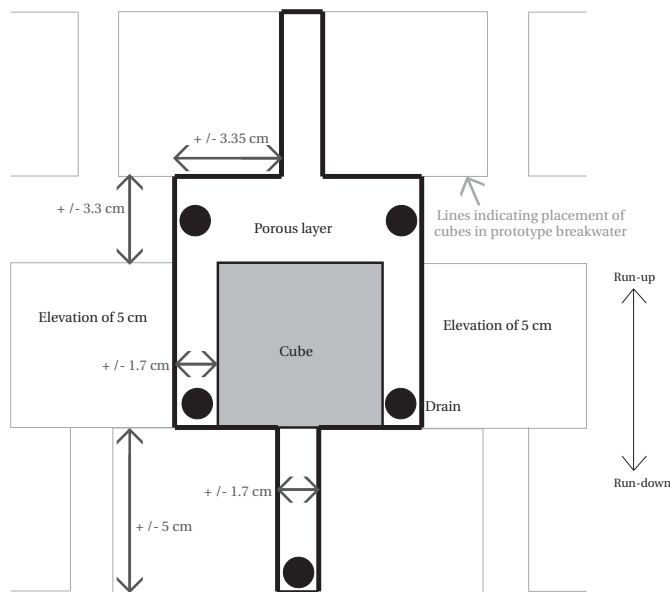


Figure 4.6: Detailed illustration of embedded cube near cube

### 4.1.2. LIMITATIONS

With the shown test set-up limitations are initiated. For instance, the breakwater porosity is not represented. Next to that, the slope roughness is not equal to the roughness of a prototype breakwater. Therefore, the test results are only valid for research purposes and cannot be applied directly to design guidelines.

### 4.1.3. WAVE FLUME

The experiments are performed in the wave flume in Stevinlab III of Delft University of Technology. The wave flume has dimensions of  $L \times b \times h = 45 \times 0.8 \times 0.95 \text{ m}$ . The wave generator in the flume is equipped with active wave absorption and can generate spectral wave periods from 0.85 s up to 4 s and spectral wave heights up to 0.18 m.

## 4.2. SCALING

The physical behaviour of a model has to represent the behaviour of the prototype breakwater. Therefore, various criteria of similitude have to be met (Frostick, McLelland & Mercer, 2011). The first criteria represents the geometric similarity. This implies that the geometry of the model has to represent the geometry of the prototype. The second criteria is the kinematic similarity, implying a similarity of motion of fluid particles between the model and prototype. The parameters related to time are therefore scaled in such a way that they represent the fluid particle motions of the prototype. The third criteria represents dynamic similarity. It refers to similarity of masses and forces between model and prototype. It is however impossible to create complete dynamic similarity, since density, surface tension and dynamic viscosity cannot be scaled in practice. Therefore, specific rules apply for breakwater modelling. These rules are derived from the dimensionless relationships shown in this section.

### 4.2.1. DIMENSIONLESS RELATIONSHIPS

The first dimensionless relation is the Froude number (Equation 4.1), representing the ratio between inertia and gravitation. To maintain the similarity, the Froude number of the model has to be the same as the Froude number for the prototype. Therefore, it is derived that the scaling factor for length ( $N_l$ ) is a function of the velocity and time according to the following relationship:  $N_u = N_T = N_l^{0.5}$ .

$$Fr = \frac{u}{\sqrt{gh}} \quad (4.1)$$

The second dimensionless relation is the Reynolds number, as presented by Dai & Kamel (1969), see Equation 4.2. This equation represents the ratio of inertia over viscosity and is expressed as a function of, among others, the significant wave height ( $H_s$ ) and nominal diameter ( $D_n$ ). This equation is used to check the requirement of maintaining full turbulent flow in the model. Dai & Kamel (1969) found that this requirement is met for  $Re > 3 * 10^4$ .

$$Re = \frac{\sqrt{gH_s}D_n}{\nu} \quad (4.2)$$

The Weber number represents the ratio between inertia and surface tension (Equation 4.3). Also this number cannot be met in a scale model. It is therefore important to keep the effect of surface tension to a minimum. That implies a minimum wave height of 5 cm with a wave period larger than 0.35 s. Furthermore, the wave run-up has to be at least 0.022 m (Pullen et al., 2007).

$$We = \frac{\rho u^2 L}{\sigma} \quad (4.3)$$

The fourth dimensionless relation is the Strouhal number (Equation 4.4), representing the ratio between the local inertia and the convective inertia. This means that (Von Karman) vortex shedding effects will have the same frequency. The same scaling relationship as Froude scaling is derived:  $N_u = N_T = N_l^{0.5}$ .

$$St = \frac{L}{uT} \quad (4.4)$$

The last dimensionless relation represents the stability of the armour units (Equation 4.5). The relation requires that the ratio of wave height over the relative density, multiplied by the dimension of the unit has to be the same for prototype and model.

$$N_s = \frac{H_s}{\Delta D_n} \quad (4.5)$$

#### 4.2.2. DIMENSIONS MODEL AND HYDRAULIC CONDITIONS

The determining factor for the scaling process is the required dimension of the scaled unit, in which an accelerometer, cables and weight are fitted. It is found that a cube model with a height of 5 cm is satisfactory. To demonstrate the scaling process, a comparison is made with a fictional prototype with height of 1 m. Based on relations for the Froude and Strouhal number and using a general scaling ratio of 1/20, the scaling ratio for length is equal to 1/20.

On the hydraulic side restrictions regarding the wave flume, as shown in Section 4.1.3, have to be taken into account. A motivation is given for the chosen test range and cube density. Research by Van Gent (as cited in CIRIA, CUR & CETMEF (2007)) resulted in a relation for the start of damage ( $N_{od} = 0$ ) of single layer cubes:

$$\frac{H_s}{\Delta D_n} = 2.9 - 3.0 \quad (4.6)$$

According to CUR C70 (CUR, 1989) the damage number is related to the number of moved units with a reduction of  $\frac{H_s}{\Delta D_n} - 0.5$ , see Section 2.1.2. Therefore the start of movement is expected to be approximately:

$$\frac{H_s}{\Delta D_n} = 2.4 - 2.5 \quad (4.7)$$

To obtain sufficient measurements from accelerations of the cube, it is important that sufficient movement occurs. Therefore a range of  $\frac{H_s}{\Delta D_n} = 2.3 - 6$  is chosen. Since the wave flume restrictions are limiting the stability number (Equation 4.5), a model cube density of  $1500 \text{ kg/m}^3$  is applied. This density is combined with a significant model wave height ( $H_{m0}$ ) of 0.06 – 0.16 m. The wave steepness ( $s_{m-1.0} = 0.02 - 0.04$ ) is chosen such that common wind wave characteristics are represented (both plunging and surging breakers). This results in a range of wave periods of  $T_{m-1.0} = 1.1 - 2.5 \text{ s}$ .

It is expected that for the irregular wave tests a large variation in accelerations is obtained, caused by the statistical variation in wave conditions. Therefore, it is chosen to start with regular waves, to minimize the scatter. For comparison, the regular waves have to represent the total range of the irregular waves. Consequently, the following wave heights apply:  $H = 0.12 - 0.21 \text{ m}$ . The wave steepness has a range from  $s = 0.02 - 0.09$ .

The chosen test ranges comply with the wave flume restrictions in Section 4.1.3. The Reynolds numbers have a range starting at  $1.2 * 10^5$ , and therefore satisfy the requirement of maintaining fully turbulent flow. Furthermore, the range of wave heights and wave periods satisfy the requirements derived from the Weber number ( $H > 5 \text{ cm}$  and  $T > 0.35 \text{ s}$ ).

Note that the density of the cube is not in line with common prototype densities. The density of the model cube corresponds with a prototype density according to the following elaboration: the density is scaled with the stability number. Since a difference exists in the density of sweet water in the flume ( $1000 \text{ kg/m}^3$ ) and the density of seawater ( $1025 \text{ kg/m}^3$ ), the density of the cube has to change according to Equation 4.5. The density of the prototype cube becomes:  $1538 \text{ kg/m}^3$ .

The wave heights and wave periods of the model correspond with the following conditions for the prototype breaker:  $H_{m0} = 1.2 - 3.2 \text{ m}$  and  $T_{m-1.0} = 5.0 - 11.2 \text{ s}$ . These conditions represent common wind wave conditions. The scaling is based on the Froude and Strouhal number and correspond with a ratio of 1/20 for the wave heights and  $\sqrt{1/20}$  for the wave periods.

### 4.3. MEASUREMENT EQUIPMENT

An accelerometer is used to measure the magnitude of angular acceleration of the center of the armour unit, from which the angular velocity can be inferred. The device is fitted in the center of the armour unit. The unit itself has

to be waterproof and it needs to have a sufficient mass and mass distribution. The accelerations are linked to wave conditions. Wave gauges are used to measure the wave conditions. Furthermore, velocities on the slope and pressures exerted on a fixed cube, are measured for future CFD-modelling. This section describes in detail the set-up and usage of measurement equipment.

### 4.3.1. ACCELEROMETER

A market study is conducted to find a suitable accelerometer. An overview of the market study is shown in Appendix D. An important conclusion from the study is that an accelerometer with a similar measurement range and frequency as in Sokolewicz (1986) cannot be used for the current research, due to cost considerations. Therefore, it is chosen to measure the accelerations corresponding to movement, instead of impact (see Figure 4.7). Integration of those accelerations over time gives the impact velocity (Hibbeler, 2006). This implies that the accelerations due to movement can be directly related to the velocities before collision by integration. Hence, a large advantage is that the velocities before collision can be directly obtained, instead of relating the impulse of impact with the impulse of movement.

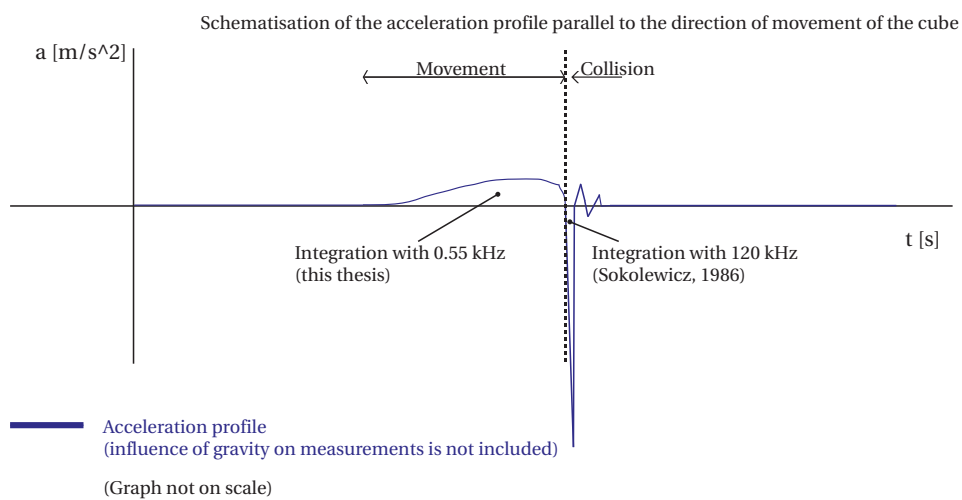


Figure 4.7: Differences in measurements of this Master's thesis in comparison with Sokolewicz (1986)

In addition, the wiring might be of influence to the armour unit movement. Therefore, a wireless application is investigated. Unfortunately, this appears to be not feasible, since the development such application requires a time span that does not fit in the current research. Instead, it is chosen to connect the accelerometer to thin wires.

#### ACCELEROMETER TYPE

The used accelerometer is of the piezo-resistive type and goes under the name ADXL335, and is manufactured by Analog Devices. The accelerometer can measure in three directions with a measurement range from  $-5g$  to  $+5g$ . The maximum sampling frequency is  $1600\text{ Hz}$  for the x and y direction and  $550\text{ Hz}$  for the z-direction. The measurement range is estimated to be sufficient based on calculations with the analytical model in Chapter 3 and validation tests (Appendix E).

Figure 4.8 shows the platform on which the accelerometer is attached. This platform has dimensions of 19 by 19 mm and a weight of 3.14 gram. Three capacitors of  $0.1\ \mu\text{F}$  set a frequency response of  $50\text{ Hz}$ , in which each capacitor applies for each measurement direction. The maximum frequency response of  $1600\text{ Hz}$  is obtained by removing these capacitors. A disadvantage with this solution is the increase in noise. A second solution is to keep the noise at a minimum by replacing the standard capacitors for capacitors with a lower resistance (however lower frequency than first solution). The platform provides a connection with power supply and measured outputs to a computer in x-y-z-direction. The accelerometer output is ratiometric, meaning that the output voltage changes linearly with the measurement of accelerations. The linear response is dependent on the input voltage. For a power supply of  $3\text{ V}$  the device gives an output change of  $0.3\text{ V}$  for a change of  $1\text{ g}$ . Zero acceleration is measured at a Voltage output of  $1.5\text{ V}$ . The obtained signals in Volt are processed with computer software "DasyLab".

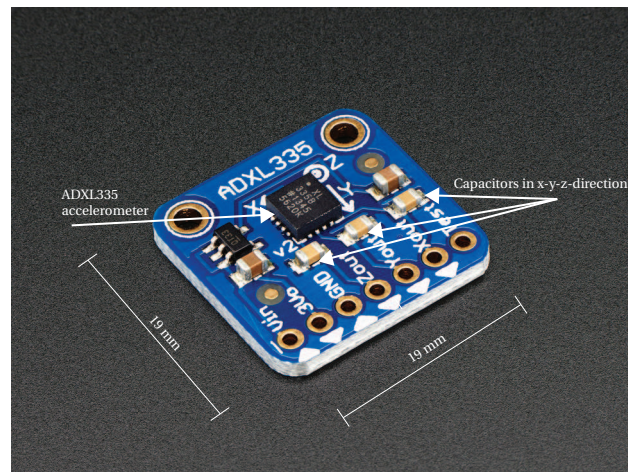


Figure 4.8: Accelerometer ADXL335 (Adafruit, n.d.)

Possible deviations from the numbers shown in previous paragraph are a consequence of temperature, amplifier noise and factory errors. These deviations are summed up in Table 4.1 (Analog Devices, 2009).

Table 4.1: Measurement errors in accelerometer (Analog Devices, 2009)

<b>Sensor input</b>		
Nonlinearity	+ - 0.3	%
Interaxis alignment error	+ - 0.1	°
Cross-axis sensitivity	+ - 1	%
<b>Ratiometry (measured change from 25°C)</b>		
Sensitivity Change Due to Temperature	+ - 0.01	%/°C
0 g bias due to temperature	+ - 1	mg/°C
<b>Noise</b>		
Noise floor, x and y-direction for 1600 Hz	0.006	g
Noise floor, z-direction for 550 Hz	0.012	g

For usage, 5 wires are soldered to the platform. These wires provide an electricity supply of 3 V and make sure that measurement data is transferred to a computer. To exclude influence of the wires during the test, thin and flexible wires were used. In addition, more flexibility is created by not bundling the wires.

#### CALIBRATION

Since the initial output of the accelerometer is in Volt, the signal has to be translated to  $m/s^2$ . To achieve this, the accelerometer is calibrated by making use of gravity. If one of the accelerometer axes is aligned parallel to the direction of gravitation, the measured acceleration should be equal to  $9.81 m/s^2$  in that direction. The other directions should give an acceleration of  $0 m/s^2$ . Furthermore the sum of the acceleration vectors over the three directions is always  $9.81 m/s^2$ , irrespective of the accelerometer orientation. Consequently, a linear relation between Voltage and  $m/s^2$  is derived.

Note that the accelerometer measures the gravitation exerted by, for instance, the wooden base, in opposite direction of the "real" gravitation. An illustration is shown in Figure 5.2.

#### VALIDATION

To determine the applicability of the accelerometer for measuring movement of an armour unit, three validation tests are conducted:

1. Slow rotation
2. Fast rotation
3. Falling test

The first test determines qualitatively whether gravitation before, during, and after rotation is correctly represented. The second test combines the acceleration due to rotation and gravity. The third test determines whether the accelerations due to movement are correctly displayed quantitatively. The second and third test are assumed to have the same order of magnitude of movement as the cube in the wave flume. Therefore, the behaviour of the accelerometer in the wave flume is expected to be similar to the validation tests. The elaboration and results of the tests are shown in Appendix E. The results of the tests show that the accelerometer accurately measures movement and gravity. Therefore, it is concluded that the accelerometer is suitable for measuring movements in the wave flume. In addition, it is observed that the movements are fully captured in all tests. Consequently, it is concluded that the measurement range and frequency of the accelerometer are sufficient for the measurement of movement.

#### ACCELERATING CUBE

The accelerometer is fitted in a solid cube made from PVC. A round hole in the center of the unit allows placement of the accelerometer. The accelerometer is kept in its place with casting resin. This material prevents accidental movement of the accelerometer inside the unit and water to reach the accelerometer.

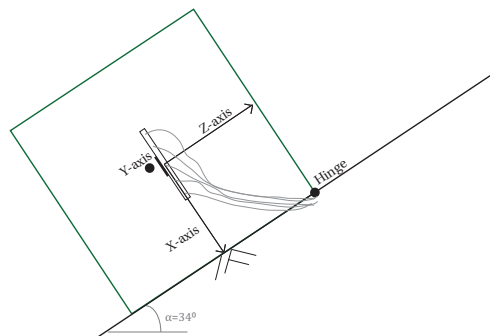


Figure 4.9: Orientation accelerometer inside cube

Figure 4.9 shows the orientation of the accelerometer axes inside the cube. The x-axis is positioned perpendicular to the slope. The y-axis is positioned parallel to the width of the wooden base. The z-axis is positioned parallel to slope and upward. With this orientation, the x-axis and z-axis measure the gravity and accelerations. The y-axis is supposed to measure an acceleration equal to  $0 \text{ m/s}^2$ . This orientation has the advantage that the positioning of the wires is convenient. From the center of the cube, the wires are lead to the side of the cube. Consequently, the wiring goes through a hole near the hinge. This set-up gives negligible influence of the wires to the movements. In addition, the cube cannot collide on top of the wire. This excludes wire breakage during the experiments.



Figure 4.10: Placement of cube measuring pressure (upper cube) and cube measuring accelerations (lower cube)

Figure 4.10 shows the placement of the cube with accelerometer (lower cube) in the wave flume. The hinge is attached to the slope via a steel plate behind the cube. The wires go trough the wooden base via the hole next to the steel plate.

### 4.3.2. PRESSURE SENSOR

A reference for future CFD-modelling is obtained with a solid, non-moving cube on the slope containing a pressure sensor, see Figure 4.10. This sensor measures water pressures in the center of the front surface of the cube, see Figure C.7. This implies an orientation down slope, parallel to the slope surface. The measurements provide indirectly an indication of the order of magnitude of the wave forcing.

A Honeywell pressure sensor with a range of 0.5 PSI is used. The sensor measures the pressure relative to the air pressure. Calibration is conducted by measuring the relative depth of the pressure sensor in a water basin. By varying the depth, a linear relation is established between the Voltage output and the pressure in Pascal.

Possible measurement errors might occur due to possible temperature differences between air and water. In addition, despite the precise fitting and shaping of the sensor in the cube, air entrapment resulting in measurement errors cannot be neglected.

### 4.3.3. CAMERAS

Wave front velocities are estimated crudely, based on video images. For that purpose an industrial camera is used from "The Imaging Source" with sensor of type Aptina MT9P031. The camera shutter is of the "rolling" type. A configured resolution of 640x480 pixels is used. With this configuration the sensor samples a frame within 8 ms, corresponding to a maximum frequency of 123 Hz. With a run-up speed that is expected to be around 1.5 m/s (15 Hz), calculated with Equation 3.4, the sampling configuration of the camera is much higher than the run-up. Therefore the "rolling effect" can be neglected. Consequently, it is concluded that the camera gives reliable results for the tests. The camera is mounted on top of the wave flume, perpendicular to the slope. Calibration is done with the horizontal black lines of 1 cm on the slope. The lines are shown in Figure 4.10.

Another camera is next to the flume and captures the water velocities and movements of the cube from a side view. This camera is from "Basler" and has a global shutter. The other specifications are more or less similar to the camera from The Imaging Source. The camera is calibrated with black lines of 1 cm in the windows of the wave flume.

An external lamp set up next to the flume ensures enhancement of the captured images. Furthermore, the cameras are externally triggered with electric pulses via computer software DasyLab. This makes sure that all measurements start at the same time. Additionally, during the tests it is chosen to set a shutter frequency of 60 Hz, since a higher frequency demands too much storage capacity. This frequency is however still sufficient to capture the wave run-up (15 Hz). The captured frames are processed with manufacturer specific software and are stored as images. The placement of the cameras and lamp set is shown in Figure 4.11.

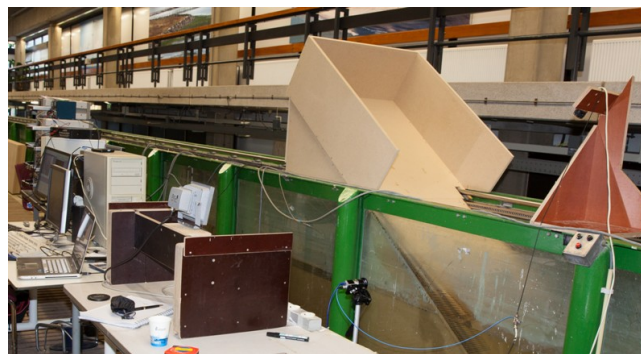


Figure 4.11: Overview set-up wave flume

### 4.3.4. WAVE GAUGES

For the measurement of regular waves, two wave gauges, known as "Deltares Wave Height Meters", are applied, to separate the incoming wave from the reflected wave. The horizontal distance from the first wave gauge to the toe of the structure is kept equal to 2 m. This distance is chosen in order diminish the influence of the structure to the measurement of waves. The second wave gauge is placed at a distance from the first wave gauge equal to a quarter of the wave length.

For the measurement of irregular waves, three wave gauges are necessary to separate reflection. In analogy with the test series with regular waves, the distance between the toe of the structure and the first wave gauge is 2 m. The second wave gauge is placed at 0.4 m from the first wave gauge. The third wave gauge is kept at a distance of 0.3 m from the second wave gauge.

The calibration is carried out by assessing various relatively measured depths between the water level and the wave gauge. The measurement signals are amplified prior to connection with a computer. The signals are saved with software DasyLab.

#### 4.4. TEST PROGRAM

Since irregular wave tests give a large variation in accelerations, it is chosen to start with regular waves. Irregular waves are used in the second round of tests to represent prototype breakwater conditions. For that purpose a Jonswap spectrum is chosen to simulate a common breakwater in coastal regions with young sea states as good as possible. For the tests with the embedded cube, only measurements with irregular waves are conducted. In addition, due to time restrictions, the position of the cube was kept constant for this type of layer. The cube was placed at position <sup>1</sup>  $Y/D_n = -2$  because most movement was observed with the other, conventional layer.

Table 4.2 shows the test program for regular waves. The hydraulic conditions are indicated as the conditions derived from wave gauge measurements after data processing. For position  $Y/D_n = -2$  a relatively lower start condition (Reg35 and Reg36) is chosen, since the start of movement was already observed at conditions Reg37 and Reg38. Furthermore, during the series for regular waves, the influence of the porosity underneath the cube is tested for the start of movement. For that purpose, a hole is drilled underneath the cube. A cap made from rubber is used to cover the hole for tests without any porosity. As no difference was observed between the situations with hole and without hole, the tests with hole were aborted.

Table 4.3 shows the test program for irregular waves. Range "EI" stands for the tests with the embedded cube. For that layer, the test range with  $s_{m-1.0} = 0.02$  was aborted since no movement was observed. In addition, deviations in the test range for different positions on the slope are determined by observations. In case the cube moves in an early stage, a lower test range was conducted. In case only few movements are observed, the range was extended with higher wave heights.

<sup>1</sup>Please note that the positions  $Y/D_n$  are presented as the positions of the cube defined before the tests. After data processing it was found that the positions were slightly different during the tests. These actual positions are shown in Tables 4.2 and 4.3 and are denoted in the remainder of the report as  $[Y/D_n]_p$ . Consequently, the following positions correspond to one another:  $Y/D_n = -2 \iff [Y/D_n]_p = -1.67$ ,  $Y/D_n = 0 \iff [Y/D_n]_p = 0.33$ ,  $Y/D_n = 2 \iff [Y/D_n]_p = 2.33$

Table 4.2: Test program for regular waves

Range	Name	Wave height $H$ [m]	Wave period $T$ [s]	Wave steepness $s$ [-]	Position $[Y/D_n]_p$ [-]	Water depth $d$ [m]
Reg	1	0.13	1.69	0.03	2.33	0.55
Reg	2	0.14	0.92	0.10	2.33	0.55
Reg	3	0.13	2.19	0.02	2.33	0.55
Reg	4	0.14	1.03	0.08	2.33	0.55
Reg	5	0.15	2.39	0.02	2.33	0.55
Reg	6	0.17	1.13	0.08	2.33	0.55
Reg	7	0.24	2.59	0.02	2.33	0.55
Reg	19	0.12	1.31	0.05	0.33	0.65
Reg	20	0.11	0.92	0.08	0.33	0.65
Reg	21	0.14	2.19	0.02	0.33	0.65
Reg	22	0.14	1.03	0.08	0.33	0.65
Reg	23	0.16	2.40	0.02	0.33	0.65
Reg	24	0.17	1.13	0.09	0.33	0.65
Reg	25	0.21	2.63	0.02	0.33	0.65
Reg	26	0.19	1.22	0.08	0.33	0.65
Reg	27	0.19	2.80	0.02	0.33	0.65
Reg	28	0.21	1.31	0.08	0.33	0.65
Reg	35	0.09	1.71	0.02	-1.67	0.75
Reg	36	0.08	0.81	0.08	-1.67	0.75
Reg	37	0.12	1.97	0.02	-1.67	0.75
Reg	38	0.11	0.92	0.09	-1.67	0.75
Reg	39	0.14	2.19	0.02	-1.67	0.75
Reg	40	0.14	1.03	0.08	-1.67	0.75
Reg	41	0.15	2.39	0.02	-1.67	0.75
Reg	42	0.16	1.13	0.08	-1.67	0.75
Reg	43	0.21	2.61	0.02	-1.67	0.75
Reg	44	0.19	1.22	0.08	-1.67	0.75

Table 4.3: Test program for irregular waves

Range	Name	Wave height $H_{m0}$ [m]	Wave period $T_{m-1.0}$ [s]	Wave steepness $s_{m-1.0}$ [-]	Stability number $\frac{H_{m0}}{\Delta D_n}$ [-]	Position $[Y/D_n]_p$ [-]	Water depth $d$ [m]
I	1	0.06	1.33	0.02	2.3	2.33	0.55
I	2	0.06	0.97	0.04	2.3	2.33	0.55
I	3	0.09	1.68	0.02	3.4	2.33	0.55
I	4	0.08	1.19	0.04	3.4	2.33	0.55
I	5	0.12	1.94	0.02	4.6	2.33	0.55
I	6	0.11	1.44	0.04	4.5	2.33	0.55
I	7	0.15	2.16	0.02	5.9	2.33	0.55
I	8	0.14	1.57	0.04	5.6	2.33	0.55
I	11	0.06	1.36	0.02	2.3	0.33	0.65
I	12	0.06	0.99	0.04	2.3	0.33	0.65
I	13	0.09	1.68	0.02	3.5	0.33	0.65
I	14	0.09	1.22	0.04	3.4	0.33	0.65
I	15	0.12	1.99	0.02	4.6	0.33	0.65
I	16	0.11	1.40	0.04	4.6	0.33	0.65
I	17	0.15	2.16	0.02	5.9	0.33	0.65
I	18	0.14	1.53	0.04	5.7	0.33	0.65
I	21	0.06	1.37	0.02	2.3	-1.67	0.75
I	22	0.06	0.97	0.04	2.3	-1.67	0.75
I	23	0.09	1.72	0.02	3.5	-1.67	0.75
I	24	0.09	1.22	0.04	3.4	-1.67	0.75
I	25	0.12	1.94	0.02	4.6	-1.67	0.75
I	26	0.11	1.36	0.04	4.6	-1.67	0.75
I	27	0.15	2.28	0.02	5.9	-1.67	0.75
I	28	0.14	1.57	0.04	5.7	-1.67	0.75
EI	24	0.09	1.19	0.04	3.4	-1.67	0.75
EI	26	0.11	1.36	0.04	4.6	-1.67	0.75
EI	28	0.14	1.56	0.04	5.6	-1.67	0.75
EI	30	0.17	1.72	0.04	6.8	-1.67	0.75

## 4.5. EXPECTATIONS

In analogy with Sokolewicz (1986) and using common sense, the following results are expected:

1. The accelerations are dependent on the wave height and become larger with larger wave height.
2. The accelerations are dependent on the breaker type, and therefore the wave steepness. Probably the largest accelerations are found with collapsing breakers.
3. The start of movement is dependent on the choice of regular or irregular waves.
4. The accelerations are dependent on the position on the slope. Probably the highest accelerations are found near the waterline at  $\frac{Y}{D_n} = 0$ .
5. The accelerations observed with irregular waves have a large scatter.
6. More movements occur with higher significant wave heights during tests with irregular waves, as a higher percentage of high waves cause movement.
7. Higher waves are necessary to initiate movement for a cube surrounded by other cubes. Therefore, less movements occur for an embedded cube.
8. With surging breakers, the contribution of the wave impact to movements is negligible. The cube starts to move with sufficient drag.

## 4.6. VISUAL OBSERVATIONS

During the tests the behaviour of the rotating cube is characterised by the following aspects:

1. Higher wave heights result in higher impacts. The first item in Section 4.5 corresponds to this observation. During the test the impacts were heard. The sounds increased with increasing wave height.
2. The majority of the movements is caused by collapsing breakers. However, a difference between the magnitude of accelerations of the various breaker types was not visually observed. Hence, to compare this observation with item 2 in Section 4.5, data-analysis is necessary.
3. No difference in start of movements is observed between regular and irregular waves. This is not in line with the expectations in Section 4.5 (item 3). This is probably caused by the fact that the range of hydraulic conditions for regular waves is based on the expected highest waves in the irregular wave series. Sokolewicz (1986) however, used a wave height ( $H$ ) that was equal to ( $H_s$ ).
4. Position  $Y/D_n = -2$  causes most movement. In addition, the initiation of movement occurs at a lower wave height, in comparison with other positions on the slope. This implies that a dependency in position on the slope is observed, which is in line with the expectations. However, this also means that a position slightly below mean water level (see Figure 4.2) causes most movement, which is different from the research by Sokolewicz (1986). Nevertheless, during this Master's thesis it is observed that the cube at position  $Y/D_n = -2$  is still exposed to the air. Therefore, the cube experiences direct wave attack, which is caused by run-up. Consequently, a high amount of movements is within expectations, from a physical point of view.
5. For the irregular wave tests, more movements occur with increasing wave height, which is in line with item 6 in Section 4.5.
6. For the embedded cube, movement only occurs when a breaker collapses right on top of the cube. In case of surging breakers, no movement is observed at all. This is in line with the expectations in Section 4.5 (item 7), in which less movements were expected for the series with the embedded cube.
7. For surging breakers, the cube starts to move a while after the wave front passing. Therefore, it is likely that drag is dominant for surging breakers. This is in line with the expectations (Section 4.5, item 8).

Further evidence, comparisons and conclusions have to follow from data-analysis.

# 5

## DATA PROCESSING

For the purpose of providing new knowledge to computer application "Rocking", the focus during the data processing is on three aspects. To provide input for the start of the Monte Carlo simulation, information from accelerations due to movement is of vital importance. Therefore, a relation between accelerations - velocities and hydraulic conditions is sought. In addition, one of the major uncertainties in "Rocking" is the number of collisions per moving unit, see Chapter 2. Lastly, it is important to know under which conditions these collisions start to play a role. The data provides a check for the start of movement, based on the theory in Section 4.2.2.

### 5.1. INTERPRETATION

The three aspects are found by processing the data from the accelerometer. This section provides an interpretation of the acceleration signals, in x-y-z-direction. Figure 5.1 shows typical plot of the data obtained by measurements of a moving cube during a test with regular waves. The first three plots represent the acceleration signals in x-y-z-direction.

Peaks in the acceleration signals are clearly distinguished, which represent collisions. It is seen that all large peaks occur at the same time over the three axes. From a physical point of view it is self-evident that this has to be the case. Therefore, it is concluded that the peaks are correctly represented in time.

Taking a closer look at the third upper plot in Figure 5.1, two types of series of peaks can be distinguished: series with a majority of negative peaks, and series with a majority of positive peaks. The first series of peaks occur after upward movement. As the accelerometer z-axis is positioned in the direction of upward movement (see Figure 5.2), the resulting collisions display negative peaks since they are in opposite direction of movement. The second series go together with downward movement. The movement is in negative direction relative to the accelerometer z-axis. Consequently, the collision to the wooden base causes a velocity drop, corresponding to acceleration peaks in opposite direction of the movement direction, which in this case are positive peaks. In addition, it is observed that relatively more peaks result from the second series, implying that the cube bounces more than in the first series. This behaviour is explained by material differences in the test set-up: rubber was placed underneath the cube's initial position, see Section 4.4. The position of collision for the first series was characterised by only a wooden base. This difference in material usage did however not affect the movements.

In the third upper plot of Figure 5.1, parts with straight, horizontal lines are observed. These lines can be divided into two ranges corresponding with the magnitude of Voltage output. The horizontal lines indicate no movement. Therefore, the accelerometer solely measures accelerations due to gravitation. Consequently, the magnitude of Voltage output is solely dependent on the orientation of the accelerometer z-axis relative to the axis of gravitation. From Figure 5.2 it is clear that the angle between gravitation and the z-axis is smallest for the initial position, since the z-axis moves away from the gravitational component during upward rotation. This implies a measurement of higher accelerations in the initial position. Please note that the gravitation is measured positively in upward direction by the accelerometer. As a consequence, the range of horizontal lines with relatively higher Voltage outputs correspond with the initial position, as a higher Voltage output implies a smaller angle between the accelerometer z-axis and the gravitational axis. Accordingly, the lower range of Voltage outputs corresponds with the position on the slope after upward movement. Hence, it is reasoned that the non-horizontal parts in the line (excluding the peaks) correspond

to movement. From analysis of the horizontal lines, it is reasoned that upward movement corresponds to a decline in Voltage output. Logically, downward movement is observed with increasing Voltage output. Figure 5.5 shows the considered areas of upward and downward movement.

Those horizontal lines are however not observed for the acceleration signals in x-direction (Figure 5.1, first plot). Further examination points out that the accelerometer x-axis, excluding the peaks, follows the signal from wave gauge 3 (Figure 5.1, second lower plot). Even a variation in the accelerometer x-axis was observed without movement of the cube. This disturbance is however striking, since during regular wave series only the first two wave gauges were used. The third wave gauge was not connected. Analysis shows that the signal for wave gauge 3 appears to follow the signal of wave gauge 2. Consequently, the signal shown for the accelerometer x-axis appears to be disturbed by the signal of wave gauge 2. Furthermore, analysis shows that the accelerometer y-axis is also disturbed by wave gauge 2, but to a lesser extent. Luckily the disturbance in the signal from the accelerometer z-axis is negligible. A possible cause for the disturbance, known as crosstalk, is the difference in amplification for various measurement devices in combination with the order of wiring. Solving the crosstalk was not part of this Master's thesis.

Unfortunately, after processing it appears that the crosstalk in the accelerometer x-axis does not allow processing of movements. Additionally, since the accelerometer y-axis is perpendicular to the plane of movement, it does not measure movement and change in gravitation. Therefore, only the accelerometer z-axis can be used during the analysis of data.

## 5.2. VELOCITIES BEFORE COLLISION

The velocities of the movements of the cube are important input values for the computer application "Rocking". Therefore, the obtained acceleration signals from the wave flume tests are analysed. Unfortunately, due to crosstalk, only the signals from the accelerometer z-axis are available (see Section 5.1). This section shows however that it is possible to obtain the velocities of the cube by processing one accelerometer axis.

### 5.2.1. EQUATIONS OF MOTION

Figure 5.2 shows the model cube during upward movement. The accelerometer z-axis is oriented parallel to the slope in initial position. In case the cube is dislodged by wave forces, a rotation occurs around the shown rotational point. The measured acceleration signal during movement is decomposed in three different components. The first component is the tangential acceleration ( $a_T$ ). This vector is oriented parallel to the plane of rotation and keeps the same angle ( $\phi_T$ ) to the z-axis during movement. The second component is the centripetal acceleration ( $a_n$ ), which is oriented perpendicular to the plane of rotation. This vector keeps an angle of  $0.5\pi$  radians to the tangential acceleration during movement. Consequently the angle of the centripetal acceleration to the z-axis is equal to the angle of the tangential acceleration (see Figure 5.2). The third component is the acceleration due to gravitation ( $a_g$ ). This vector is constant in magnitude ( $9.81 \text{ m/s}^2$ ) and in direction. Therefore the angle relative to the z-axis is the sum of the initial orientation ( $\phi_g = 0.31\pi$ ) and the turning angle ( $\theta$ ). Note that the accelerometer measures the acceleration  $a_g$  exerted by the wooden base, in opposite direction of the "real" gravitation.

The measured signal in the accelerometer z-axis is described by Equation 5.1. In the equation all three acceleration components in Figure 5.2 are described.

$$a_z = a_T \cos \phi_T + a_n \cos \phi_T + a_g \cos(\phi_g + \theta) \quad (5.1)$$

To approximate Equation 5.1 it is necessary to rewrite the expressions on the right hand side in terms of the angle of rotation (see Equation 5.2). The tangential component ( $a_T$ ) is rewritten as a second order derivative of the angle multiplied by the perpendicular distance ( $r$ ) to the rotational point. Furthermore, the normal component is rewritten using Newton's second law in which  $a_n = -r\omega^2$ . A substitution of  $\omega = d\theta/dt$  results in  $a_n = -r(d\theta/dt)^2$ . In addition, it is self-evident that  $a_g = 9.81 \text{ m/s}^2$ . Therefore the gravitational acceleration is equal to gravity ( $a_g = g$ ).

$$a_z = r \frac{d^2\theta}{dt^2} \cos \phi_T - r \left( \frac{d\theta}{dt} \right)^2 \cos \phi_T + g \cos(\phi_g + \theta) \quad (5.2)$$

Finally, Equation 5.2 is rewritten in terms of the nominal diameter ( $D_n$ ), in which the term  $r \cos \alpha$  equals  $D_n/2$ .

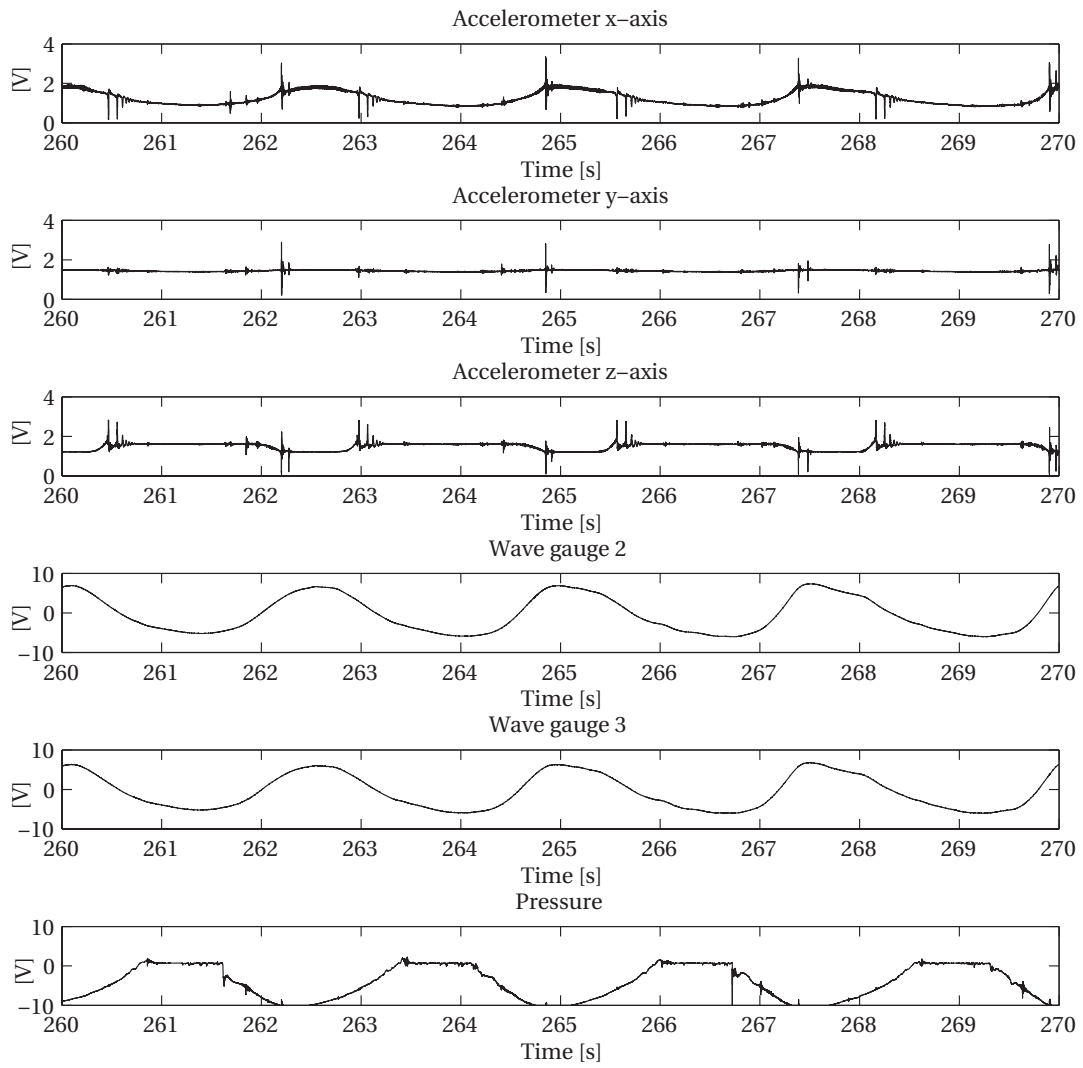


Figure 5.1: Raw data signals from measurements, in Voltage

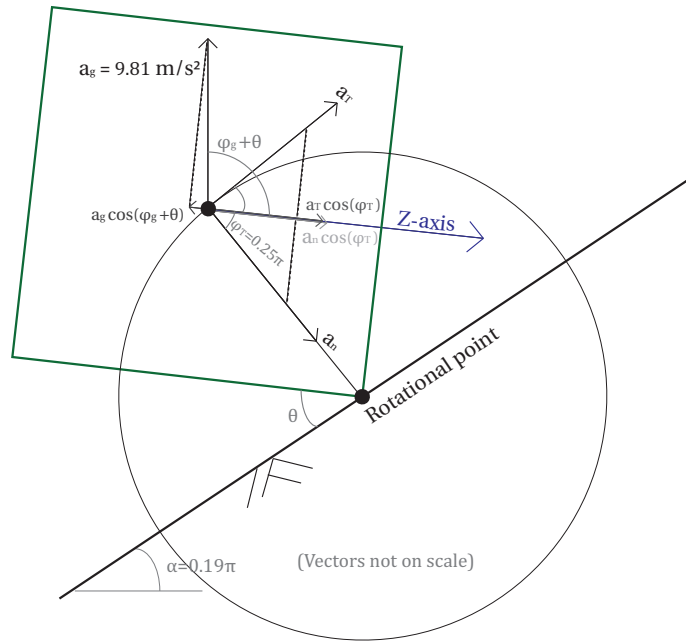


Figure 5.2: Decomposition acceleration signal for cube moving upward

$$a_z = \frac{D_n}{2} \frac{d^2\theta}{dt^2} - \frac{D_n}{2} \left( \frac{d\theta}{dt} \right)^2 + g \cos(\phi_g + \theta) \quad (5.3)$$

For downward movement the tangential component and normal component are oriented in opposite direction. Furthermore, the angle of rotation is considered to be positive in opposite direction. This implies a positive movement downslope. The following relationship applies:

$$a_z = -\frac{D_n}{2} \frac{d^2\theta}{dt^2} + \frac{D_n}{2} \left( \frac{d\theta}{dt} \right)^2 + g \cos(\phi_g + 0.5\pi - \theta) \quad (5.4)$$

Equation 5.3 and 5.4 are of second-order, non-linear and non-homogeneous ( $a_z$  is a function of time). Therefore an analytical solution is not possible (Boyce & Di Prima, 2010). Additionally, Appendix F shows that the numerical approach is not convergent. Therefore, the differential equation is simplified and corrected with a synthetic model in Section 5.2.2.

### 5.2.2. SYNTHETIC MODEL

To simplify the differential equation, it is necessary to know which terms are important. Therefore, a synthetic model is used to approach the signal measured in the wave flume. The following critical parameters are used to define the synthetic model:

1. The acceleration signal before and after movement, measuring solely gravitation. With this, information about the orientation of the cube before and after movement is obtained.
2. The time period of movement. Within this time period, movement over a certain distance occurs.

With these parameters and an assumption for the tangential acceleration of the cube during movement, the acceleration measured in the z-axis ( $a_z$ ) is approached. For this purpose Equations 5.3 and 5.4 are used. Subsequently, the synthetic model is compared to the acceleration signals of regular waves. Iteration shows that a linear increase in tangential acceleration approaches more or less the measured signals for both surging and collapsing conditions ( $s = 0.02$  and  $s = 0.09$  for regular waves respectively). Figure 5.3 show the plots generated by the synthetic model and

the measured signals. It is observed that the model is suitable for both upward and downward movement. Furthermore, figure 5.4 shows the model for an extreme case with  $H = 0.19$  m,  $s = 0.08$ . It is observed that the time span over which the cube moves upward is very short, which results in high impact velocities. Nevertheless, it is seen that the model follows measured signal accurately.

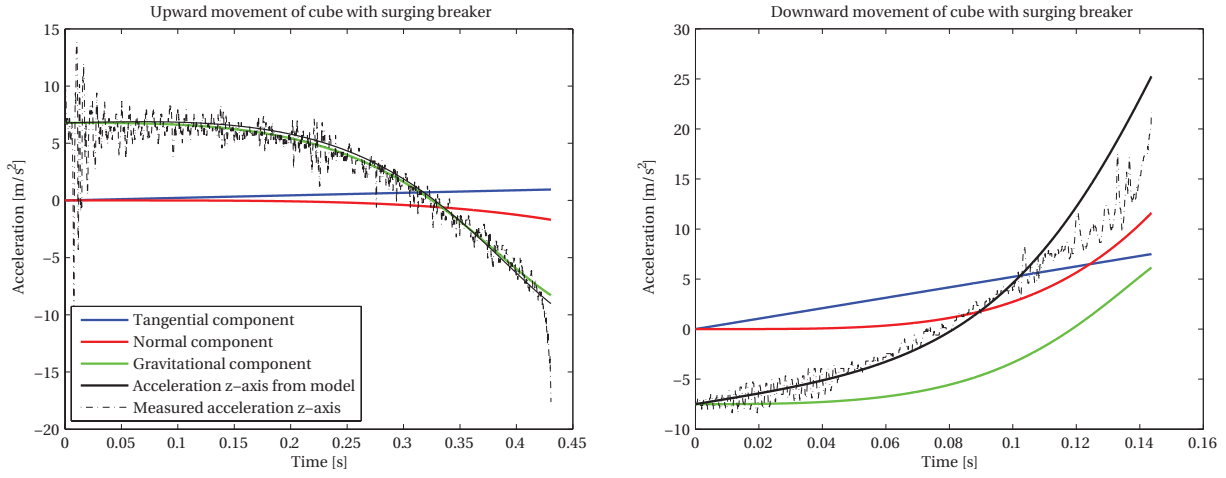


Figure 5.3: Comparison synthetic model with measured signal for surging breakers

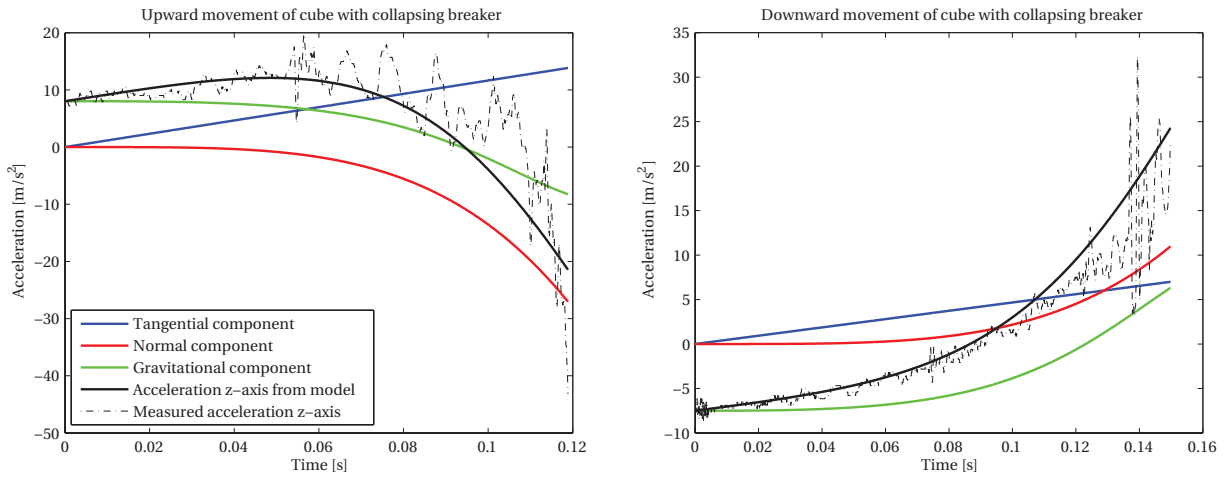


Figure 5.4: Comparison synthetic model with measured signal for collapsing breakers, extreme case

Additionally, Figures 5.3 and 5.4 show plots for each component of the differential equations 5.3 and 5.4. It is observed that the acceleration in the z-axis follows to a great extent the trend of the gravitational component. This implies that the gravitational component is dominant. Therefore, it is chosen to simplify the differential equations by neglecting the tangential and normal component. Nevertheless, a comparison between the gravitational component and the acceleration in the z-axis shows that still a relatively large error is caused by this simplification. Therefore, correctional terms, representing the tangential and normal components, are added to the simplified differential equations 5.5 and 5.6.

$$a_z = C_{tm} - C_{nm} + g \cos(\phi_g + \theta) \quad (5.5)$$

$$a_z = -C_{tm} + C_{nm} + g \cos(\phi_g + 0.5\pi - \theta) \quad (5.6)$$

Equation 5.5 represents the upward rotations and Equation 5.6 represents the downward rotations. The tangential component is represented by parameter  $C_{tm}$ . Since the synthetic model follows more or less the measured signal, it is chosen to derive the tangential component from the synthetic model and to impose it in the simplified differential

equations. The same applies for the normal component ( $C_{nm}$ ). Consequently, the correctional terms are described as in Equations 5.7 and 5.8. Parameter  $\theta_m$  is the angle derived from the synthetic model.

$$C_{tm} = \frac{D_n}{2} \frac{d^2\theta_m}{dt^2} \quad (5.7)$$

$$C_{nm} = \frac{D_n}{2} \left( \frac{d\theta_m}{dt} \right)^2 \quad (5.8)$$

With the synthetic model, the equations of motions are simplified and can be solved analytically. Rewriting Equations 5.5 and 5.6 give solutions for the angle of the cube over time, see Equations 5.9 and 5.10 respectively. Differentiation of these equations result in the angular velocities according to the following relationship:  $\omega = \frac{d\theta}{dt}$ . The velocities just before the occurrence of peaks represent the angular velocities before collision ( $\omega_{collision}$ ), see Section 5.2.3.

$$\theta = \arccos((a_z - C_{tm} + C_{nm})/g) - \phi_g \quad (5.9)$$

$$\theta = \arccos((a_z + C_{tm} - C_{nm})/g) - \phi_g \quad (5.10)$$

### 5.2.3. SIGNAL PROCESSING AND FILTERING

The data from measurements in z-axis ( $a_z$ ) needs to be processed before it can be used as input in Equations 5.9 and 5.10. The processing is essential since irregularities have a strong negative influence to the solution, see Appendix F. These irregularities are caused by noise from the measurement equipment, by turbulence from the wave action and by collisions. Furthermore, only the parts of the signal in which the unit moves are taken into account in Equations 5.9 and 5.10. Figure 5.5 shows a part of the data in which a unit moves upwards with the wave run-up, and afterwards moves downward again to its initial position. The MATLAB routine that is used to process the data and to solve the simplified differential equations is shown in Appendix G. This routine is applied for data from both regular and irregular wave conditions. For the embedded cube, minor adjustments regarding the angle of rotation and pressure signal are made (see Appendix G).

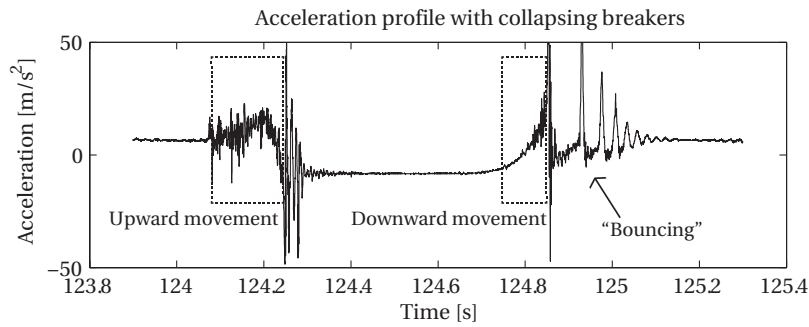


Figure 5.5: Indication upward and downward movement in accelerometer data

During data processing it is noticed that irregularities in the data signals become larger with differentiation. Filtering of the data only provides minor corrections for the errors, since too much filtering gives an incorrect representation of the data. The noisy velocity profile for a time period of movement is shown in Figure 5.6. It is shown that irregularities are much larger for velocities in comparison with the profile of the angle. For statistical analysis the resulting noisy velocity signal is further smoothed (green line). The velocity at the end of the time line is taken as the velocity of collision. Despite the smoothing, significant errors due to irregularities have to be kept in mind during interpretation.

## 5.3. NUMBER OF COLLISIONS

One of the major uncertainties in "Rocking" is the number of collisions per moving unit, see Chapter 2. Therefore in the current research, the number of collisions are retrieved from the test series for irregular waves, by analysing the

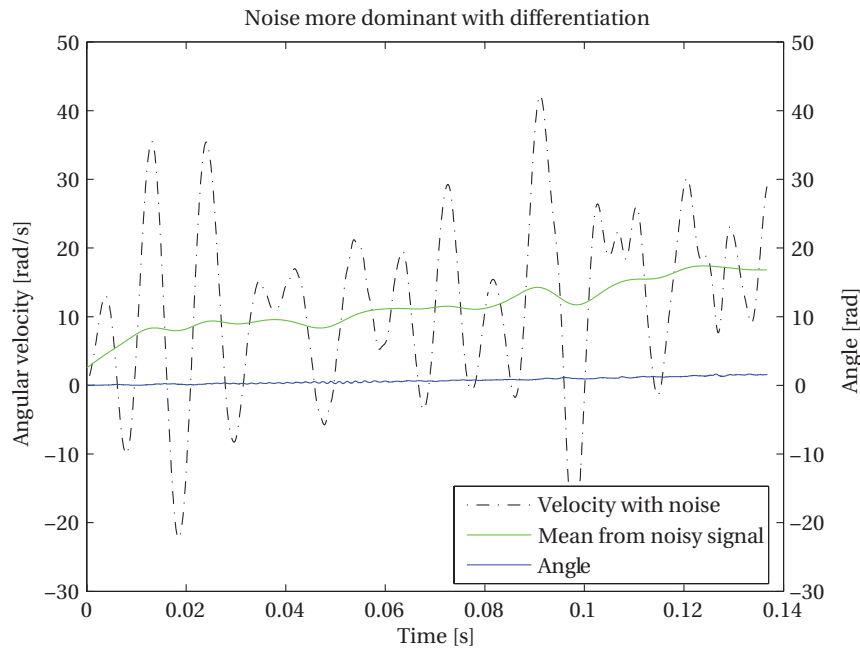


Figure 5.6: Velocity signal in time, showing the influence of noise

data from the accelerometer z-axis. The collisions are taken into account in case a similar pattern occurs as in Figure 5.5, implying a full rotation. With this, the cube undergoes a collision in upward direction and in downward direction. Movements in which the cube rotates under a smaller angle are therefore not taken into account. This choice is made since during the data processing it is not known which collisions affect the strength of the cube. Therefore, it is subjective to state whether a cube that rotates under a specific angle has to be taken into account. In addition, the full rotations allow automatised processing.

Next to that, during one impact multiple collisions occur shortly behind each other. This implies that the cube bounces. The amount of collisions and the period until the next collision are, among others, dependent on material characteristics. In order to keep it general, one impact is counted as one collision. Additional research is necessary to determine the amount of collisions of prototype concrete cubes during impact.

#### 5.4. START OF COLLISIONS

It is of importance for application "Rocking" to have information about the start of collisions, see Chapter 2. With the test series for irregular waves, relations for the stability number  $\frac{H_{m0}}{\Delta D_n}$  are derived.

Similar to Section 5.3 the collisions are taken into account if a full rotation is observed. The start of collision is regarded as the wave condition prior to the wave condition in which collisions are observed. With this methodology the start of collisions is dependent on the chosen build up of wave height during the test series. Therefore, a range in stability numbers is given, starting from the stability number corresponding to no collisions until the stability number corresponding to collisions. In addition, the test series with the embedded cube and a wave steepness of  $s_{m-1.0} = 0.04$ , show that in none of the tested conditions zero collisions occurred. Therefore, the dataset containing collisions is extrapolated. For consistency, the extrapolation steps are chosen to be equal to the steps in the range of hydraulic conditions. As a result, a range for the start of movement is found, similar to other conditions.

#### 5.5. DETECTION OF COLLISIONS

The detection of collisions is necessary to process the velocities before collision, number of collisions and start of collisions. The collisions were detected manually for the number of collisions and start of collisions. Later on, the detection of collisions was automatised to process the velocities before collision. Both methods used the following criteria for the conventional layer:

1. The smoothed signal goes below a threshold of  $-8 \text{ m/s}^2$ .
2. The (not smoothed) signal is characterised with steep peaks that go below a threshold of  $-40 \text{ m/s}^2$  after upward movement.
3. The (not smoothed) signal is characterised with steep peaks that exceed a threshold of  $40 \text{ m/s}^2$  after downward movement.

The criteria were slightly adjusted for the embedded cube:

1. The smoothed signal goes below a threshold of  $1 \text{ m/s}^2$ .
2. The (not smoothed) signal is characterised with steep peaks that go below a threshold of  $-40 \text{ m/s}^2$  after upward movement.
3. The (not smoothed) signal is characterised with steep peaks that exceed a threshold of  $40 \text{ m/s}^2$  after downward movement.

In addition, the automatised detection uses the data from the pressure sensor for the following process: If the raw, smoothed pressure signal exceeds a certain threshold, then it is observed that wave impact is sufficient for potential movement. Based on this threshold, the signal is divided into parts, in which potentially one movement upward and one movement downward occurs. Subsequently, the parts are checked on movement individually, using the mentioned criteria. Each detected movement is equal to one collision. This implies that, if movement occurs for one individual part, always two collisions occur (from one upward and one downward movement). If no movements are detected in a part, that part is deleted from the calculation. More information regarding the automatised detection can be found in Appendix G.

# 6

## ANALYSIS RESULTS

This chapter provides an analysis of the results. Firstly, the results from the regular wave series are compared with the analytical model. Secondly, the results from the irregular wave series are analysed in terms of amount of collisions and velocities before collision. The supportive graphs for analysis of the velocities before collision are shown in Appendix H. Lastly, general observations during data processing, which provide insight in the behaviour of the cube, are discussed.

### 6.1. ANALYTICAL MODEL VERSUS MEASUREMENTS

To determine whether the analytical model represents the velocities before collision in a realistic manner, the outcome of the analytical model is compared with the velocities before collision from the regular wave series. The analytical model assumes a position of the cube at the waterline ( $Y/D_n = 0$ ). Hence, the results from the measurement series with position  $[Y/D_n]_p = 0.33$  are used for comparison. Please note that the difference in order of magnitude of velocities of collision between positions  $Y/D_n = 0$  and  $Y/D_n = 0.33$  is investigated for the analytical model. It is concluded that the difference between the two positions is negligible. Consequently, a comparison between the analytical model and measurements is allowed.

Figure 6.1 shows plots of both the results from the analytical model and the regular wave series for upward rotation. The mean velocities from the measurements are plotted as blue lines and the standard deviations are indicated with errorbars. The green lines represent the results from the analytical model.

It is observed in Figure 6.1 that the continuous lines are positioned above the dashed lines from the same colour. This implies that the regime with  $s = 0.08$  results in higher impact velocities in comparison with  $s = 0.02$ , for both the analytical model and the measurements. Furthermore, it is observed that all lines display an upward trend. This indicates an increase in impact velocities with increasing wave height for all models. Next to that, the green lines are in a much higher position than the blue lines, implying that the velocities of collision from the analytical model are much higher than the measurements. For  $s = 0.02$ , the velocities from the analytical model are approximately a factor 8 higher than the measurements. This factor is equal to approximately 4 for  $s = 0.08$ . This indicates an overestimation of the impact velocities from the analytical model in comparison with the measurements.

It is concluded that the analytical model shows similar dependencies regarding the wave height and wave steepness. However, the order of magnitude of the velocities is overestimated. Hence, the analytical model is too conservative. Possible causes for the differences in order of magnitude are discussed in Section 3.4. From Section 3.4, it is clear that a number of assumptions and simplifications are made for the analytical model. Therefore, the analytical model and all its assumptions should be researched more thoroughly, to come to accurate armour unit impact velocities on a simplified breakwater slope.

### 6.2. ANALYSIS NUMBER OF COLLISIONS

Figures 6.2, 6.3 and 6.4 present the results of the number of collisions for irregular wave tests. The separate figures indicate the number of collisions on a specific position on the slope. The axes of the figures are presented in dimensionless

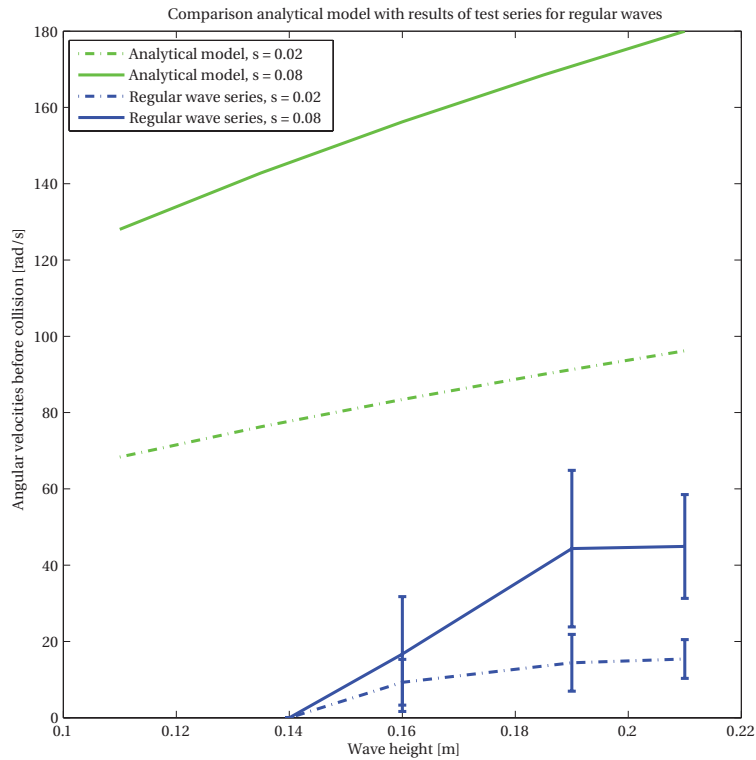
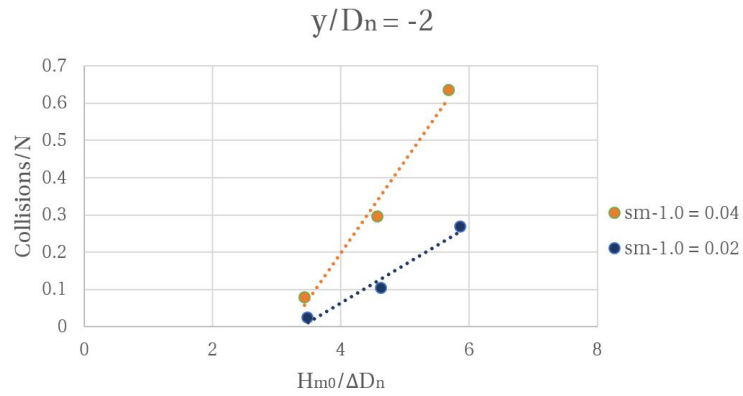
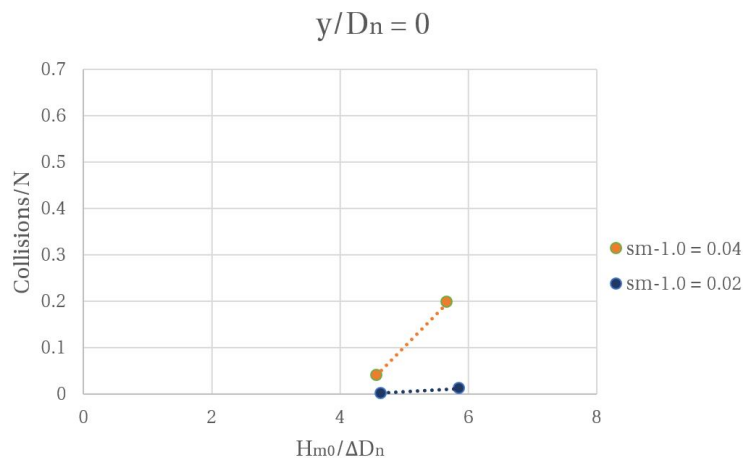
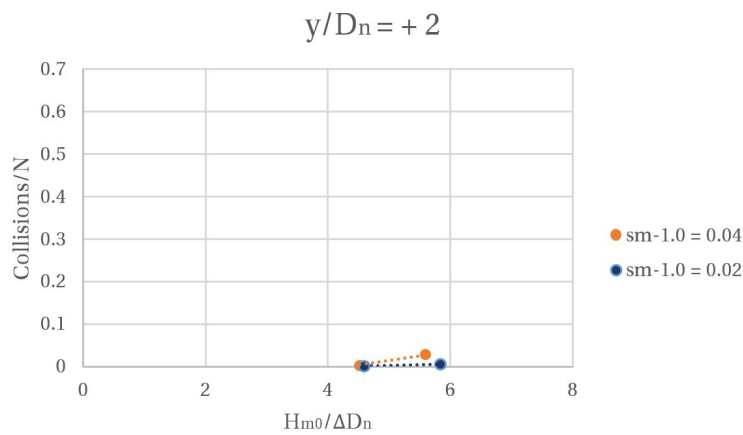


Figure 6.1: Comparison impact velocities from analytical model with regular waves, upward rotation

form by dividing the collisions by the number of waves (y-axis) and using the stability parameter for the x-axis. In all figures, trends are shown for wave steepnesses  $s_{m-1,0} = 0.04$  and  $s_{m-1,0} = 0.02$ . All graphs show clear upward trends, implying that a growing significant wave height results in an increase in the number of collisions. This is valid for all tested positions on the slope and all tested conditions for wave steepness. In addition, it is observed that in all graphs the trend for  $s_{m-1,0} = 0.04$  is positioned above the trend for  $s_{m-1,0} = 0.02$ . This indicates that a wave steepness of 0.04 gives more collisions compared to a wave steepness of 0.02.

Figures 6.5 and 6.6 present graphs for a constant wave steepness. Consequently, the tested positions on the slope can be compared. Furthermore, the embedded cube is included to compare the different type of layers. Analysis of both figures points out that a decreasing position on the slope result in a relative higher trend in the plots. This implies that relatively more collisions occur with a lower position on the slope. This observation is only valid for the tested range of positions. The range is relatively small, since the cube in lowest position on the slope is still exposed to the air with wave run-down. Next to that, a comparison of the embedded cube with the conventional layer with position  $Y/D_n = -2$  (Figure 6.5) show large difference in trend positioning in the graphs. The trend indicating the conventional layer is positioned much higher in the graph, indicating more collisions for a certain wave height. From a theoretical point of view this is expected, since a surrounded layer gives more shelter to the cube. This is due to the fact that the surface area exposed to direct wave attack is reduced. Therefore, a higher wave forcing is necessary to create movement (see Chapter 3). Since no movement was observed for the range with steepness of  $s_{m-1,0} = 0.02$  (embedded cube), it is also concluded that a conventional layer gives a higher amount of collisions.

Section 2.1.2 shows that the average number of collisions was regarded to be equal to 3 by CUR C70 for each hydraulic and geometric condition. The results of the current research however show that the number of collisions is dependent on the wave height, wave steepness and position on the slope. Furthermore, the visual observations in Section 4.6 are in line with the results. Additionally, the research by CUR C70 did not take into account fatigue since only a limited amount of collisions were assumed. It is however observed that for some conditions a large number of collisions occurred. Therefore, fatigue should be incorporated in future versions of "Rocking".

Figure 6.2: Number of collisions for position on slope  $Y/D_n = -2$ Figure 6.3: Number of collisions for position on slope  $Y/D_n = 0$ Figure 6.4: Number of collisions for position on slope  $Y/D_n = 2$

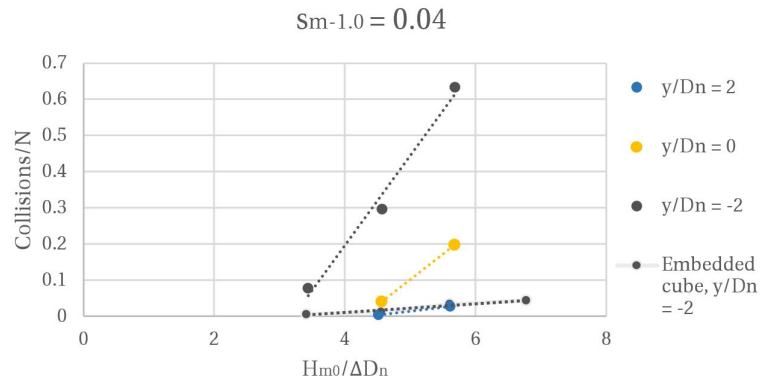


Figure 6.5: Number of collisions for steepness  $s_{m-1.0} = 0.04$

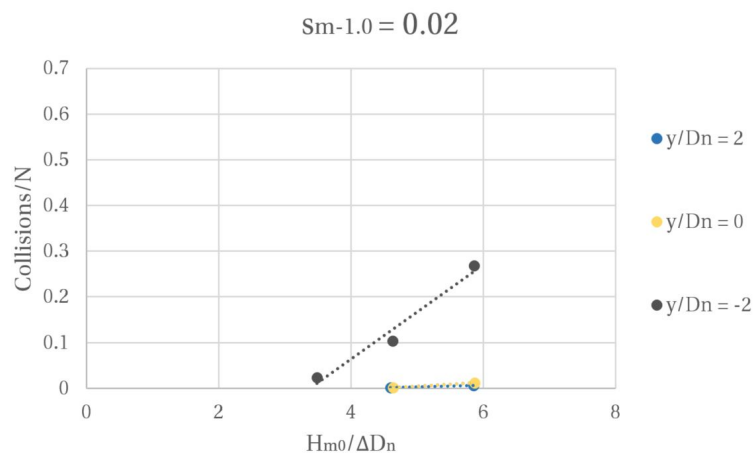


Figure 6.6: Number of collisions for steepness  $s_{m-1.0} = 0.02$

### 6.3. ANALYSIS START OF COLLISIONS

The results for the start of collisions of the wave range with position  $Y/D_n = -2$  are presented in Equations 6.1, 6.2 and 6.3. For a wave steepness of  $s_{m-1.0} = 0.04$ , the following relationship applies:

$$\frac{H_{m0}}{\Delta D_n} = 2.3 - 3.4 \quad (6.1)$$

A wave steepness of  $s_{m-1.0} = 0.02$  corresponds with the following relationship:

$$\frac{H_{m0}}{\Delta D_n} = 2.3 - 3.5 \quad (6.2)$$

For the embedded cube the following relationship applies:

$$\frac{H_{m0}}{\Delta D_n} = 2.3 - 3.4 \quad (6.3)$$

It is observed that all hydraulic conditions for a position of  $Y/D_n = -2$ , both exposed and embedded cube, result in the same range for the start of collisions. This is only applicable for the range with wave steepness of  $s_{m-1.0} = 0.04$  for the embedded cube, since during the other tests with steepness range of  $s_{m-1.0} = 0.02$ , no movements were observed at all. In addition, the embedded cube and the conventional layer cannot be directly compared, since the angle of rotation differs for each layer. Furthermore, the wave steepness appears to provide negligible influence to the relationship for start of collisions. This observation for steepness is compared with the derived equations for other positions on the slope. The position  $Y/D_n = 0$  provides the following relationship for a wave steepness of  $s_{m-1.0} = 0.04$ :

$$\frac{H_{m0}}{\Delta D_n} = 3.4 - 4.6 \quad (6.4)$$

For a steepness of  $s_{m-1.0} = 0.02$  the following relationship applies ( $Y/D_n = 0$ ):

$$\frac{H_{m0}}{\Delta D_n} = 3.5 - 4.6 \quad (6.5)$$

A cube in position of  $Y/D_n = 2$  gives the following results for the start of collisions regarding a steepness of  $s_{m-1.0} = 0.04$ :

$$\frac{H_{m0}}{\Delta D_n} = 3.4 - 4.5 \quad (6.6)$$

The steepness  $s_{m-1.0} = 0.02$  ( $Y/D_n = 2$ ) provides the following relationship:

$$\frac{H_{m0}}{\Delta D_n} = 3.5 - 4.6 \quad (6.7)$$

Equations 6.4 and 6.5 show that the range in start of movement is equal. Therefore, an influence of wave steepness for position  $Y/D_n = 0$  is not observed. The same applies for Equations 6.6 and 6.7. Consequently, no influence of the wave steepness is found for all positions on the slope, unlike the relations provided by CUR C70 and Van der Meer (1988). Furthermore, a difference in start of collisions is observed for the position  $Y/D_n = -2$  compared to the other positions. A lower range for  $Y/D_n = -2$  indicates that the cube starts to collide with a lower wave height.

In Section 4.2.2, an equation by Van Gent (as cited in CIRIA, CUR & CETMEF (2007)) and the translation to the start of movement by CUR C70 (CUR, 1989) are shown. The resulting equation 4.7 is compared with the results in this section. It is observed that the values are within the range of the start of collisions of position  $Y/D_n = -2$ . The differences between the tests of model breakwaters and the current test set-up however have to be kept in mind during comparison. For instance, the used structural geometry is different and the density of the cube is also different.

## 6.4. ANALYSIS VELOCITIES BEFORE COLLISION

In analogy with the research conducted by CUR C70 (see Section 2.1.3), probability distributions are fitted for the velocities before collision of the irregular wave tests. In addition, parameter dependencies are assessed and compared with the relationships derived by CUR C70.

The results for the angular velocities before collision are plotted in dimensionless form ( $\omega/\sqrt{gD_n}$ ) in probability distribution graphs, in which the dependencies in wave height, wave steepness and position on the slope are shown (see Appendix H). An overview of all figures is given in Table H.1. It is chosen to plot the velocities of upward movement and downward movement separately from each other, since it was observed that the data follow different trends. In addition, the interpretation of the results is done with caution because during data processing, it was observed that irregularities in the signal resulted in large errors (see Chapter 5). Assuming that the noise is around a mean, which is the representative signal, the mean of multiple velocity points is the representative velocity. Consequently, data sets with a large number of data points are assumed to give a representative trend. Furthermore, in a few cases, the resulting velocities of collision become negative, caused by irregularities. These points are not taken into account in the probability graphs because it is certain, from a physical point of view, that these velocities before collision are incorrect.

### 6.4.1. PROBABILITY DISTRIBUTION

The distribution for the impact velocities is fitted visually by comparing multiple distribution graphs. The distribution graph for which the data represents a linear trend is chosen as the fitting distribution. Figures H.1, H.2 and H.4 display plots of the angular velocity and probability on Rayleigh paper. For an upward rotation with steepness of  $s_{m-1.0} = 0.04$ , a Rayleigh distribution seems to be the best fit. From a logical point of view, the Rayleigh distribution seems better suited, since the irregular significant wave height distribution is Rayleigh, and is related to the impact velocity via  $u = \sqrt{gH}$ . However, the measured distribution is different from the exponential distribution found during the research by CUR C70 (Equation 2.7). The differences in the distribution relationships are however small, since the Rayleigh and exponential distribution come from the same family. Figures H.5, H.7 and H.8 provide plots of the angular velocities with steepness of  $s_{m-1.0} = 0.02$  in an exponential probability graph. For an upward rotation with steepness of  $s_{m-1.0} = 0.02$ , an exponential distribution appears to be more suitable. This distribution corresponds with the distribution of Equation 2.7 found in the CUR C70 program. Furthermore, Figures H.9 to H.16 show plots of angular velocities before collision during downward rotation on a Weibull distributed graph. The distribution of downward rotations seem to fit with a Weibull distribution. This distribution is from the same family of distributions as the exponential and Rayleigh distribution. Therefore, the differences between the distribution relationships remain small.

To provide more certainty for the type of distribution, statistical analysis should be conducted. In addition, the errors caused by the irregularities in datasets might contribute to differences in distribution, as shown in Section 5.2.3. Therefore, it is necessary to avoid differentiation in future research.

### 6.4.2. SIGNIFICANT WAVE HEIGHT DEPENDENCIES

Figure H.1 shows the datasets of three significant wave height conditions for a wave steepness of  $s_{m-1.0} = 0.04$  and the position  $Y/D_n = -2$  for upward rotation. Firstly, it is noticed that all datasets have a large scatter in data points. This is according to the expectations, since the wave forcing in a irregular wave field also has a large scatter. Secondly, it is distinguished that the highest significant wave height provides a less steep trend than the datasets for the lower wave heights. In addition, the dataset representing angular velocities before collision for a significant wave height of  $H_{m-1.0} = 0.11m$  is less steep than the dataset for significant wave height of  $H_{m-1.0} = 0.09m$ . This implies that the probability to exceed a certain angular velocity is larger for higher wave heights. Therefore, a significant wave height dependency is observed. A similar dependency is observed in Equations 2.12 and 2.15. Therefore, the results of current research correspond with the measurements by CUR C70.

Figure H.2 shows the datasets of two wave heights at  $Y/D_n = 0$  and  $s_{m-1.0} = 0.04$  during upward rotation. Only the position on the slope differs with Figure H.1. However, straightforward significant wave height dependencies are not found. The datasets overlap each other. More detailed analysis showed that the two datasets in Figure H.2 differ considerably in amount of data points. Hence, the datasets cannot be compared using the shown probability plot. Therefore, Figure H.3 is used. This figure shows on the x-axis a division of the number of data points that exceed a certain velocity by the number of waves. On the y-axis the angular velocities before collision are plotted. It is observed that the dataset with higher significant wave height is situated on the left side of the dataset with lower significant

wave height. In contrast to Figure H.2, Figure H.3 plots the probability of exceedance. Therefore, a dataset on the left side of the graph correspond with a higher probability of exceedance and with that a higher chance to exceed a certain velocity. Consequently, the dataset with  $H_{m0} = 0.14m$  results in a larger probability of exceedance, implying an increasing probability of exceedance with increasing significant wave height. This corresponds with the observations in Figure H.1 and the research by CUR C70 (see Section 2.1.3).

For the position  $Y/D_n = 2$ , a limited amount of collisions occurred. As a consequence, a small amount of data points resulted from processing. The combination of amount of data points and the occurring errors during data processing, result in possibly non-representative observations. Nonetheless, a significant wave height dependency is observed in Figure H.4 that correspond to the previous figures; however, more data points have to be obtained before drawing any conclusions.

For the wave series with steepness of  $s_{m-1.0} = 0.02$ , Figure H.5 is analysed, which shows the data for position  $Y/D_n = -2$ . The other positions on the slope with similar wave steepness are not analysed, since they consist of an insufficient amount of data points. From Figure H.5 it is noticed that the highest significant wave height produce the highest steepness in the graph, followed up by  $H_{m-1.0} = 0.12m$  and lastly  $H_{m-1.0} = 0.09m$ . This is in contradiction with the earlier observed dataset for a steepness of  $s_{m-1.0} = 0.04$  and the research by CUR C70. Theoretically this also does not make sense, since a larger significant wave height corresponds with larger wave forcing, which contributes to large velocities before collision. As a result, the probability to exceed a certain velocity should be larger for a larger significant wave height. Therefore, the datasets are plotted again in Figure H.6. This plot shows the division of the number of exceedances by the number of waves, in analogy with Figure H.3. The gradient of the datasets show that the largest significant wave height results in the largest probability of exceedance, followed up by  $H_{m0} = 0.12m$  and  $H_{m0} = 0.09m$ . Consequently, an increase in significant wave height corresponds with an increase in probability of exceedance of a certain angular velocity of collision. This observation is in line with the expectations, the results for a wave steepness of  $s_{m-1.0} = 0.04$  and the research by CUR C70.

Figure H.9 shows the distribution of angular velocities for downward movement, a steepness of  $s_{m-1.0} = 0.04$  and position  $Y/D_n = -2$ . The graph shows clearly that the dataset of the highest significant wave height is positioned relatively low. However, the datasets of  $H_{m-1.0} = 0.11m$  and  $H_{m-1.0} = 0.09m$  overlay each other. Therefore, a plot showing the division of the number of exceedances by the number of waves is used, see Figure H.10. This figure shows a clear relationship of the significant wave height, in which the largest significant wave height contribute to the largest probabilities of exceedance. Consequently, it is concluded that an increase in probability of exceedance of the velocity of collision corresponds with an increase of the significant wave height. This is in line with the research by CUR C70 and the analysis for upward movement. A similar analysis of Figures H.11 and H.14 also confirm these observations. Hence, similar significant wave height dependencies are observed for all conditions of downward movement that contain sufficient data.

As a result, all tests, both upward and downward movement, result in a higher probability of exceedance of the impact velocity. This is in line with the observations during the laboratory tests in which an louder impact is heard for increasing significant wave height.

### 6.4.3. WAVE STEEPNESS DEPENDENCIES

For upward movement, Figures H.17 and H.18 show clear differences between the datasets with steepness  $s_{m-1.0} = 0.04$  and  $s_{m-1.0} = 0.02$ . The dataset with  $s_{m-1.0} = 0.04$  is positioned vertically lower, implying a higher probability of exceedance for a certain impact velocity compared to the dataset of  $s_{m-1.0} = 0.02$ . As result, both figures show consequent results and indicate that a steepness of  $s_{m-1.0} = 0.04$  result in a higher probability of exceedance.

Downward movement results in the same observations as for the upward movement for Figure H.19. Figure H.20 however shows an opposite relationship. The trend with steepness of  $s_{m-1.0} = 0.02$  is vertically lower than the trend with steepness of  $s_{m-1.0} = 0.04$ . The data points are however observed to be lying close to one another, implying a weak steepness relation. Therefore, a plot showing the division of the number of exceedances by the number of waves is used, see Figure H.21. This figure clearly shows that a wave steepness of  $s = 0.04$  results in a higher probability of exceedance. This observation corresponds with the observations in Figure H.19 and the observations for upward movement. Furthermore, the outcome is line with the expectations in Section 4.5.

Equations 2.12 and 2.15 derived by CUR C70 are not related to wave steepness. The research by Sokolewicz (1986) points out that the wave steepness was not varied in the test program. In this Master's thesis, a wave steepness dependency is clearly observed. Therefore, a parameter which takes into account the wave steepness in Equations 2.12 and 2.15 is recommended.

#### 6.4.4. SLOPE POSITION DEPENDENCIES

Figure H.22 shows that the position  $Y/D_n = -2$  provides the highest probability of exceedance for a certain angular velocity of collision, for a wave steepness of 0.04 during upward rotation. After all, the dataset is positioned relatively lower in the graph. However, since the dataset of position  $Y/D_n = 2$  overlays the other datasets, a clear dependency on slope position cannot be derived. Again, a plot showing the division of the number of exceedances by the number of waves is used, see Figure H.23. It is clearly observed that the dataset representing position  $Y/D_n = -2$  is most left in the graph, followed up by position  $Y/D_n = 0$  and  $Y/D_n = 2$ . This implies that a relatively lower position on the lower on the slope gives a relatively higher probability of exceedance. This is in contradiction with the findings by CUR C70 (Section 2.1.3), in which the position around the waterline gave the highest impacts. However, it must be noted that the differences between the slope positions are relatively small, due to the fact that in the current tests, the cube in the lowest position is still exposed to the air during wave run-down. Therefore, the range of positioning is directly exposed to wave impacts, and is regarded to be around the waterline. Hence, it is concluded that a high variability in velocities is observed in the zone exposed to wave impacts. For a steepness of  $s_{m-1.0} = 0.02$  (Figure H.24) a dependency in positioning cannot be observed since a small amount of data points was obtained.

The plot showing the datasets for downward movement (Figure H.25,  $s_{m-1.0} = 0.04$ ) indicates a clear opposite trend. The position  $Y/D_n = -2$  results in the lowest probability of exceedance in velocity of collision. Furthermore, it is observed that position  $Y/D_n = 0$  results in the highest probability of exceedance. These findings are different from upward movement. Therefore, a check is conducted with a plot showing the division of the number of exceedances by the number of waves, see Figure H.26. To determine breakage of concrete cubes, the interest lies in the higher impact velocities. Consequently, the upper part of the graph is analysed. From 25 *rad/s* onwards, it is clearly observed that position  $Y/D_n = 0$  results in the highest probability of exceedance, followed up by position  $Y/D_n = -2$  and lastly position  $Y/D_n = 2$ . Therefore, Figure H.25 and Figure H.26 both show that position  $Y/D_n = 0$  results in the highest probability of exceedance. Apparently, the dependency in position on the slope differs in upward and downward movement. The findings for downward movement are more in line with Equations 2.12 and 2.15 by CUR C70.

Equivalent for both directions of movement is that position  $Y/D_n = 2$  results in the lowest probability of exceedance.

#### 6.4.5. UPWARD VERSUS DOWNWARD MOVEMENT

Figures H.28 and H.29 show clear differences between the data from upward and downward movement. It is observed that the downward movements follow much steeper distribution trends. This implies that the accelerations during upward movement have a larger scatter. As a consequence, both relatively lower and relatively higher velocities occur with upward movement. This can be explained by presuming that during downward movement, the gravitational component is more dominant than during upward movement, since gravitation is positive in direction of downward movement. Consequently, upward movement is more driven by wave forcing, which has a large scatter during irregular wave series. As a consequence, a higher velocity (e.g. 30 *rad/s*) results in a larger probability of exceedance for upward movement. A lower velocity (e.g. 5 *rad/s*) results in a higher probability of exceedance for downward movement. Hence, in terms of design, the upward movement is determining in case higher velocities occur. The research by CUR C70 does not distinguish differences in direction of movement.

#### 6.4.6. EMBEDDED CUBE

The results for the embedded cube are plotted in Figures H.30, H.31 and H.32. Since only a limited amount of data points are available, any dependency derivation is possibly inaccurate. Moreover, a suitable distribution graph cannot be obtained. Nevertheless, the observation of Figures H.30 and H.32 show a significant wave height dependency in which the probability of exceedance of a certain angular velocity increases with significant wave height.

### 6.5. GENERAL DISTRIBUTION FUNCTION FOR VELOCITIES BEFORE COLLISION

For practical application in "Rocking", a more general distribution function is preferred, which takes into account the combined velocities before collision from upward and downward movement, the positions on the slope and the wave conditions. This section elaborates on such a general distribution function and analyses the dependencies of the function regarding the significant wave height, wave steepness, position on slope and degree of exposure of the cube. The supplementing graphs are shown in Appendix H.

### 6.5.1. PROBABILITY DISTRIBUTION

Figures H.33 - H.51 show plots for the general distribution, in which the upward and downward velocities before collision are combined. In most figures, two major bends are observed (e.g. Figure H.33). These bends have similar shapes in all figures. These bends are probably caused by the difference in steepness between the trend for upward and downward movement (See Figure H.28).

Figures H.33, H.35 and H.37 show plots of the datasets for a wave steepness of  $s_{m-1.0} = 0.04$  on Weibull paper. Each figure shows datasets of different significant wave heights for a fixed position on the slope. With these plots, the dependency on distribution for all parameters, except the wave steepness, can be investigated. It is observed that, despite the bending, all datasets appear to follow more or less the fitted lines that are based on the Weibull distribution. This distribution is visually observed to be a best fit for all datasets, in comparison with other distribution types. Hence, it is concluded that the probability distribution function of the datasets is described most accurately with a Weibull distribution, for a wave steepness of  $s_{m-1.0} = 0.04$ .

Figures H.39, H.41 and H.42 show plots of the datasets for a wave steepness of  $s_{m-1.0} = 0.02$  on Weibull paper. It is observed that, despite the bending, the datasets also follow more or less the Weibull distribution. This is similar to the observations for a wave steepness of  $s_{m-1.0} = 0.04$ . Hence, it is concluded that both wave steepnesses show a similar probability distribution. However, it must be kept in mind that Figures H.41 and H.42 have a limited number of data points. Hence, any derived distribution for positions  $Y/D_n = 0$  and  $Y/D_n = 2$ , with a wave steepness of  $s_{m-1.0} = 0.02$ , might be inaccurate.

In conclusion, the general distribution function is described by a Weibull distribution. This derived Weibull distribution does not correspond to the derived exponential distribution by CUR C70. However, the two distributions are from the same family of distributions. Hence, the differences between the distribution functions are small.

### 6.5.2. SIGNIFICANT WAVE HEIGHT DEPENDENCIES

Figure H.33 shows plots of various wave heights for a fixed wave steepness of  $s_{m-1.0} = 0.04$  and position  $Y/D_n = -2$ . It is observed that, across the majority of data points, the black points are positioned highest, followed by the green points and lastly, the blue points. This implies that the data points from wave height  $H_{m0} = 0.09m$  are positioned highest and the data points from wave height  $H_{m0} = 0.14m$  are positioned lowest. The graph displays the probability of non-exceedance in the y-axis. Hence, a lower positioning in the y-axis means a lower probability of non-exceedance, and thus, a higher probability of exceedance. Consequently, a higher significant wave height gives a higher probability of exceedance of a certain angular velocity. However, some data-points overlap each other in Figure H.33. To be certain about the wave height dependencies, the datasets are plotted in an exceedance graph over the number of waves, see Figure H.34. The differences between the datasets are clearly distinguished. A significant wave height of  $H_{m0} = 0.14m$  is positioned relatively on the left side, followed by  $H_{m0} = 0.11m$  and lastly,  $H_{m0} = 0.09m$ . In this graph, a positioning on the left means a higher probability of exceedance of a certain angular velocity. Hence, an increasing significant wave height corresponds with an increasing probability of exceedance of a certain impact velocity.

Figure H.35 shows the datasets of various wave heights for a wave steepness of  $s_{m-1.0} = 0.04$  and position  $Y/D_n = 0$ . It is observed that the datasets are very closely positioned to one another and overlap each other at some points. Therefore, a wave height dependency cannot be directly obtained. Consequently, the datasets are plotted in a graph with the number of exceedances divided by the number of waves, see Figure H.36. The differences between the datasets are now clearly observed. The dataset of  $H_{m0} = 0.14m$  is positioned more to the left than the dataset of  $H_{m0} = 0.11m$ . Therefore, a relatively higher wave height corresponds to a higher probability of exceedance.

Figure H.37 shows the angular velocities before collision of various wave heights for a wave steepness of  $s_{m-1.0} = 0.04$  and position  $Y/D_n = 2$ . It is observed that especially the dataset of  $H_{m0} = 0.11m$  has a small amount of data points. Therefore, any derived wave height dependency might be inaccurate. Nonetheless, insight is provided (without drawing any conclusions) with plots in a graph with the number of exceedances divided by the number of waves, see Figure H.38. It is clearly observed that the dataset with  $H_{m0} = 0.14m$  is positioned more to the left, indicating a higher probability of exceedance of a certain angular velocity with relatively higher significant wave height.

A similar analysis is conducted for a wave steepness of  $s_{m-1.0} = 0.02$ . Figure H.39 shows the angular velocities before collision of various wave heights for position  $Y/D_n = -2$ . It is observed that the datasets are closely positioned to one another and overlap each other at some points. Therefore, a clear difference in probability of exceedance of the datasets is not observed. Consequently, the datasets are plotted in a graph with the number of exceedances divided by the number of waves, see Figure H.40. Differences between the datasets are clearly observed. The dataset for

$H_{m0} = 0.14m$  is positioned most to the left, followed by  $H_{m0} = 0.11m$  and lastly,  $H_{m0} = 0.09m$ . This indicates an increase in probability of exceedance of a certain angular velocity for increasing wave height. Figures H.41 and H.42 consist of a small amount of data points. Therefore, any wave height dependency is possibly inaccurate.

It is concluded that, for an increasing significant wave height, the probability to exceed a certain angular velocity increases. This trend is observed for all conditions with a large amount of data-points. This conclusion corresponds to the research by CUR C70 and the observations in Section 6.4.2.

### 6.5.3. WAVE STEEPNESS DEPENDENCIES

Figure H.43 shows plots of the datasets of the wave steepness for a fixed wave height  $H_{m0} = 0.14m$  and position  $Y/D_n = -2$ . Differences between the datasets are clearly distinguished. The green data points, corresponding to  $s_{m-1.0} = 0.02$ , are positioned higher than the blue data points, corresponding to  $s_{m-1.0} = 0.04$ . A relatively higher positioning in the graph means a relatively higher probability of non-exceedance. Consequently, a relatively lower positioning means a relatively lower probability of non-exceedance and thus, a higher probability of exceedance. Therefore, it is concluded that a wave steepness of  $s_{m-1.0} = 0.04$  results in a higher probability of exceedance in comparison with  $s_{m-1.0} = 0.02$ .

A wave steepness dependency is not directly observed in Figure H.44, as the data points overlap each other. Therefore, the datasets are plotted in a graph with the number of exceedances divided by the number of waves, see Figure H.45. It is clearly observed that the blue points are positioned more to the left than the green points. This implies that a wave steepness of  $s_{m-1.0} = 0.04$  corresponds with a higher probability of exceedance of a certain angular velocity, in comparison with  $s_{m-1.0} = 0.02$ .

The figures show that a wave steepness of  $s_{m-1.0} = 0.04$  results in a higher probability of exceedance in comparison with  $s_{m-1.0} = 0.02$ . This is in line with the observations in Section 6.4.3. CUR C70 did not take into account the dependencies by wave steepness. This research shows that the wave steepness clearly influences the magnitude of impact velocities. Therefore, it is strongly advised to take into account the dependency in wave steepness in future research.

### 6.5.4. SLOPE POSITION DEPENDENCIES

Figure H.46 shows plots of various positions of the cube on the slope, with a fixed wave steepness of  $s_{m-1.0} = 0.04$  and wave height  $H_{m0} = 0.14m$ . It is observed that all data points follow the same trend, which means that the datasets overlap with each other. Hence, a slope dependency is not observed in this figure. Consequently, the datasets are plotted in a graph with the number of exceedances divided by the number of waves, see Figure H.47. It is clearly observed that the datasets follow different trends. The data points for position  $Y/D_n = -2$  are positioned most to the left, followed by position  $Y/D_n = 0$  and lastly, position  $Y/D_n = 2$ . A positioning more to the left indicates a higher probability of exceedance of a certain angular velocity of collision. This implies that position  $Y/D_n = -2$  results in the highest probability of exceedance, followed by position  $Y/D_n = 0$  and lastly, position  $Y/D_n = 2$ . Hence, it is concluded that the probability of exceedance of a certain angular velocity is influenced by the positioning of the cube relative to the water level. A decreasing position results in higher probability of exceedance. This conclusion is only valid for the considered range in positioning, see Section 6.4.4 for further explanation.

A similar analysis is conducted for a wave steepness of  $s_{m-1.0} = 0.02$ , see Figure H.48. Due to the small amount of data points, any derivation of dependencies in positioning on the slope is possibly inaccurate. Furthermore, a slope dependency cannot be directly observed, as the data points are positioned closely to one another. To provide more insight, the datasets are plotted in a graph with the number of exceedances divided by the number of waves, see Figure H.49. A clear distinction between the datasets is observed. The dataset of  $Y/D_n = -2$  is positioned most to the left, indicating the highest probability to exceed a certain angular velocity. The other positions are positioned more closely to one another, in which position  $Y/D_n = 2$  results in a slightly higher probability to exceed a certain angular velocity.

From analysis it is concluded that the probability of exceedance of a certain angular is dependent on the positioning on the slope. For the tested range of  $s_{m-1.0} = 0.04$ , the position  $Y/D_n = -2$  gives the highest probability of exceedance. In CUR C70, a dependency on the positioning on the slope was also found. However, in that research program, the position  $Y/D_n = 0$  was found to give the highest probability of exceedance, which is different from current research. Furthermore, it is recommended to conduct more tests for the series with  $s_{m-1.0} = 0.02$  to increase the reliability of the dependencies.

### 6.5.5. EMBEDDED CUBE

Figure H.50 shows plots of the datasets for the embedded cube on Weibull paper. In this figure, the dependency on distribution type can be investigated. All datasets appear to follow more or less the fitted lines that are based on the Weibull distribution. This distribution is visually observed to be a best fit for all datasets, in comparison with other distribution types. Hence, it is concluded that the probability distribution function of the datasets is described most accurately with a Weibull distribution. This probability distribution is similar to the general distribution of the exposed cube. Therefore, it is concluded that the type of distribution function is observed to be independent from the degree of exposure of the cube. Furthermore, the probability distribution function is different from the exponential distribution function derived by CUR C70. However, the two distribution types are from the same family of distributions. Hence, the difference between the distribution functions is small.

In addition, it is observed that the datasets are very closely positioned to one another and overlap each other at some points. Furthermore, the fitted lines have different steepness and cross each other at various points. Therefore, a wave height dependency cannot be directly obtained. Consequently, the datasets are plotted in a graph with the number of exceedances divided by the number of waves, see Figure H.51. It is observed that the dataset for  $H_{m0} = 0.11m$  is positioned lowest and relatively to the right. This indicates a lower probability of exceedance of a certain angular velocity, in comparison with the other significant wave heights. Furthermore, the majority of the data points from  $H_{m0} = 0.17m$  are closely situated in between the datasets of  $H_{m0} = 0.14m$  and  $H_{m0} = 0.11m$ . However, the differences between the datasets are very small. In addition, one could question the reliability of the datasets, as only a limited number of data points are available for analysis. Therefore, a clear dependency on the significant wave height is not found for the embedded cube. More tests should be conducted to improve the reliability of the datasets.

## 6.6. ANALYSIS MAGNITUDE OF MAXIMUM IMPACT VELOCITIES

This section provides insight in the order of magnitude of maximum impact velocities and focusses on the test series of the embedded cube. This set-up provides the most realistic order of magnitude of impacts, as it is most representative in terms of a prototype breakwater slope. The impacts are compared with the results from CUR C70.

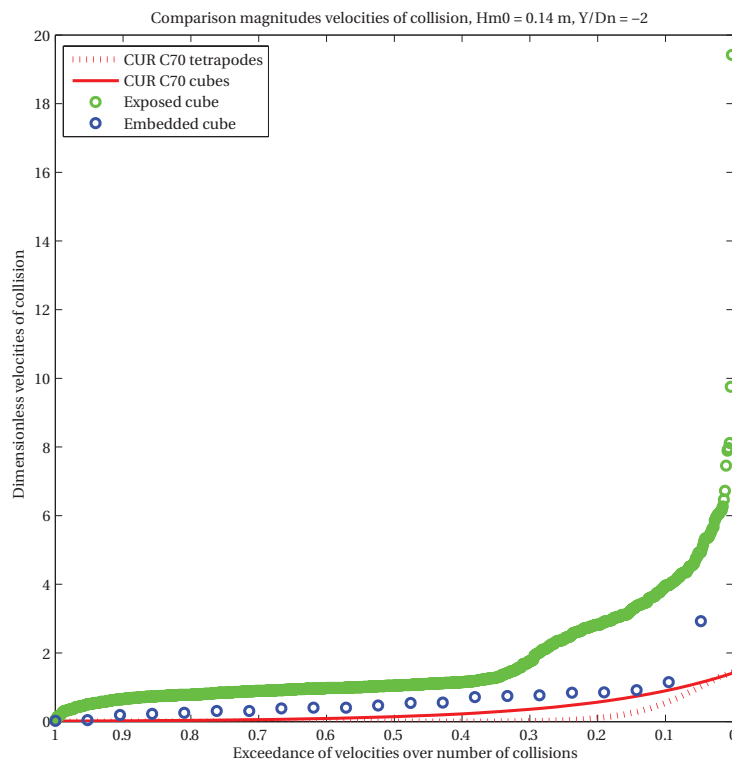


Figure 6.7: Comparison magnitude of impact velocities

### 6.6.1. COMPARISON WITH CUR C70

Figure 6.7 shows plots of the embedded cube and the results from the research by CUR C70 for tetrapodes and cubes. For this purpose, Equations 2.12 and 2.15 are used to indicate the magnitude of impacts derived by CUR C70, in which  $y/D_n = -2$ ,  $H_s = 0.14m$  and  $\Delta = 0.5$  are substituted. The choice for the position is made based on the position of the cube in the tests of the embedded layer. Sokolewicz (1986) did not define the position on the position of measurements exactly. Therefore, the more global position of  $y/D_n = -2$  is used, instead of the real position  $[y/D_n]_p = -1.67$ . Next to that, the significant wave height is chosen as such that it represents the condition of the embedded layer with most data points. Furthermore, the density of the units are chosen to be equal to the density of the cube in the current research project:  $1500kg/m^3$ .

It is observed in Figure 6.7 that the order of magnitude of the maximum (dimensionless) impact velocities of the embedded cube are around 1 [-], with an outlier of about 3 [-]. The outlier is not taken into account, as it is suspected that the high order of magnitude of the outlier is caused by irregularities in the data signal, see Section 5.2.3. Therefore, the outlier is considered to be not representative for the velocities of collision. In addition, it is observed that the data points of the embedded cube are positioned slightly higher than the line derived by CUR C70 for cubes. The difference between the results of the embedded cube and the derived relation of CUR C70 is about 0.2. This implies that the maximum impacts of the embedded cube are 25% higher than the relation from CUR C70 for cubes. The maximum impacts of the embedded cube are more or less 50% larger than the relation from CUR C70 for tetrapodes. The differences between the velocities before collision of the current research and the research by CUR C70 are explained by the differences in test set-up, mode of movement and shape of the unit. Hence, no quantitative conclusions can be drawn from this analysis. The only conclusion here is that the velocities of the embedded are more or less in the same order of magnitude, in comparison with the derived relations from CUR C70.

### 6.6.2. DEPENDENCIES MAGNITUDE MAXIMUM IMPACT VELOCITIES

To provide insight in the influence of the degree exposure of the cube, the test results of the exposed cube are included in Figure 6.7. In this plot, the velocities for the exposed cube are shown at a turning angle of 40 degrees, instead of the velocities before collisions. This allows comparison with the results of the embedded layer because the turning angle at which the velocities are compared, are equal to one another. From Figure 6.7, it is clear that the magnitude of impacts of an exposed cube are much higher than the embedded cube. The maximum velocities for the exposed cube are around 8 [-] with outliers of 10 and 19 [-]. If the outliers are neglected, the difference between the configurations is about 7. This implies that the order of magnitude of the maximum impacts are 700% larger. Hence, it is concluded that the degree of exposure of the cube is of significant influence for the magnitude of impacts.

An analysis is conducted to determine whether the order of magnitude of maximum impacts is influenced by the wave heights. From Figure H.50 it is observed that the maximum velocities of all significant wave heights, except for the outliers, are in the same order of magnitude of 1 [-]. Therefore, it is concluded that the wave height is of negligible influence for the impact velocities. This implies that a smaller significant wave height leads to similar maximum impact velocities in comparison with a larger significant wave height, provided that a unit moves. Similarly, it is concluded that for the upward and downward rotation, the maximum impact velocities are in the same order of magnitude, see Figures H.30 and H.31.

## 6.7. ADDITIONAL ASPECTS

This section analyses additional aspects which are noticed during data processing. The analysis has the purpose to obtain a better understanding of the behaviour of the cube. The first aspect is the time lag between wave impact and movement of the cube, as observed during the wave flume tests. Figure 6.8 shows a comparison between the time lag of surging breakers ( $s = 0.02$ ) and collapsing breakers ( $s = 0.08$ ). The graphs indicate the measurements in the z-axis of the accelerometer and the measurements from the pressure sensor. Wave impact goes namely together with a steep drop of the pressure signal, provided that the wave impact occurs at the same time over the width of the flume. Then, movement of the cube occurs after a time period. This time lag is for surging breakers, for the plotted situation, equal to 0.4s. To compare various conditions, the time lag is divided by the wave period. Therefore, the resulting dimensionless time lag becomes 0.15. For collapsing breakers the time lag is 0.04s, which results in a dimensionless time lag of 0.04. Consequently, it is observed that the time lag for surging breakers is much larger than the time lag for collapsing breakers. The cube starts to move later in time with surging breakers. This corresponds with the observations during the laboratory tests, see Section 4.6.

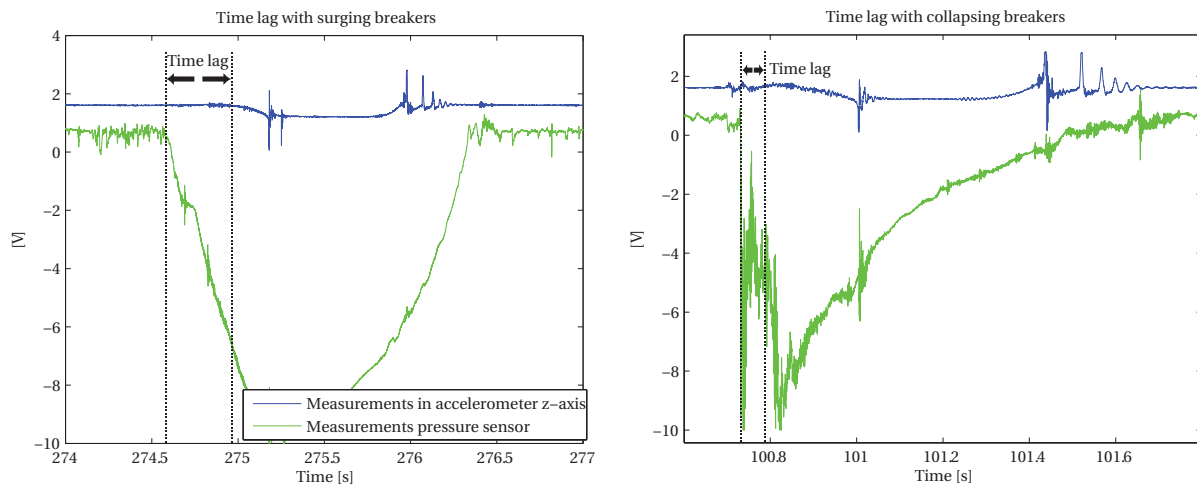


Figure 6.8: Comparison time lag between wave impact and start of movement

In addition, Figure 6.9 shows a close up of the signals during upward movement for both surging and collapsing breakers. Under collapsing breaker conditions, the signal is characterised by steep peaks prior to movement. These peaks represent wave impact. Since a rather smooth signal is seen for surging breakers, it is concluded that the wave impact plays a less important role. This is in line with the observations for the time lag, in which longer time lag implies less importance of wave impact. Hence, the forcing due to drag is dominant for surging breakers. With this, a check is conducted for the assumptions in Chapter 3. Since the equation for wave impact was not taken into account for surging breakers, the analytical model corresponded correctly with the analysis. Additionally, due to the steep peaks, the wave impact cannot be neglected for collapsing breakers. The assumption in Chapter 3 corresponds with the analysis.

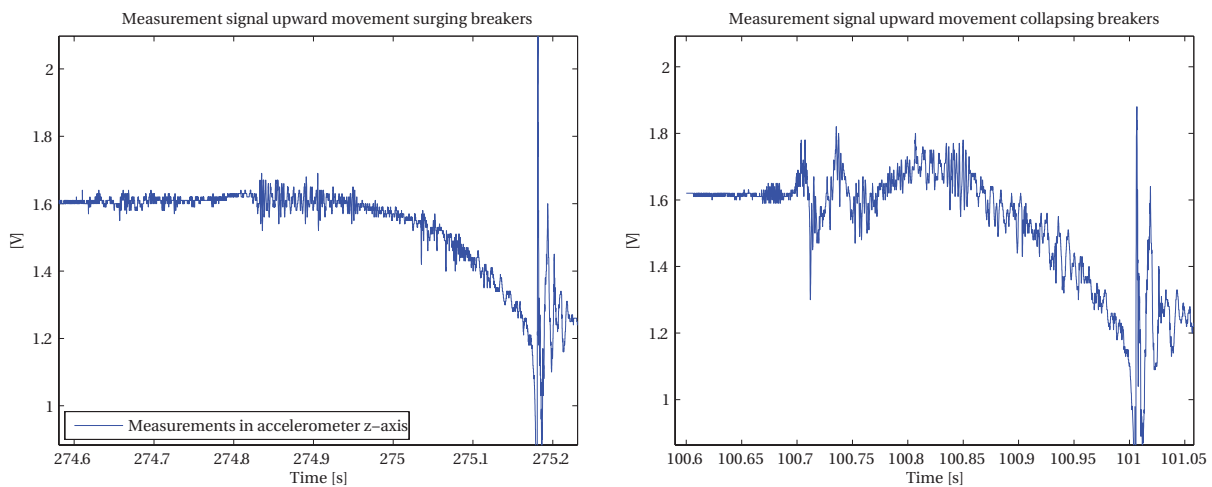


Figure 6.9: Comparison of the signals of upward movement under surging and collapsing breaker conditions

Furthermore, during movement of the cube, more irregularities in the signal are observed for collapsing breakers (see Figure 6.9). Also more peaks in the pressure signal are observed (Figure 6.8). These observations are explained by the fact that under surging conditions, negligible wave breaking occurs. This goes together with a relatively small amount of turbulence in the wave front. Less turbulence consequently implies less deviations in the mean of a signal and also less noise. Figure 6.10 shows that much more disturbances in the water are seen during collapsing breaker conditions. These disturbances are generated by wave breaking and make the capturing of movement of the cube by camera impossible. Hence, it is likely that the disturbances, corresponding to turbulence, create the additional noise in the signal for collapsing breakers.

Last but not least, at the beginning of movement, an upward trend in the acceleration signal for collapsing breakers is observed. This trend is however not observed in surging breaker conditions (Figure 6.9). An explanation is obtained

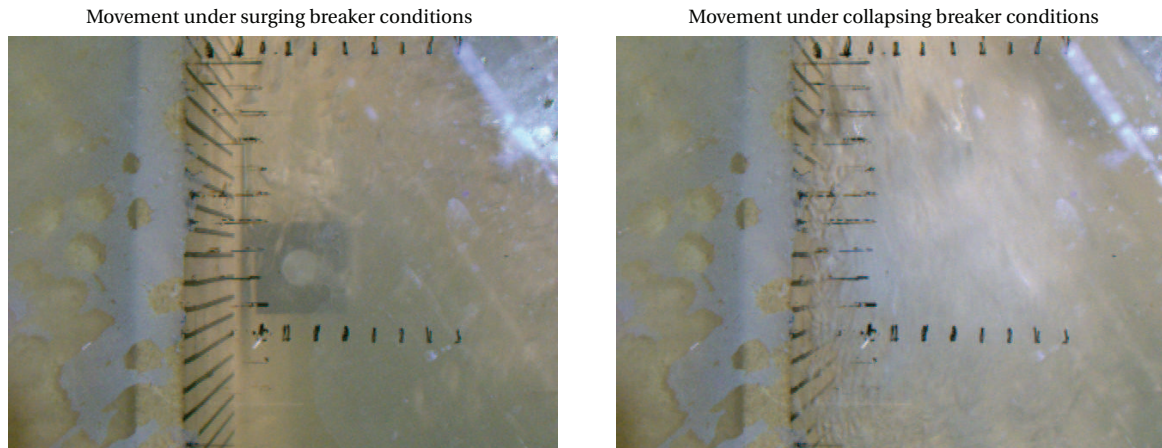


Figure 6.10: More foam during collapsing breaker conditions

by comparing the time periods for which movement occurs. For collapsing breakers, a much shorter time period of movement is seen. Hence, it requires higher accelerations of the cube to move over the same angle. As a consequence, the influence of tangential and normal acceleration is larger, compared to the measurement of the gravitational acceleration (see Section 5.2.2). For instance, Figure 5.4 (left graph) shows that the tangential component has an upward trend. Since the normal component is only important at the end of the period of movement (exponential growth), the gravitational and tangential component dominate in the first part of movement. The magnitude of the tangential component is dictated by the magnitude of movement of the cube. For a larger acceleration, a larger tangential component is found. Therefore, the upward trend in the measurement signal for collapsing conditions is depending on the magnitude of the tangential component, which becomes more dominant for a shorter time period of movement.

# 7

## CONCLUSIONS

Prototype single layer armour units on a breakwater slope are observed to break. To predict when breakage occurs, the objective of this research project is to obtain knowledge on, and measurements of the rocking behaviour and failure mode of single layer armour units. First, previously conducted research by CUR C70 was analysed. Second, a single cube on a breakwater slope is subjected to investigations. Third, an analysis of the results was conducted and compared with the results from CUR C70. Finally, important conclusions are reached, that are, on multiple aspects, different from previously conducted research on double layer armour units. This chapter elaborates on these conclusions.

### 7.1. NUMBER OF COLLISIONS

The number of collisions is an important input value in "Rocking". The research by CUR C70 assumed roughly that the number of collisions per moving unit was on average equal to 3. From analysis of the collisions of the cube during the irregular wave series of current research, it is found that this assumption by CUR C70 is inaccurate. The number of collisions appears to be dependent on many parameters, such as the wave height, wave steepness, position on slope and degree of exposure of the cube to wave attack. For some conditions, the amount of collisions becomes very large. Consequently, fatigue plays a more important role in the strength of armour units.

For future research and design studies, it is recommended to take the number of collisions into account as a variable that is dependent on the hydraulic and geometric conditions. Furthermore, it is recommended to take into account fatigue in calculations regarding the strength of concrete, for instance in "Rocking".

### 7.2. INFLUENCE WAVE STEEPNESS ON IMPACT VELOCITIES

The equations describing the impact velocities are the starting points of the calculation in "Rocking". Hence, an accurate physical representation of those equations is of paramount importance for the accuracy of the whole numerical model. In the research by CUR C70, the influence of the wave steepness was not researched. During this research project, it is found that the wave steepness influences the magnitude of impact velocities significantly, as the test conditions with  $s_{m-1,0} = 0.04$  results in a higher probability of exceedance of a certain velocity before collision in comparison with  $s_{m-1,0} = 0.02$ . Therefore, for an accurate physical representation, a parameter that includes the wave steepness in the equations for the impact velocities, is recommended.

### 7.3. WEIBULL DISTRIBUTION FUNCTION FOR IMPACT VELOCITIES

Probability distributions are visually fitted for the cube's velocities before collision. It is found that different distributions fit the datasets for different hydraulic conditions and type of movement. These distributions are constantly of the exponential, Rayleigh and Weibull type, which come from the same family of distributions and hence, have similar distribution functions. Hence, from a practical point of view, a general distribution for all parameters is preferred.

Despite some bends in the plots, the datasets, for both exposed and embedded cube, follow the fit for the Weibull distribution. Hence, it is concluded that a general distribution is described with a Weibull distribution. Furthermore, it is concluded that the general fit is dependent on the wave height, wave steepness and position on the slope.

CUR C70 found a general fit based on the exponential distribution. Both the Weibull and exponential distribution are from the same family of distributions and therefore, the differences in type of distribution between CUR C70 and current research remain small. However, major differences are found in the exclusion of the wave steepness by CUR C70 and the differences in the dependencies of the position of the cube on the slope for the exposed cube. For future research, it is recommended to conduct statistical analysis to find the right probability distribution for the datasets. Furthermore, it is recommended to make a distribution function which takes into account parameters for the wave height, wave steepness and position on the slope. Additionally, it is recommended to conduct tests with an extended range of positions on the slope to derive better dependencies. Lastly, it is recommended to conduct more tests with an extended test range of wave heights for the test with  $s_{m-1,0} = 0.02$  and the tests with the embedded cube, for more data points and thus, more reliability in the datasets.

#### 7.4. TYPE OF MOVEMENT

Section 6.4.5 points out that clear differences exist between the probability distributions for upward and downward movement. In terms of design, it is concluded that the upward movement determines the probability of exceedance of extreme velocities. The research by CUR C70 did not distinguish these type of movements. It is the question whether these specific types of movement play an important role in future research, as the movements of the cube were restricted with a hinge. It is in future research more preferable to exclude the hinge to have more realistic movements. The obtained knowledge from this Master's thesis that contributes to further research is that different types of movement result in different impact velocities and hence, multiple types of movements should be considered to find the governing impacts.

#### 7.5. ADDITIONAL CONCLUSIONS

*Maximum Impact Velocities:* A comparison between the maximum impact velocities of the embedded cube with the results from CUR C70 are made. It is concluded that the impact velocities of both researches in the same order of magnitude. In addition, it is shown that the degree of exposure of the cube is of significant influence for magnitude of maximum impact velocities. Last but not least, it is remarkable to find that the order of magnitude of impact velocities does not change for changing significant wave height. This implies that a small significant wave height can cause large impact velocities. However, the amount of data points of the embedded layer are small and the error due to noise in the tails of the distributions might become large. Hence, more experiments have to be conducted in the future to support this conclusion.

*Analytical Model:* The analytical model was created to determine the velocities before collision of the cube based on literature. A comparison of the analytical model with the test results of the regular wave series shows that the analytical model have similar dependencies regarding the wave height and wave steepness. However, the order of magnitude of the velocities is overestimated. Hence, it is concluded that the analytical model is too conservative. The analytical model and all its assumptions should be researched more thoroughly, to come to accurate armour unit impact velocities on a simplified breakwater slope.

*Start of Collisions:* An analysis is conducted for which hydraulic conditions the cube starts to move and collide. It was found that the start of collisions is independent from the wave steepness. This is in contrast to the relations provided by CUR C70 and Van der Meer (1988). In addition, position  $Y/D_n = -2$  resulted in a lower stability number and is therefore normative in terms of design. This conclusion is only valid for the tested positions on the slope, since it cannot be ruled out that other, not tested positions result in lower stability numbers. A test with a conventional breakwater slope in future would provide better results for the start of collisions.

*Wave Impact, Turbulence and Acceleration Profile:* To provide insight in the movements of the cube, aspects such as the influence of wave impact on the cube, the influence of turbulence and speed of movement on the profile of the measurement signal are considered. It is concluded that wave impact is negligible in case of surging breakers. Next to that, the degree of noise in the measurement signal is partially caused by the degree of turbulence. A higher degree of turbulence is observed for collapsing breakers. In addition, a different acceleration profile occurs with movements over shorter duration. This knowledge can be taken into account in the interpretation of data in future research.

# 8

## RECOMMENDATIONS

This chapter provides recommendations regarding the performed work during this Master's thesis. Next to that, the opportunities for further research are discussed. Addressed is the suitability of the accelerometer for further research. Furthermore an action plan to reach the main objective is presented. Lastly, opportunities outside the scope of "Rocking" are addressed.

### 8.1. OPPORTUNITIES FOR CURRENT RESEARCH

The elaboration of opportunities for improvement of current research is divided into three parts: laboratory experiments, data processing and analysis.

#### 8.1.1. LABORATORY EXPERIMENTS

*Check for crosstalk:* During the processing of data it was observed that the x-axis and y-axis of the accelerometer were disturbed by the wave gauges. This phenomenon was not noticed during the flume tests, since the peaks made the signal still look representative. In future tests it is recommended to check the signals carefully, by doing a direct data processing after the first test. Possibly, the order of connection together with the degree of amplification of the signals caused the crosstalk. Hence, it is recommended to check the connections of the electronic equipment more carefully in close consultation with laboratory experts.

*Orientation accelerometer inside cube:* Due to the current orientation of the accelerometer parallel to the faces of the cube, see Figure 4.9, the z-axis and x-axis both measure three acceleration components: the tangential acceleration, normal acceleration and gravitational acceleration. However, by aligning the x-axis in the direction of the tangential component, see Figure 8.1, the measurement of the normal component is excluded. This is due to the fact the tangential and normal component have a relative angle of  $0.5\pi$  radians. As a consequence, the measurement in the z-axis is parallel to the normal component, which excludes the measurement of the tangential acceleration. With this configuration, the equations of motion in Section 5.2.1, can be further simplified.

*Gyroscope:* The elaboration can be even further simplified in case an additional gyroscope is used, in which the angular velocities are directly measured. The modes of movement and velocities before collision can be derived with the combined information of the angular velocities from the gyroscope and cube's orientation before and after movement from the accelerometer. This methodology is preferred because of its simplicity in data processing.

*More positions on slope:* In Section 6.4.4 it was mentioned that the tested positions on the slope cover a small range, as all positions are exposed to direct wave attack. It is expected that, the number of collisions and impact magnitude decrease outside the zone of direct wave attack. Additional tests, in which the range in position on the slope is extended, are necessary to verify these expectations.

*Realistic angle of movement:* The angle over which the cube could rotate was kept to be equal to 90 degrees for the conventional layer, for a simplistic representation. In reality, such a large degree of movement is rare. The surrounding armour units form the limitation for the degree of rotation, in a conventional breakwater layer. An angle of rotation for the conventional layer, which is equal to the tested embedded cube, is more realistic.

*More tests to generate more data points:* To establish dependencies for the probability distributions and to fit the data as good as possible, a large dataset is necessary. In particular, the datasets for steepness of  $s_{m-1,0} = 0.02$  and for the embedded cube lack data. Therefore, it is recommended to conduct more tests to improve the reliability and accuracy of the data.

*Extend test range with higher significant wave heights:* More collisions occur with a higher wave height, as observed during analysis. Hence, to obtain a larger dataset, relatively higher wave heights could be considered. This extension in wave heights is particularly applicable to the conditions with steepness of  $s_{m-1,0} = 0.02$  and the embedded cube.

*More modes of movement:* In a conventional breakwater layer, multiple modes of movement are imaginable. In fact, the armour unit could move in all degrees of freedom depending on the placement configuration of the surrounding units. During the current tests, only rotations in one axis were considered. Therefore, it is recommended to expand the modes of movement.

*More realistic embedded cube:* It was attempted to create a more representative configuration with the embedded cube. However, this layer still lacks major characteristics of a conventional breakwater layer. For instance, the slope roughness is wrongly represented. Next to that, the porosity of the tested layer is completely different. Furthermore, a continuous slope, without crest was used. By improving these aspects, a more realistic breakwater layer is created.

*Start of movement for different positioning of hinge:* The hinge was positioned on the upper side of the cube during the experiments. This has consequences for the results in start of movement, as only the start of movement upwards is measured. However, it is imaginable that downward movement is determining. After all, the mass is directed downwards, contributing positively for downward movement. Next to that, surely different hinge configurations have to be tested in order to compare the impacts of upward and downward movement, if it is chosen to work with a smaller angle of rotation.

*Different armour units:* A similar research could be conducted for different types of armour units. One out of the many types of armour units is the hexapod shown in Appendix I. This armour unit is designed for experimental purposes and represents the characteristics of common interlocking single layer armour units. Other types of armour units that could be considered are: Accropode, Coreloc and Xbloc.

*3D-printed shape:* The usage 3D-printing allows fabrication of complex shapes in a cost-effective manner. An example is shown in Appendix I. The unit is designed as such that it can be opened and closed practically, which allows changing of components and wires of the electronic devices during the tests.

### 8.1.2. DATA PROCESSING

*Application model:* It was found that differentiation of a dataset, containing irregularities, causes large errors. Hence the results for the velocity of impact are possibly inaccurate. The current research uses the synthetic model in Section 5.2.2 to determine the tangential and normal acceleration. The usage of the synthetic model could be expanded to simulate the acceleration signal measured in the z-axis and to use that signal in further processing. Hence, this approach is not influenced by noise. Consequently, differentiation of the "artificial" signal does not result in errors.

*Input from three accelerometer axes:* In case no crosstalk in the x-axis of the accelerometer was found, a more accurate approach could be used. First, the same approach as in Section 5.2.2 could be used to determinate the angle of the cube over time. Secondly, the angle ( $\theta$ ) is substituted as a known parameter in the following equation of motion for the measurements in x-axis (upward movement):

$$a_x = -\frac{D_n}{2} \frac{d\omega}{dt} - \frac{D_n}{2} \omega^2 - g \cos(\phi_g + \theta) \quad (8.1)$$

In which  $\omega$  stands for the angular velocity. The equation is similar to Equation 5.3 and only differs in sign, since the x-axis is situated at an angle 90 degrees from the z-axis (see Figure 4.9). Furthermore, the relation  $\omega = \frac{d\theta}{dt}$  is substituted in Equation 8.1. Hence, the equation becomes a first order differential relation, in which the gravitational component is already known. This relation is easier to approximate than Equation 5.3. In addition, differentiation is avoided with this methodology and therefore more accurate results could be obtained. A similar relation can be derived for downward movement. This methodology is recommended in future research with accelerometer measurements.

*Different orientation:* As pointed out in Section 8.1.1 the alignment of the accelerometer axes in the direction of tangential and normal acceleration allow simplification of the equations of motion. Figure 8.1 shows the proposed alignment. Consequently, the equations of motions for upward movement in the x-axis and z-axis become:

$$a_z = \frac{D_n}{2} \frac{d^2\theta}{dt^2} + g \cos(\phi_g + \theta) \quad (8.2)$$

$$a_x = -\frac{D_n}{2} \omega^2 - g \cos(\phi_g + \theta) \quad (8.3)$$

This implies that coefficient  $C_{nm}$  in the synthetic model in Section 5.2.2 is neglected. Furthermore, the relation for  $a_x$  becomes an ordinary equation, which could be solved analytically using the methodology in paragraph "Input from three accelerometer axes". A similar procedure can be conducted for downward movement.

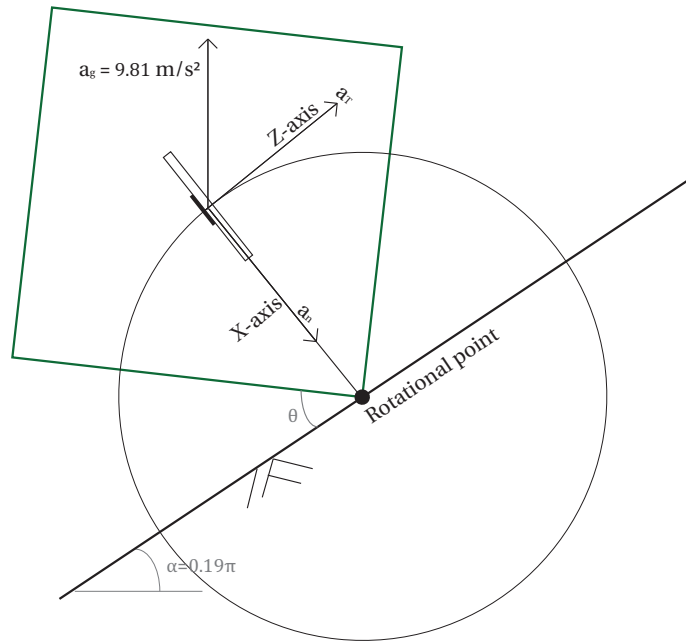


Figure 8.1: Alignment accelerometer axes parallel to the tangential and normal acceleration

*Gyroscope:* The elaboration can be even further simplified, with an additional gyroscope. The gyroscope provides direct information about the angular velocity  $\omega$ . In this case the accelerometer is used to provide information about the orientation of the cube before and after movement, and thus the mode and type of movement. Hence, the velocities before collision can be determined directly. As a consequence, usage of the synthetic model in Section 5.2.2 and the equations of motions are not necessary. The usage of the gyroscope is recommended as the method for ideal measurement because of the simplicity in data-processing.

*Three-dimensional movements:* In case multiple modes of movement are considered (future research), the three-axis accelerometer and gyroscope come in handy. First, rotations in three-dimensional space are discussed. The gyroscope measures the angular velocities in the x-y-z-axis. Combining the three axes gives the total angular velocity, with the relation  $\omega = \sqrt{\omega_x^2 + \omega_y^2 + \omega_z^2}$ . The added acceleration vectors from the accelerometer before and after movement in x-y-z-direction provide information about the orientation of the cube. The difference in orientation before and after movement gives information about the angle of movement and type of movement. Furthermore, in case translations occur, a change in the accelerometer signal is observed, while no angular velocity is measured by the gyroscope. The acceleration signal before and after movement gives the same output in Voltage, since the measurements of gravity remains equal. By integration over time of the combined acceleration signal over the three axes during movement, the velocities before collision are obtained. Care has to be taken in filtering noise and impacts from the accelerometer signals, as they can be mixed up with movements. In addition, the situation becomes more complex in case at the same time translations and rotations occur. It is advised to follow the explained methodology for rotations. Subsequently, integration of the angular velocities gives the angle in time. Together with information about the initial

and final orientation of the unit from the accelerometer, the orientation of the cube in time during movement is obtained. Consequently, Equation 5.3 can be completed, in which a general three-dimensional acceleration component ( $a$ ) taking into account rotations is derived ( $a_z$  is replaced by  $a$  in Equation 5.3). This component can be decomposed into accelerations as a consequence of rotations for the accelerometer x-y-z-axis, since the orientation of movement is known. Subsequently, the accelerations due to rotation can be subtracted from the acceleration signals corresponding to the accelerometer x-y-z-direction. The remaining accelerations are the accelerations due to translation. Integration of these (combined over x-y-z-direction) accelerations gives the velocities before collisions due to translation. Rewriting the angular velocity (from rotations) into the velocity in  $[m/s]$  allows summation of the velocities due to translation and rotation.

### 8.1.3. ANALYSIS

*Statistical analysis:* In Section 6.4.1 the data was fitted by visual observations. To provide more certainty in the type of distribution, a statistical analysis should be conducted.

*Relationships for "Rocking":* The research by CUR C70 yielded Equations 2.12 and 2.15. These equations were used by "Rocking" to calculate impact velocities. Similar relations could also be derived from current data, in which the various dependencies are included as a parameter.

## 8.2. APPLICABILITY ACCELEROMETER ADXL335

For future laboratory tests it is important to know the performance and applicability of the applied accelerometer ADXL 335. The accelerometer is well suited in serving the purpose of measuring movements, instead of collisions. In none of the tests it was observed that the device could not capture the movements (order  $> 0.1s$ ) or that the accelerations (order  $+ - 1g$ ) became larger than the measurement range. This implies that the sampling rate (0.002s) and measurement range (order  $+ - 3g$ ) are sufficient. In addition, the movements of the cube were unaffected by the device and the wiring. Hence, for similar tests in future research, this device is highly recommended.

To simplify data processing, an additional gyroscope is recommended, see Section 8.1.2. In addition, it is imaginable that in future research multiple degrees of freedom of movement are tested, for instance in model breakwaters. For these type of tests, application of the gyroscope is necessary, see Section 8.1.2. A wireless application is also recommended, since the chance becomes larger that the wiring forms resistance, in case multiple degrees of freedom of movement are tested.

## 8.3. ACTION PLAN ROCKING

As shown in Section 1.4, the main objective of the current research is described as follows:

Obtaining knowledge on, and measurements of the rocking behaviour and failure mode of single layer armour units

To reach this objective a number of steps were defined:

1. Analysing previously conducted research and application "Rocking".
2. Obtaining knowledge on the impacts and amount of collisions.
3. Obtaining knowledge on the number of colliding units in relation to the hydraulic conditions.
4. Obtaining knowledge on the type of movements and collisions.
5. Obtaining knowledge on the force-time relationships for specific armour unit concrete characteristics.
6. Obtaining knowledge on the stresses for specific armour unit characteristics.
7. Obtaining knowledge on the strength of the armour unit.
8. An update of numerical application "Rocking".

This Master's thesis focused on the first two steps. Based on the obtained knowledge, opportunities are discussed for the current and subsequent steps.

#### OBTAINING KNOWLEDGE ON THE IMPACTS AND AMOUNT OF COLLISIONS

With the results of the current Master's thesis, information is provided for the impact velocities and number of impacts for one unit. However, these results are valid for the simplified test set-up, and cannot be applied directly in "Rocking". Therefore, it is necessary to conduct similar research for representative model breakwaters. Additionally, different type of armour units could be investigated.

A model breakwater allows armour unit movements in multiple degrees of freedom. To capture the movements, the first step is to develop more advanced measurement equipment. A wireless device in which both accelerometer and gyroscope are imposed, is recommended (see Section 8.2).

#### OBTAINING KNOWLEDGE ON THE NUMBER OF COLLIDING UNITS IN RELATION TO THE HYDRAULIC CONDITIONS

To determine the number of rocked units, a large number of units could be equipped with accelerometers. The output signals from the accelerometers are a reliable source to detect rocking on the armour units. In this manner, the number of rocked units can be estimated during wave flume tests.

#### OBTAINING KNOWLEDGE ON THE TYPE OF MOVEMENTS AND COLLISIONS

For the determination of the moment of force in "Rocking", it is necessary to have knowledge of the type of movement. During the research by CUR C70, this was not investigated in detail. The application of a gyroscope makes it possible to conduct detailed research into the type of movements and collisions.

#### OBTAINING KNOWLEDGE ON THE FORCE-TIME RELATIONSHIPS FOR SPECIFIC ARMOUR UNIT CONCRETE CHARACTERISTICS

In the research by CUR C70, it was assumed that the armour units are applied with commonly used concrete characteristics. However, in case high density concrete armour units are applied in future projects, the characteristics change. Research into these concrete characteristics has to point out whether the load-time relationships shown in Section 2.1.4 are representative.

#### OBTAINING KNOWLEDGE ON THE STRESSES FOR SPECIFIC ARMOUR UNIT CHARACTERISTICS

The stresses in the units are dependent on the place of collision and mode of movement. "Rocking" uses the governing mode of movement. Subsequently, the stresses were calculated using a linear elastic approach. For more accuracy, it is possible to use more sophisticated models. Furthermore, the governing stresses have to be determined for each type of armour unit separately, since different modes of movement are governing.

#### OBTAINING KNOWLEDGE ON THE STRENGTH OF THE ARMOUR UNIT

Inconsistencies in the reports of CUR C70, caused differences in the relationships for the armour unit's strength. More research in concrete technology is necessary, to point out the cause for these differences. In addition, fatigue was not taken into account. Since for certain conditions, a large number of collisions was observed to occur, it is advised to incorporate fatigue into "Rocking". Additionally, during one impact multiple collisions were observed. However, the number of collisions per impact is dependent on the material characteristics. More research into concrete characteristics is necessary to determine the number of collisions, as it is of great importance for fatigue.

#### AN UPDATE OF NUMERICAL APPLICATION "ROCKING"

The probabilistic distribution for the number of movements (Section 2.1.2) was not taken into account in "Rocking". The total number of moved units is calculated deterministically, before the start of the Monte Carlo simulation, see Figure 2.3. For higher accuracy of results, it is advised to include the calculation in the Monte Carlo simulation.

In addition, it is recommended to perform a FORM analysis. With this, an understanding of the influence of the inserted parameters can be found, or in other words, the sensitivity of the parameters can be found. This allows the developer to see which parameters influence the outcome most and with that, the developer knows which parameters to fine tune to come to a reliable result. Furthermore, a more detailed analysis of the deterministic input parameters is recommended, to determine that they are actually non-variable.

#### **8.4. ADDITIONAL OPPORTUNITIES**

1. General research into the breakage of single layer armour units, taking into account multiple failure mechanisms.
2. Research into the overall breakwater stability in case of armour unit breakage.
3. Research into movements of prototype breakwater armour units. An application of measurement devices in existing prototype breakwaters.
4. Development of numerical models (CFD-modelling), using the measurements of current Master's thesis as reference data.
5. Research into wave run-up and run-down velocities on breakwater slopes.

# BIBLIOGRAPHY

- Adafruit (n.d.). Accelerometer ADXL335. Retrieved from <https://www.adafruit.com/products/163>.
- Analog Devices (2009). Datasheet ADXL335. Retrieved from <https://www.sparkfun.com/datasheets/Components/SMD/adxl335.pdf>.
- Battjes, J. A. (1969). Run-Up Distributions of Waves Breaking on Sloping Walls. Delft: Delft University of Technology.
- Bosman, G., Meer, J. W., Hoffmans, G., Schüttrumpf, H., & Verhagen, H. J. (2008, September). Individual overtopping events at dikes. In *International Conference on Coastal Engineering (ICCE), 2008, Hamburg*. World Scientific.
- Boyce, W. E., & Di Prima, R. C. (2010). *Elementary Differential Equations and Boundary Value Problems*. New York: Wiley and Sons.
- Burcharth, H. F. (1992). Design of rubble mound breakwaters. Structural Integrity. Aalborg: Aalborg University.
- Burcharth, H. F., & Zhou, L. (1995). Rubble mound breakwater failure modes. Aalborg: Aalborg University.
- Burcharth, H. F., Liu, Z., & Troch, P. (1999). Scaling of core material in rubble mound breakwater model tests. In *Fifth International Conference on Coastal and Port Engineering in Developing Countries*. COPEDEC.
- Chella, M. A., Torum, A., & Myrhaug, D. (2012). An overview of wave impact forces on offshore wind turbine substructures. *Energy Procedia*, 20, 217-226.
- CIRIA, CUR & CETMEF (2007). *The Rock Manual. The use of rock in hydraulic engineering* (Vol. 683). CIRIA.
- CLI (2011). Accropode II Design Guidelines Tours. CLI.
- Civiel Centrum Uitvoering Research en Regelgeving (1989). Golfbrekers. Sterkte Betonnen Afdekelementen. Integratie van Fasen 1-3. Verslag werkgroep 1. Civiel Centrum Uitvoering Research en Regelgeving.
- Civiel Centrum Uitvoering Research en Regelgeving (1990a). Golfbrekers. Sterkte Betonnen Afdekelementen. Samenvatting onderzoek. Verslag werkgroep 1. Civiel Centrum Uitvoering Research en Regelgeving.
- Civiel Centrum Uitvoering Research en Regelgeving (1990b). Golfbrekers. Sterkte Betonnen Afdekelementen. Toepassingen. Verslag werkgroep 1. Civiel Centrum Uitvoering Research en Regelgeving.
- Dai, Y. B., & Kamel, A. M. (1969). *Scale Effect Tests for Rubble-mound Breakwaters: Hydraulic Model Investigation*. US Army Engineer Waterways Experiment Station.
- Deltares (2014). Sal Rei Harbour Breakwater Testing. Retrieved from: <https://www.deltares.nl/en/projects/sal-rei-harbour-breakwater-testing/>
- Frostick, L. E., McLelland, S. J., & Mercer, T. G. (Eds.). (2011). *Users guide to physical modelling and experimentation: Experience of the HYDRALAB network*. CRC Press.
- Gent, M. R. A., & Luís, L. (2013). Application of Cubes in a single layer. In *Proc. 6th SCACR conference on applied coastal research, Lisbon*.
- Gent, M. R. A. (2002). Low-exceedance wave overtopping events, WL Delft project id. DC030202/H3803.
- Gijssman, R., de Haan, F. S., de Koning, R. J., Le, T. N., & Steeneken, S. P. (2015). Part 2 - Report Durban Dig-Out Port (Multidisciplinary Project Report). Delft: Delft University of Technology.
- Goseberg, N., Nistor, I., & Stolle, J. (2015). Tracking of "Smart" debris location based on RFID technique. In *Proceedings of Coastal Structures & Solutions to Coastal Disasters Joint Conference, Boston*.
- Handleiding Rocking (1990).

- Hibbeler, R. C. (2006). Hibbeler, R. C. (2006). *Mechanica voor technici. Dynamica* (3rd ed.). Pearson Education.
- Hofland, B. (2005). Rock and Roll (Ph.D. Thesis). Delft: Delft University of Technology.
- Horden, W. C. (1986). De faalkans van een golfbreker door rocking van de afdekelementen. Aanzet berekeningsprocedure, onzekerheden en onderzoekspunten. Delft: Delft University of Technology.
- Huis, J. C., Stuij, J., Walther, A. W., & Westen, J. M. (1987). *The closure of tidal basins*. Delft: Delft University Press.
- Journée, J. M. J., Massie, W. W. (2001). *Offshore Hydromechanics*. Delft: Delft University of Technology.
- Latham, J.P., Xiang, J., Anastasaki, E., Guo, L., Karantzoulis, N., Viré, A., & Pain, C. (2014). Numerical modelling of forces, stresses and breakages of concrete armour units. In *Proceedings for the International Conference on Coastal Engineering*, pp. 1–13.
- Meer, J. W. (1988). Stability of cubes, tetrapods and accropode. *Proc. Breakwaters*, 88.
- Mier, J. G. M., & Lenos, S. (1991). Experimental analysis of the load-time histories of concrete to concrete impact. *Coastal engineering*, 15(1-2), 87-106.
- Morison, J. R., Johnson, J. W., & Schaaf, S. A. (1950). The force exerted by surface waves on piles. *Journal of Petroleum Technology*, 2(05), 149-154.
- Nes, C. P. (1994). Stresses in tetrapod armour units exposed to wave action (MSc. Thesis). Delft: Delft University of Technology.
- Pullen, T., Allsop, N. W. H., Bruce, T., Kortenhuis, A., Schüttrumpf, H., & Meer, J. W. (2007). Wave Overtopping Of Sea Defence And Related Structures. Environment Agency, ENW, KFKI.
- Sadraey, M. H. (2012). *Aircraft Design: A Systems Engineering Approach*. John Wiley & Sons.
- Sarpkaya, S. T. (2010). *Wave Forces on Offshore Structures*. Cambridge University Press.
- Schüttrumpf, H., & Oumeraci, H. (2005). Layer thicknesses and velocities of wave overtopping flow at seadikes. *Coastal Engineering*, 52(6), 473-495.
- Scott, R. D., Turcke, D. J., & Baird, W. F. (1986). A unique instrumentation scheme for measuring loads in model dolos units. *Coastal Engineering Proceedings*, 1(20).
- Sokolewicz, M. J. (1986). Impulsbelastingen voor kubussen en tetrapodes als gevolg van rocking bij golfaanval (MSc Thesis). Delft: Delft University of Technology.
- TAW (2002). Technical report wave run-up and wave overtopping at dikes. Delft, Technical Advisory Committee.
- Tiny-Circuits (n.d.). Tiny Duino. Retrieved from <https://www.tiny-circuits.com/>.
- U.S. Army Corps of Engineers. (1984). *Shore Protection Manual*. Washington DC: USACE.
- Zwanenburg, S. A. A. (2012). The influence of the wave height distribution on the stability of single layer concrete armour units (MSc. Thesis). Delft: Delft University of Technology.

# A

## STRUCTURE SCHEME "ROCKING"

An detailed overview of the steps and computations of the program rocking is given as a structure diagram, in Dutch ("Handleiding Rocking" , 1990).

## Structuurdiagram "Rocking" voor tetrapods

1	Invoer algemene gegevens
2	Selecteer een combinatie $Pr\{H_s\}$ en $Y/D_n$
3	Bereken $H_s = \text{functie} ( Pr\{H_s\} )$
4	$N_{obots} = \text{functie} ( H_s, S_m, \Delta, D_n, N_{golven} )$ $N_{od} = \text{functie} ( H_s, S_m, \Delta, D_n, N_{golven} )$ Bereken rondom deze lijnen $\pm 5\%$ interval
5	Twee reductiefactoren voor de sterkte: $k_v = \text{functie} ( D_n )$ volume effect $k_t = \text{functie} ( D_n )$ temperatuurseffect
6	<i>Start Monte Carlo simulatie voor bepaling breukkans</i>
7	for $i=1$ to $N_{obotssimulaties}$ Trek random een botsnelheid uit: $Pr\{V\} = \text{Exp}[ - ( V^A - B ) / C ]$ Met: $A = 1.00$ $B = \text{functie1} ( Y/D_n, H_s / (\Delta D_n), \text{type element} )$ $C = \text{functie2} ( Y/D_n, \text{type element} )$ Bovendien bevat functie1 een normaal verdeelde stochast
8	Trek random uit normale verdeling: $f_{ck} = \text{functie} ( m, \sigma ) = \text{druksterkte beton}$ $K_{e1} = \text{functie} ( m, \sigma ) = \text{contactstijfheid beton}$ $f_0 = \text{functie} ( m, \sigma ) = \text{treksterkte beton}$ Bereken hieruit plastische bezwijkbelasting $K_p = \text{functie} ( M50, f_{ck} )$
9	Kies random een arm, behorende bij de berekening van de spanning Bepaling van impuls is afhankelijk van: <ul style="list-style-type: none"><li>- Percentage rotatie/ translatie</li><li>- Mate van inklemming</li><li>- Botsmechanisme</li></ul> Bepaling massa's $M_1 = \text{massa bewegende element (M50)}$ $M_2 = \text{massa getroffen element, kan ingeklemd zijn (M50 --> oneindig)}$ $\alpha = \text{meewerkende massa} = ( M_1 * M_2 ) / ( M_1 + M_2 )$
	<i>Soort beweging</i>

10	<p>Translatie</p> $\text{Impuls} = M50 * V$ $V_{\text{bots}} = V$ <p>Rotatie</p> $\text{Arm impuls} = \text{functie (arm spanning)}$ $\text{Impuls} = ( I_0 * \omega ) / \text{excentriciteit}$ $\omega = V / ( 0.65 D )$ $V_{\text{bots}} = \text{Impuls} / M1$
11	<p>Elastoplast model</p> <p>Bepaal:</p> <ul style="list-style-type: none"> <li>- <math>P_m</math> = Maximaal ontwikkelde kracht in element</li> <li>- <math>T_m</math> = Tijdsduur waarover de maximale kracht wordt opgebouwd</li> </ul> <p>Invoer:</p> <ul style="list-style-type: none"> <li>- <math>V_{\text{bots}}</math></li> <li>- Impuls</li> <li>- Meewerkende massa</li> </ul>
12	<p>Bereken uit <math>P_m</math> de maximaal optredende spanning in element</p> $S_{\text{max}} = \text{functie} ( P_m, D_n )$
13	<p>Bepaal snelheidsfactor trekspanning</p> $k_s = \text{functie}( S_{\text{max}}, T_m )$ <p>Bepaal toelaatbare treksterkte</p> $f_{\text{toel}} = k_v * k_s * k_t * f_0$ <ul style="list-style-type: none"> <li>- <math>k_v</math> = volume effect</li> <li>- <math>k_t</math> = temperatuurseffect</li> </ul>
14	<p>Test Monte Carlo simulatie</p> $S_{\text{max}} > f_{\text{toel}} \rightarrow \text{element bezwijkt}$ <p style="text-align: center;">Verhoog aantal bezweken elementen</p>
15	<p>Breukkans</p> $\Pr\{ \text{Breuk van 1 element} \} = \text{Aantal bezweken elementen} / N_{\text{botsSim}}$
16	<p>Totaal aantal gebroken elementen na 3 botsingen (voorwaardelijke kans):</p> <p>Na botsing 1: <math>N_{\text{broken}} = N_{\text{tot}} * \Pr\{\text{breuk van 1 element}\}</math></p> <p>Resterend: <math>N_{\text{tot}}' = N_{\text{tot}} - N_{\text{broken}}</math></p> <p>Na botsing 2: <math>N_{\text{broken}}' = N_{\text{tot}}' * \Pr\{\text{breuk van 1 element}\}</math></p> <p>Resterend: <math>N_{\text{tot}}'' = N_{\text{tot}}' - N_{\text{broken}}'</math></p> <p>Na botsing 3: <math>N_{\text{broken}}'' = N_{\text{tot}}'' * \Pr\{\text{breuk van 1 element}\}</math></p> <p>Totaal aantal gebroken elementen = <math>N_{\text{broken}} + N_{\text{broken}}' + N_{\text{broken}}''</math></p>

17

Integratie over talud  $[-2 H_s \dots +H_s]$

Stapgrootte  $2 \cdot D_n$ . Voor  $Y/D_n = -4, -2, 0$  en  $+2$  is  $N_{\text{tot}}$  bekend.

Uit de verdeling van  $N_{\text{tot}}$  over het talud volgt totaal  $N_{\text{broken}}$

Daarmee is het  $H_s$  het aantal gebroken elementen bepaald

# B

## MATLAB ROUTINE “ROCKING”

```
1 %% Numerical application "Rocking" - applied for Tetrapodes
2 clear all; close all; clc;
3
4 % Since the original "Rocking" program cannot be executed on current
5 % Windows systems, the original code is translated into a MATLAB script, as
6 % shown below. The conducted calculation applied for Tetrapodes only. The
7 % script is adjusted for the errors shown in Chapter 2.
8
9 %% Input
10
11 % Gravitational constant [m/s^2]
12 g = 9.81;
13
14 % Design wave height [m]
15 Hs = 6.5;
16
17 % Design wave period [s]
18 Tm = 18;
19
20 % Number of waves [-]
21 Nwaves = 6200;
22
23 % Density water [kg/m^3]
24 rhow = 1025;
25
26 % Density concrete [kg/m^3]
27 rhoc = 2400;
28
29 % Mass unit [kg]
30 M = 48000;
31
32 % Compressive strength [N/mm^2] (Normal distribution)
33 mufck = 30;
34 sigmafck = 6.75;
35
36 % Tensile strength [N/mm^2] (Normal distribution)
37 mufc0 = 3;
38 sigmafco = 0.9;
39
40 % Constant upward trend force - time relationship [N/mm^1.5] (Normal distribution)
41 mukel = 175000;
42 sigmakel = 0.001*1000;
43
44 % Percentage translation
45 Ptrans = 0.5;
46
47 % Nominal diameter [m]
48 Dn = (M / rhoc)^(1/3);
49
```

```

50 % Wave steepness [-]
51 sm = (2*pi*Hs)/(g* (Tm^2) );
52
53 % Density ratio [-]
54 Delta = (rhoc-rhow)/rhow;
55
56 % Height tetrapod [m]
57 Htetrapod = Dn/0.654;
58
59 % Waist tetrapod [m]
60 Wtetrapod = (pi/32)*(0.47* (Dn/0.654))^3;
61
62 % Leg tetrapod [m]
63 ctetrapod = 0.477*Htetrapod;
64
65 % Diameter end of leg of tetrapod [mm]
66 d=0.302*Htetrapod*1000;
67
68 % Constant a
69 mua = 1;
70 sigmaa = 0.164;
71
72 % Position on slope
73 y= -4*Dn;
74
75 % Volume and temperature effects
76 Kvoltemp = (0.94 * Dn ^(-0.12) + 0.74 * Dn ^(-0.20) - 1);
77
78 % Number of simulations
79 Nbots = 10000
80
81 %% Number of collisions
82 % The number of collisions is not taken into account in the Monte Carlo
83 % analysis in the Rocking program. For consistency, the
84 % same is done for the MATLAB sheet. However, it is recommended to include
85 % the calculation in the Monte Carlo simulation since parameter alphas is
86 % probabilistic. For now, alphas is taken as a deterministic parameter with
87 % mean of 1.
88
89 % Parameter alphas, normally distributed with mean of 1 and st.dev. of 0.082
90 alphas = 1;
91
92 % Number of displaced units
93 Nod = ( ((Hs/(alphas*Delta*Dn))*sm^(0.2) - 0.85) * (Nwaves^(0.25))/3.75)^(1/0.5)
94
95 % Number of moving units
96 Notot = ( ((Hs/(alphas*Delta*Dn)+0.5)*sm^(0.2) - 0.85) * (Nwaves^(0.25))/3.75)^(1/0.5)
97
98 %% Monte Carlo simulation
99 Nfail=0; % Number of initially failed units on specified position in breakwater
100
101 for i=1:Nbots
102
103     % Draw random impact velocity vbots
104     Pr1(i) = rand;
105     Pr2(i) = rand;
106     alpha(i) = normrnd(0.081,0.0016); % stochastic constant
107     B(i) = 0.0051*exp(-0.4 *abs(y/Dn))* Hs/(Delta*Dn);
108     C(i) = 0.0103* exp(-0.4 *abs(y/Dn));
109     V(i) = ( -B(i)*log(Pr1(i))+ C(i) * alpha(i))^(1/1.43) * sqrt(g*Dn); % velocity
110
111     % Draw random concrete particulars
112     fck(i) = normrnd(mufck,sigmafck); % Compressive strength
113     f0(i) = normrnd(mufc0,sigmafc0); % Tensile strength
114     Kel(i) = normrnd(muke1,sigmakel); % Contact stiffness
115     ke1(i) = Kel(i)*1.09*Dn;
116     ke2(i) = 0.7*ke1(i);
117     kp(i) = (d/420)^2 * 90^2 * (pi/4) * (fck(i)/45) *150;
118
119     % Draw random added mass
120     alphas(i) = randi([0.5*M,M]);

```

```

121
122 % Draw random a lever for the computation of the tension
123 Pr3(i) = rand;
124 if Pr3(i) > 0.5 % 50 percent of collisions take place at maximum of lever
125     arms(i) = ctetrapod; % arm sigma
126     IO(i) = 0.551 * M * (Dn/0.654)^2; % mass of inertia
127 else
128     arms(i) = 2*Pr3(i)*ctetrapod;
129     IO(i) = 0.354 * M * (Dn/0.654)^2;
130 end
131 armr(i) = 0.85* arms(i) + 0.47* Htetrapod; % arm r
132
133 % Determine momentum of hit for a percentage translation or rotation
134 Pr4(i) = rand;
135 if Pr4(i) < Ptrans % Impuls and vbots for translation
136     vbots(i) = V(i);
137     Impuls(i) = M * vbots(i);
138 else
139     Impuls(i) = ( IO(i)/armr(i) ) * ( V(i)/Dn ); % Momentum and vbots for rotation
140     vbots(i) = Impuls(i) / M;
141 end
142
143 % Determine falling leg of P-T diagram
144 P2max(i) = ( 1.25* alphamass(i) * vbots(i)^2 * ke2(i)^(1/1.5) )^0.6;
145 t2max(i) = 1.47* ( 1.25* ( alphamass(i)/( vbots(i)^0.5 * ke2(i) ) ) )^0.4;
146 tee2(i) = (t2max(i)/(pi/2)) * acos( ( P2max(i)*t2max(i) - 0.5 * M * vbots(i) * (pi/2) ) / ...
147     ( P2max(i) * t2max(i) ));
148 tb(i) = (t2max(i)/(pi/2)) * asin( kp(i) / P2max(i) );
149 if P2max(i) < kp(i) % Calculation plastic or elastic deformation,
150     te2(i) = tee2(i); % Elastic
151     Pe2(i) = P2max(i) * sin( (te2(i)*(pi/2)) / t2max(i));
152     A2(i) = 0.5 * Impuls(i); % Surface area, differently defined in "Rocking" (0.5MV)
153 else
154     te2(i) = tb(i); % Plastic
155     Pe2(i) = kp(i);
156     A2(i) = ( (P2max(i)* t2max(i)) / (pi/2) )*(1-cos( (te2(i)/t2max(i)) * (pi/2)));
157 end
158
159 % Determine rising leg of P-T diagram
160 Plmax(i) = ( 1.25* alphamass(i) * vbots(i)^2 * ke1(i)^(1/1.5) )^0.6;
161 tlmax(i) = 1.47* ( 1.25* ( alphamass(i)/( vbots(i)^0.5 * ke1(i) ) ) )^0.4;
162 tel(i) = (tlmax(i)/(pi/2)) * asin( Pe2(i) / Plmax(i) );
163 Al(i) = ( (Plmax(i)* tlmax(i)) / (pi/2) )*(1-cos( (tel(i)/tlmax(i)) * (pi/2)));
164
165 % Determine maximum force and time in model
166 F(i) = Pe2(i); % Max force
167 if P2max(i) < kp(i) % Development of max force in time for elastic
168     tm(i)=tel(i);
169 else
170     tp(i) = ( Impuls(i) - (A1(i)+A2(i)))/ Pe2(i); % Development of max force in time for ...
171     plastic
172     tm(i) = tel(i) + tp(i);
173 end
174
175 % Determine stresses in tetrapod (different approach than in literature)
176 % Mmax(i) = F(i)*arms(i); % WITH THEORY
177 % sigma(i) = Mmax(i)/( (pi/32) * (0.47 * (Dn/0.654)^3)); % WITH THEORY
178 sigma(i) = armsigma(i) * 22.3 * F(i)/ (Dn^2); % WITH ROCKING
179
180 % Determine factor for speed of collision
181 sigmav(i) = sigma(i) / tm(i);
182 Kv(i) = ( sigmav(i) / 0.1 )^0.042;
183
184 % Determine strength
185 fc(i) = Kvoltemp * Kv(i) * f0(i);
186
187 % Determine failure
188 if sigma(i)/1000 > fc(i)
189     Nfail=Nfail+1;
190 end

```

```
190 end
191
192 %% Probability of failure and number of broken units for a local position Y/Dn
193
194 Nfailtot = Nfail; % Total number of failures in Monte Carlo
195 Probfail = Nfailtot/Nbots % Probability of failure
196
197 % Number of remaining elements after 3 times collision
198 Notot1 = Notot - Probfail * Notot;
199 Notot2 = Notot1 - Probfail * Notot1;
200 Notot3 = Notot2 - Probfail * Notot2;
201
202 % Number of broken elements
203 Nbroken = Notot - Notot3
204
205
206 %% Output
207
208
209 % Nbots =
210 %
211 %      10000
212 %
213 %
214 % Nod =
215 %
216 %      0.0592
217 %
218 %
219 % Notot =
220 %
221 %      0.0635
222 %
223 %
224 % Probfail =
225 %
226 %      4.0000e-04
227 %
228 %
229 % Nbroken =
230 %
231 %      7.6156e-05
```

# C

## IMPLEMENTATION TEST SET-UP IN WAVE FLUME

In this chapter, some pictures regarding the test set-up in the wave flume are shown.

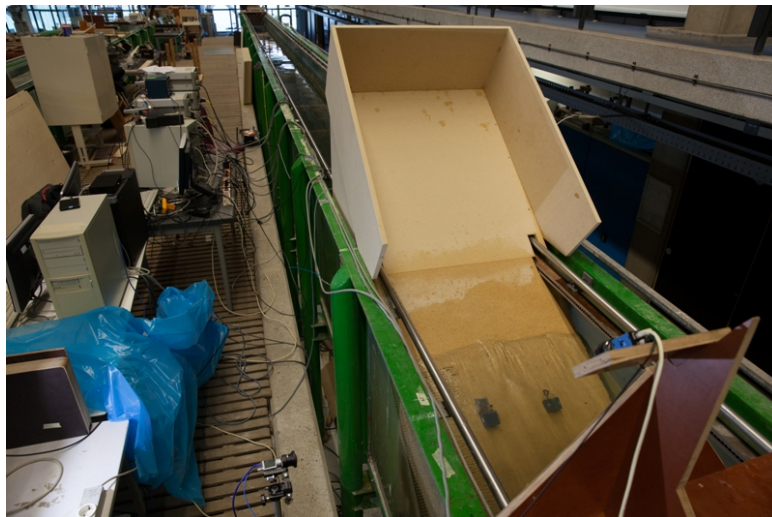


Figure C.1: Test set-up with series for exposed cubes. The slope provides undisturbed wave run-up



Figure C.2: Detailed set-up of cubes



Figure C.3: Wave run-up for exposed cubes. No movement

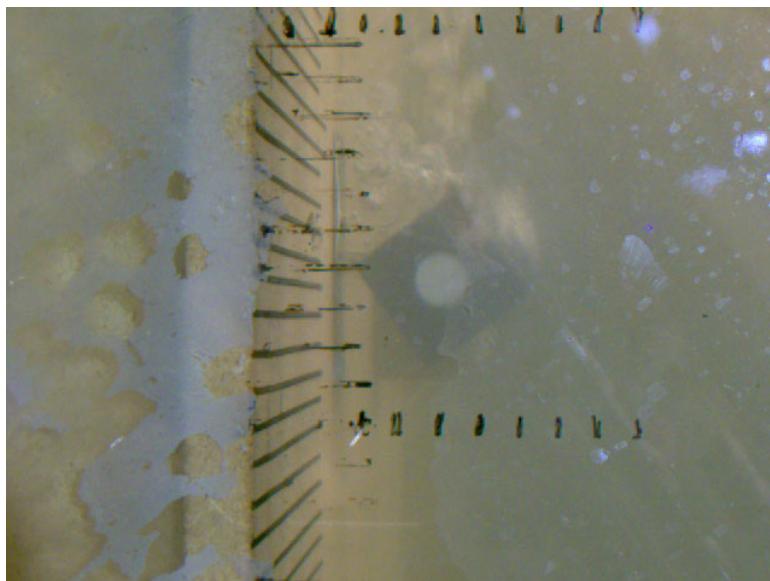


Figure C.4: Upward movement for exposed cube with accelerometer



Figure C.5: Wave run-up for the embedded cubes



Figure C.6: Transition between the embedded cube and slope. Transition angle = 1:6

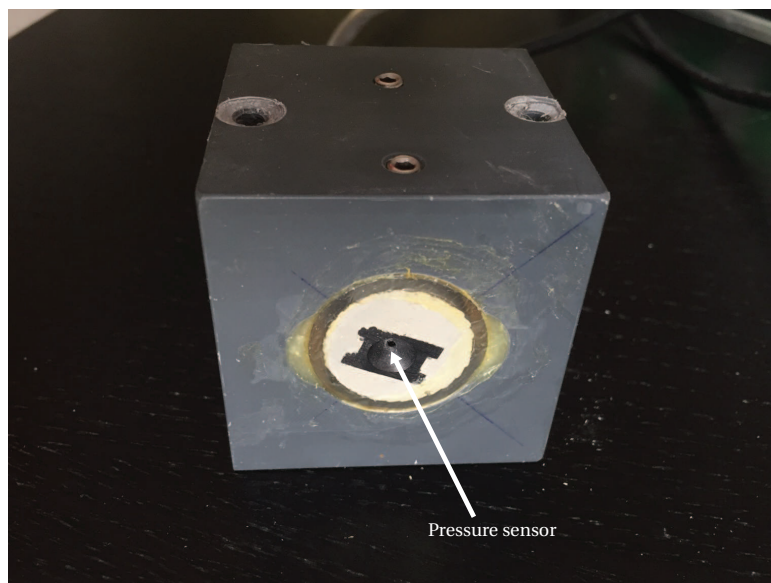


Figure C.7: Placement of pressure sensor in the center of the front face of the cube.

# D

## MARKET STUDY ACCELEROMETERS

An overview is given of a market study that is conducted to find a suitable accelerometer.

### D.1. REQUIREMENTS

Based on Sokolewicz (1986), requirements for the accelerometer are drafted. This section gives a motivation for the requirements.

In the past, similar measurements were conducted for Tetrapodes (Sokolewicz, 1986). The used accelerometer was Bruel and Kjaer, type 4344 with the ability to sample up to 120 *kHz*.

#### D.1.1. FREQUENCY

According to the research of Sokolewicz (1986) the duration of a collision peak was about 0.4 *ms*, which is approximately 2500 *Hz*. To capture the peak precisely, the sampling frequency of the accelerometer should be ideally ten times larger. Therefore a sampling frequency of 25 *kHz* is desired.

#### D.1.2. ACCELERATIONS

The maximum observed accelerations were 65 *g* with a wave height of 18 *cm* (Sokolewicz, 1986). More or less similar conditions are expected to happen in this research. Therefore the measurement equipment should be able to measure accelerations up to 65 *g*. However, since these high peaks do not occur frequently, they do not contribute to the statistical value. Furthermore, a difference in material properties may cause lower peak accelerations. Therefore, equipment that can measure lower accelerations should not be excluded. They should be tested “in the dry” with the same movements as with rocking.

#### D.1.3. DIMENSIONS

It is chosen to work with a cube with a height of 5 *cm*. The maximum dimensions for the measurement device are approximately 2x2x4 *cm* (bxhxl). Any larger accelerometer might cause trouble in the mass and mass distribution of the armour unit.

#### D.1.4. MEASUREMENT DIRECTIONS

To capture armour unit movement as precisely as possible, the accelerometer should measure in 3 directions. This implies measurements in x-y-z-direction.

## D.2. SUITABLE DEVICES BASED ON REQUIREMENTS

Based on the requirements, an overview of accelerometers that approach the requirements is shown in Table D.1. These accelerometers are however of the piezo-electric type and require specific wires and amplifiers. Consequently the total costs of all equipment for all accelerometer types is beyond budget of this research.

Table D.1: Overview accelerometers that approach the requirements

<b>Name</b>	Bruel and Kjaer 4520	Bruel and Kjaer 4529-B	Acoutronics 3023A1	PCB 356B21	PCB 356A16
<b>Type</b>	Piezo-electric	Piezo-electric	Piezo-electric	Piezo-electric	Piezo-electric
<b>Measurements</b>	x-y-z	x-y-z	x-y-z	x-y-z	x-y-z
<b>Dimensions</b>	17.4 x 9.14 x 9.02 mm	25 x 17 x 17 mm	17.7 x 9.1 x 12.3 mm	10.2 x 10.2 x 10.2 mm	20.3 x 14 x 14 mm
<b>Weight</b>	3 gram	14.5 gram	4 gram	4 gram	7.4 gram
<b>Frequency</b>	7 kHz	6 kHz	10 kHz	7 kHz	5 kHz
<b>Accelerations</b>	500 g	71 g	500 g	500 g	50 g
<b>Output</b>	4 pin connector	4 pin connector	4 pin connector	mini 4 pin connector	4 pin connector
<b>Notes</b>	-	Mounting clip			

## D.3. NEW APPROACH

No accelerometer can approach the requirements without exceeding the budget. Therefore a new measurement methodology is developed. It is decided to measure the accelerations corresponding to movement of the cube. The integration of the accelerations corresponding to movement over time gives the impact velocity. For this purpose mass produced, piezo-resistive accelerometers are suitable, which are within budget.

## D.4. WIRELESS APPLICATION

Present-day technologies make wireless accelerometer applications possible. Since wires might be of influence for the unit's movements, a wireless application would be preferred. A suitable device is developed by Tiny Circuits and goes under the name Tiny Duino (Tiny-Circuits, n.d.).

The device is essentially a small computer and runs with programming software from Arduino. The following components are needed for application (Tiny-Circuits, n.d.):

1. Processor board
2. Battery
3. USB-connection
4. MicroSD
5. MicroSD holder
6. Bosch Accelerometer

All components together have dimensions of approximately 2x2x2 cm. However, this application goes together with many uncertainties. For instance, it is doubtful whether the wireless connection works under water. Next to that, it is not known how long the battery life is. Consequently, complications such as replacing batteries in a unit, with the requirement to be watertight, play an important role. In addition, assembling and programming has to be done by the user, which probably takes a considerable amount of time. Therefore it is expected that the time to develop such an application goes beyond the planning in the current research.

It is therefore chosen to apply a wired accelerometer. The choice for the type of wired accelerometer was dependent on the delivery time. Since Deltares already had the ADXL335 in stock, it was chosen to make use of that type.

# E

## VALIDATION ACCELEROMETER

To determine the applicability of the accelerometer for measuring movement, three validation tests are conducted: slow rotation, fast rotation and falling tests.

### E.1. SLOW ROTATION

The first test determines whether gravitation during the change of orientation is properly represented. The correct display of gravitation is of essential importance for the data analysis, since the latter is dominant, see Chapter 5.

The accelerometer is slowly rotated from one orientation to another. Accelerations due to movement are considered to be negligible because of the slow and constant movement. The test is repeated several times with rotations over several orientations. The tests are conducted at a sampling rate of 50 Hz, in which the resistances are not removed from the accelerometer. An example of the results is shown in Figure E.1.

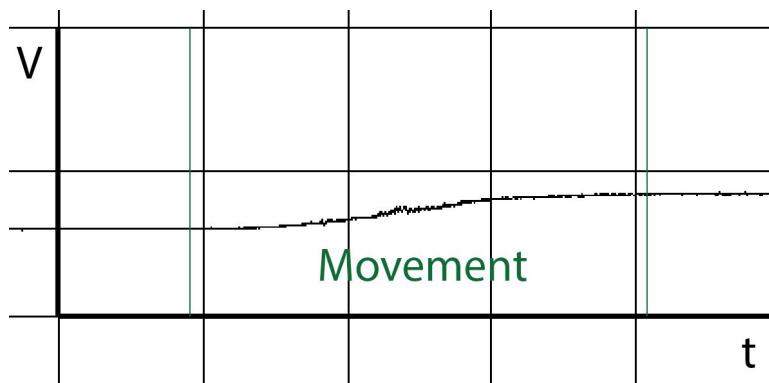


Figure E.1: Result validation test slow rotation

Observed is a difference in Voltage output before and after the movement, corresponding to an orientation difference before and after the movement. Furthermore, the relatively constant movement corresponds correctly with the more or less linear change in gravitation during movement. The transition between movement and no movement is smooth, which corresponds to a negligible effect of the acceleration due to movement. It is concluded that the change in orientation results in a correct change in output Voltage. Furthermore, the accelerometer noise is damped due to the presence of the resistances and the resulting low sampling frequency. This effect is seen with the relatively smooth graph in Figure E.1.

### E.2. FAST ROTATION

The second test determines whether the accelerations are correctly displayed qualitatively for the type of movement that will be observed in the wave flume. This type of movement includes both accelerations as a result of gravity and

accelerations due to fast movement.

The test includes a simple set-up of a scaled armour unit on a slope, which rotates over a fixed point. The accelerometer is attached in the center of the armour unit. The armour unit is released from an unstable point and rotates under to the influence of gravity downwards. Subsequently it collides with the slope. The test is conducted at a sampling rate of 50 Hz and is repeated several times (the resistances are not removed from the accelerometer).

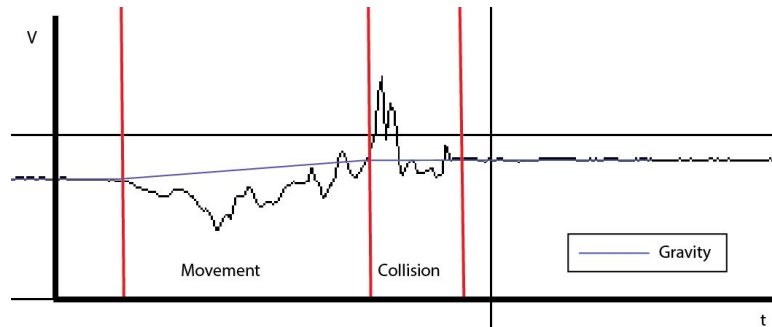


Figure E.2: Result validation test fast rotation

Figure E.2 shows the measured accelerations from a test. It is observed that the Voltage output before and after the rotation differs, corresponding with a difference in orientation of the armour unit. The part in which the unit rotates is divided in two parts: movement and collision. Movement is observed with a negative acceleration peak relative to the measured acceleration in static situation. This corresponds to an object in free fall, where  $9.81 \text{ m/s}^2$  is measured in static situation and  $0 \text{ m/s}^2$  during the free fall. The unit is subsequently stopped by collision, resulting in an acceleration peak in positive direction relative to the static situation. The unit bounces multiple times on the slope resulting in multiple collision peaks. Figure E.2 includes the trend of accelerations generated by the effect of gravity. Furthermore, it is seen that small acceleration peaks disturb the trend of movement. Since all noise from the measurement equipment is damped with the sampling frequency of 50 Hz, it is not likely that the measurement equipment is causes these vibrations. Possibly the simple test set-up and the influence of the wiring are the main cause of the problem. In addition, the acceleration peaks of the collision are expected to be much higher in reality (Sokolewicz, 1986). The low sampling frequency is the main cause for not capturing the collision peaks in a proper manner. It can be concluded that in general the accelerometer captures fast movement in a qualitatively understandable manner. However, additional tests with a different set-up need to be conducted to determine the cause of noise in the acceleration profile and the real shape of collision.

### E.3. FALLING TESTS

The last test determines whether the accelerations of movement are correctly displayed quantitatively and provides answers to the source of noise during movement and the acceleration shape of collision.

The accelerometer is attached to a cone. The cone is dropped from a height of 2 cm, 5 cm, and 10 cm. The test set-up is constructed in such a way that the orientation of the accelerometer is fixed. Furthermore, the wiring and materials are combined in a more careful manner than the test with fast rotation, eliminating vibrations during movement as much as possible. The resistances are removed from the accelerometer, allowing a high sampling frequency of at least 550 Hz. Figure E.3 shows the test set-up and Figures E.4 and E.5 show examples of the resulting graphs from the falling tests.

It is observed that the rotating test show a similar acceleration pattern as the falling test. The measured acceleration drops from a value of  $9.81 \text{ m/s}^2$  to a value slightly above  $0 \text{ m/s}^2$  during the free fall. This is in line with the theory of an idealized object in free fall, where a change in acceleration of  $9.81 \text{ m/s}^2$  is expected. The influence of the air resistance during the experiments explains the lower acceleration value during free fall. Furthermore it is clearly seen that the time period of movement is longer for a larger falling height. The collision is characterized by steep peaks in opposite direction of the acceleration during movement (Starting at  $t = 5.4$  for Figure E.4 and  $t = 6.57$  for Figure E.5). The peaks of collision are not captured since they exceed the measurement range of the accelerometer. With a higher sampling frequency, also more noise is seen. For analysis purposes this noise is filtered out, see the graphs on the right side in Figures E.4 and E.5. Furthermore it is observed that the magnitude of irregularities, is much smaller

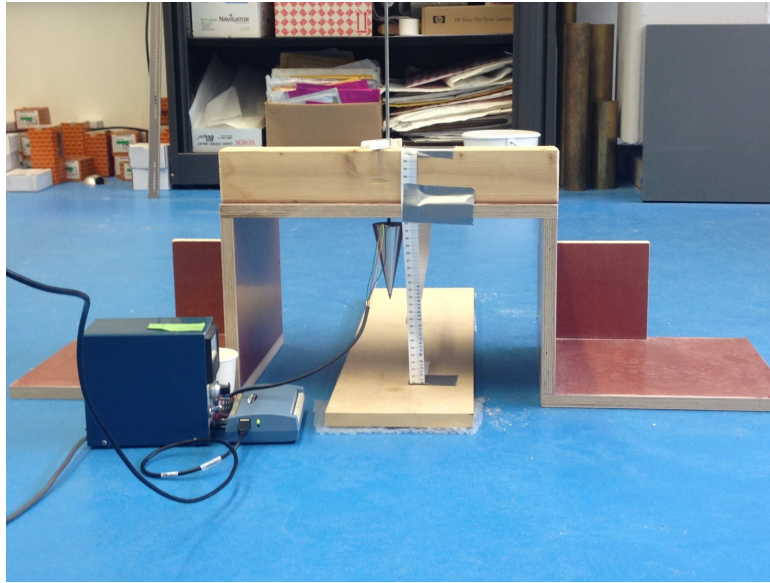


Figure E.3: Set-up falling tests with cone

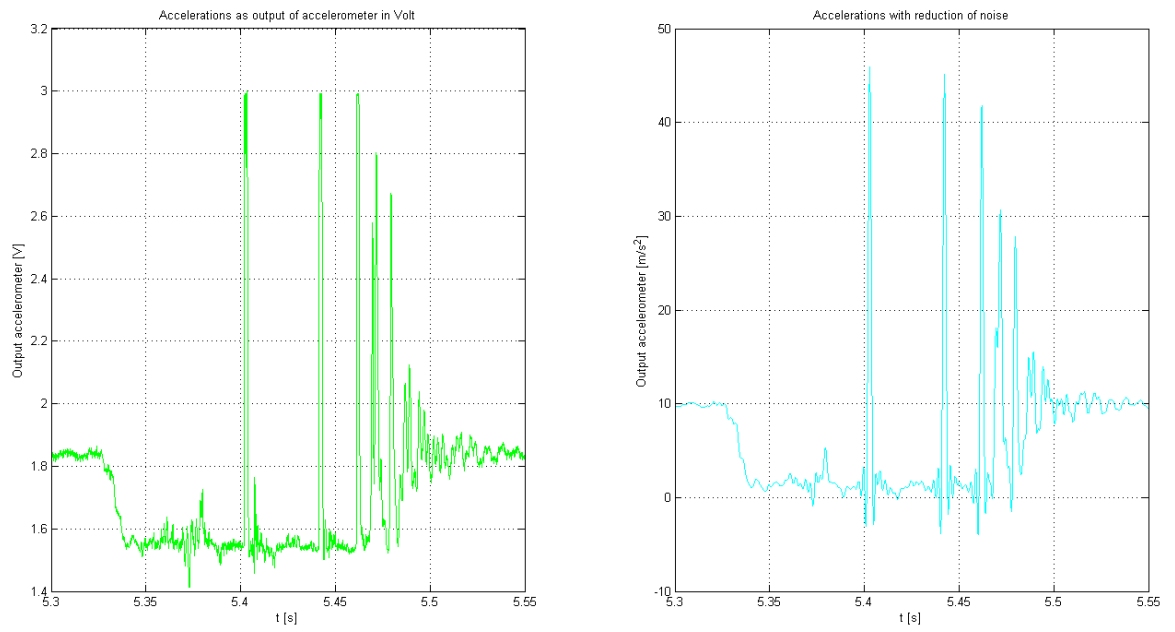


Figure E.4: Measurement of accelerations for test with falling height of 2 cm

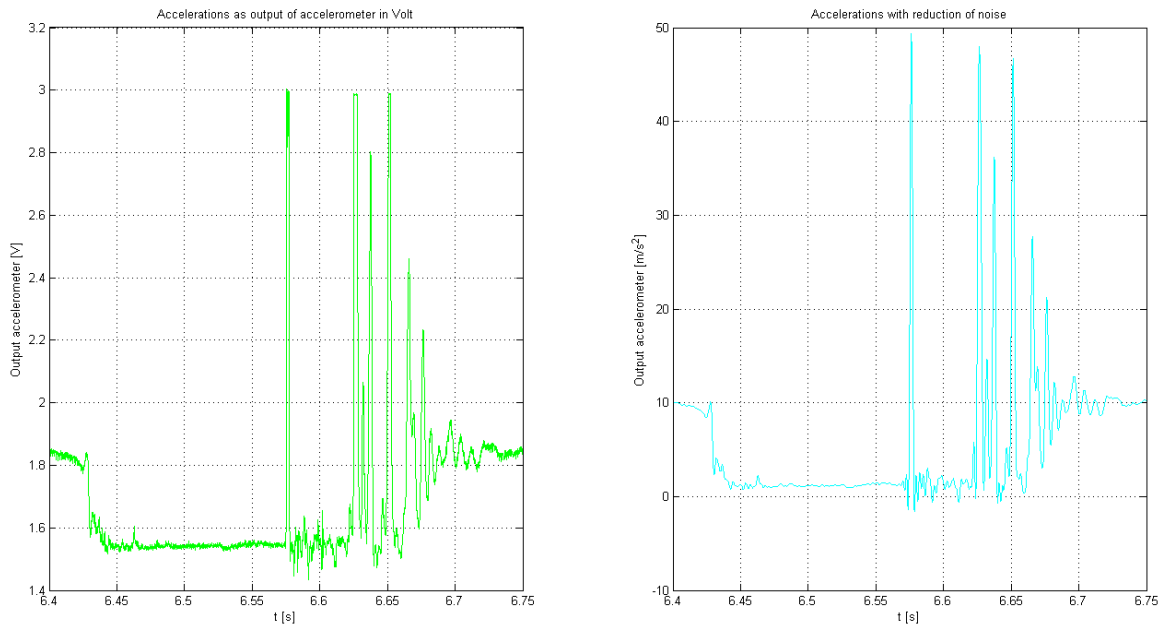


Figure E.5: Measurement of accelerations for test with falling height of 10 cm

in comparison with Figure E.2. Hence, it is concluded that the irregularities observed in during the falling tests are the result of material usage and tests set-up and are not caused by incorrect measurements.

To assess whether the measured accelerations are qualitatively correct, the tests were captured with a camera from Imaging Source. For comparison, the measured accelerations during movement from the accelerometer are integrated over time. Velocities from the camera are obtained by measuring the differences between recorded frames. The velocity before collision is calculated with information from the distance in meters per pixel and the frame rate per second. The resulting velocities before collision from both accelerometer and camera for a number of falling heights are plotted in Figure E.6. It is seen that the fitted curves of the camera and accelerometer correspond neatly to one another. In relation to the theoretical curve where air resistance is neglected, an increasing falling height makes velocities relatively smaller. This can be explained by the influence of air resistance, which plays a more dominant role over larger falling distances. Differences in results between individual tests can be explained by small differences in test set-up, the influence of horizontal vibrations during movement and the incorrect display of frame shots from the camera. Nevertheless, these differences are relatively small and therefore it is concluded that the accelerometer provides reliable answers to capture movement of an armour unit.

## E.4. CONCLUSION

The results of the tests show that the accelerometer accurately measures movement and gravity. It is likely that similar conditions of movement and gravity occur in the wave flume as during the tests. Therefore, it is concluded that the accelerometer is suitable for measuring movements in the wave flume. In addition, it is observed that the movements are fully captured in all tests. Consequently, it is concluded that the measurement range and frequency of the accelerometer are sufficient for the measurement of movement.

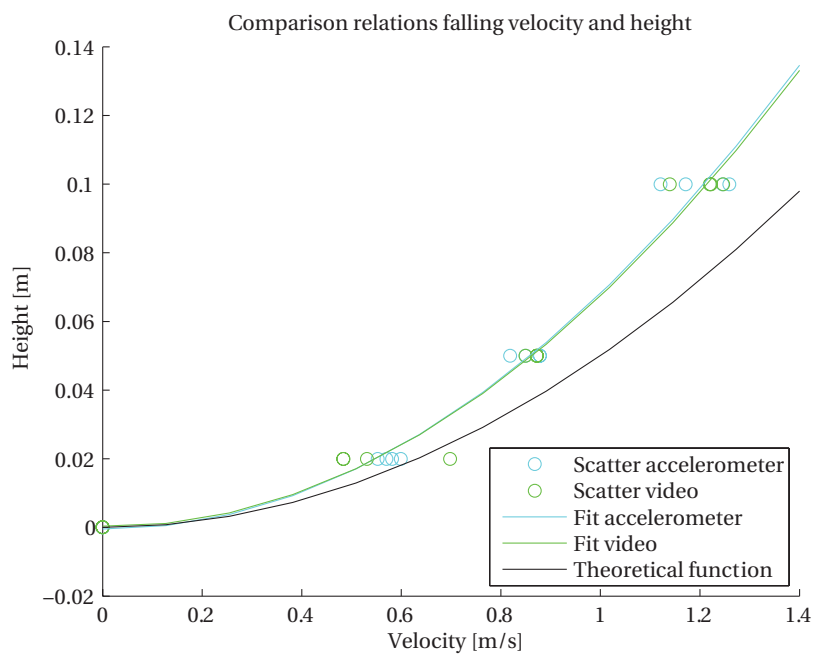


Figure E.6: Graph comparing the falling velocities from the accelerometer, camera and from theory

# F

## APPROACH DIFFERENTIAL EQUATION USING NUMERICAL METHODS

In Section 5.2 the differential equations 5.3 and 5.4 are derived. These differential equations appear to be of second-order, non-linear and non-homogeneous. Therefore the equations have to be approached numerically. The solutions are approached using MATLAB ODE solvers. In order to determine whether the numerical methodology is sufficiently accurate and stable, multiple tests are conducted.

### F.1. SYSTEM OF EQUATIONS

MATLAB only calculates first order differential equations. Therefore, the Equations 5.3 and 5.4 are rewritten in terms of a system of equations. The following equations apply for the upward movement of the cube (shown in Figure 5.2):

$$z(1) = \theta \quad (\text{F1})$$

$$z(2) = \frac{dz(1)}{dt} = \frac{d\theta}{dt} \quad (\text{F2})$$

$$\frac{dz(1)}{dt} = z(2) \quad (\text{F3})$$

$$\frac{dz(2)}{dt} = z(2)^2 - \frac{2g}{D_n} \cos(\phi_g + z(1)) + \frac{2a_z(t)}{D_n} \quad (\text{F4})$$

For downward movement the tangential and normal component are oriented in opposite direction. Furthermore, the angle of rotation is considered to be positive in opposite direction. This implies a positive movement downslope. Consequently Equation F4 is rewritten, see Equation F5.

$$\frac{dz(2)}{dt} = z(2)^2 + \frac{2g}{D_n} \cos(\phi_g + 0.5\pi - z(1)) - \frac{2a_z(t)}{D_n} \quad (\text{F5})$$

### F.2. STATIC CUBE

First, the general MATLAB routine ODE45 is tested. A situation is tested in which the cube does not move, implying that the z-axis acceleration ( $a_z$ ) has a constant output coming from the axis of gravity. This measurement of acceleration is for all time steps equal to  $-g \sin(-\alpha)$ . Consequently, the output has to be close to a turning angle ( $\theta$ ) of 0 radians and a angular velocity ( $\omega$ ) of 0 *rad/s*.

The initial conditions are defined as  $z(1) = 0$  and  $z(2) = 0$ , corresponding to an angle of 0 radians and a angular velocity of 0 *rad/s*. The resulting outcome of the computation is shown in Figure F1. The analytical solutions are supposed to lay on the horizontal axis. However, it is observed that this is not the case. The numerical computation gives an error.

The graph shows that the error grows in time. It is therefore concluded that the numerical method is unstable and therefore not convergent.

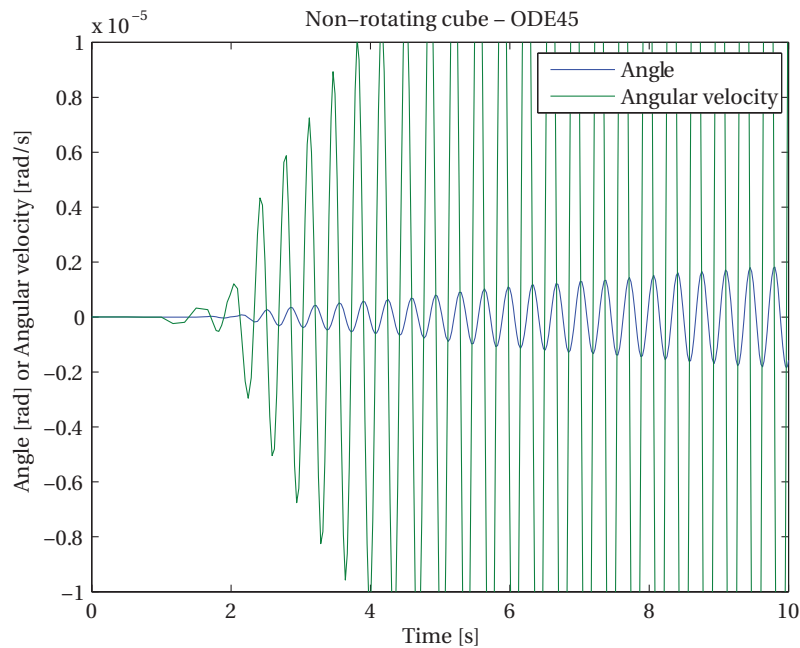


Figure E1: Results computation of non-moving cube with MATLAB routine ODE45

A different method named ODE15s is tested. Again, the same conditions as in the ODE45 case are applied. The results are shown in Figure E.2. It is observed that the error is very small (order  $10^{-16}$ ). Furthermore, the error does not seem to grow in time and is therefore considered to be stable. It is consequently concluded that this method is convergent. The ODE15s method is therefore preferred.

The measured acceleration signal contains irregularities due to electronic noise and turbulence. Therefore, it is important to know what happens to the signal containing irregularities. The same conditions are used as in the previously discussed cases. The only difference is a white noise signal, representing the irregularities in the measurements. The computation is conducted with MATLAB solver ODE15s. The white noise signal is imposed as a variation in the constant acceleration signal of parameter  $a_z$ . From this it is observed that solution is severely affected by the irregularities. The noise becomes much larger for the solution for the velocities. In some cases the solution even becomes unstable. Consequently it is concluded that the irregularities in the signal result in either large errors or instability of the solution. Therefore it is important to filter noise and vibrations out of the signal before approaching the differential equations.

### F.3. ROTATING CUBE

With MATLAB routine ODE15s the angle and velocity of a rotating cube are approached numerically. The rotation is characterised by a linearly increasing tangential acceleration. This characterisation is chosen because it approaches the behaviour of the cube in the wave flume, in both upward and downward movement, see Section 5.2. The cube rotates  $0.5\pi$  radians during a period of 0.30 s for upward movement and 0.16 s for downward movement. These conditions are chosen, since they are equal to the periods of rotation for regular wave conditions with wave height equal to 0.21 m and steepness equal to 0.02. In addition, initial conditions in which  $z(1) = 0$  and  $z(2) = 0$  are used. The result of the calculations appear to be either highly inaccurate or the following message is displayed:

"Warning: Failure at t=2.646072e+02. Unable to meet integration tolerances without reducing the step size below the smallest value allowed (9.094947e-13) at time t."

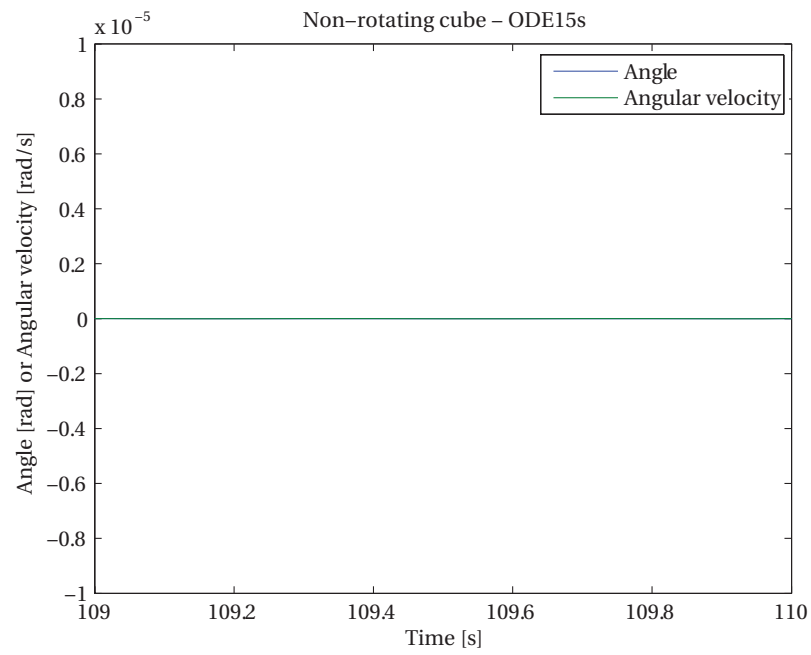


Figure E2: Results computation of non-moving cube with MATLAB routine ODE15s

This message implies that the solution goes to infinity at a certain time step. The numerical approach is unstable and therefore not convergent. It is therefore necessary to simplify the differential equation in order to obtain accurate and stable results.



## MATLAB ROUTINE FOR DATA PROCESSING

The MATLAB routine shown in this section is used to process the accelerometer signal. The routine is written in such a way that it automatically determines the periods of upward and downward movement. Consequently it determines the angle of rotation over time and the angular velocities. Lastly, the angular velocities before collision and time periods of movements are saved into separate text files. The routine is applied for both regular and irregular waves. After processing of all data files, the results from the text files are loaded into another MATLAB routine which is written to produce statistical plots. That routine is not included since it solely contains standard codes for loading and plotting.

The total computation takes about 5 to 10 minutes, depending on the number of movements. To complete the computation successfully, a minimum of 6 GB free random access memory is needed, since the data files are for irregular waves are large.

To provide guidance through the code, a motivation of various sections is given. First, the file containing data from measurements is loaded (line 8 - 16). Since it is a large file (Dasylab saved samples of 16000 *Hz*) only the column containing the time (first column), the accelerometer *z*-axis (third last column) and the pressure signal (last column) are loaded. The pressure signal is needed to determine whether a wave hits the cube, which is an indication of a possible start of movement.

Lines 20 - 27 describe the selection of the time periods in which the waves are generated. This reduces the computational time and possible errors in the signals due to calibration and set-up of the measurement equipment. The start time and end time has to be determined separately for each test. In addition a time period is determined in which no movement occurs and in which the signal is constant. This time period is used for calibration and determination of the initial orientation of the accelerometer.

In lines 32 - 48 the data is calibrated and filtered from noise and vibrations. The degree of filtering depends on two questions: does the filtered graph follow the actual graph accurately and are the irregularities sufficiently filtered? These questions are contradictory and therefore, the shown values are found to be optimal.

Lines 53 - 158 divide the data in periods of movement. First the maxima in pressure signal are used to divide the data into periods, in which sufficient wave action against the block occurs. For each period it is determined whether movement of the block occurs. In case (sufficient) movement occurs, the time periods for upward and downward movement are determined. If during a period upward movement occurs, but no downward movement, the routine rejects the movement and takes no movement into account for the considered period. This type of coding makes sure that errors in the estimation of movement, due to for instance vibrations and impacts, are not taken into account.

Lines 161 - 268 calculate the angles and angular velocities based on the synthetic model determined in Section 5.2.2 for each period of data that contains movement. This calculation is conducted for both upward movement and downward movement. In addition, an extra filter is applied on the obtained angles in time. After all, the differentiation will blow up irregularities leading to significant errors. At the end of the loop, only the angular velocities that represent the angular velocities before collision, are saved. This approach saves random access memory and speeds up the computation.



```

59 azsss = azss(tstart:tend);
60
61 for ii=1:length(ppp)-1
62     if any( azss(ppp(ii):ppp(ii+1)) < -8 )
63         P(ii) = ppp(ii);
64     end
65 end
66
67 % Continue with calculation if periods are observed with inclusion of
68 % movement
69 if exist('P','var') == 1
70     P(P == 0) = [];
71
72 % Find positions in time for up and down movement
73 Min1 = zeros(1, length(P)-1);
74 Min2 = zeros(1, length(P)-1);
75 Max2 = zeros(1, length(P)-1);
76 Start = zeros(1, length(P)-1);
77 apeak = zeros(1, length(P)-1);
78 abpeak = zeros(1, length(P)-1);
79 apeakd = zeros(1, length(P)-1);
80 abpeakd = zeros(1, length(P)-1);
81 apeak2 = zeros(1, length(P)-1);
82 avzz = avz(tstart:tend);
83
84 for i=1:length(P);
85
86     % Find start position equal to up movement
87     ap = find(azss(P(i):P(i)+64000)<mean(azs(tquietstart:tquietend))+1 & ...
88             azss(P(i):P(i)+64000)>mean(azs(tquietstart:tquietend))-1);
89     Start1 = ap(diff(ap)>100);
90     if isempty(Start1)
91         Start(i) = 0;
92         P(i) = 0;
93     else
94         Start(i) = Start1(1);
95
96     % Find end position for up movement, equal to min azs
97     % Peaks
98     apeak1 = find(avzz(P(i)+Start(i):P(i)+64000)<-40); %-15
99     apeak2 = apeak1(apeak1 + Start(i) > 1600 & apeak1 + Start(i) < (P(i)+64000-P(i)));
100    if isempty(apeak2)
101        Start(i) = 0;
102        P(i) = 0;
103        abpeak(i) = 0;
104    else
105        abpeak(i) = apeak2(1);
106
107    % Find start position elaboration for down movement
108    Min = P(i)+Start(i)+abpeak(i):P(i)+64000;
109    Minnn = find(azsss(Min)<-8);
110    if isempty(Minnn)
111        Start(i) = 0;
112        P(i) = 0;
113        abpeak(i) = 0;
114        Minn = 0;
115    else
116        Minnm = find(azsss(P(i)+Start(i)+abpeak(i)+Minnn(1)+1200:P(i)+64000)>-8);
117        Minn = Minnm(1);
118        Min2(i) = Minn(end)+Minnn(1)+1200;
119
120    % Find end position for down movement
121    Max = P(i)+Start(i)+abpeak(i)+Min2(i):P(i)+64000;
122    apeakd1 = find(azsss(Max)>15);
123    if isempty(apeakd1)
124        Start(i) = 0;
125        P(i) = 0;
126        abpeak(i) = 0;
127        Minn = 0;
128        Min2(i) = 0;

```

```

129     apeakd(i) = 0;
130     else
131     apeakd(i) = apeakd1(1);
132     abpeakd1 = find(diff(avzz(P(i)+Min2(i):P(i)+Min2(i)+apeakd(i)))< 1);
133     abpeakd(i) = abpeakd1(end);
134     end
135     end
136     end
137     end
138
139 end
140
141 % Delete cells containing zeros
142 P(P == 0) = [];
143 Start(Start == 0) = [];
144 abpeak(abpeak == 0) = [];
145 Min2(Min2 == 0) = [];
146 abpeakd(abpeakd == 0) = [];
147
148 % Define time periods of upward and downward movements
149 Startup = P+Start;
150 Endup = P+ Start+ abpeak;
151 Startdown = P +Start+abpeak + Min2;
152 Enddown = P + Start+abpeak + Min2 + abpeakd;
153
154 tt=T(tstart:tend);
155 MovementPeriodUp = tt(Endup)-tt(Startup);
156 MovementPeriodDown = tt(Enddown)-tt(Startdown);
157 MeanPeriodUp = mean(MovementPeriodUp);
158 MeanPeriodDown = mean(MovementPeriodDown);
159
160 % Make matrices with zeros for velocities and pressure
161 tt=T(tstart:tend);
162 k = 1:length(Enddown);
163 TTup(k) = Endup(k)-Startup(k);
164 TTdown(k) = Enddown(k)-Startdown(k);
165 az_up = zeros(max(TTup),length(k));
166 az_d = zeros(max(TTdown),length(k));
167 t_up = zeros(max(TTup),length(k));
168 t_d = zeros(max(TTdown),length(k));
169 az_down = zeros(max(TTdown),length(k));
170 t_down = zeros(max(TTdown),length(k));
171 Vdown = zeros(1,length(k));
172 Vup = zeros(1,length(k));
173 thetaup = zeros(1,length(k));
174 thetadown = zeros(1,length(k));
175 thetaupstart = zeros(1,length(k));
176 Vupstart = zeros(1,length(k));
177 thetadownstart = zeros(1,length(k));
178 Vdownstart = zeros(1,length(k));
179 Tup = zeros(1,length(k));
180 Tdown = zeros(1,length(k));
181
182 g = 9.81;
183 Dn = 0.05;
184
185 % Calculate angles and angular velocities
186 for k = 1:length(Enddown);
187     %% Up-movement
188
189     % Impose anceleration signal for up-movement
190     az_up(1:length(avzz(Startup(k):Endup(k))),k) = avzz(Startup(k):Endup(k));
191     t_up(1:length(tt(Startup(k):Endup(k))),k) = tt(Startup(k):Endup(k));
192     TTT = linspace(0,MovementPeriodUp(k),length(avzz(Startup(1,k):Endup(1,k))));
193
194     % Substrant signal from linear model
195     StAngle = anos( azsss(Startup(1,k))/g );
196     EdAngle = anos( azsss(Startdown(1,k))/g );
197     phig = StAngle;
198     Dist = EdAngle - StAngle;
199     Dist(Dist<1.3) = 1.5708;

```

```

200     agem = 2*Dist/(TTT(end) - TTT(1))^2;
201     amax = 2*agem;
202     att = linspace(0,amax,length(TTT));
203     at = (Dn/2)*att;
204     V = 0.5.*att.*TTT;
205     an = -(Dn/2).*(V.^2);
206
207     % Estimation angle and velocity for up-movement
208     aangle = avzz(Startup(1,k):Endup(1,k)).' - at - an;
209     angle = anos(aangle/g)-phig;
210     angle = sqrt(real(angle).^2+imag(angle).^2);
211
212     Nz = 2; % Filter order
213     Wnz = 100/8000; % Normalised cutoff frequency at 100 Hz
214     [Cz,Bz] = butter(Nz,Wnz,'low'); % Create smooth function
215     angles = filtfilt(Cz,Bz,angle);
216     angles(angles > Dist)=[];
217     TTT(find(angles == angles(end))+1:find( TTT == TTT(end))) = [];
218     Tup(k) = TTT(end)-TTT(1);
219
220     Vmove1 = diff(angles)./diff(TTT);
221     N = 2; % Filter order
222     Wn = 30/8000; % Normalised cutoff frequency at 30 Hz
223     [C,B] = butter(N,Wn,'low'); % Create smooth function
224     Vmove = filtfilt(C,B,Vmove1);
225
226     % Save results
227     thetaup(k) = angles(end);
228     thetaupstart(k) = angles(1);
229     Vup(k) = Vmove(end);
230     Vupstart(k) = Vmove(1);
231
232     %% Down-movement
233
234     % Impose acceleration signal for up-movement
235     az_d(1:length(avzz(Startdown(k):Enddown(k))),k) = avzz(Startdown(k):Enddown(k));
236     t_d(1:length(tt(Startdown(k):Enddown(k))),k) = tt(Startdown(k):Enddown(k));
237     TTTd = linspace(0,MovementPeriodDown(k),length(avzz(Startdown(1,k):Enddown(1,k))));
238
239     % Substrant signal from linear model
240     StAngled = anos( azss(Startdown(1,k))/g );
241     EdAngled = anos( azss(Startup(1,k)-1000)/g );
242     Distd = EdAngled - StAngled;
243     Distd(Distd<1.3) = 1.5708;
244     agemd = 2*Dist/(TTTd(end) - TTTd(1))^2;
245     amaxd = 2*agemd;
246     attd = linspace(0,amaxd,length(TTTd));
247     atd = -(Dn/2)*attd;
248     Vd = 0.5.*attd.*TTTd;
249     and = (Dn/2).*(Vd.^2);
250
251     % Estimation angle and velocity for down-movement
252     aangled = avzz(Startdown(1,k):Enddown(1,k)).' - atd - and;
253     angled = anos(aangled/g)-StAngled;
254     angled = sqrt(real(angled).^2+imag(angled).^2);
255
256     anglesd = filtfilt(Cz,Bz,angled);
257     anglesd(anglesd > abs(Distd))=[];
258     TTTd(find(anglesd == anglesd(end))+1:find( TTTd == TTTd(end))) = [];
259     Tdown(k) = TTTd(end)-TTTd(1);
260
261     Vmove1d = diff(anglesd)./diff(TTTd);
262     Vmoved = filtfilt(C,B,Vmove1d);
263
264     % Save results
265     thetadown(k) = anglesd(end);
266     thetadownstart(k) = anglesd(1);
267     Vdown(k) = Vmoved(end);
268     Vdownstart(k) = Vmoved(1);
269
270

```

```
271 end
272
273 else
274     % In case of no movement, the results are zero
275     % Save results
276     thetaup = 0;
277     Vup= 0;
278     thetadown = 0;
279     Vdown= 0;
280     TTTd = 0;
281     TTT = 0;
282     angled = 0;
283     anglesd = 0;
284     angles = 0;
285     angle = 0;
286     Vmove1d =0;
287     Vmoved = 0;
288     Vmove1 = 0;
289     Vmove = 0;
290     Tup = 0;
291     Tdown = 0;
292 end
293
294 %% Save Results to textfile
295 if isempty(Vup)
296     Vup = 0;
297     Vdown = 0;
298     Tup = 0;
299     Tdown = 0;
300 end
301
302 dlmwrite('I27_results_Vup.ASC',Vup,'delimiter',';')
303 dlmwrite('I27_results_Vdown.ASC',Vdown,'delimiter',';')
304 dlmwrite('I27_results_Tup.ASC',Tup,'delimiter',';')
305 dlmwrite('I27_results_Tdown.ASC',Tdown,'delimiter',';')
```

# H

## RESULTS VELOCITIES BEFORE COLLISION

Table H.1: Overview figures angular velocities before collision

Name	Number	Title
H	1	Distribution angular velocities for variation in significant wave height, upward rotation. $s_{m-1.0} = 0.04, Y/D_n = -2$
H	2	Distribution angular velocities for variation in significant wave height, upward rotation. $s_{m-1.0} = 0.04, Y/D_n = 0$
H	3	Probability of exceedance over number of waves for variation in significant wave height, upward rotation. $s_{m-1.0} = 0.04, Y/D_n = 0$
H	4	Distribution angular velocities for variation in significant wave height, upward rotation. $s_{m-1.0} = 0.04, Y/D_n = 2$
H	5	Distribution angular velocities for variation in significant wave height, upward rotation. $s_{m-1.0} = 0.02, Y/D_n = -2$
H	6	Probability of exceedance over number of waves for variation in significant wave height, upward rotation. $s_{m-1.0} = 0.02, Y/D_n = -2$
H	7	Distribution angular velocities for variation in significant wave height, upward rotation. $s_{m-1.0} = 0.02, Y/D_n = 0$
H	8	Distribution angular velocities for variation in significant wave height, upward rotation. $s_{m-1.0} = 0.02, Y/D_n = 2$
H	9	Distribution angular velocities for variation in significant wave height, downward rotation. $s_{m-1.0} = 0.04, Y/D_n = -2$
H	10	Probability of exceedance over number of waves for variation in significant wave height, downward rotation. $s_{m-1.0} = 0.04, Y/D_n = -2$
H	11	Distribution angular velocities for variation in significant wave height, downward rotation. $s_{m-1.0} = 0.04, Y/D_n = 0$
H	12	Distribution angular velocities for variation in significant wave height, downward rotation. $s_{m-1.0} = 0.04, Y/D_n = 2$
H	13	Distribution angular velocities for variation in significant wave height, downward rotation. $s_{m-1.0} = 0.02, Y/D_n = -2$
H	14	Probability of exceedance over number of waves for variation in significant wave height, downward rotation. $s_{m-1.0} = 0.02, Y/D_n = -2$
H	15	Distribution angular velocities for variation in significant wave height, downward rotation. $s_{m-1.0} = 0.02, Y/D_n = 0$
H	16	Distribution angular velocities for variation in significant wave height, downward rotation. $s_{m-1.0} = 0.02, Y/D_n = 2$
H	17	Distribution angular velocities for variation in wave steepness, upward rotation. $H_{m0} = 0.14m, Y/D_n = -2$

Continued on next page

Table H.1 – continued from previous page

Name	Number	Title
H	18	Distribution angular velocities for variation in wave steepness, upward rotation. $H_{m0} = 0.11m$ , $Y/D_n = -2$
H	19	Distribution angular velocities for variation in wave steepness, downward rotation. $H_{m0} = 0.14m$ , $Y/D_n = -2$
H	20	Distribution angular velocities for variation in wave steepness, downward rotation. $H_{m0} = 0.11m$ , $Y/D_n = -2$
H	21	Probability of exceedance over number of waves for variation in wave steepness, downward rotation. $H_{m0} = 0.11m$ , $Y/D_n = -2$
H	22	Distribution angular velocities for position on slope, upward rotation. $s_{m-1.0} = 0.04$ , $H_{m0} = 0.14m$
H	23	Probability of exceedance over number of waves for position on slope, upward rotation. $s_{m-1.0} = 0.04$ , $H_{m0} = 0.14m$
H	24	Distribution angular velocities for position on slope, upward rotation. $s_{m-1.0} = 0.02$ , $H_{m0} = 0.14m$
H	25	Distribution angular velocities for position on slope, downward rotation. $s_{m-1.0} = 0.04$ , $H_{m0} = 0.14m$
H	26	Probability of exceedance over number of waves for position on slope, downward rotation. $s_{m-1.0} = 0.04$ , $H_{m0} = 0.14m$
H	27	Distribution angular velocities for position on slope, downward rotation. $s_{m-1.0} = 0.02$ , $H_{m0} = 0.14m$
H	28	Distribution plot showing differences between upward and downward velocities. $s_{m-1.0} = 0.04$ , $Y/D_n = -2$
H	29	Distribution plot showing differences between upward and downward velocities. $s_{m-1.0} = 0.02$ , $Y/D_n = -2$
H	30	Distribution angular velocities for the embedded cube, variation in significant wave height, upward rotation. $s_{m-1.0} = 0.04$ , $Y/D_n = -2$
H	31	Distribution angular velocities for the embedded cube, variation in significant wave height, downward rotation. $s_{m-1.0} = 0.04$ , $Y/D_n = -2$
H	32	Distribution angular velocities for the embedded cube, variation in significant wave height, downward rotation. $s_{m-1.0} = 0.04m$ , $Y/D_n = -2$
H	33	General distribution - Distribution angular velocities for variation in significant wave height. $s_{m-1.0} = 0.04$ , $Y/D_n = -2$
H	34	General distribution - Probability of exceedance over number of waves for variation in significant wave height. $s_{m-1.0} = 0.04$ , $Y/D_n = -2$
H	35	General distribution - Distribution angular velocities for variation in significant wave height. $s_{m-1.0} = 0.04$ , $Y/D_n = 0$
H	36	General distribution - Probability of exceedance over number of waves for variation in significant wave height. $s_{m-1.0} = 0.04$ , $Y/D_n = 0$
H	37	General distribution - Distribution angular velocities for variation in significant wave height. $s_{m-1.0} = 0.04$ , $Y/D_n = 2$
H	38	General distribution - Probability of exceedance over number of waves for variation in significant wave height. $s_{m-1.0} = 0.04$ , $Y/D_n = 2$
H	39	General distribution - Distribution angular velocities for variation in significant wave height. $s_{m-1.0} = 0.02$ , $Y/D_n = -2$
H	40	General distribution - Probability of exceedance over number of waves for variation in significant wave height. $s_{m-1.0} = 0.02$ , $Y/D_n = -2$
H	41	General distribution - Distribution angular velocities for variation in significant wave height. $s_{m-1.0} = 0.02$ , $Y/D_n = 0$
H	42	General distribution - Distribution angular velocities for variation in significant wave height. $s_{m-1.0} = 0.02$ , $Y/D_n = 2$
H	43	General distribution - Distribution angular velocities for variation in wave steepness. $H_{m0} = 0.14m$ , $Y/D_n = -2$

Continued on next page

Table H.1 – continued from previous page

<b>Name</b>	<b>Number</b>	<b>Title</b>
H	44	General distribution - Distribution angular velocities for variation in wave steepness. $H_{m0} = 0.11m$ , $Y/D_n = -2$
H	45	General distribution - Probability of exceedance over number of waves for variation in wave steepness. $H_{m0} = 0.11m$ , $Y/D_n = -2$
H	46	General distribution - Distribution angular velocities for position on slope. $s_{m-1.0} = 0.04$ , $H_{m0} = 0.14m$
H	47	General distribution - Probability of exceedance over number of waves for position on slope. $s_{m-1.0} = 0.04$ , $H_{m0} = 0.14m$
H	48	General distribution - Distribution angular velocities for position on slope. $s_{m-1.0} = 0.02$ , $H_{m0} = 0.14m$
H	49	General distribution - Probability of exceedance over number of waves for position on slope. $s_{m-1.0} = 0.02$ , $H_{m0} = 0.14m$
H	50	General distribution - Distribution angular velocities for the embedded cube, variation in significant wave height. $s_{m-1.0} = 0.04$ , $Y/D_n = -2$
H	51	General distribution - Probability of exceedance over number of waves for the embedded cube, variation in significant wave height. $s_{m-1.0} = 0.04$ , $Y/D_n = -2$

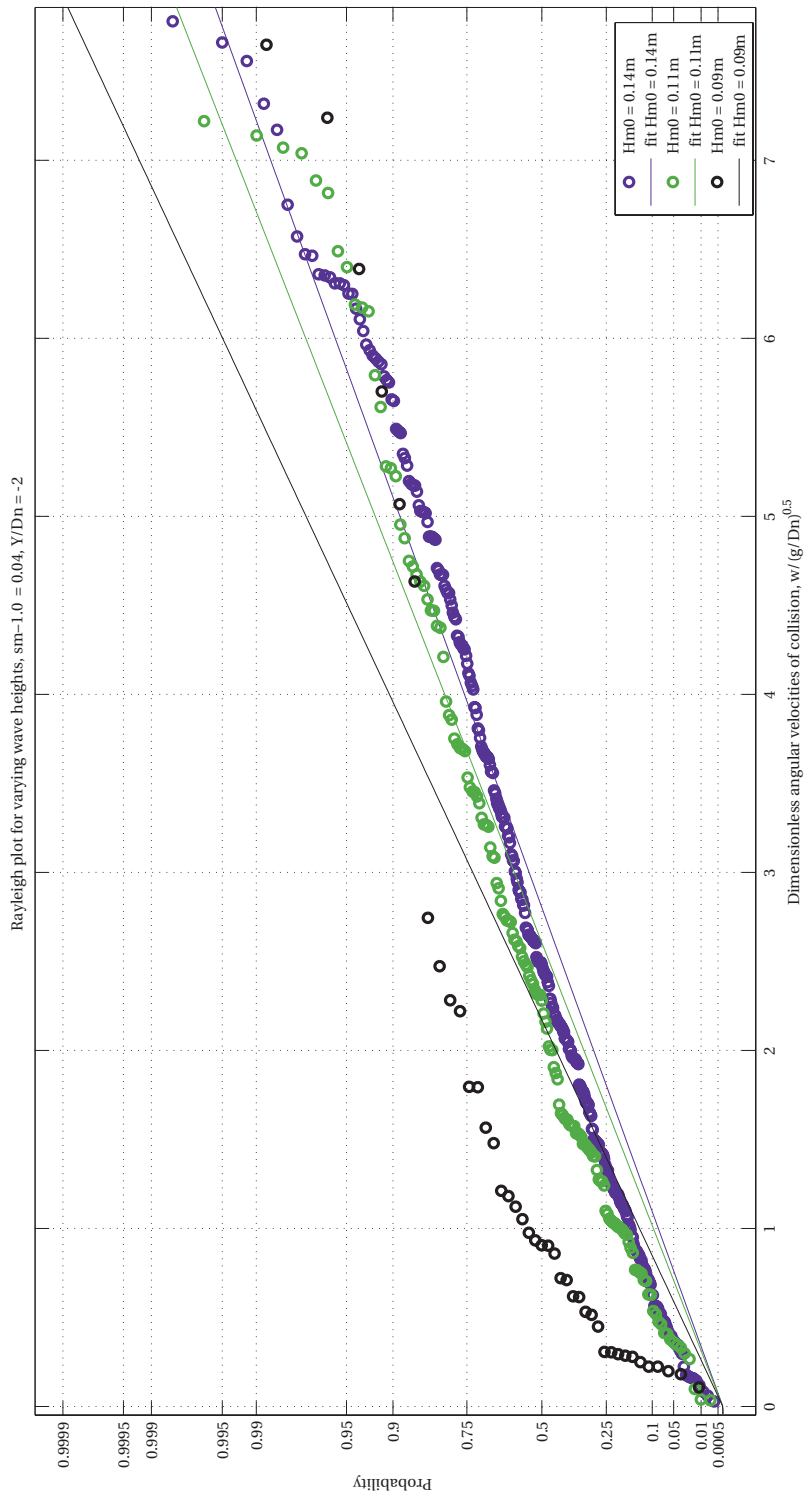


Figure H.1: Distribution angular velocities for variation in significant wave height, upward rotation.  $s_{m-1.0} = 0.04$ ,  $Y/D_n = -2$

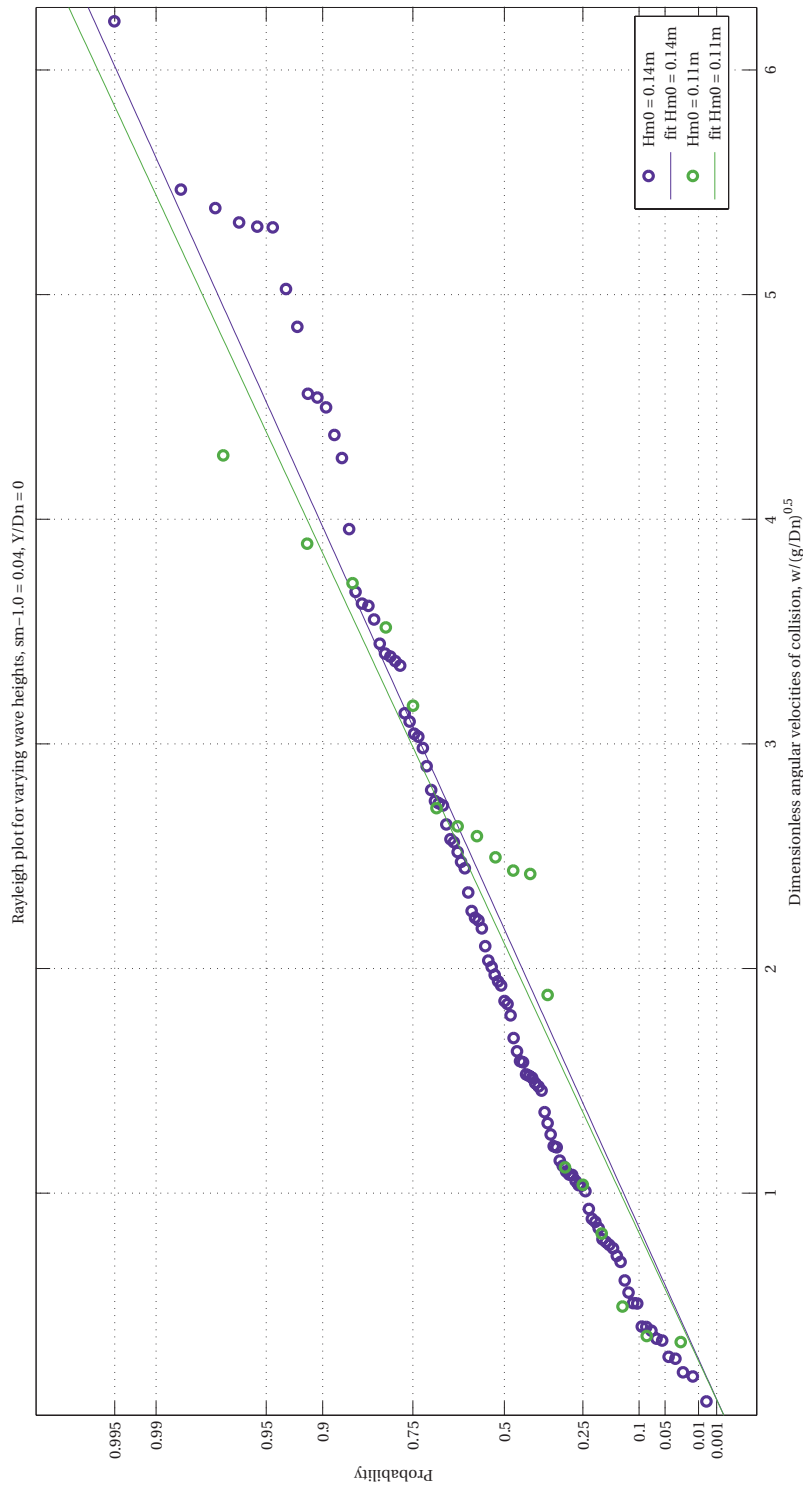


Figure H.2: Distribution angular velocities for variation in significant wave height, upward rotation.  $s_{m-1.0} = 0.04$ ,  $Y/D_n = 0$

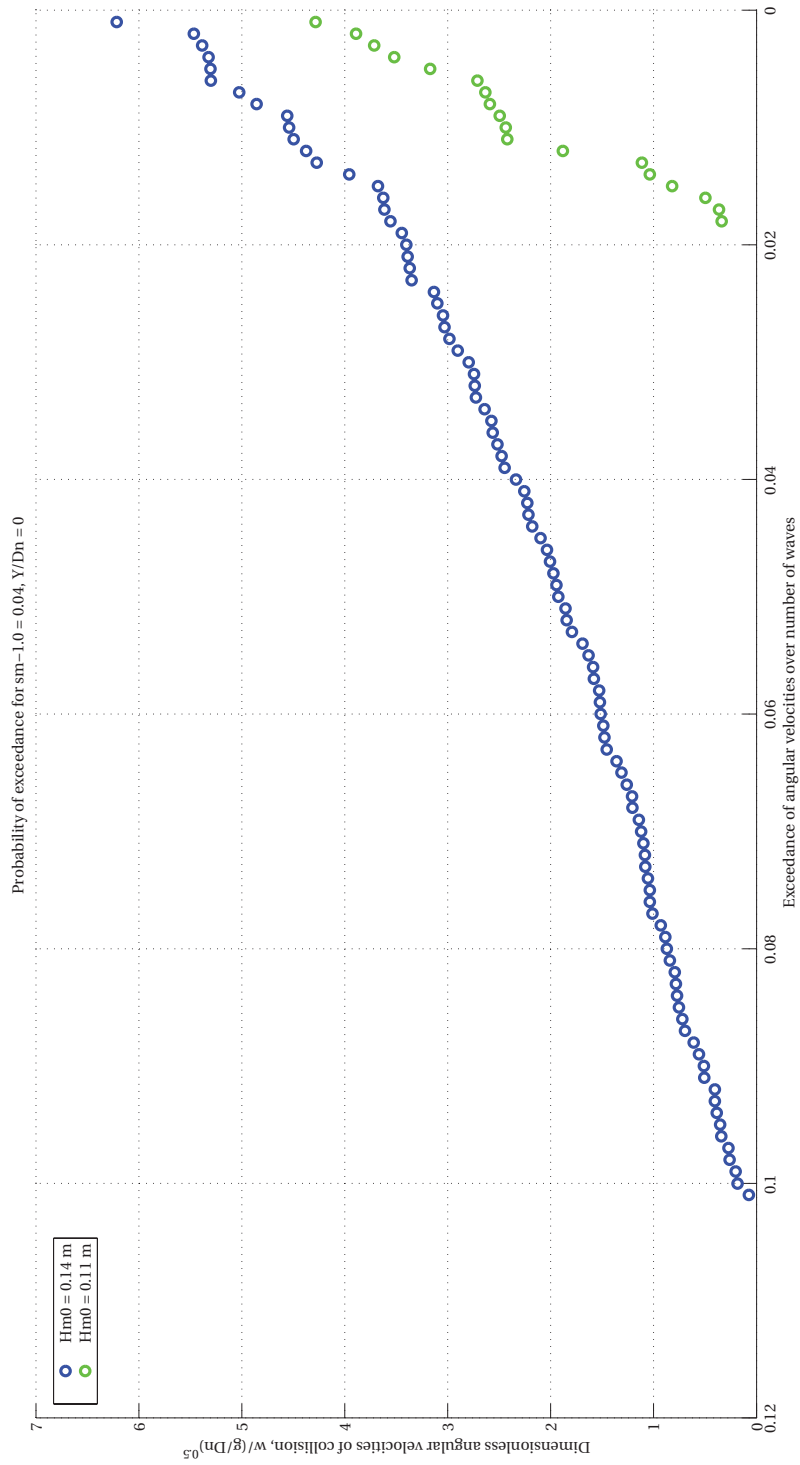


Figure H.3: Probability of exceedance over number of waves for variation in significant wave height, upward rotation.  $sm-1.0 = 0.04, Y/Dn = 0$

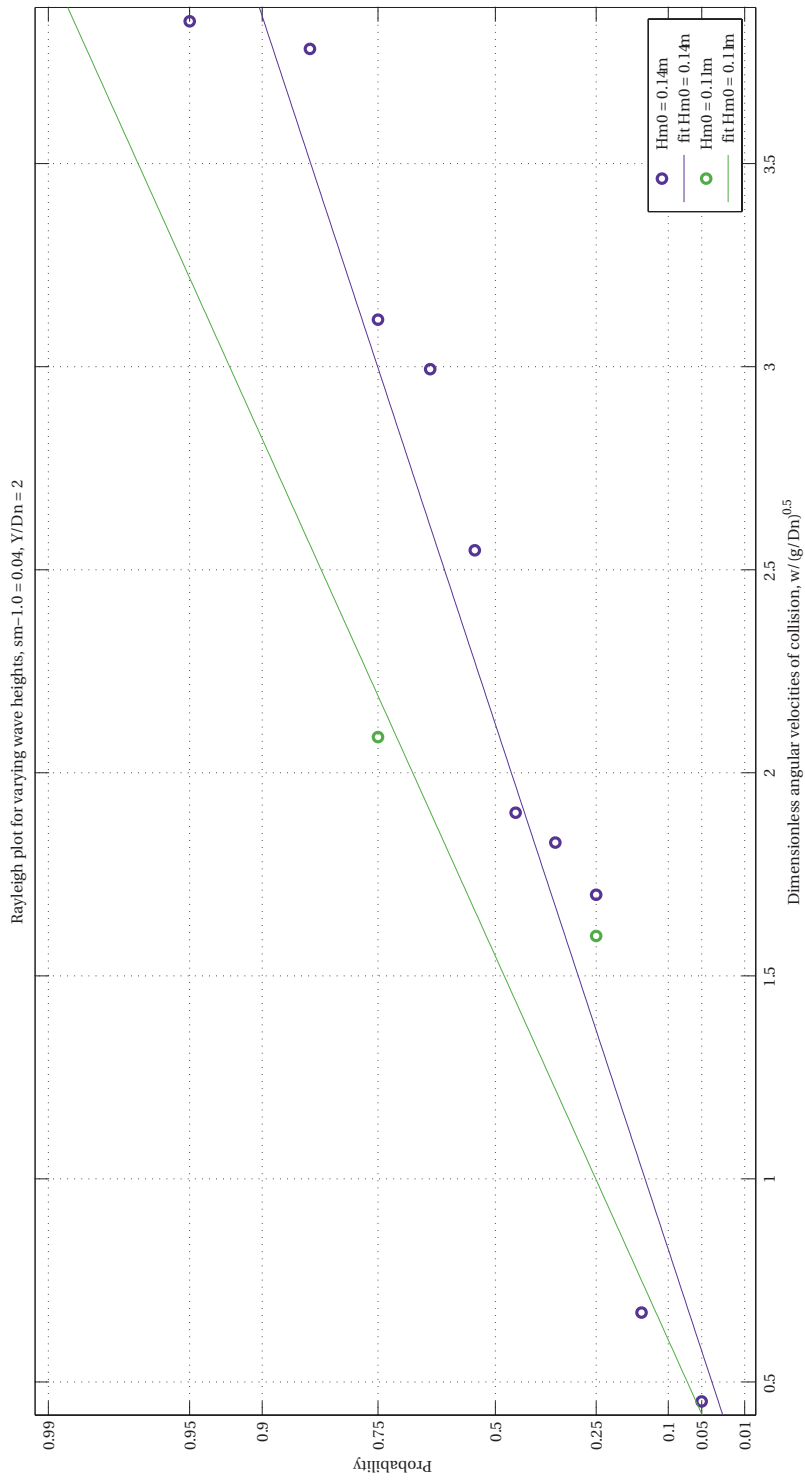


Figure H.4: Distribution angular velocities for variation in significant wave height, upward rotation.  $s_{m-1.0} = 0.04$ ,  $Y/D_n = 2$

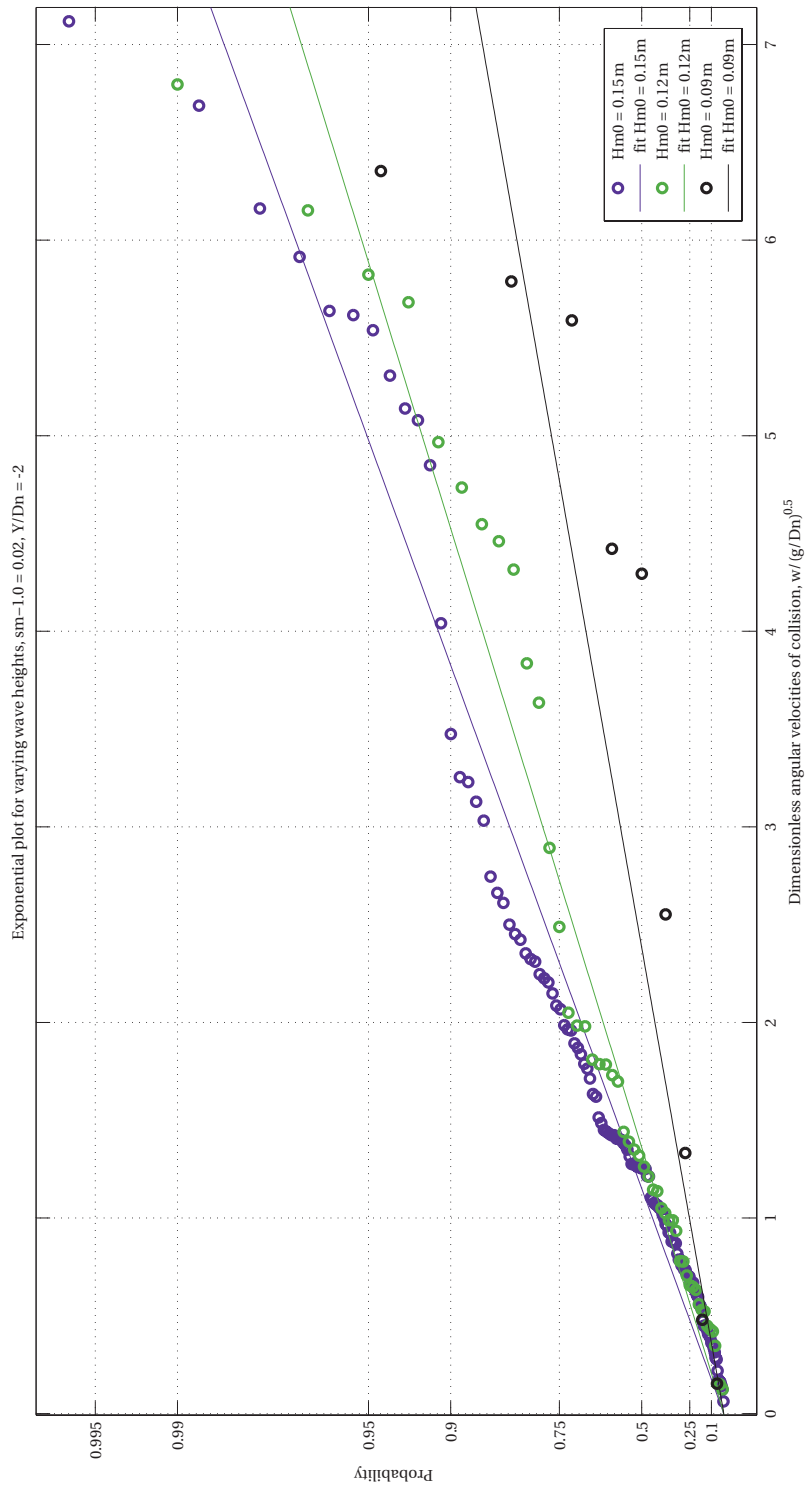


Figure H.5: Distribution angular velocities for variation in significant wave height, upward rotation.  $s_{m-1.0} = 0.02$ ,  $Y/D_n = -2$

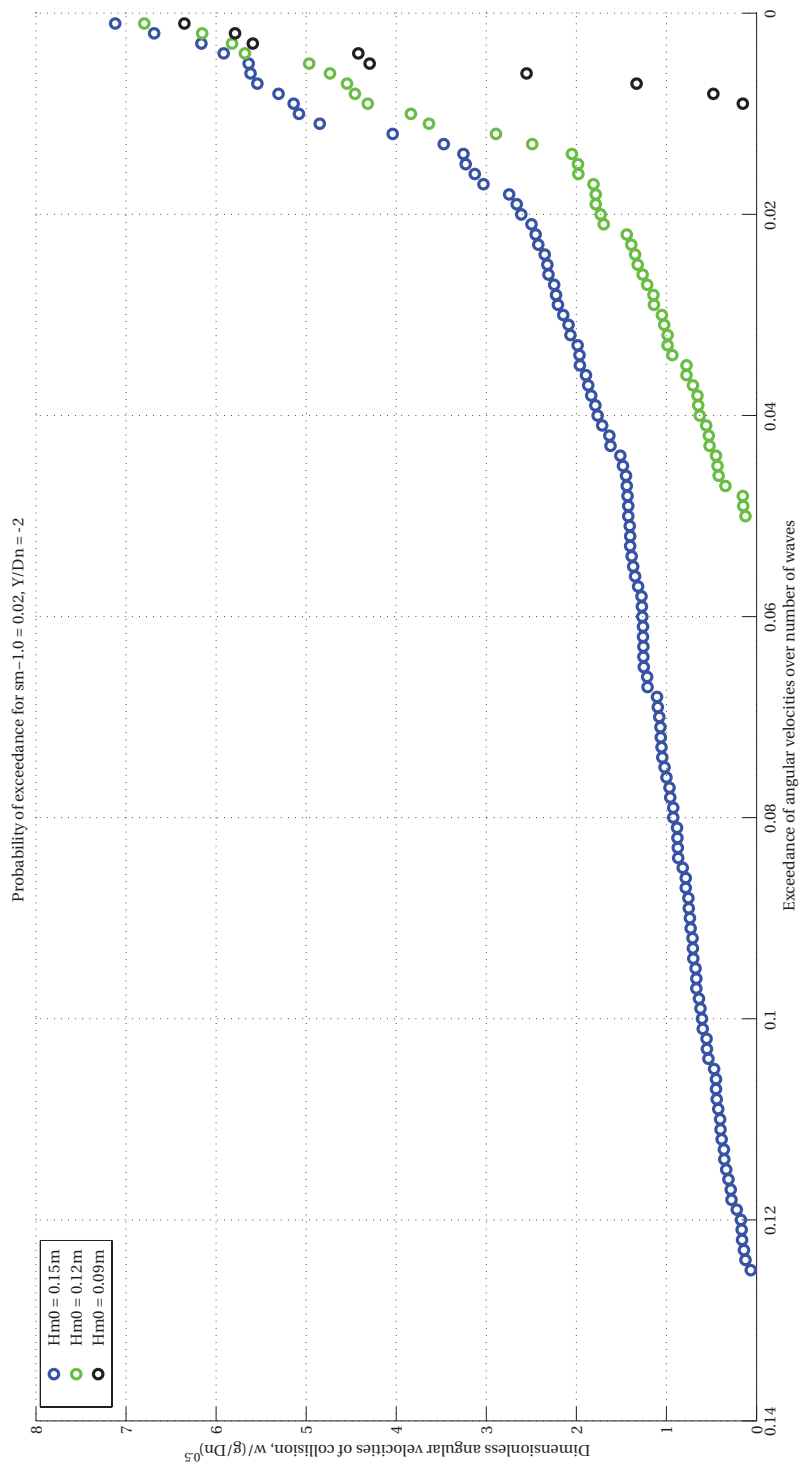


Figure H.6: Probability of exceedance over number of waves for variation in significant wave height, upward rotation.  $sm-1.0 = 0.02, Y/Dn = -2$

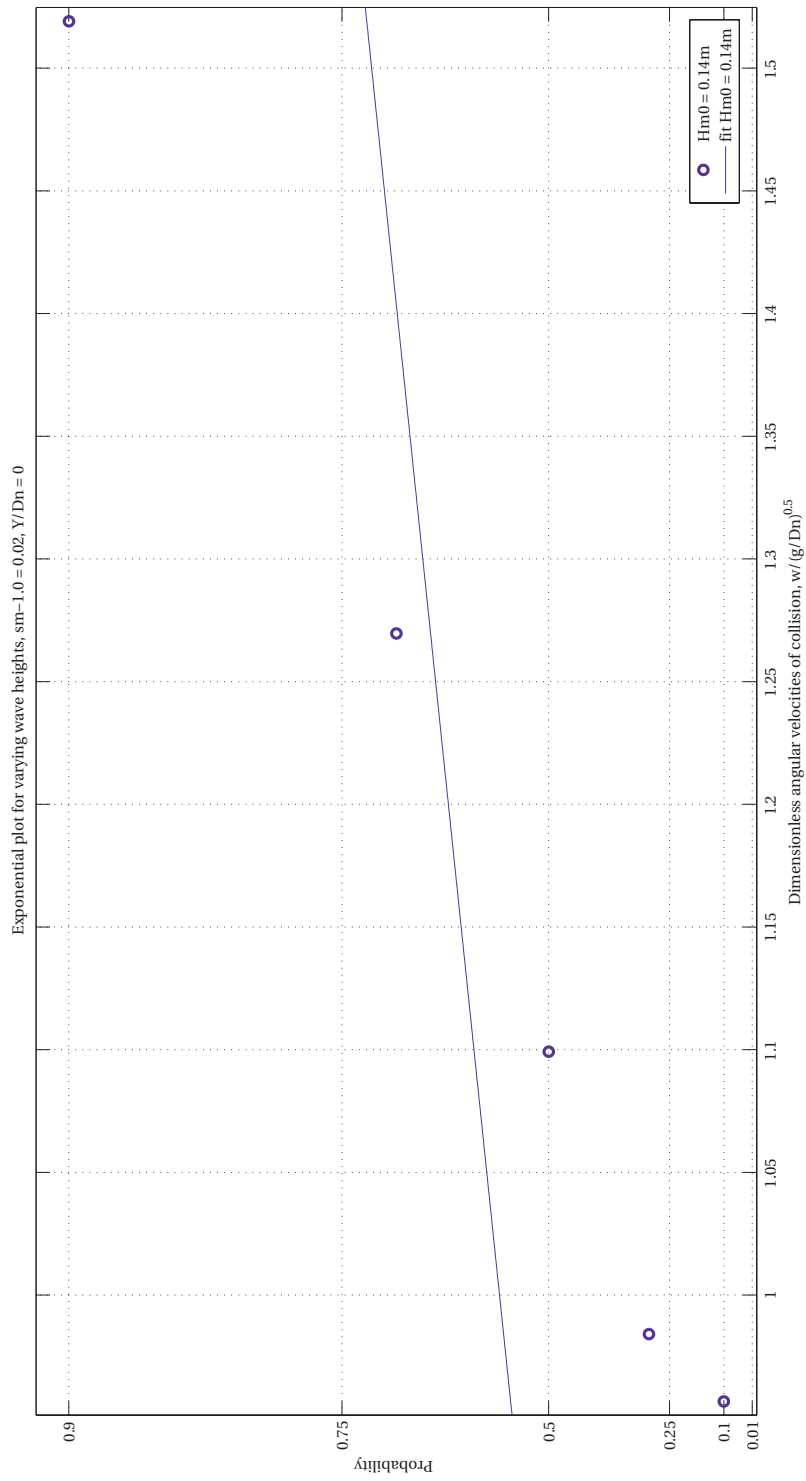


Figure H.7: Distribution angular velocities for variation in significant wave height, upward rotation.  $s_{m-1.0} = 0.02$ ,  $Y/D_n = 0$

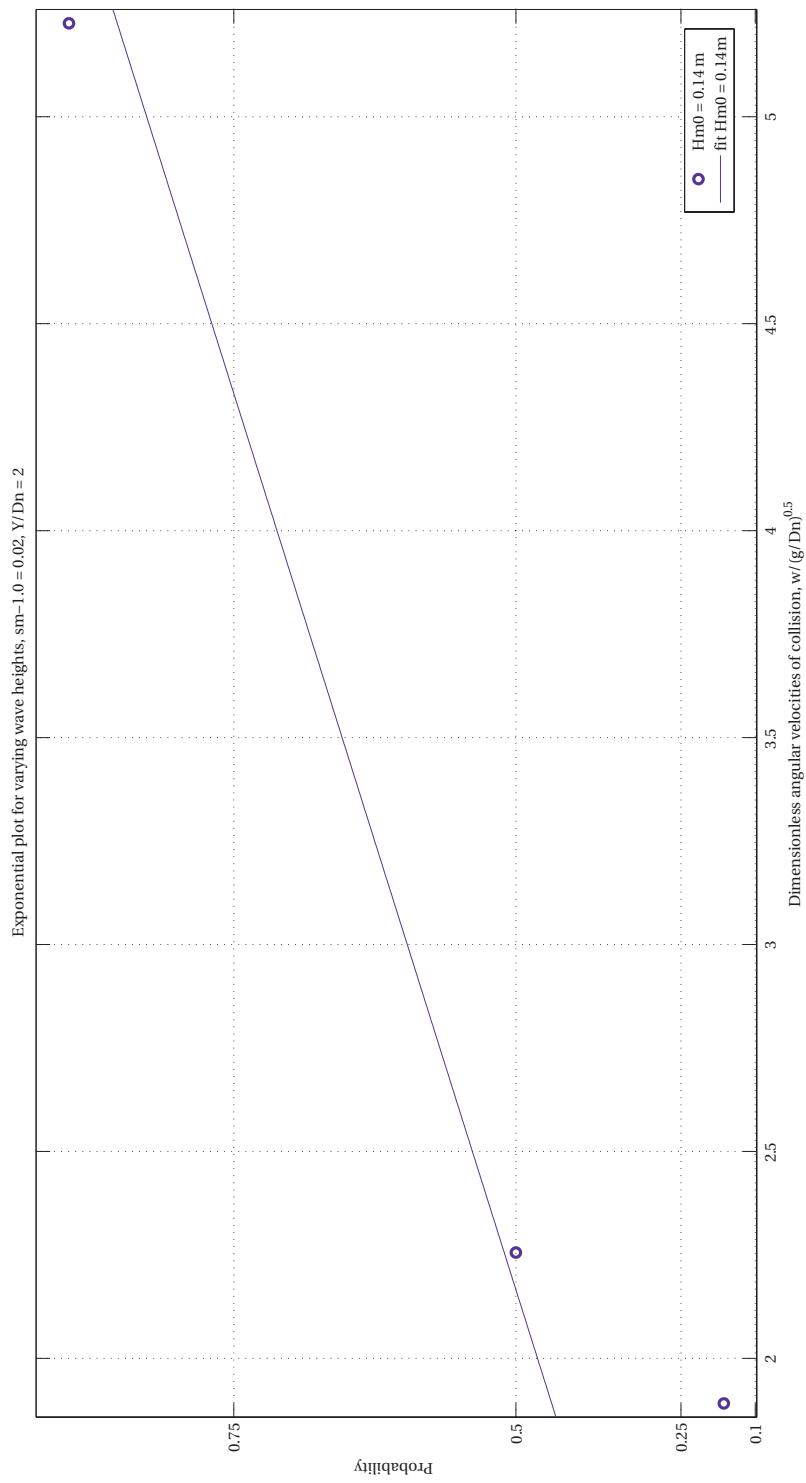


Figure H.8: Distribution angular velocities for variation in significant wave height, upward rotation.  $s_{m-1.0} = 0.02$ ,  $Y/D_n = 2$

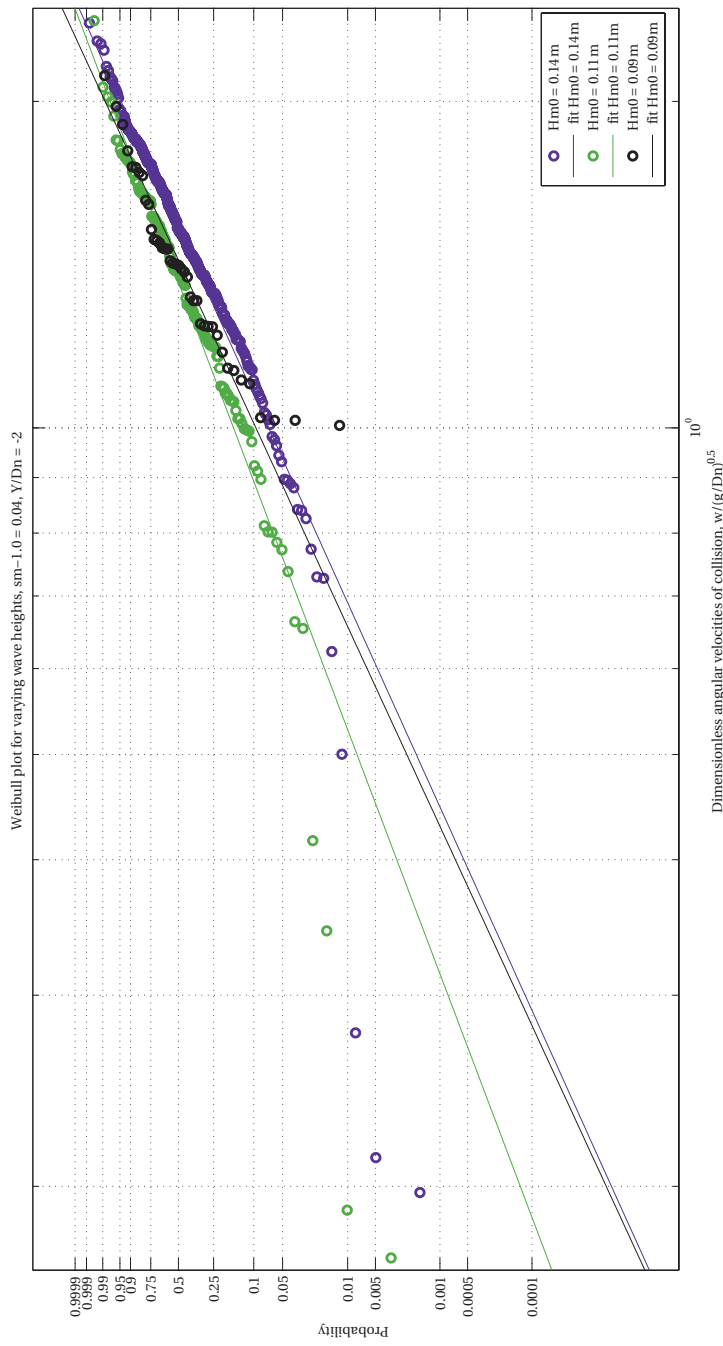


Figure H.9: Distribution angular velocities for variation in significant wave height, downward rotation.  $s_{m-1,0} = 0.04$ ,  $Y/D_n = -2$

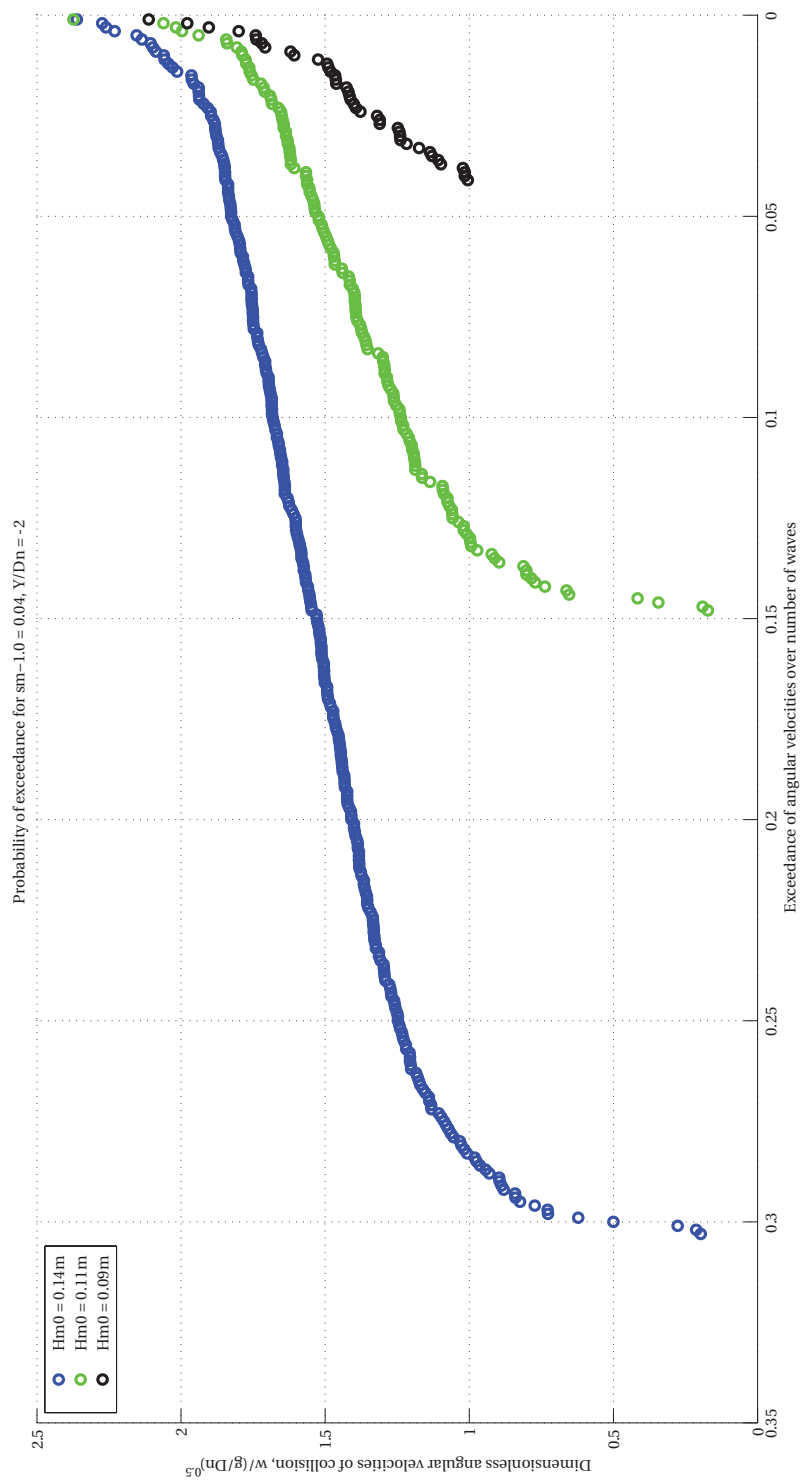


Figure H.10: Probability of exceedance over number of waves for variation in significant wave height, downward rotation.  $sm-1.0 = 0.04, Y/Dn = -2$

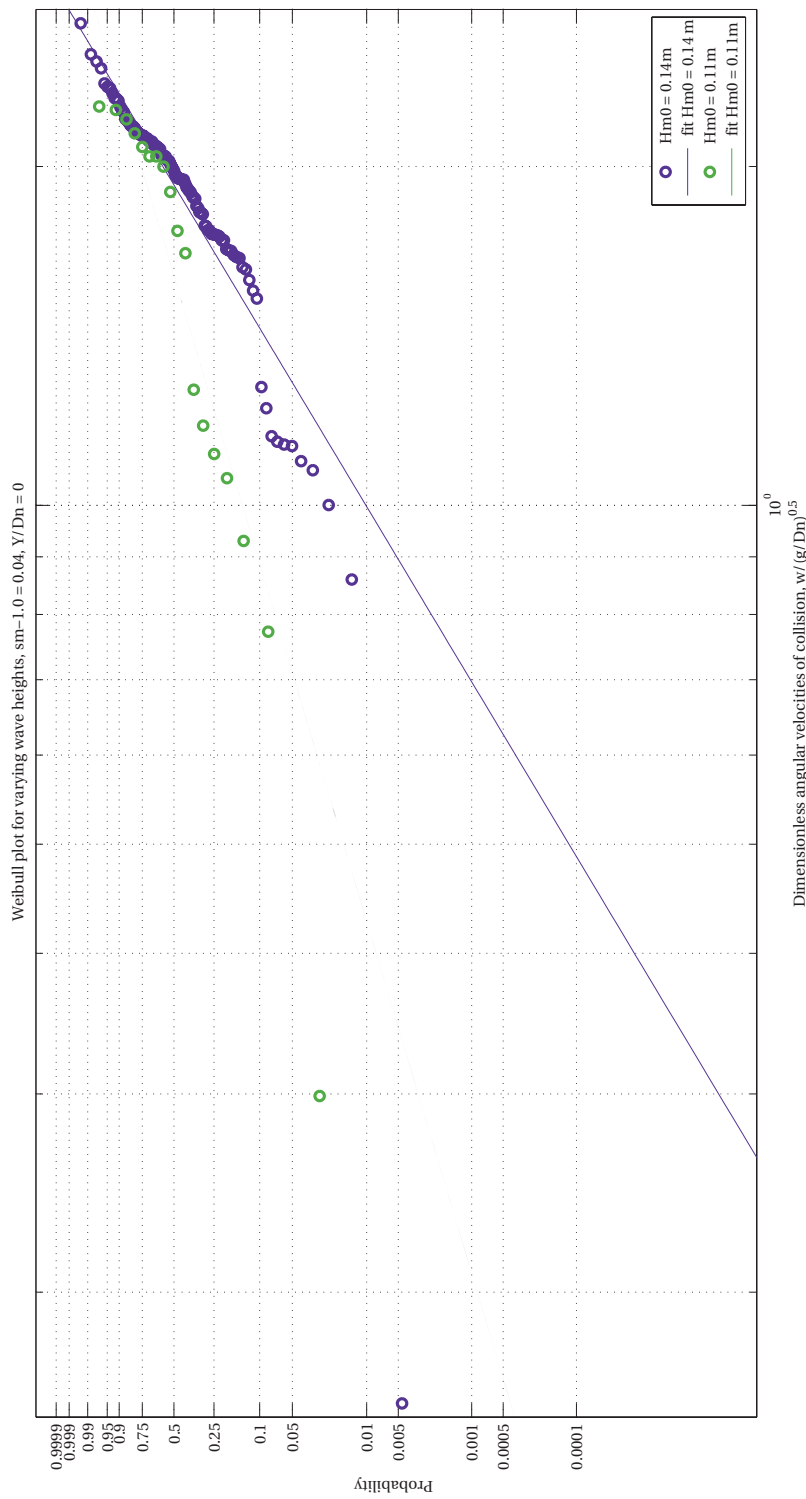


Figure H.11: Distribution angular velocities for variation in significant wave height, downward rotation.  $s_{m-1.0} = 0.04$ ,  $Y/D_n = 0$

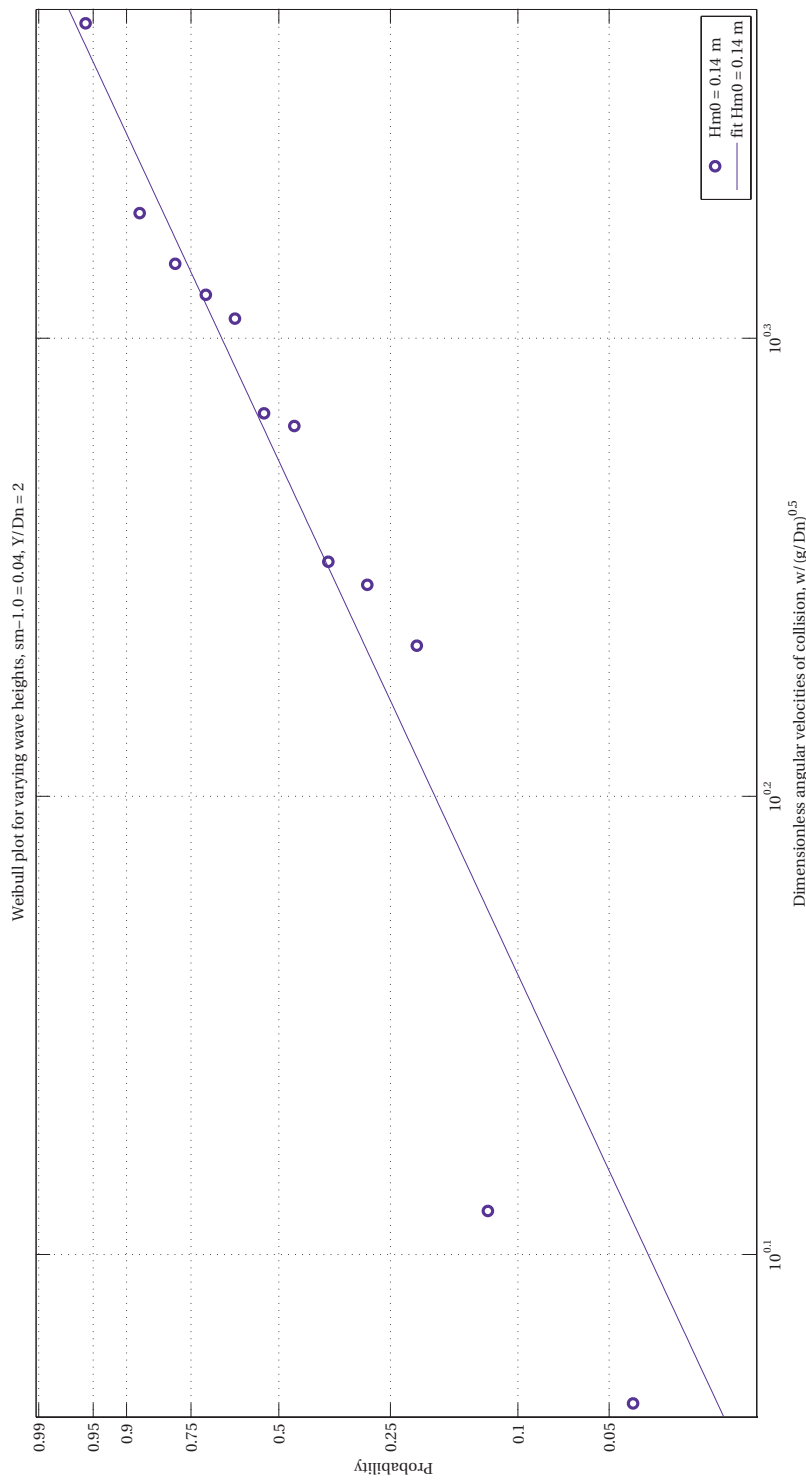


Figure H.12: Distribution angular velocities for variation in significant wave height, downward rotation.  $s_{m-1.0} = 0.04$ ,  $Y/D_n = 2$

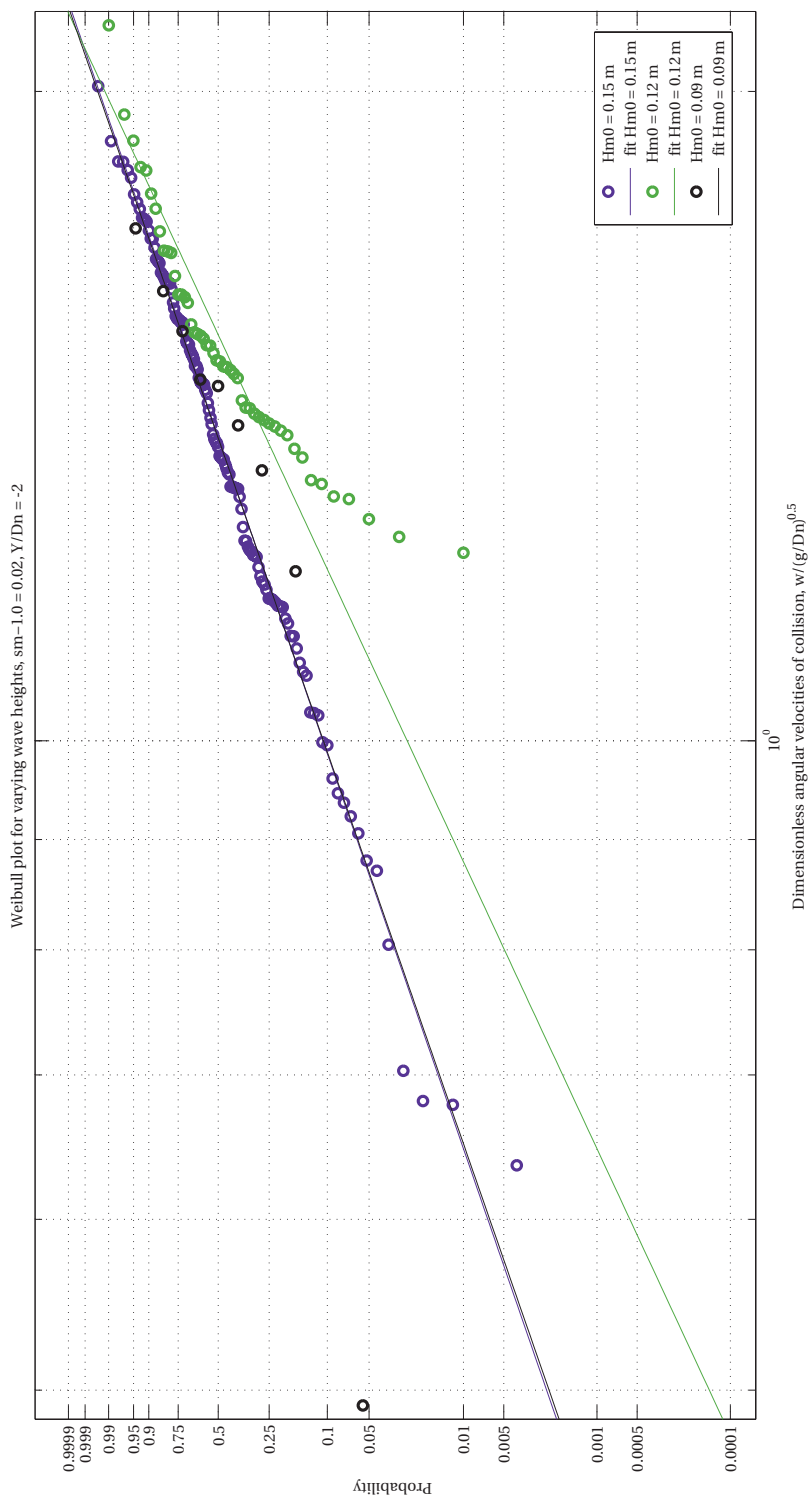


Figure H.13: Distribution angular velocities for variation in significant wave height, downward rotation.  $s_{m-1.0} = 0.02$ ,  $Y/D_n = -2$

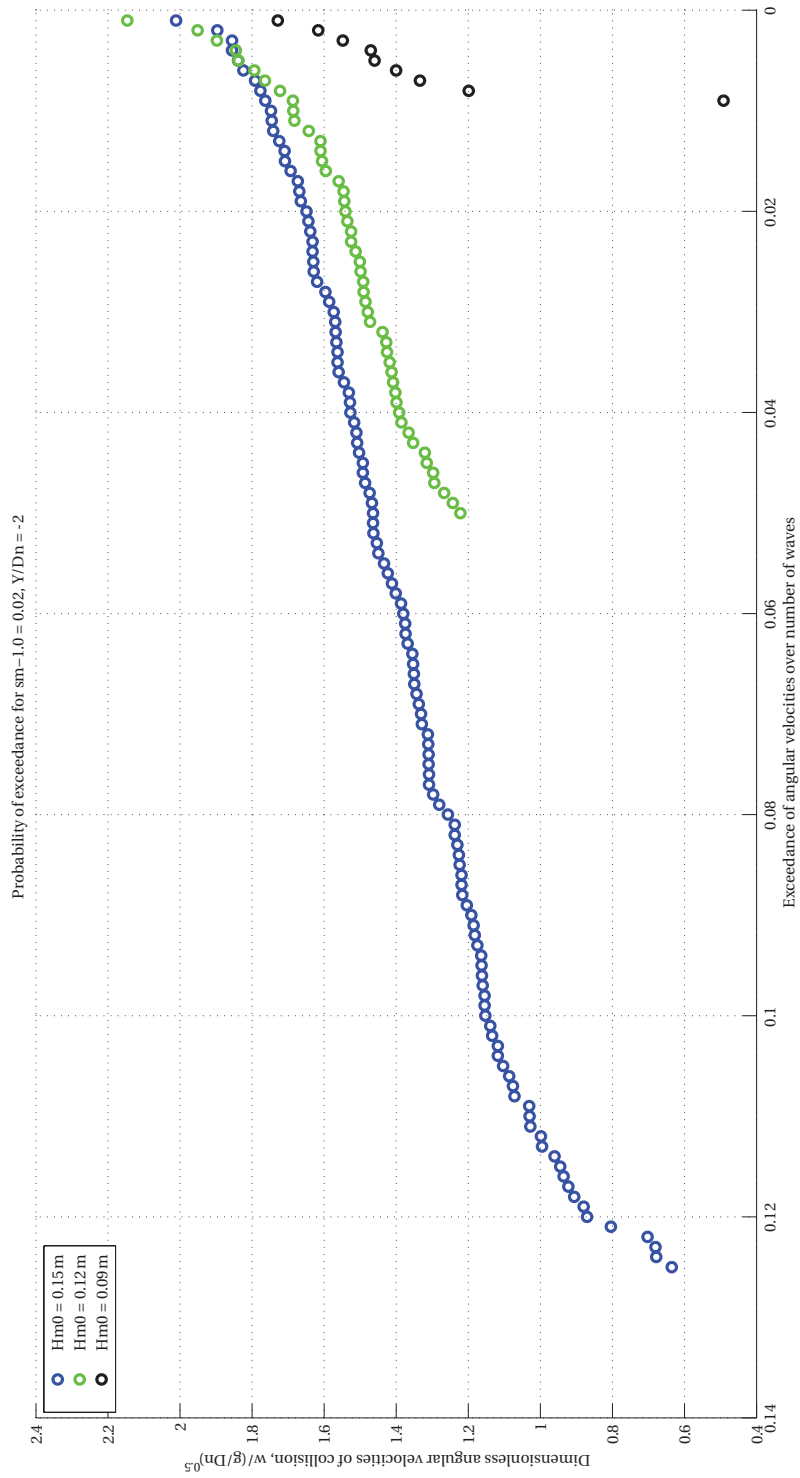


Figure H.14: Probability of exceedance over number of waves for variation in significant wave height, downward rotation.  $sm-1.0 = 0.02, Y/Dn = -2$

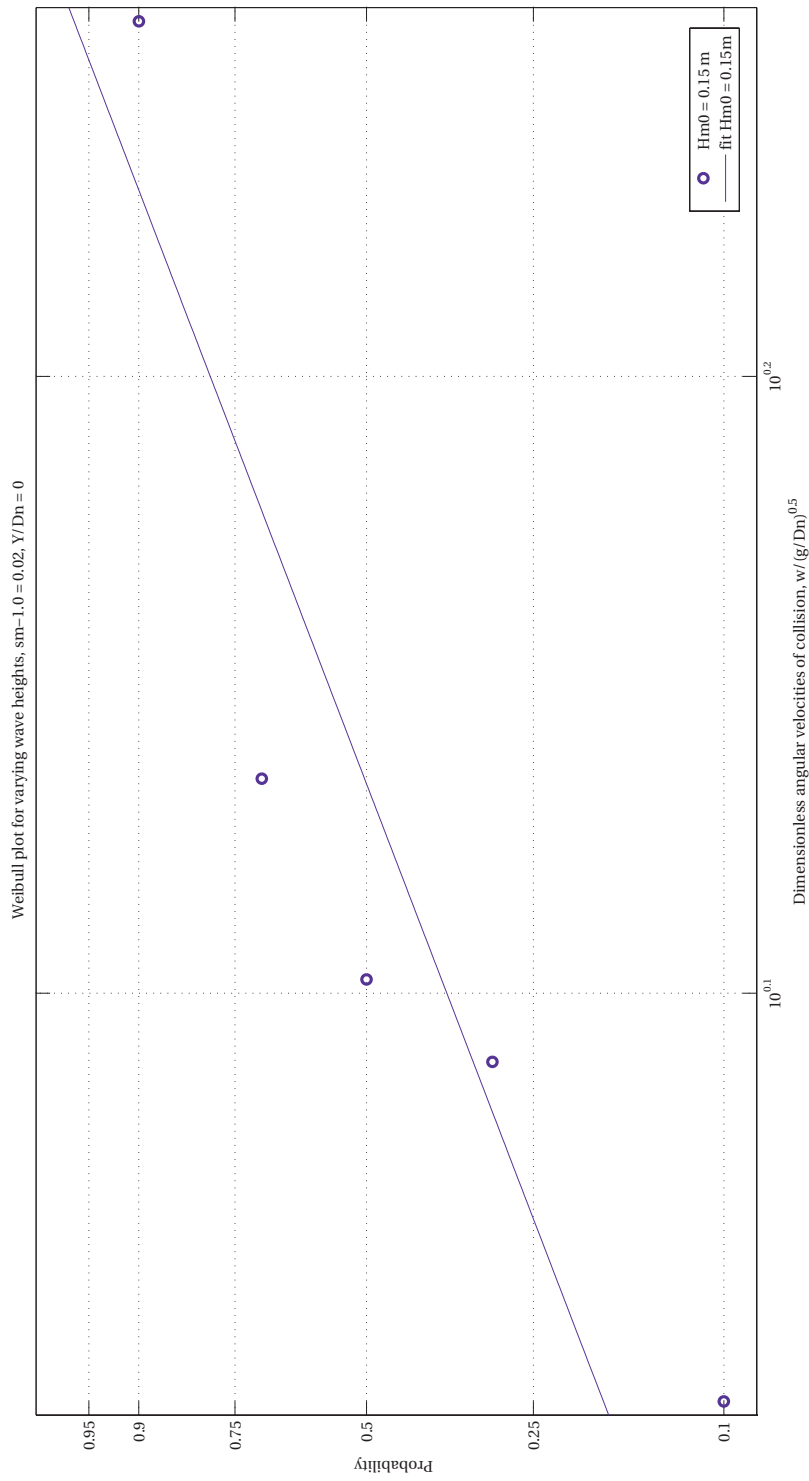


Figure H.15: Distribution angular velocities for variation in significant wave height, downward rotation.  $s_{m-1.0} = 0.02$ ,  $Y/D_n = 0$

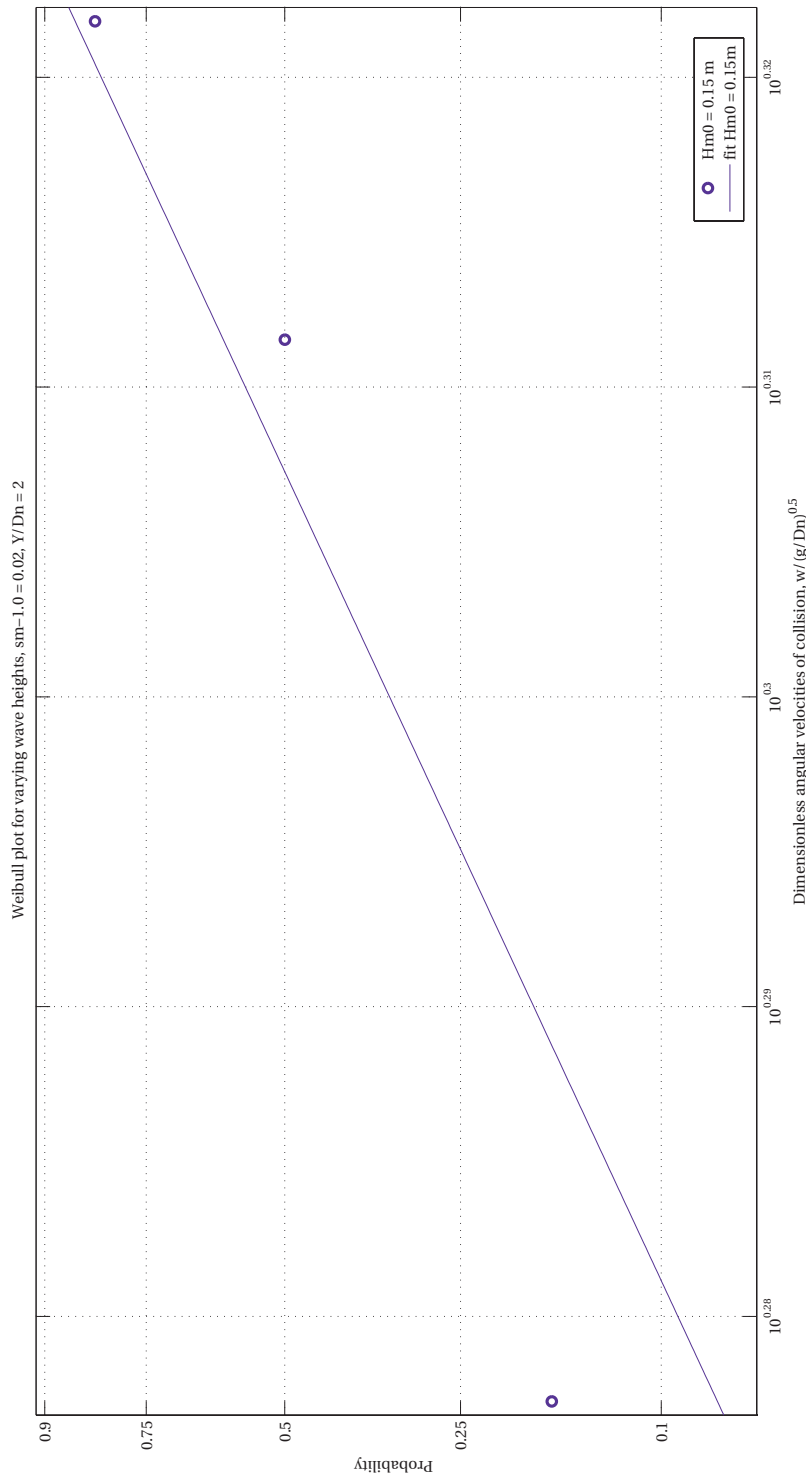


Figure H.16: Distribution angular velocities for variation in significant wave height, downward rotation.  $s_{m-1.0} = 0.02$ ,  $Y/D_n = 2$

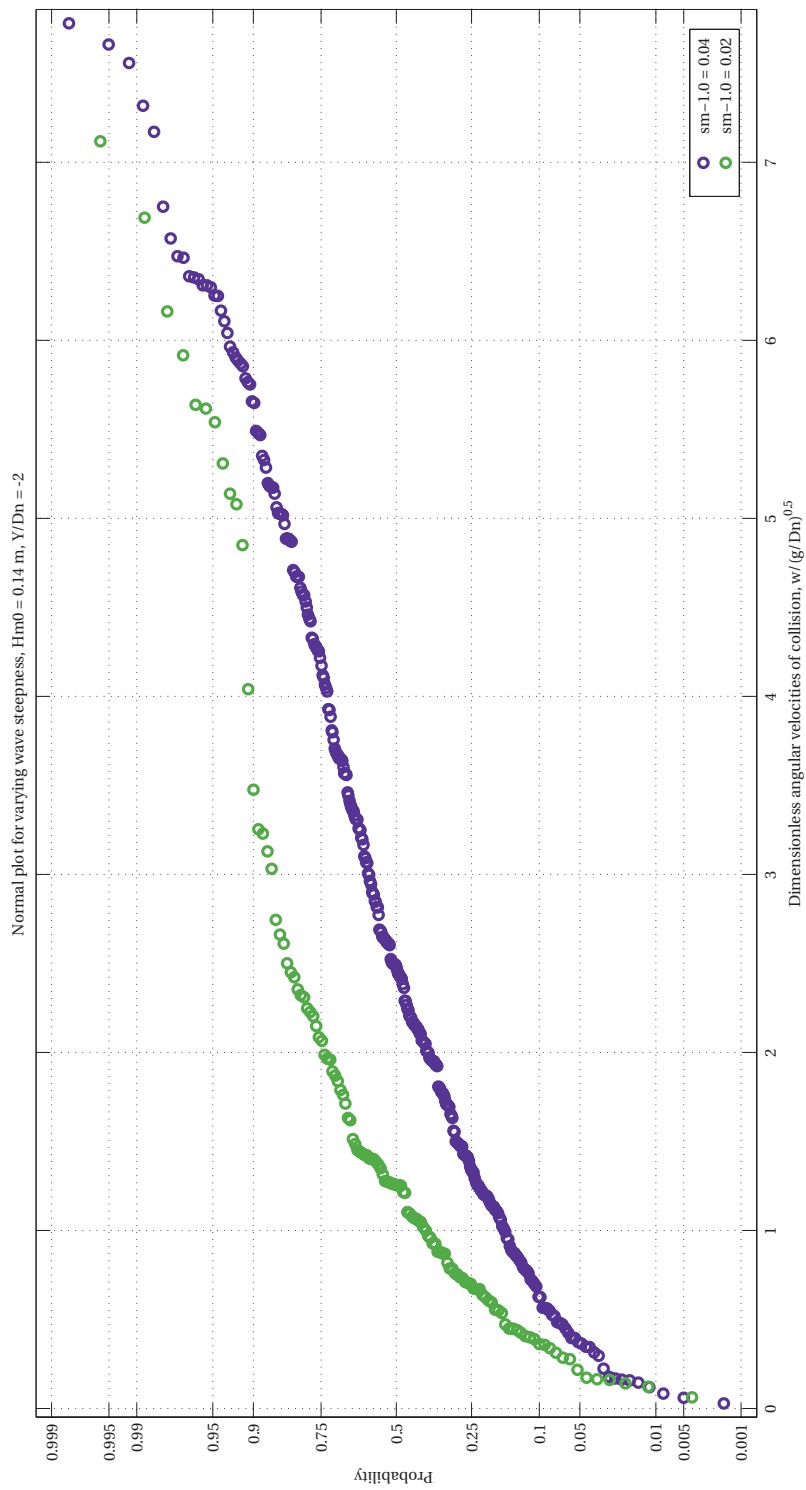


Figure H.17: Distribution angular velocities for variation in wave steepness, upward rotation.  $H_{m0} = 0.14 \text{ m}$ ,  $Y/D_n = -2$

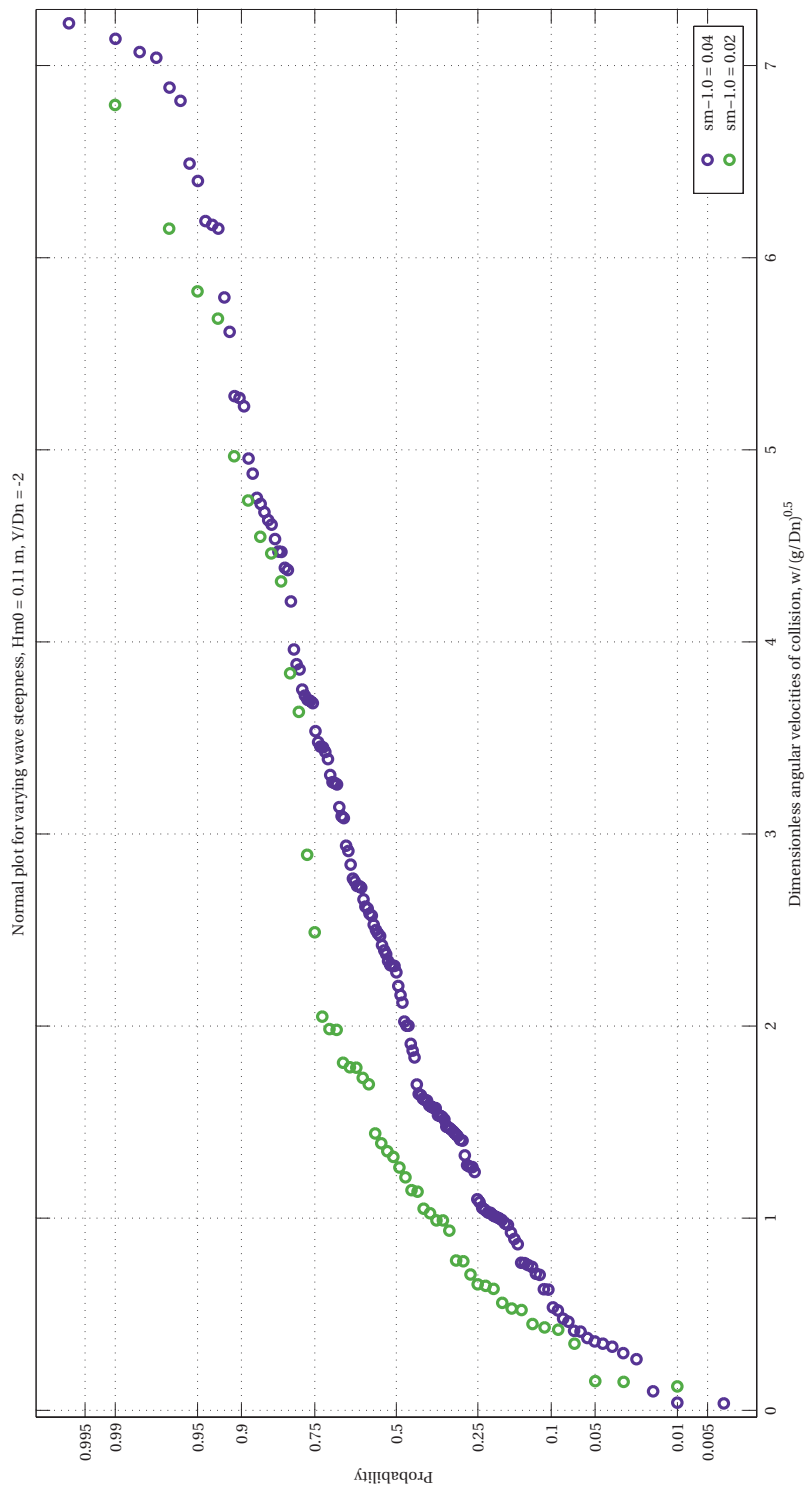


Figure H.18: Distribution angular velocities for variation in wave steepness, upward rotation.  $H_{m0} = 0.11 m, Y/D_n = -2$

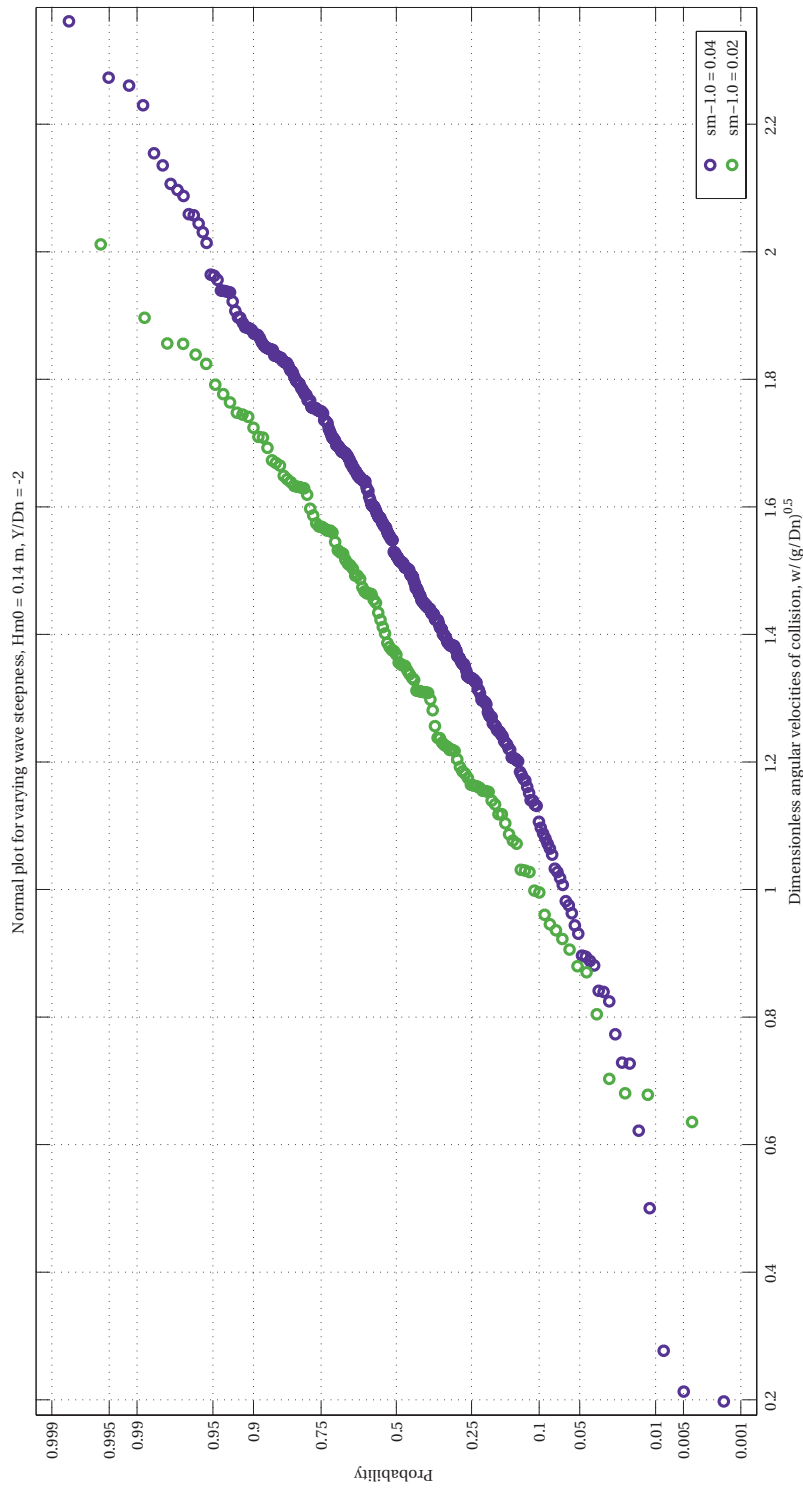


Figure H.19: Distribution angular velocities for variation in wave steepness, downward rotation.  $H_{m0} = 0.14 \text{ m}$ ,  $Y/D_n = -2$

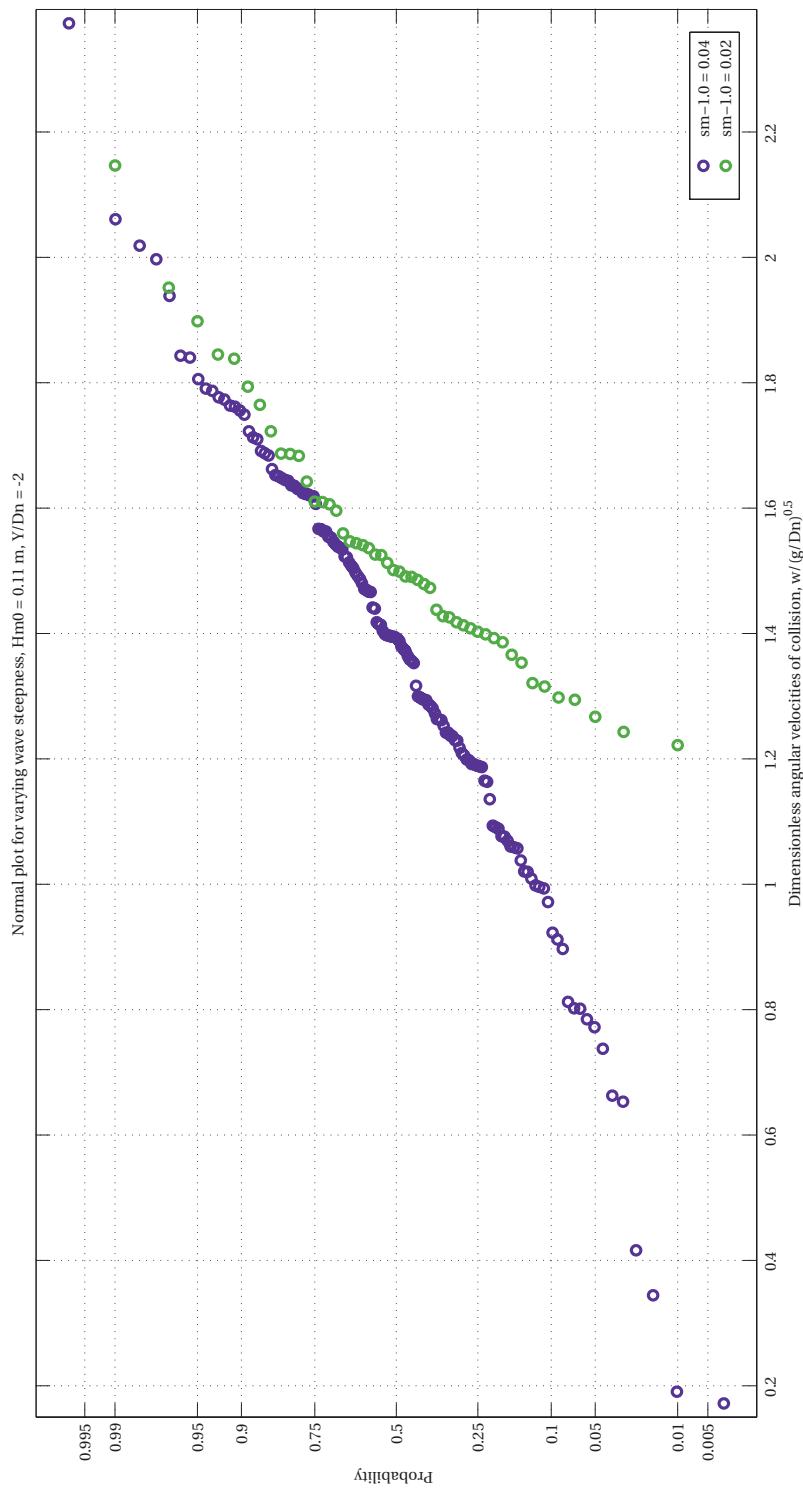


Figure H.20: Distribution angular velocities for variation in wave steepness, downward rotation.  $H_{m0} = 0.11 \text{ m}$ ,  $Y/D_n = -2$

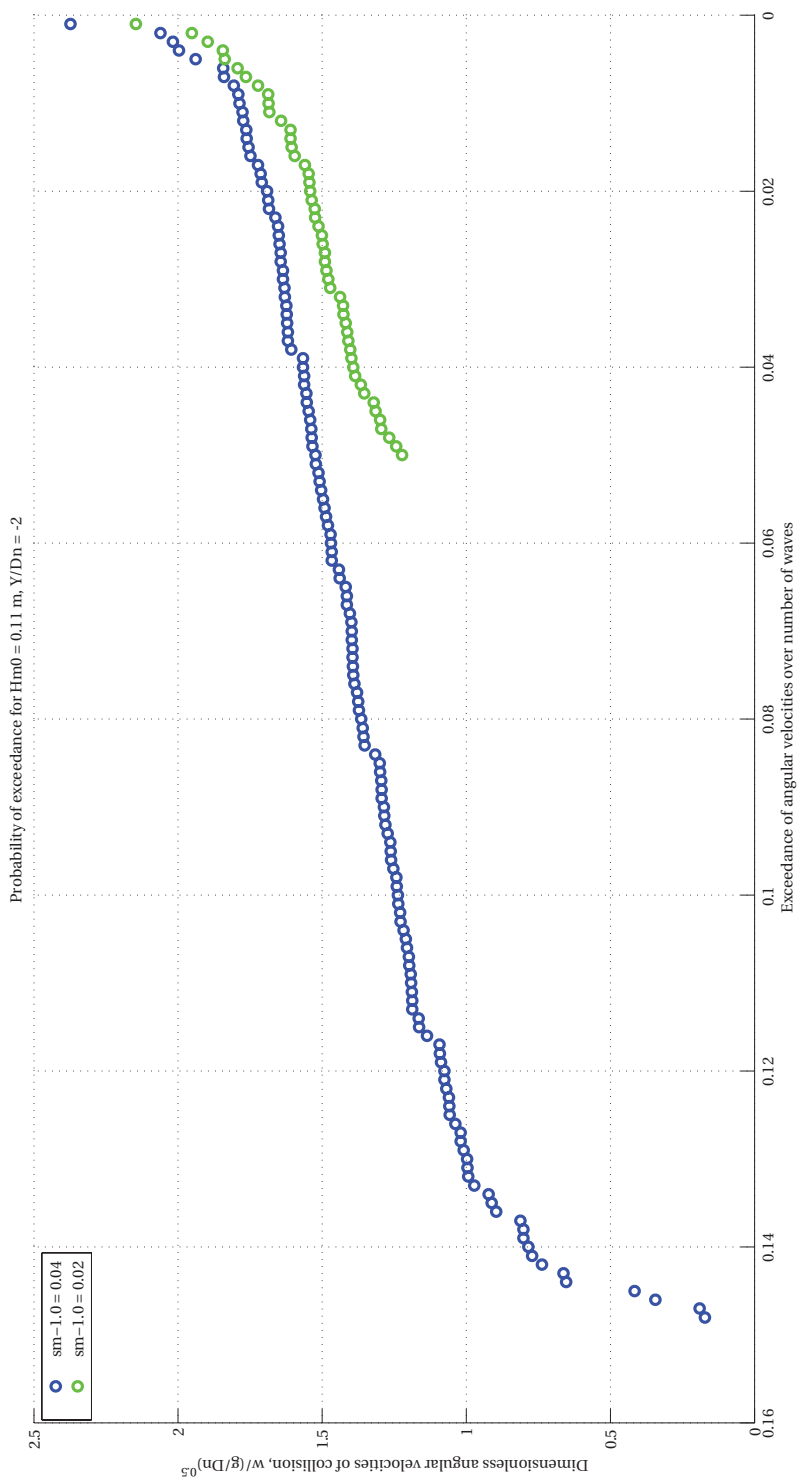


Figure H.21: Probability of exceedance over number of waves for variation in wave steepness, downward rotation.  $H_{m0} = 0.11$  m,  $Y/D_n = -2$

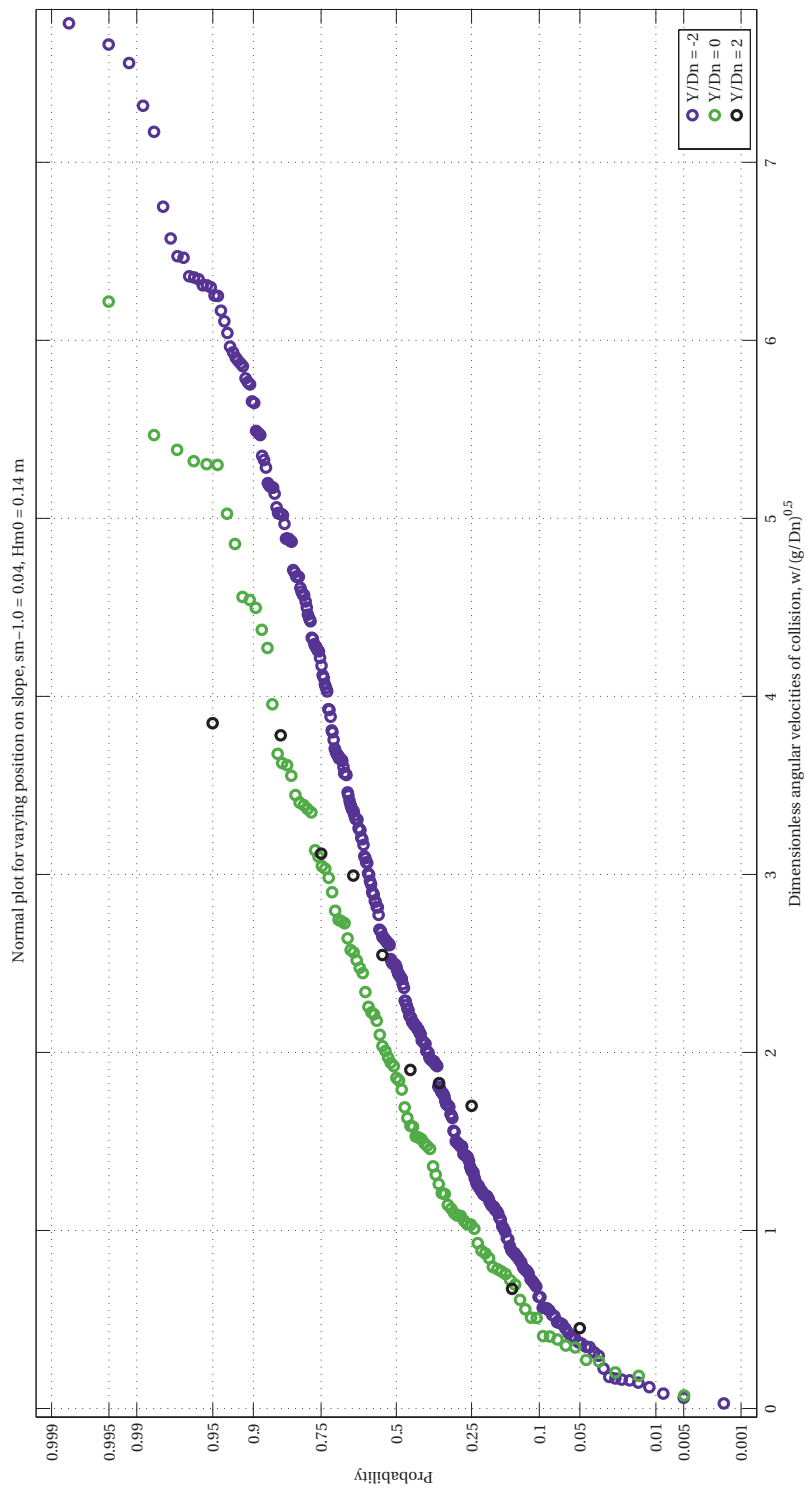


Figure H.22: Distribution angular velocities for position on slope, upward rotation.  $s_{m-1.0} = 0.04$ ,  $H_{m0} = 0.14$  m

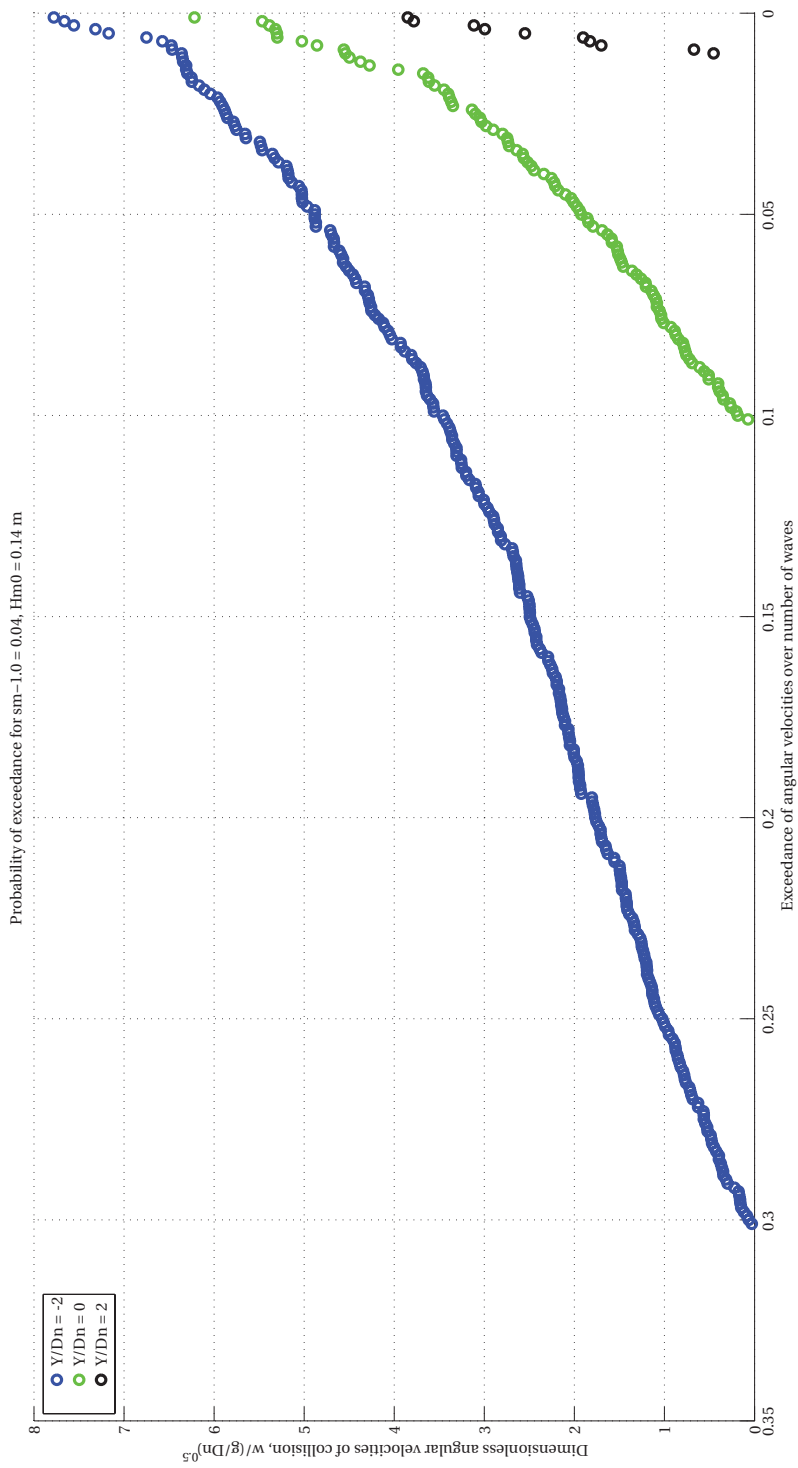


Figure H.23: Probability of exceedance over number of waves for position on slope, upward rotation.  $s_{m-1.0} = 0.04$ ,  $H_{m0} = 0.14$  m

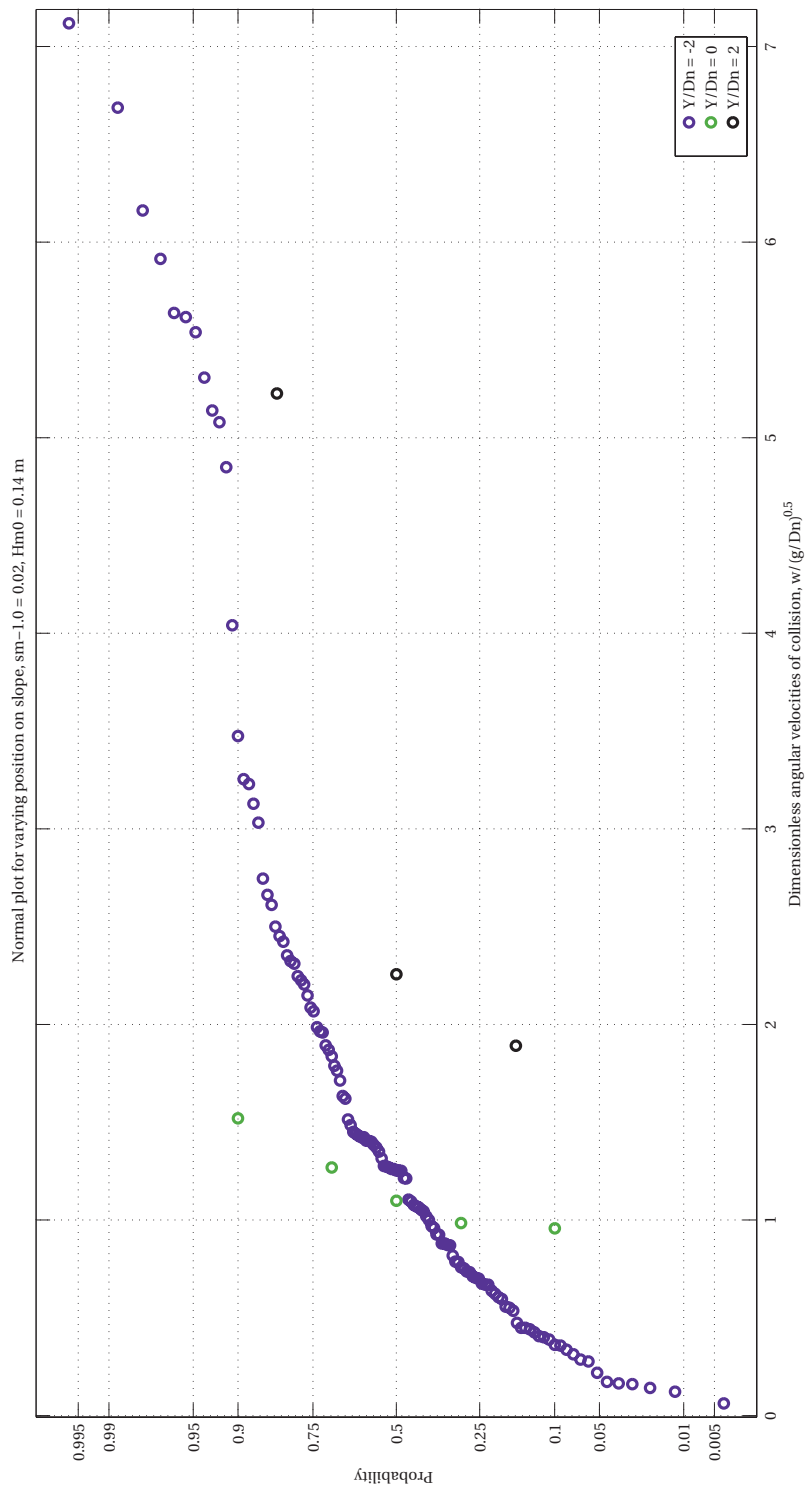


Figure H.24: Distribution angular velocities for position on slope, upward rotation.  $s_{m-1.0} = 0.02$ ,  $H_{m0} = 0.14$  m

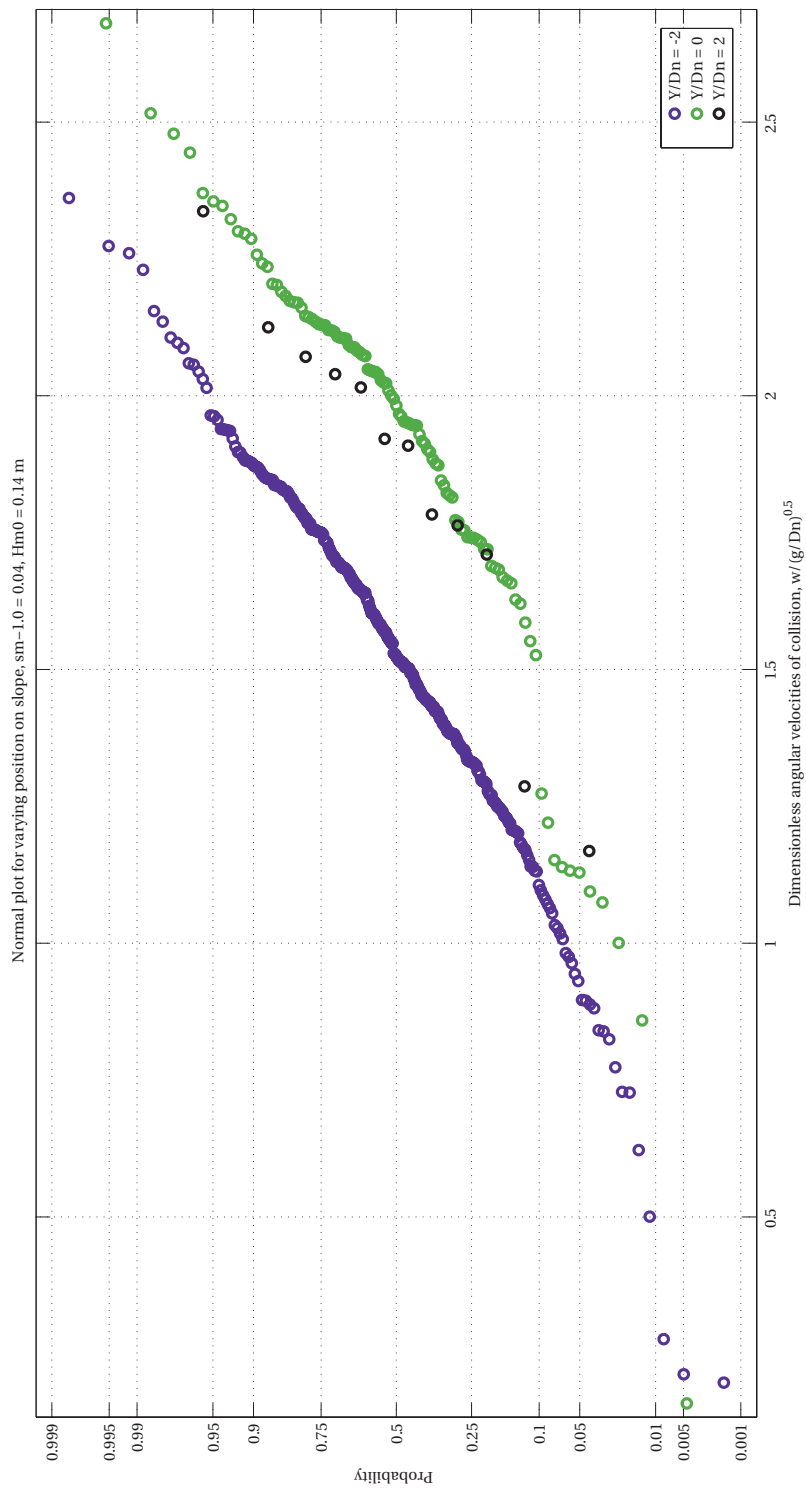


Figure H.25: Distribution angular velocities for position on slope, downward rotation.  $s_{m-1.0} = 0.04$   $H_{m0} = 0.14$  m



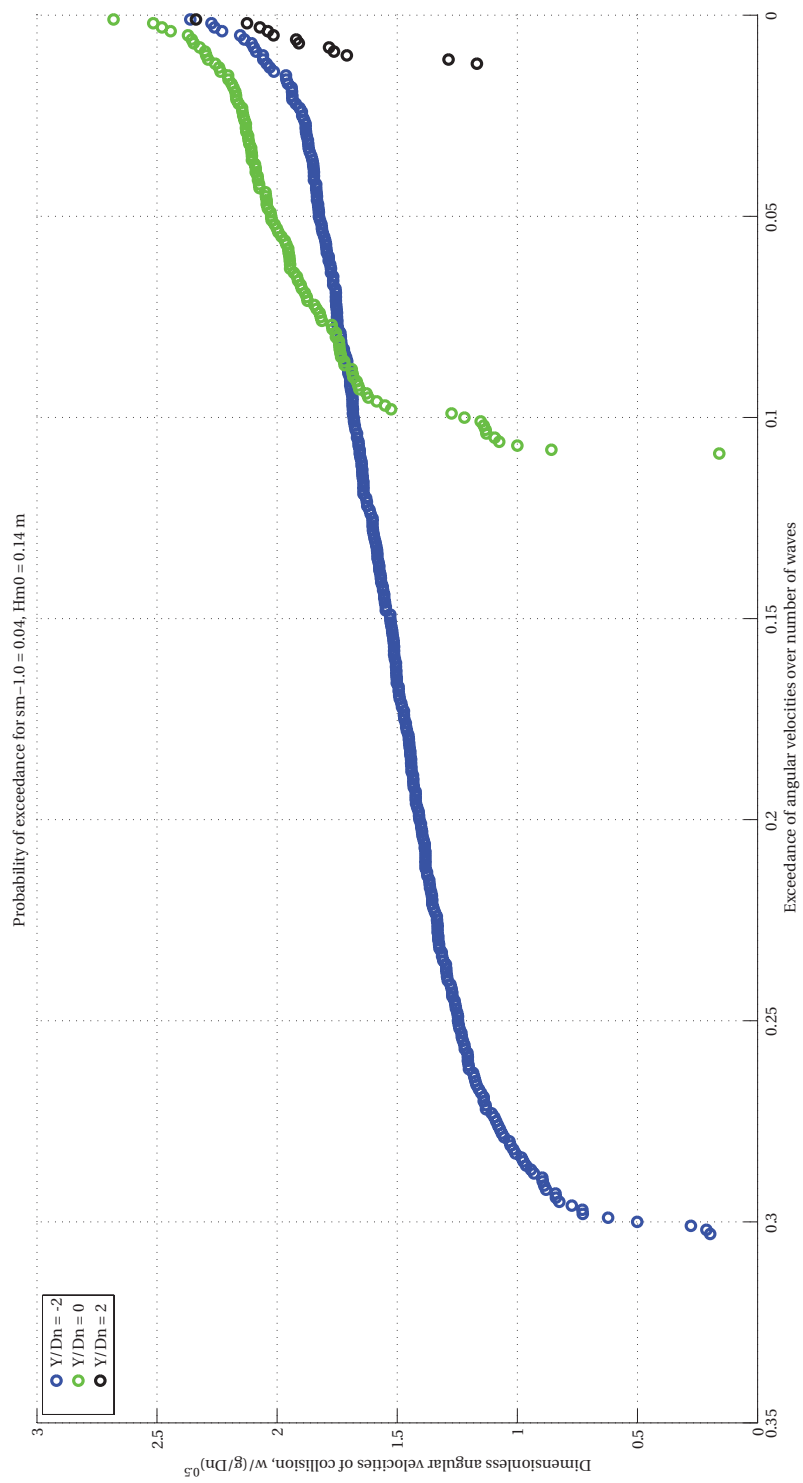


Figure H.26: Probability of exceedance over number of waves for position on slope, downward rotation.  $s_{m-1.0} = 0.04$ ,  $H_{m0} = 0.14$  m

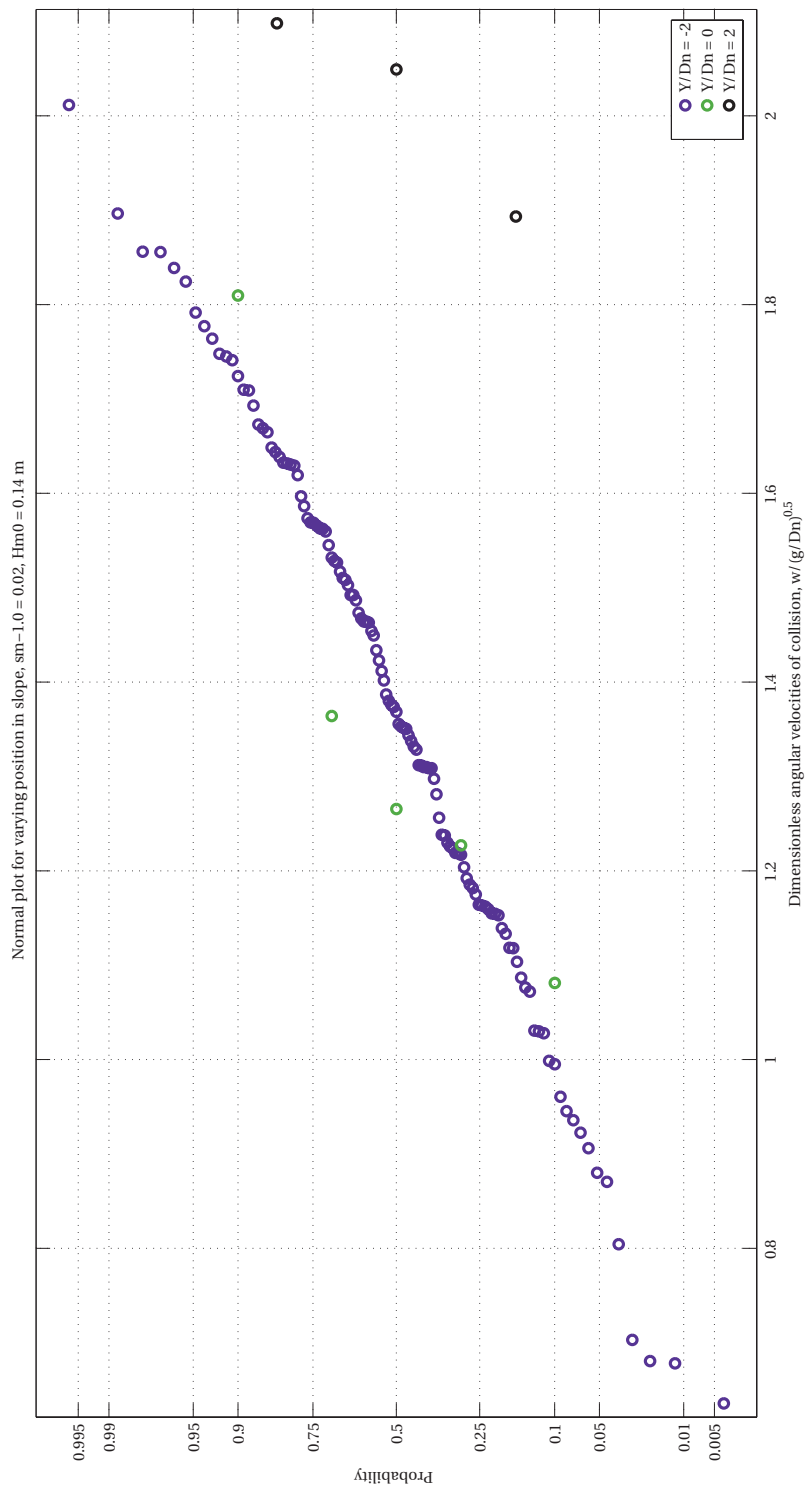


Figure H.27: Distribution angular velocities for position on slope, downward rotation.  $s_{m-1.0} = 0.02$ ,  $H_{m0} = 0.14$  m

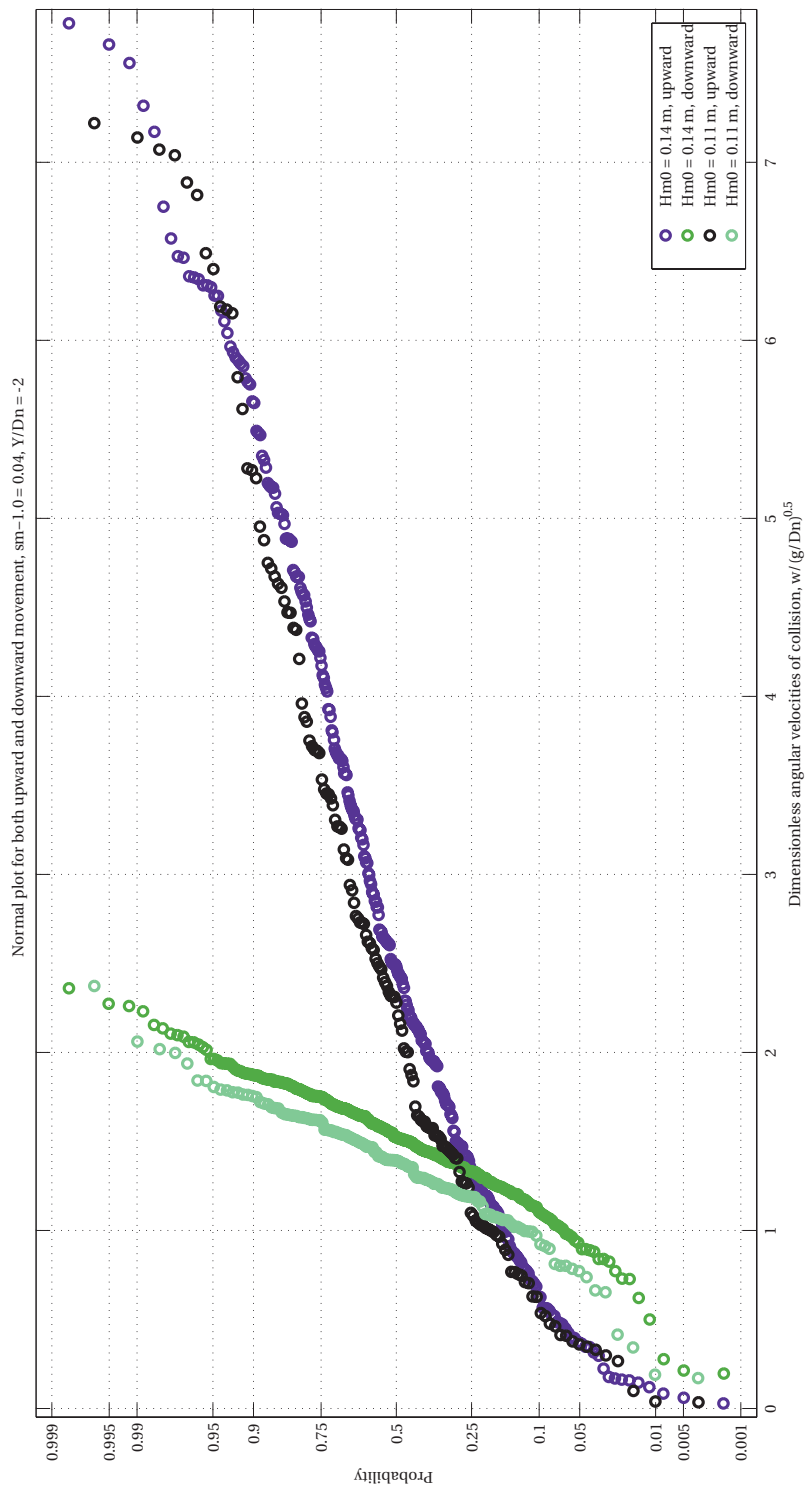


Figure H.28: Distribution plot showing differences between upward and downward velocities.  $s_{m-1.0} = 0.04, Y/D_n = -2$

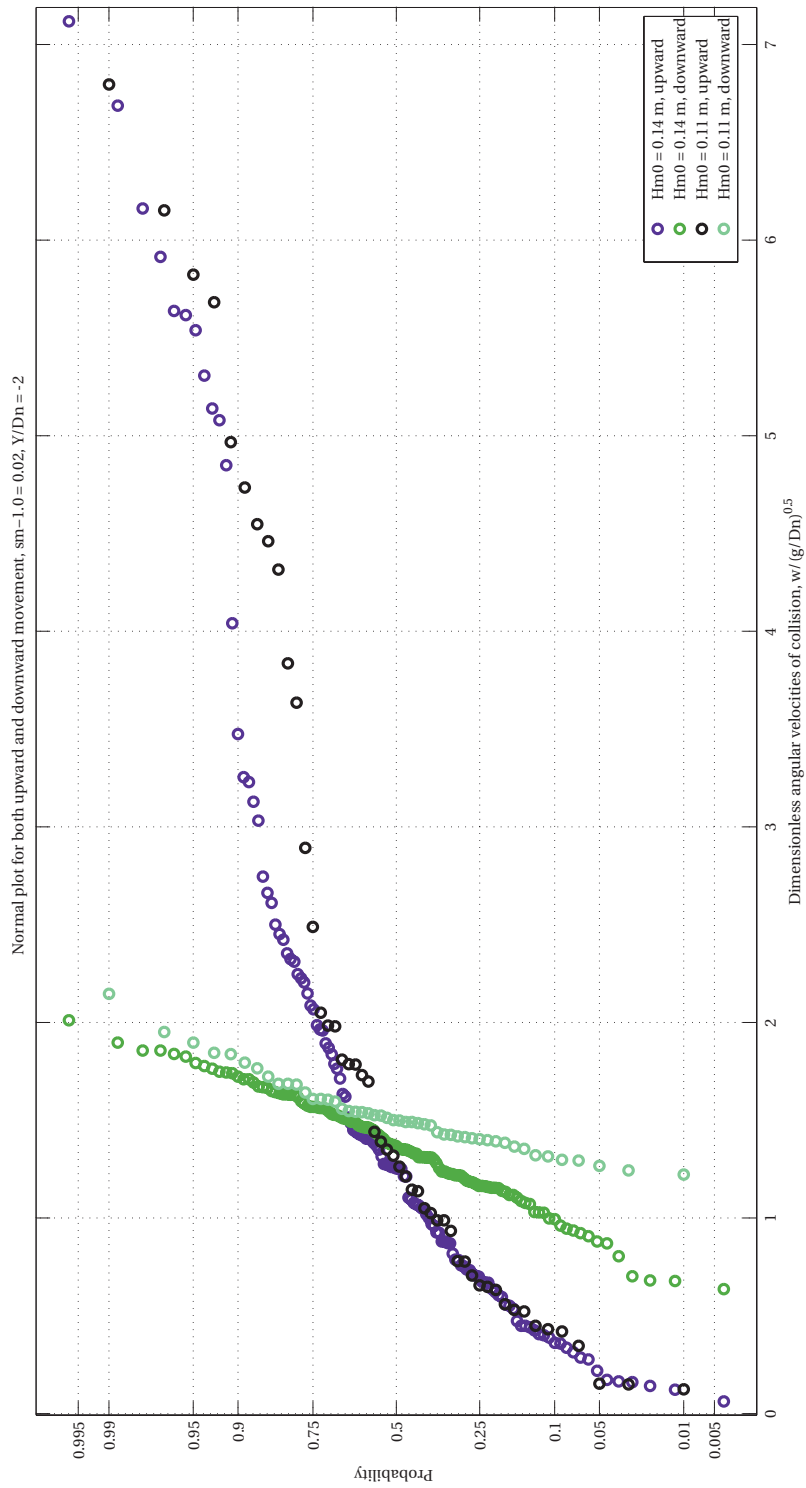


Figure H.29: Distribution plot showing differences between upward and downward velocities.  $s_{m-1.0} = 0.02, Y/D_n = -2$

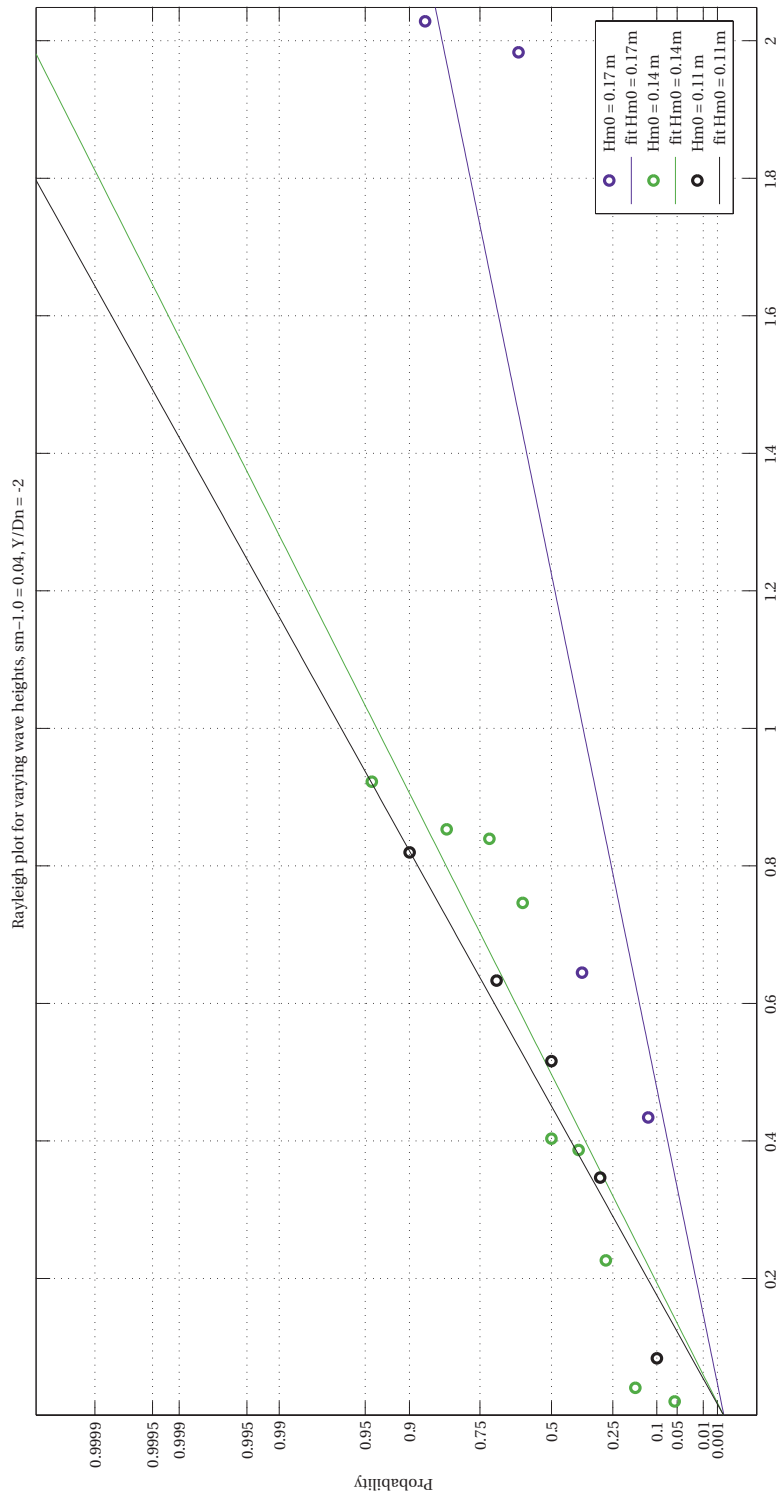


Figure H.30: Distribution angular velocities for the embedded cube, variation in significant wave height, upward rotation.  $s_{m-1.0} = 0.04$ ,  $Y/D_n = -2$

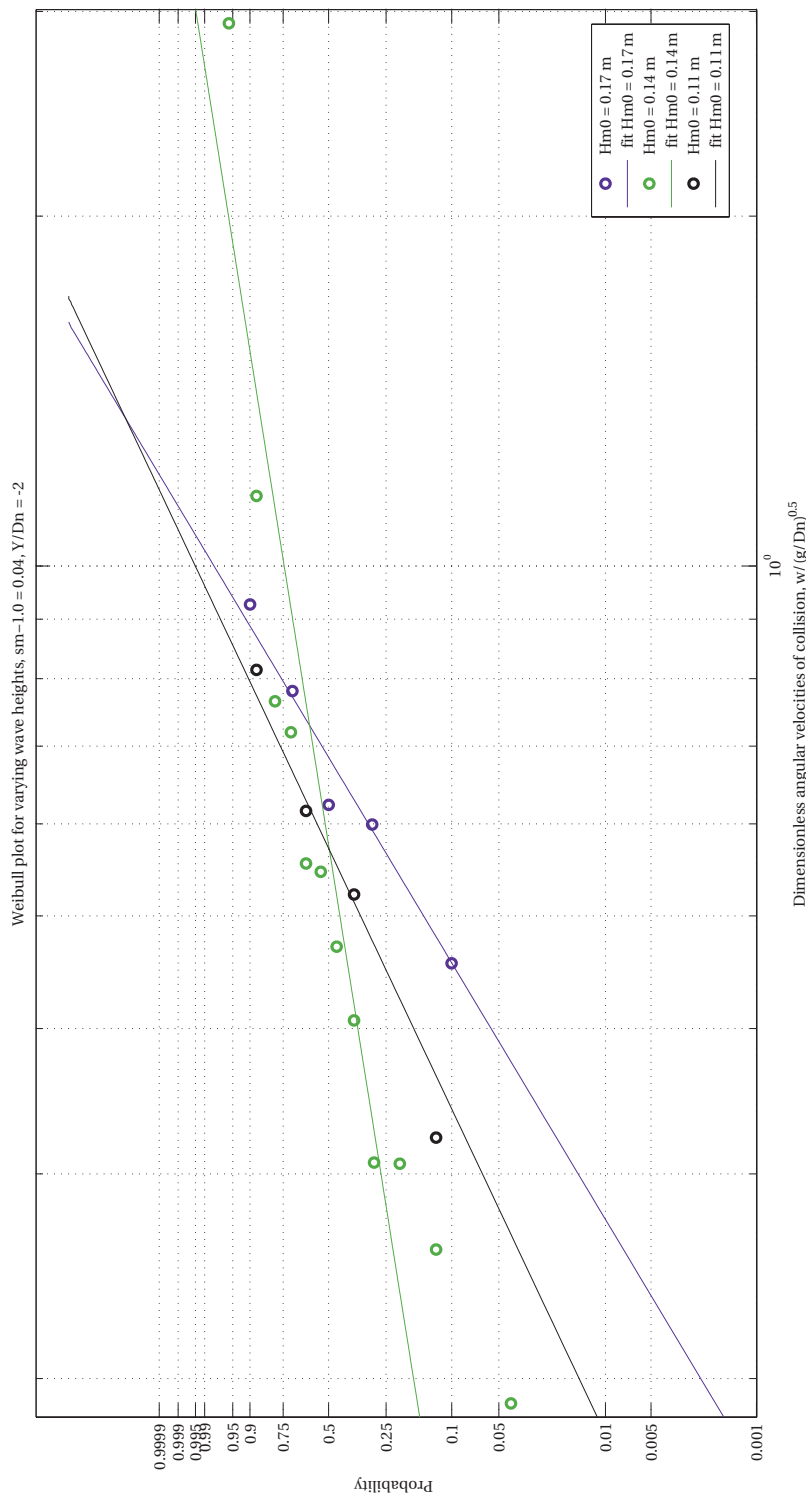


Figure H.31: Distribution angular velocities for the embedded cube, variation in significant wave height, downward rotation.  $s_{m-1.0} = 0.04$ ,  $Y/D_n = -2$

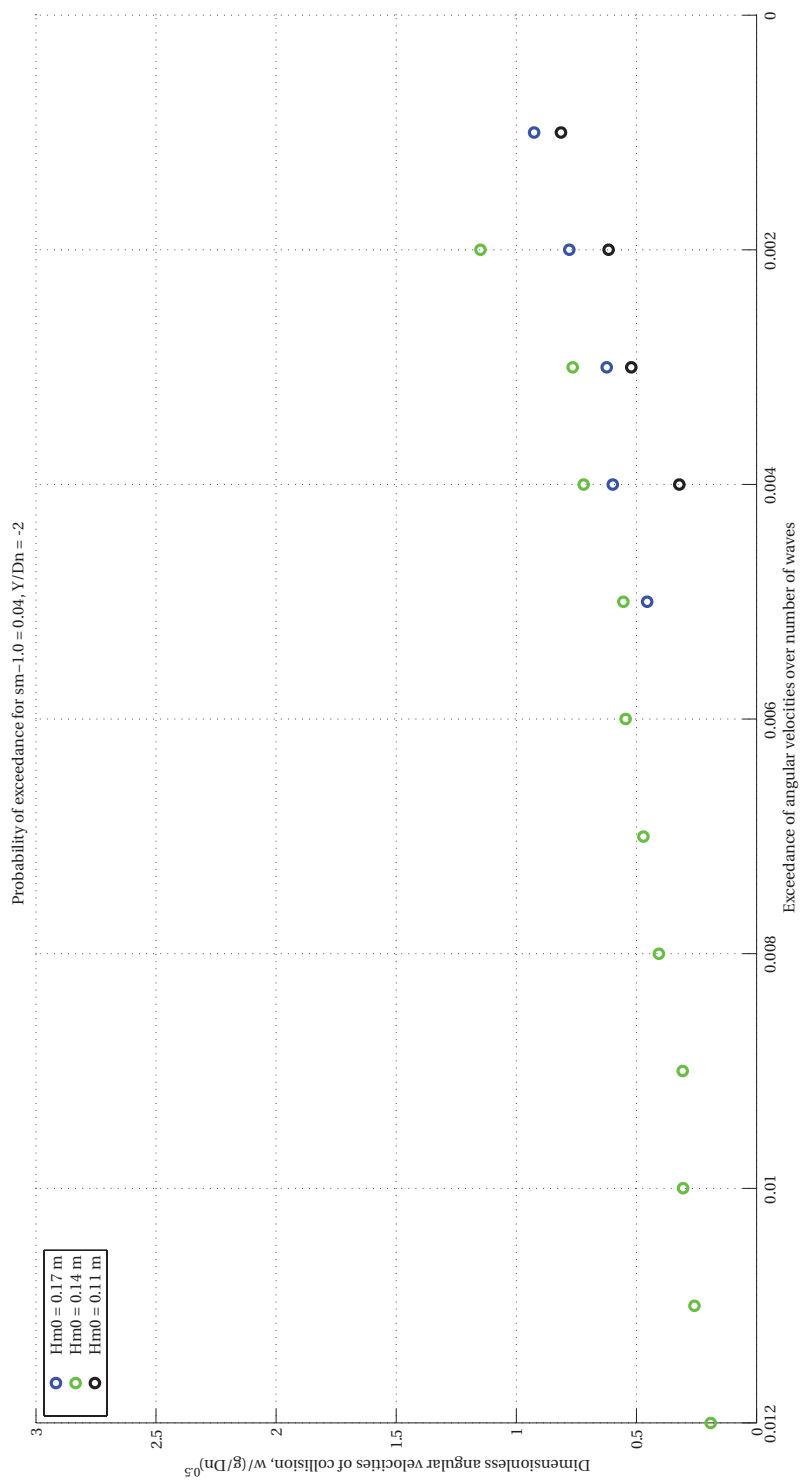


Figure H.32: Distribution angular velocities for the embedded cube, variation in significant wave height, downward rotation.  $s_m=1.0$ ,  $Y/D_n = -2$

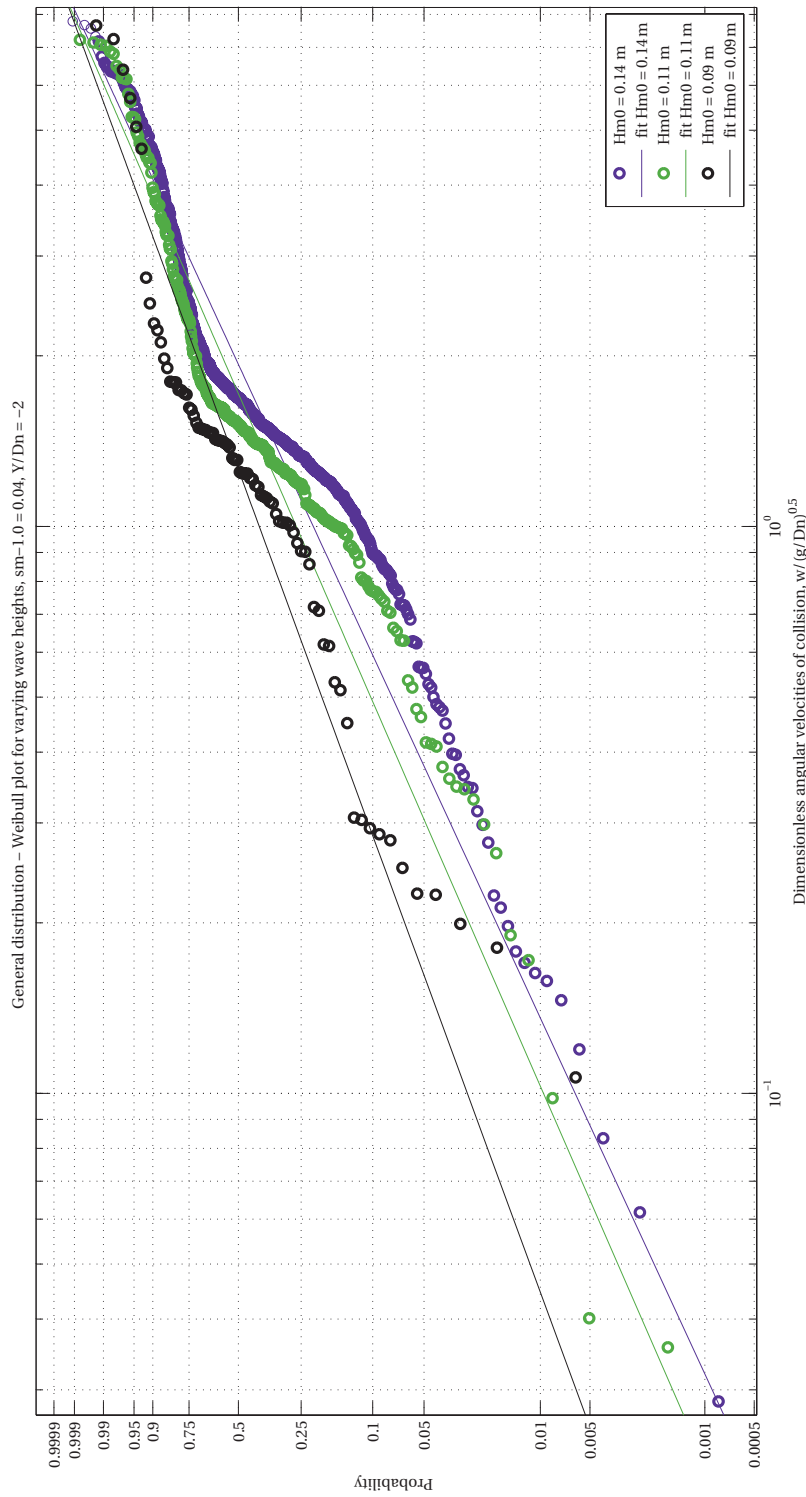


Figure H.33: General distribution - Distribution angular velocities for variation in significant wave height.  $s_{m-1.0} = 0.04$ ,  $Y/D_n = -2$

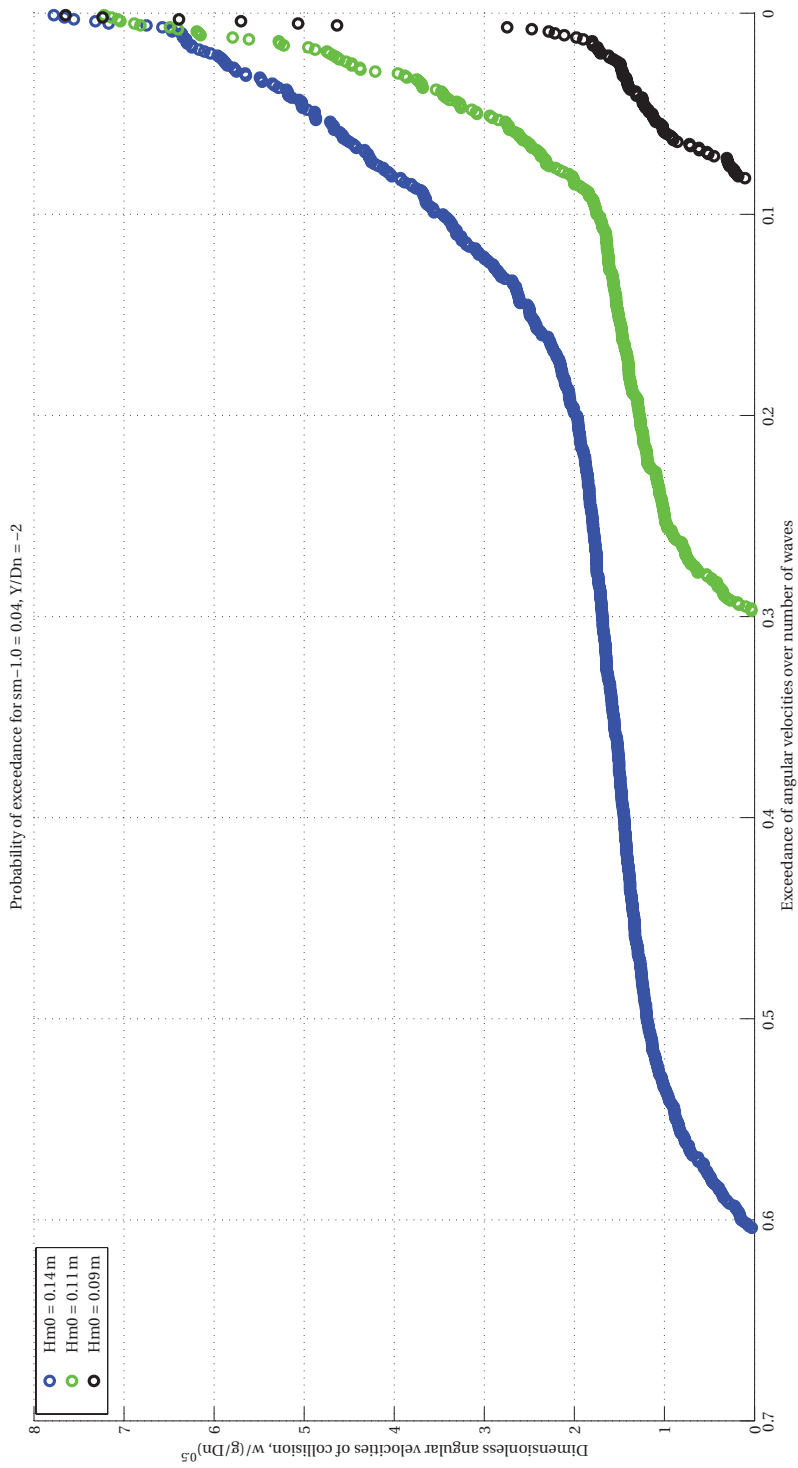


Figure H.34: General distribution - Probability of exceedance over number of waves for variation in significant wave height.  $s_{m-1.0} = 0.04, Y/D_n = -2$

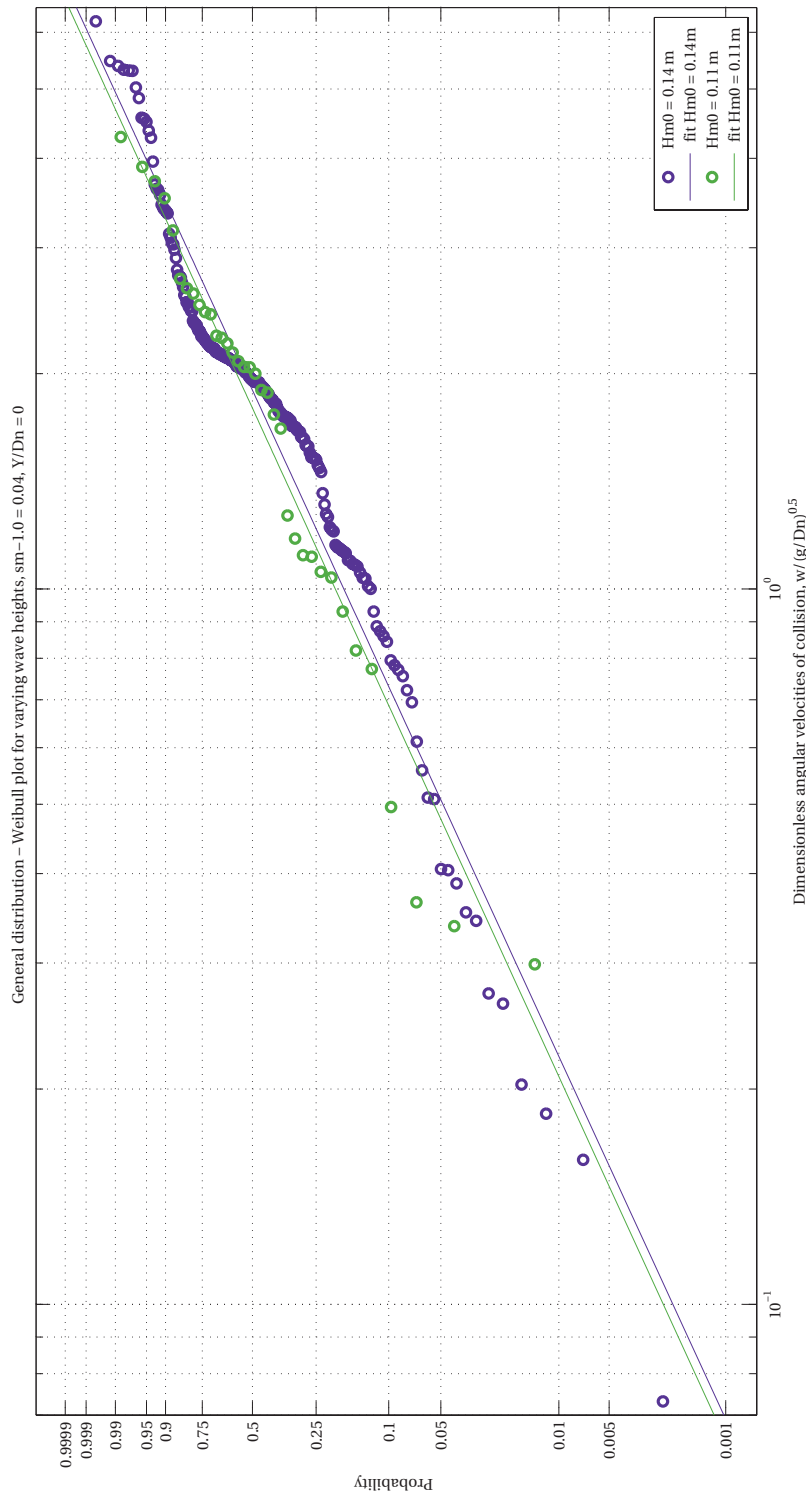


Figure H.35: General distribution - Distribution angular velocities for variation in significant wave height.  $s_{m-1.0} = 0.04$ ,  $Y/D_n = 0$

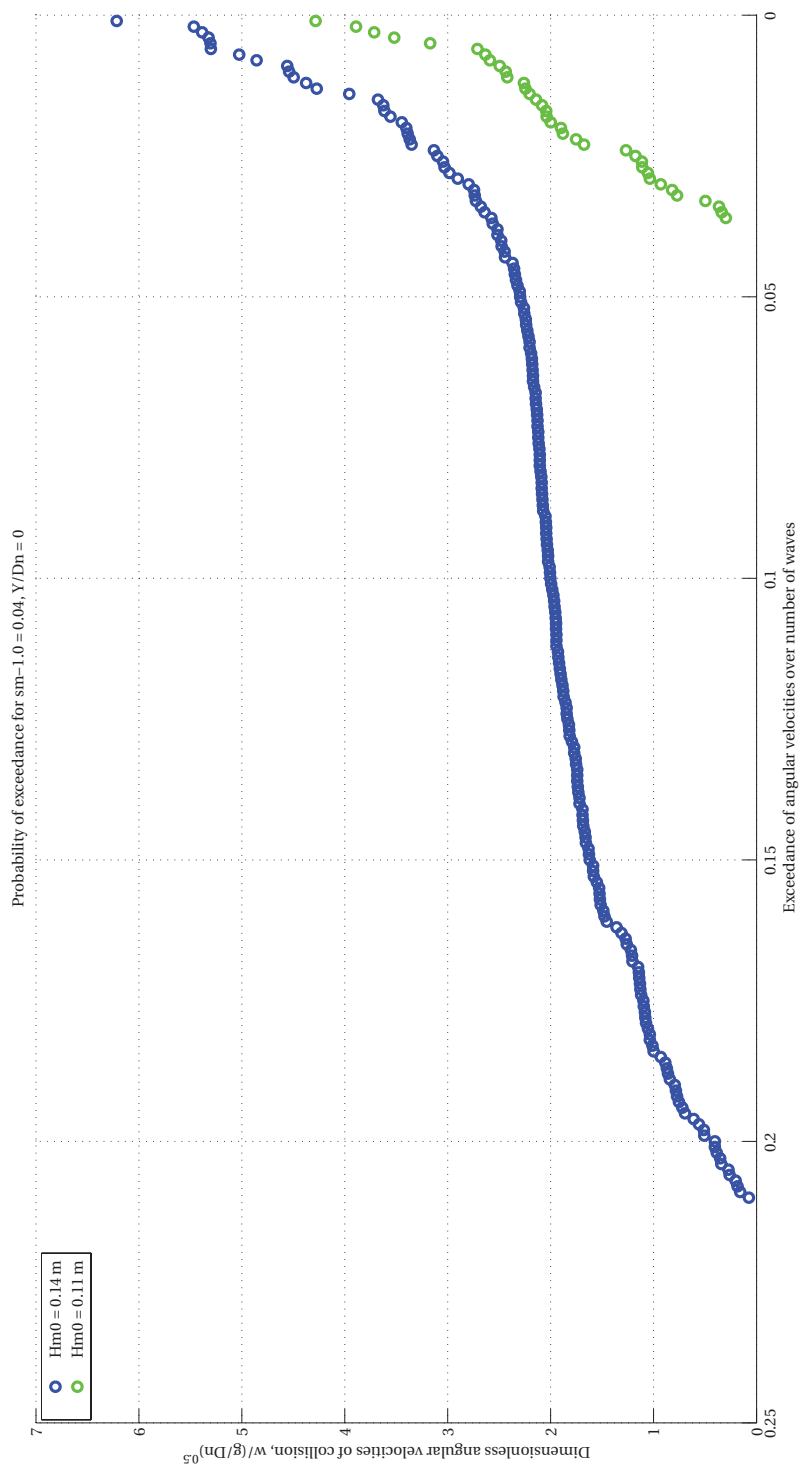


Figure H.36: General distribution - Probability of exceedance over number of waves for variation in significant wave height.  $s_{m-1.0} = 0.04, Y/D_n = 0$

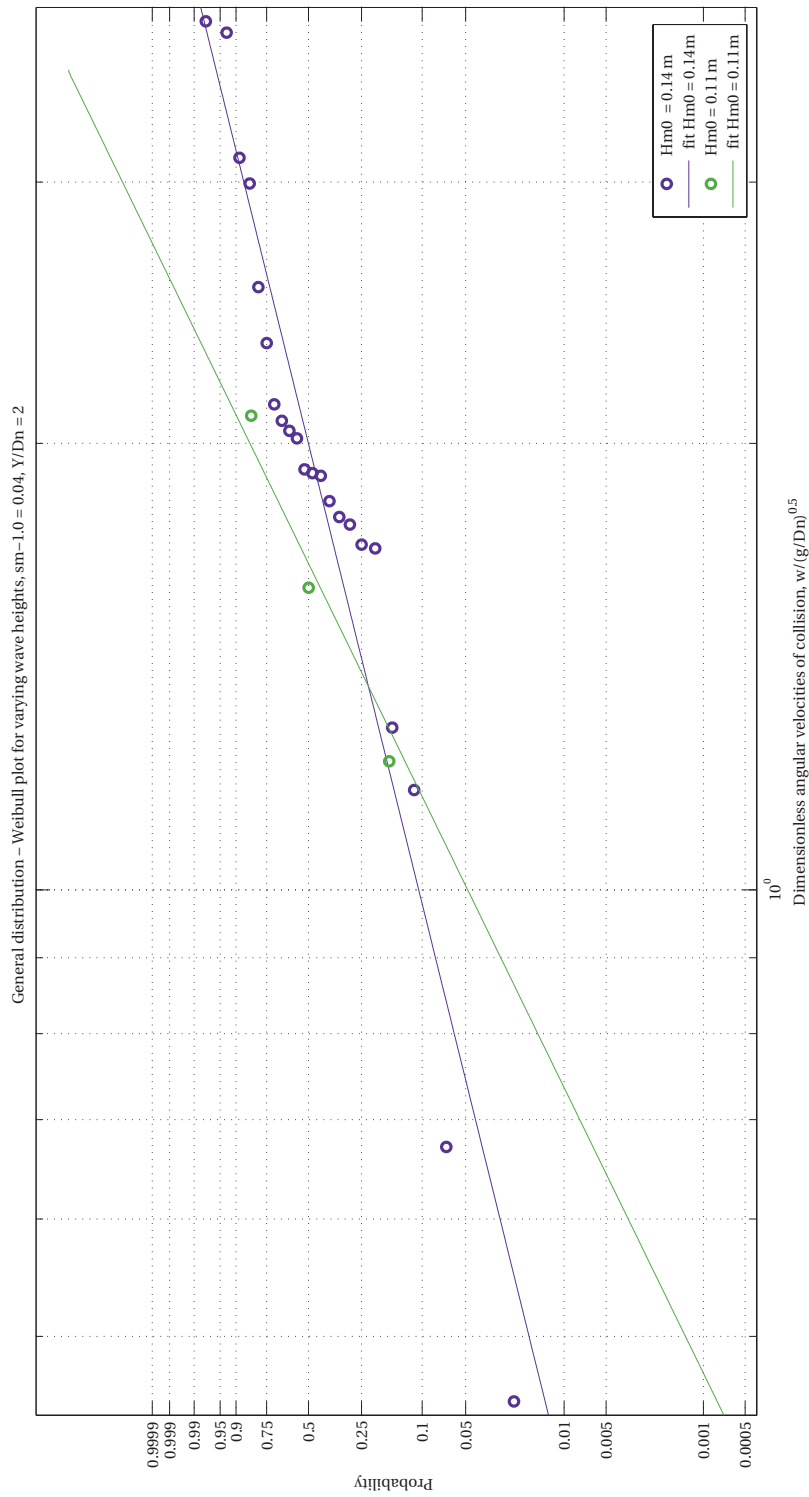


Figure H.37: General distribution - Distribution angular velocities for variation in significant wave height.  $s_{m-1.0} = 0.04$ ,  $Y/D_n = 2$

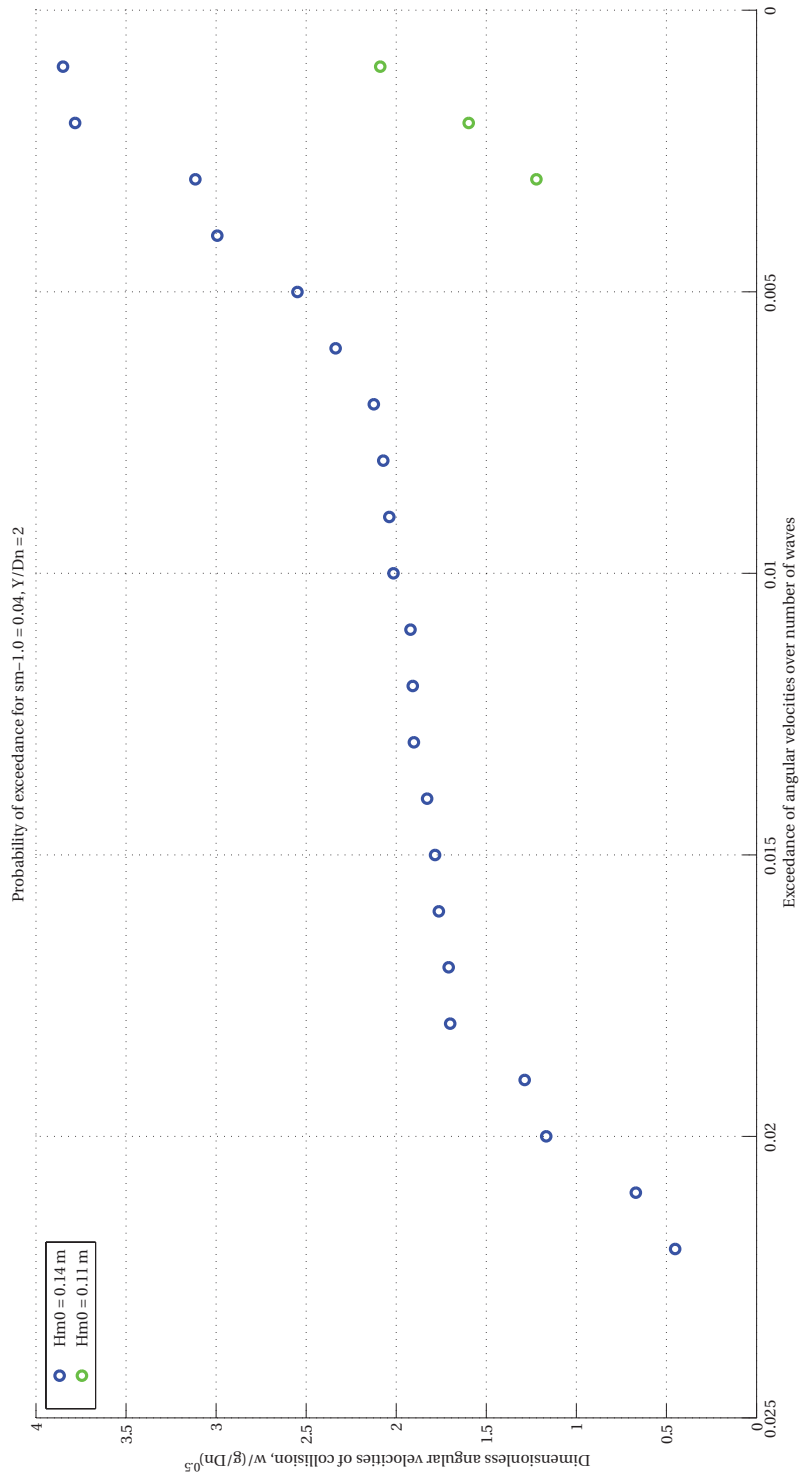


Figure H.38: General distribution - Probability of exceedance over number of waves for variation in significant wave height.  $s_{m-1.0} = 0.04, Y/D_n = 2$

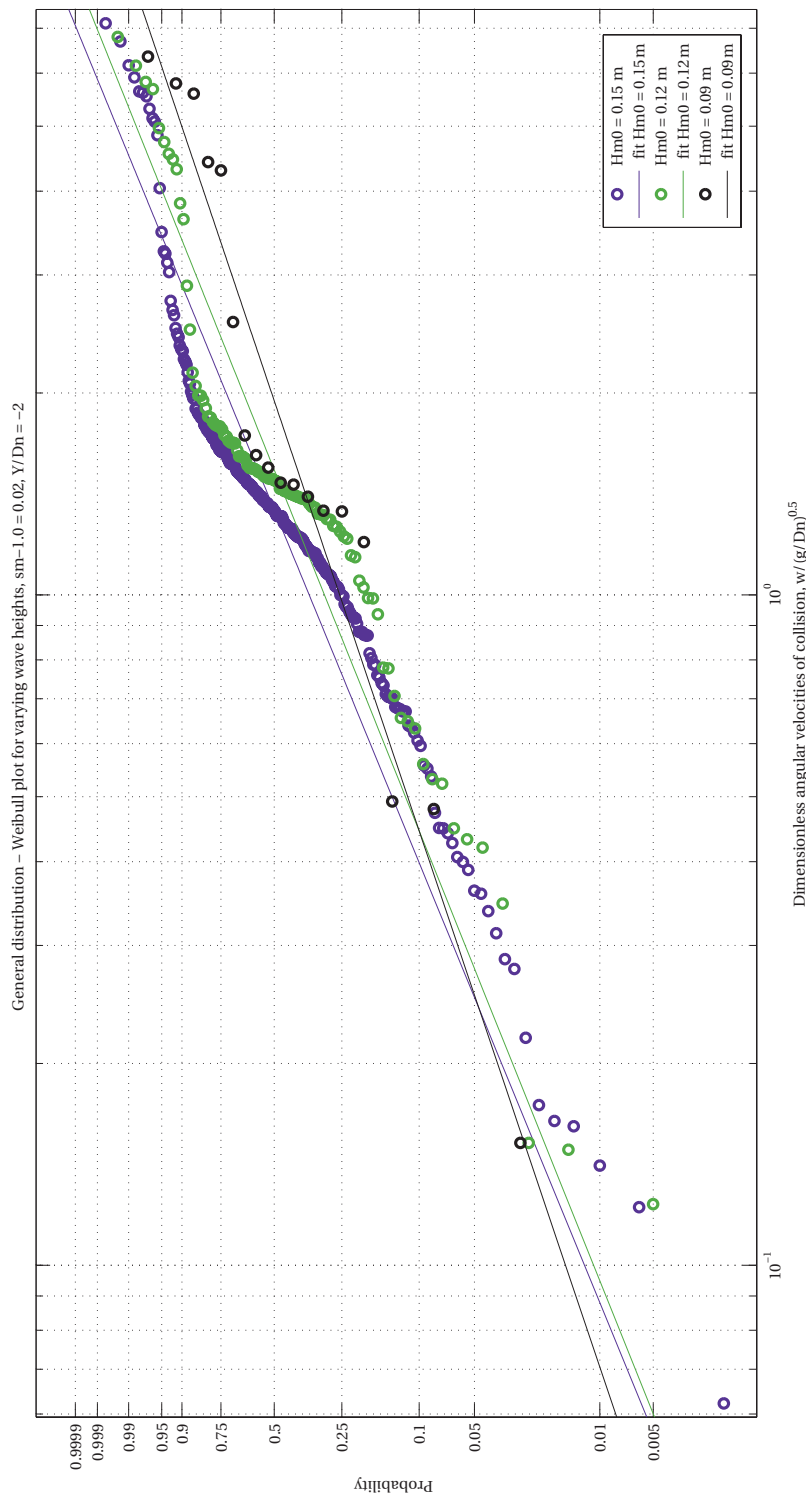


Figure H.39: General distribution - Distribution angular velocities for variation in significant wave height.  $s_{m-1.0} = 0.02$ ,  $Y/D_n = -2$

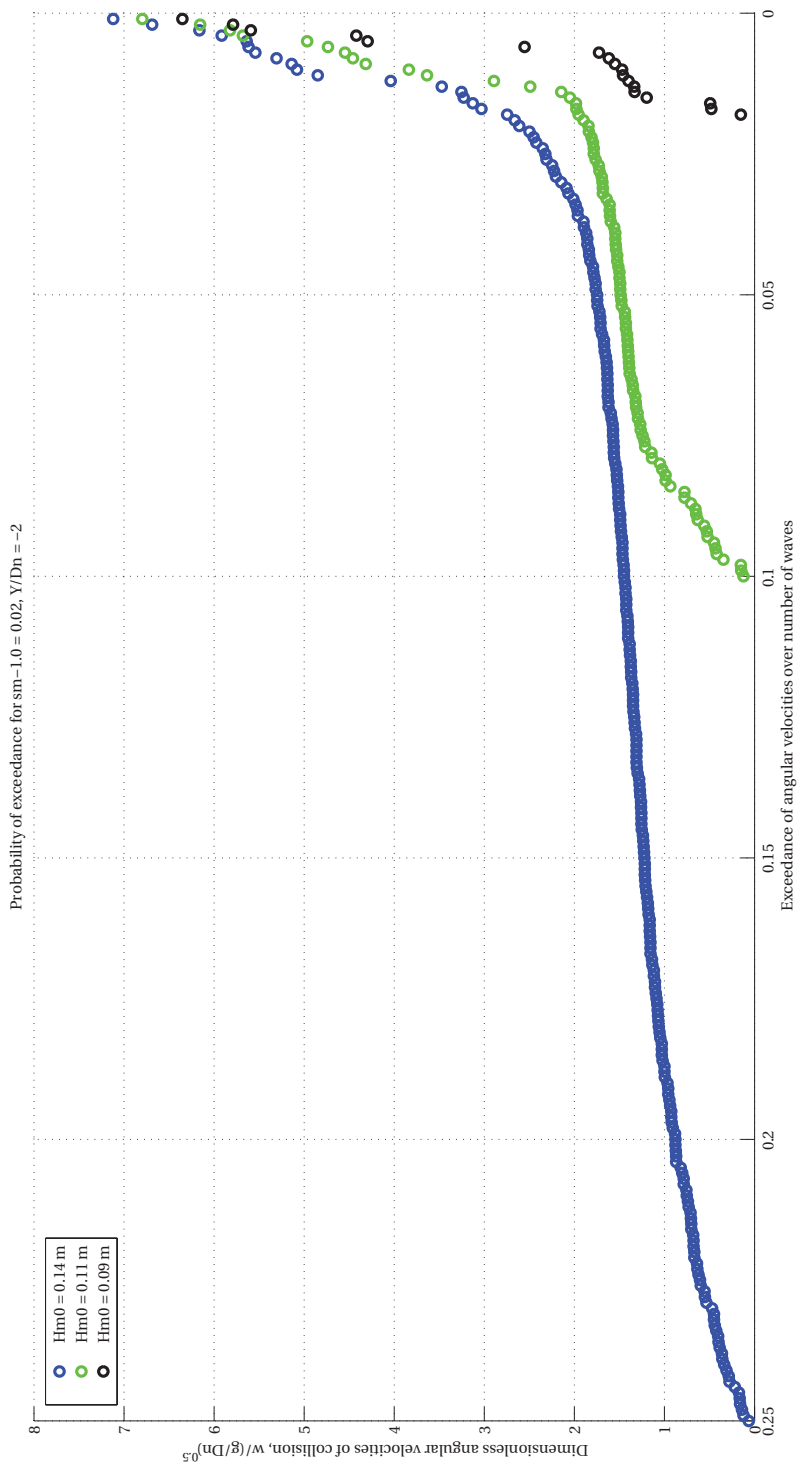


Figure H.40: General distribution - Probability of exceedance over number of waves for variation in significant wave height.  $sm-1.0 = 0.02, Y/Dn = -2$

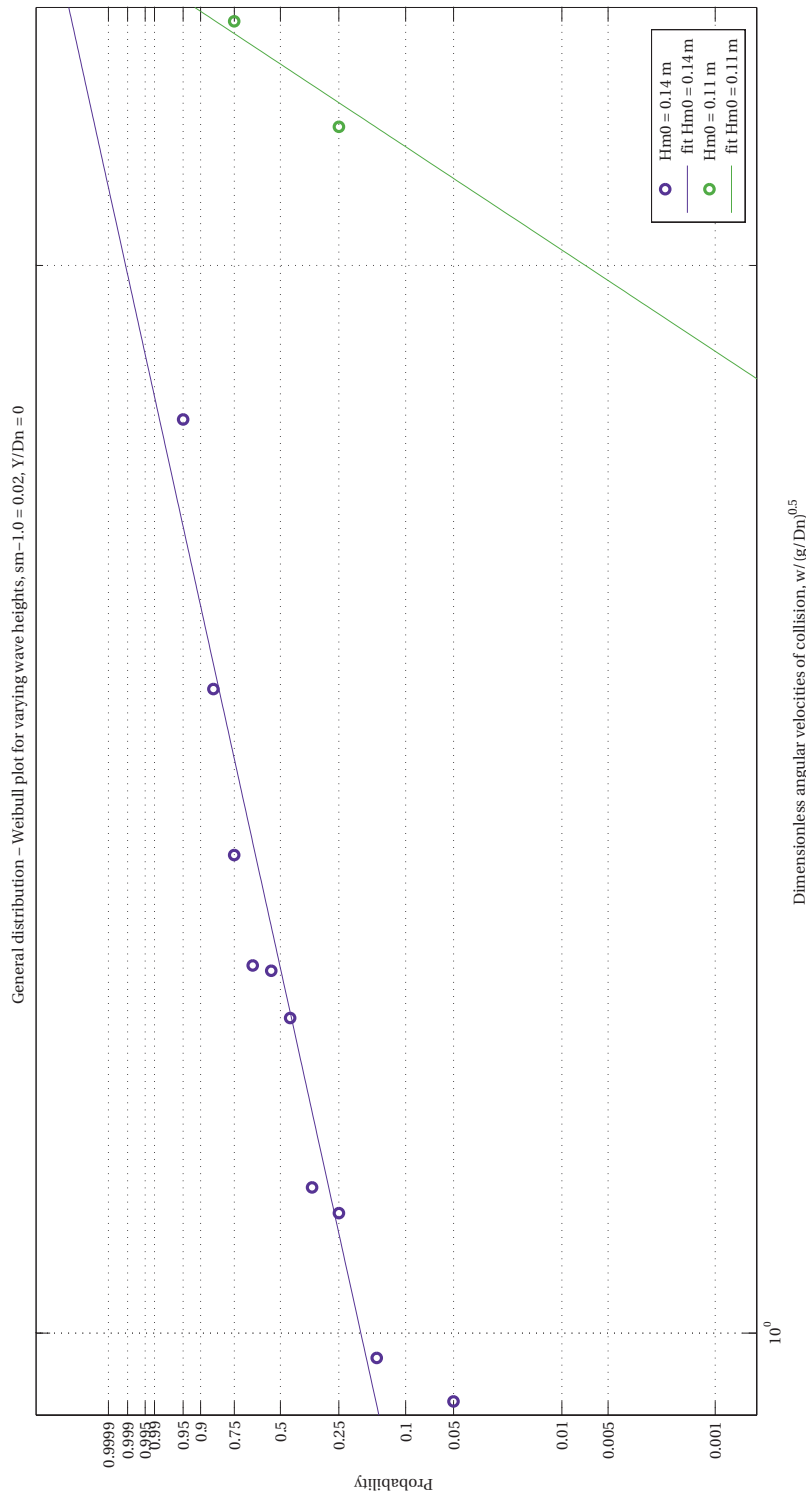


Figure H.41: General distribution - Distribution angular velocities for variation in significant wave height.  $s_{m-1.0} = 0.02$ ,  $Y/D_n = 0$

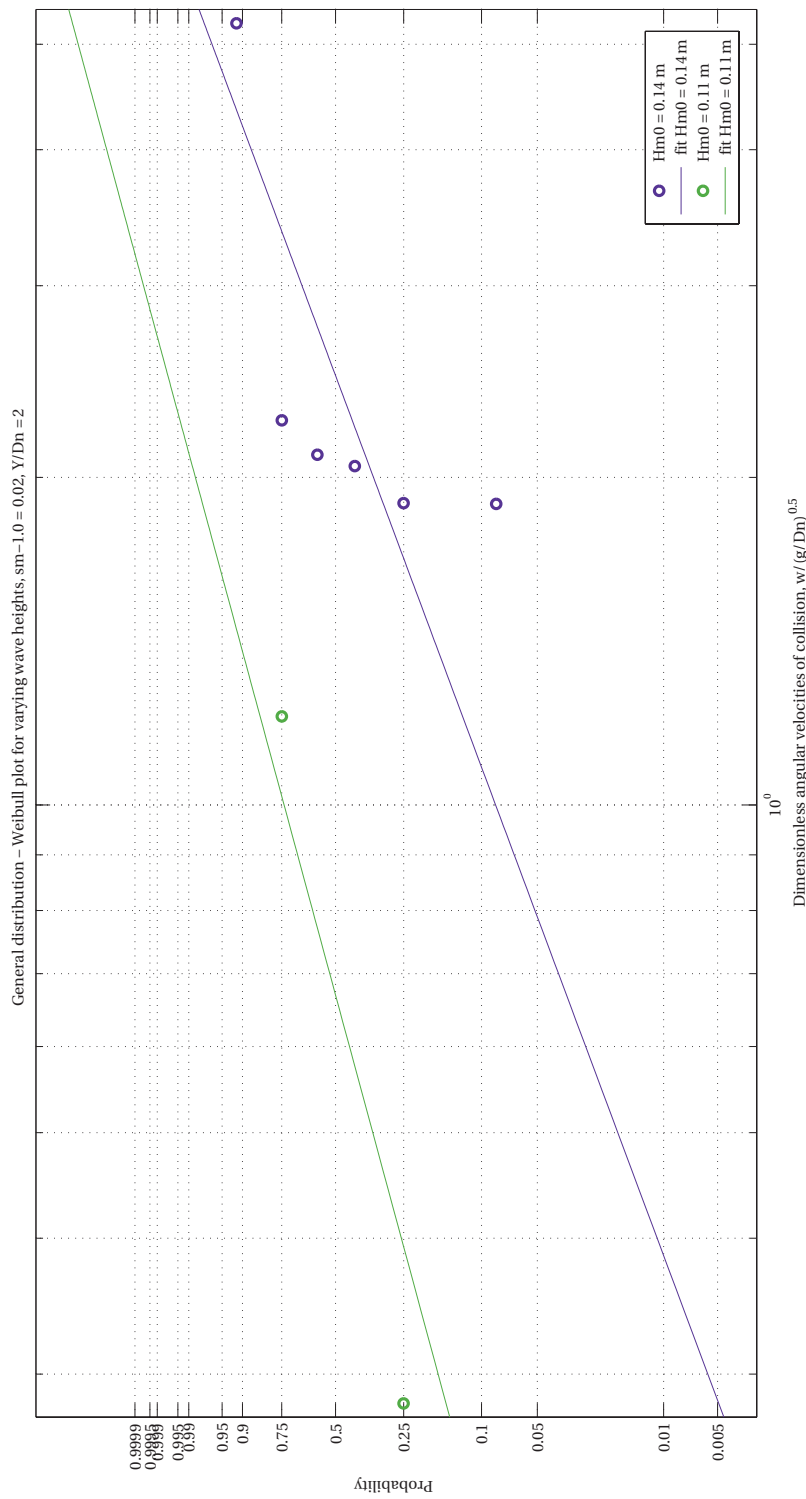


Figure H.42: General distribution - Distribution angular velocities for variation in significant wave height.  $s_{m-1.0} = 0.02$ ,  $Y/D_n = 2$

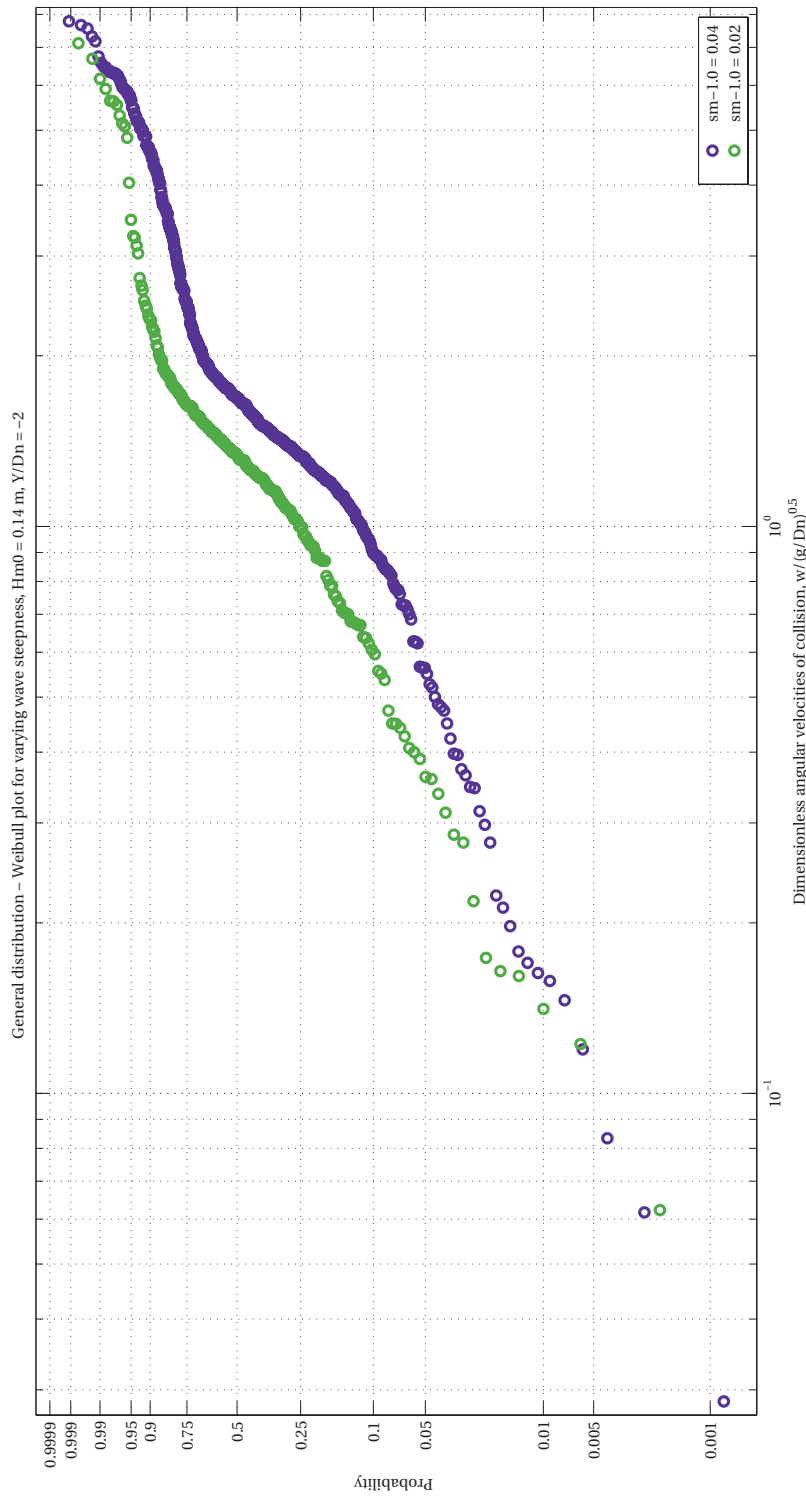


Figure H.43: General distribution - Distribution angular velocities for variation in wave steepness.  $H_{m0} = 0.14$  m,  $Y/D_n = -2$

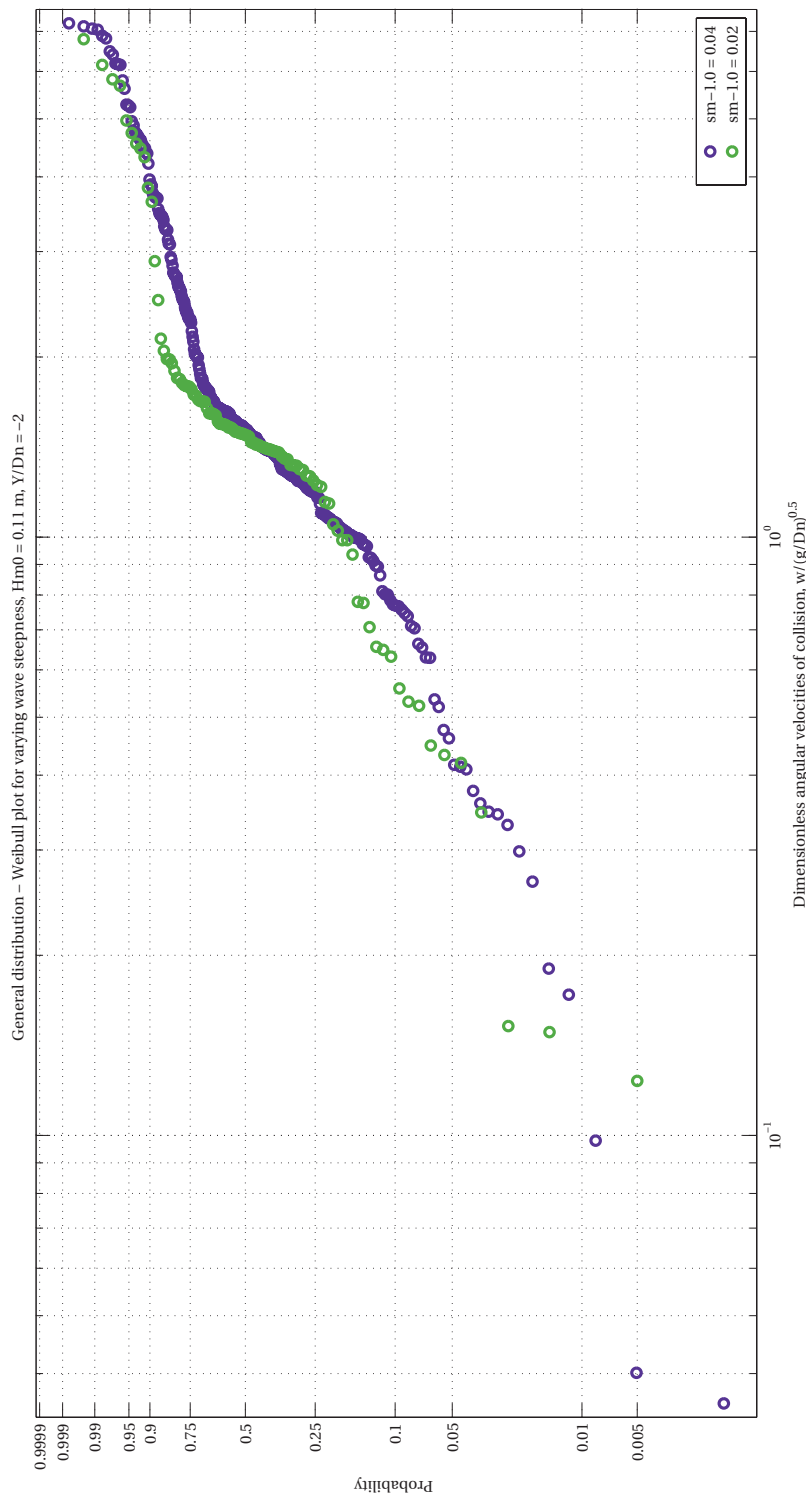


Figure H.44: General distribution - Distribution angular velocities for variation in wave steepness.  $H_{m0} = 0.11$  m,  $Y/D_n = -2$

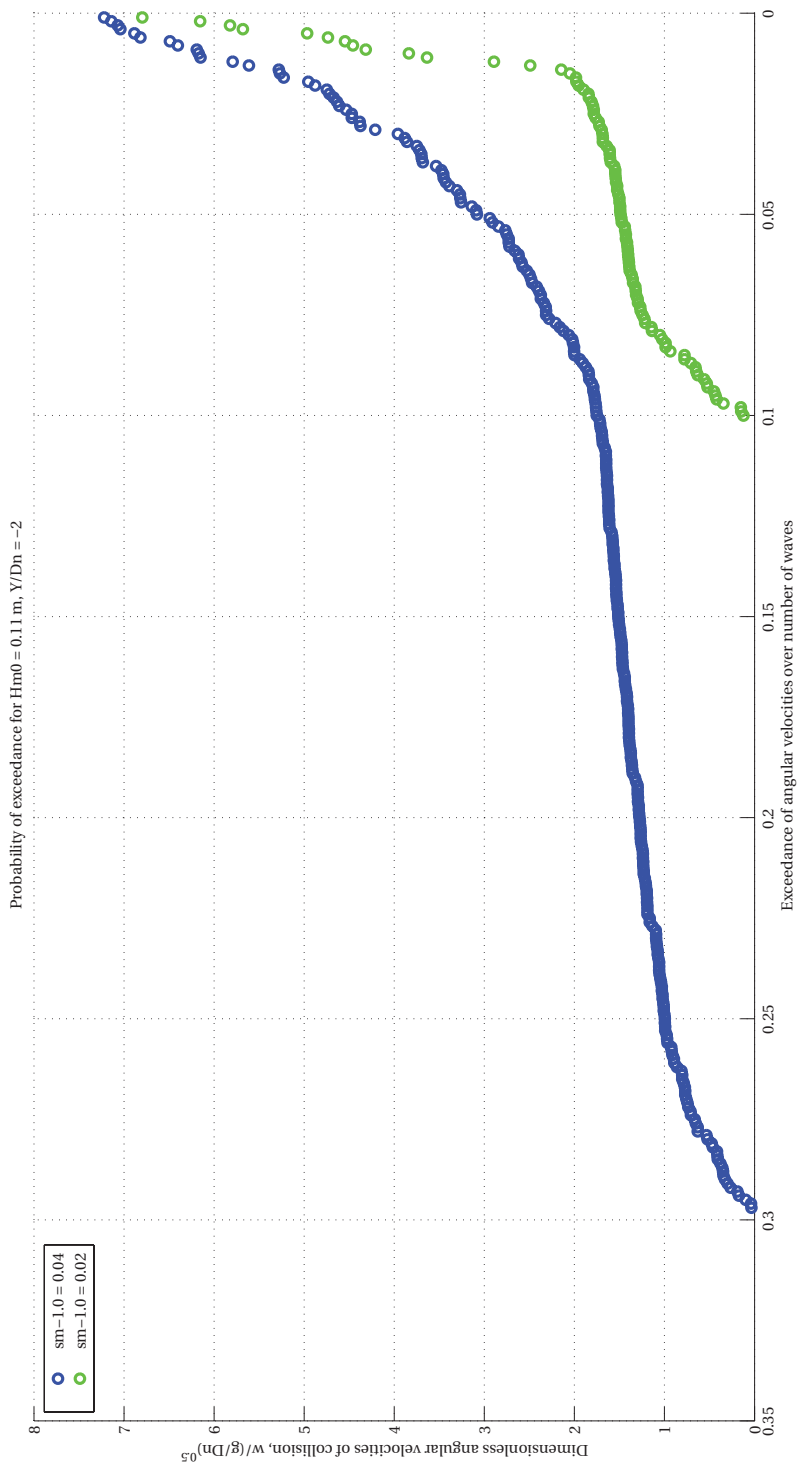


Figure H.45: General distribution - Probability of exceedance over number of waves for variation in wave steepness.  $H_{m0} = 0.11$  m,  $Y/D_n = -2$

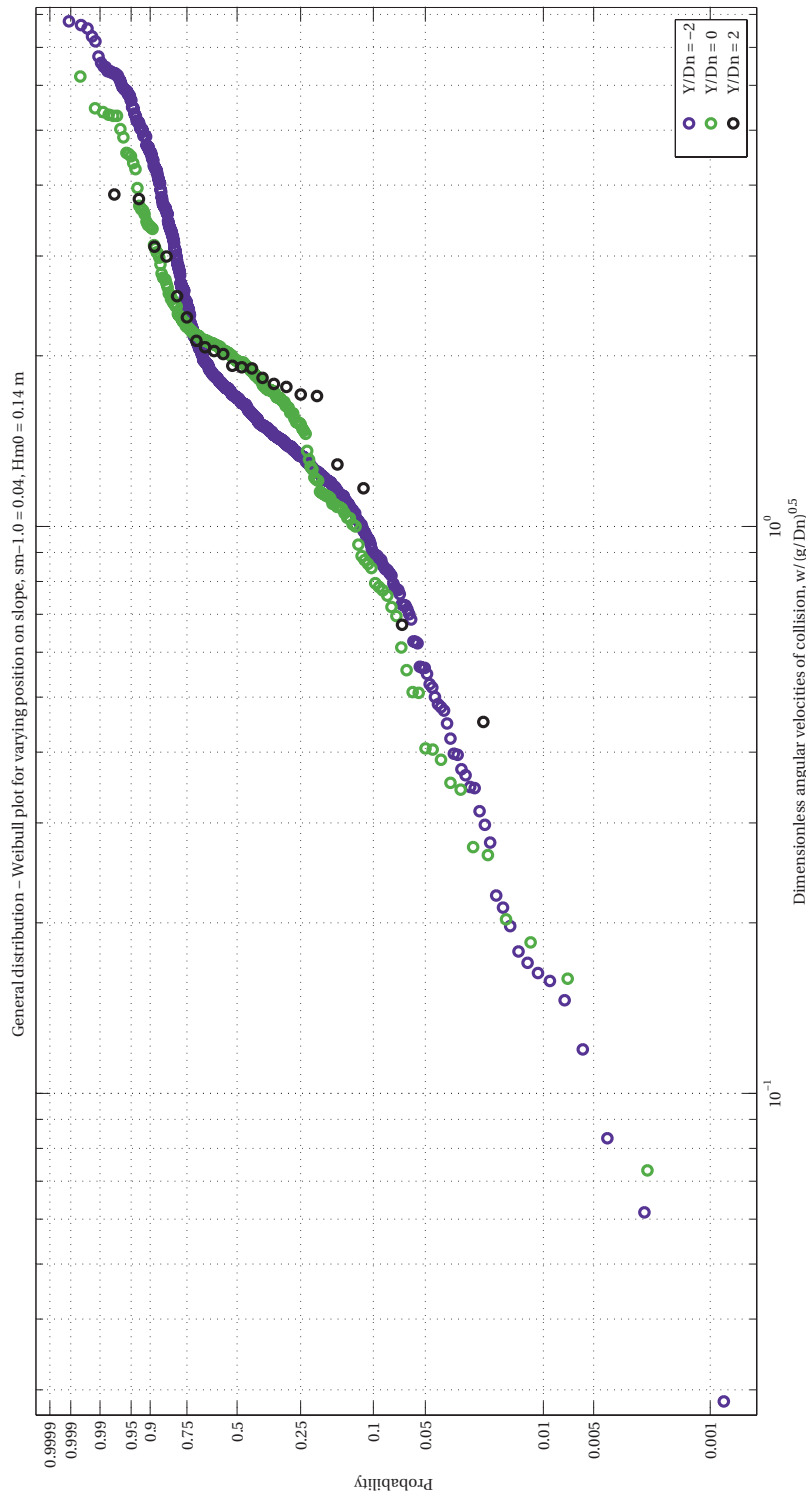


Figure H.46: General distribution - Distribution angular velocities for position on slope.  $s_{m-1.0} = 0.04$ ,  $H_{m0} = 0.14$  m

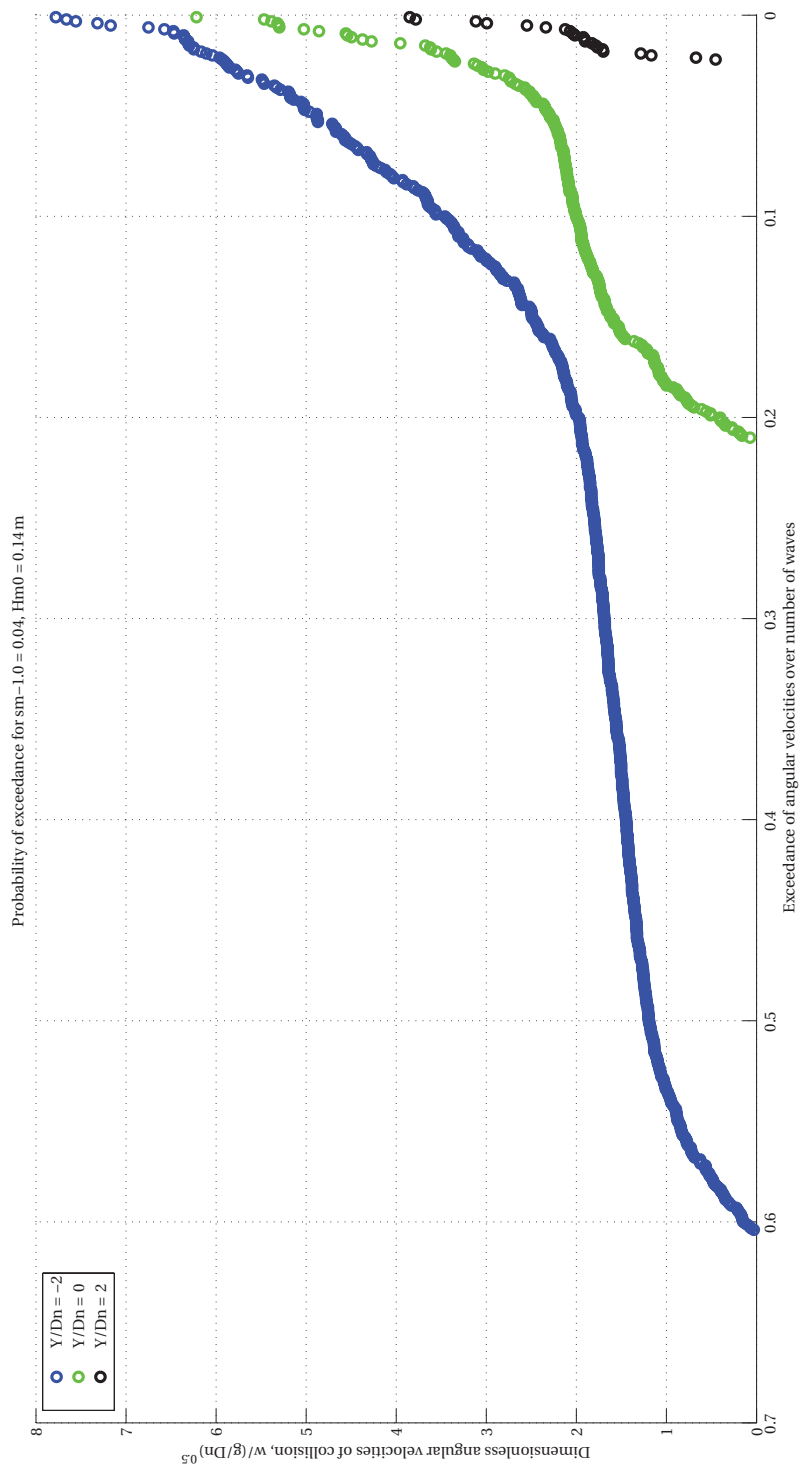


Figure H.47: General distribution - Probability of exceedance over number of waves for position on slope.  $s_{m-1.0} = 0.04$ ,  $H_{m0} = 0.14m$

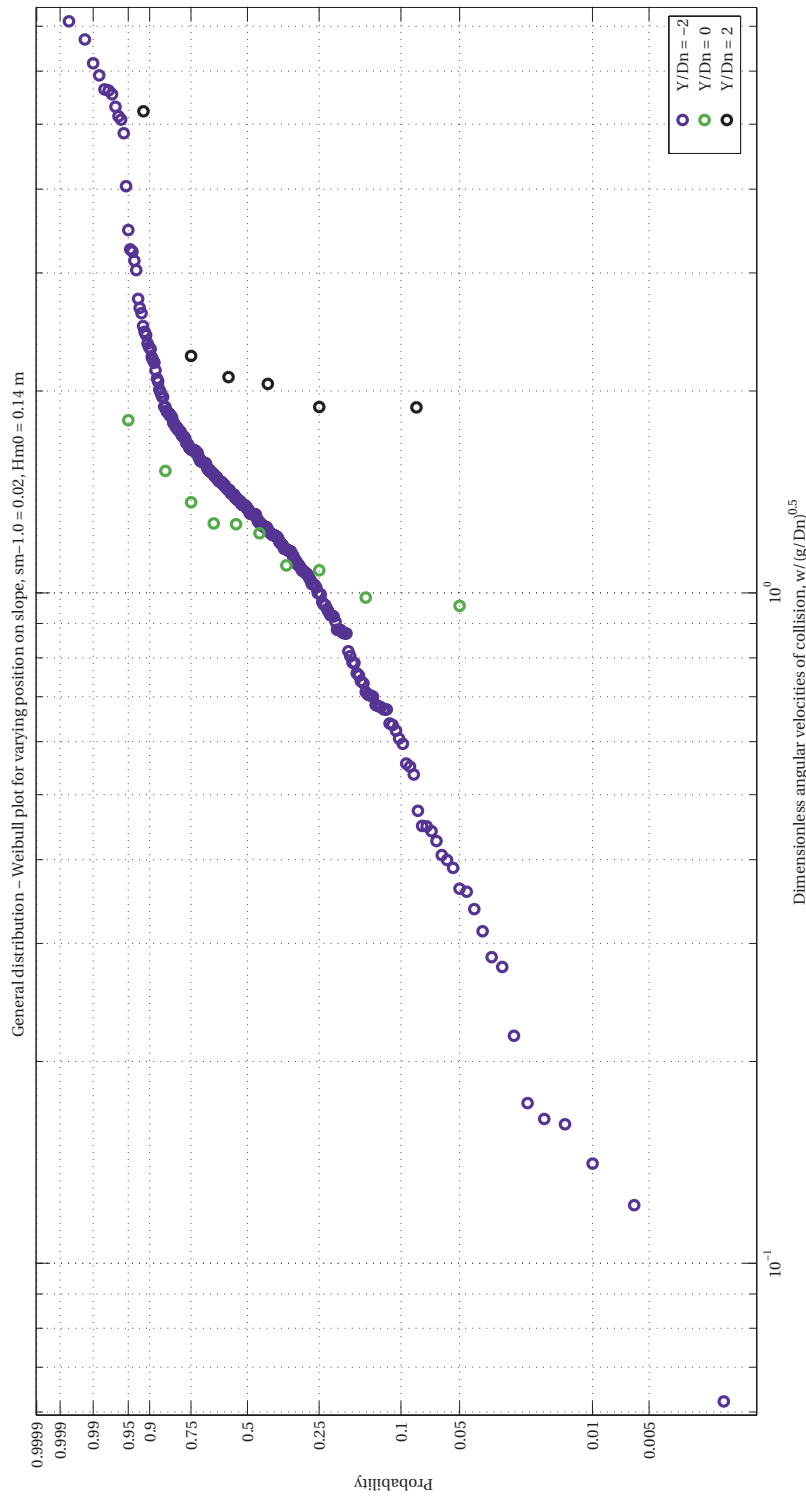


Figure H.48: General distribution - Distribution angular velocities for position on slope.  $s_{m-1.0} = 0.02$ ,  $H_{m0} = 0.14$  m

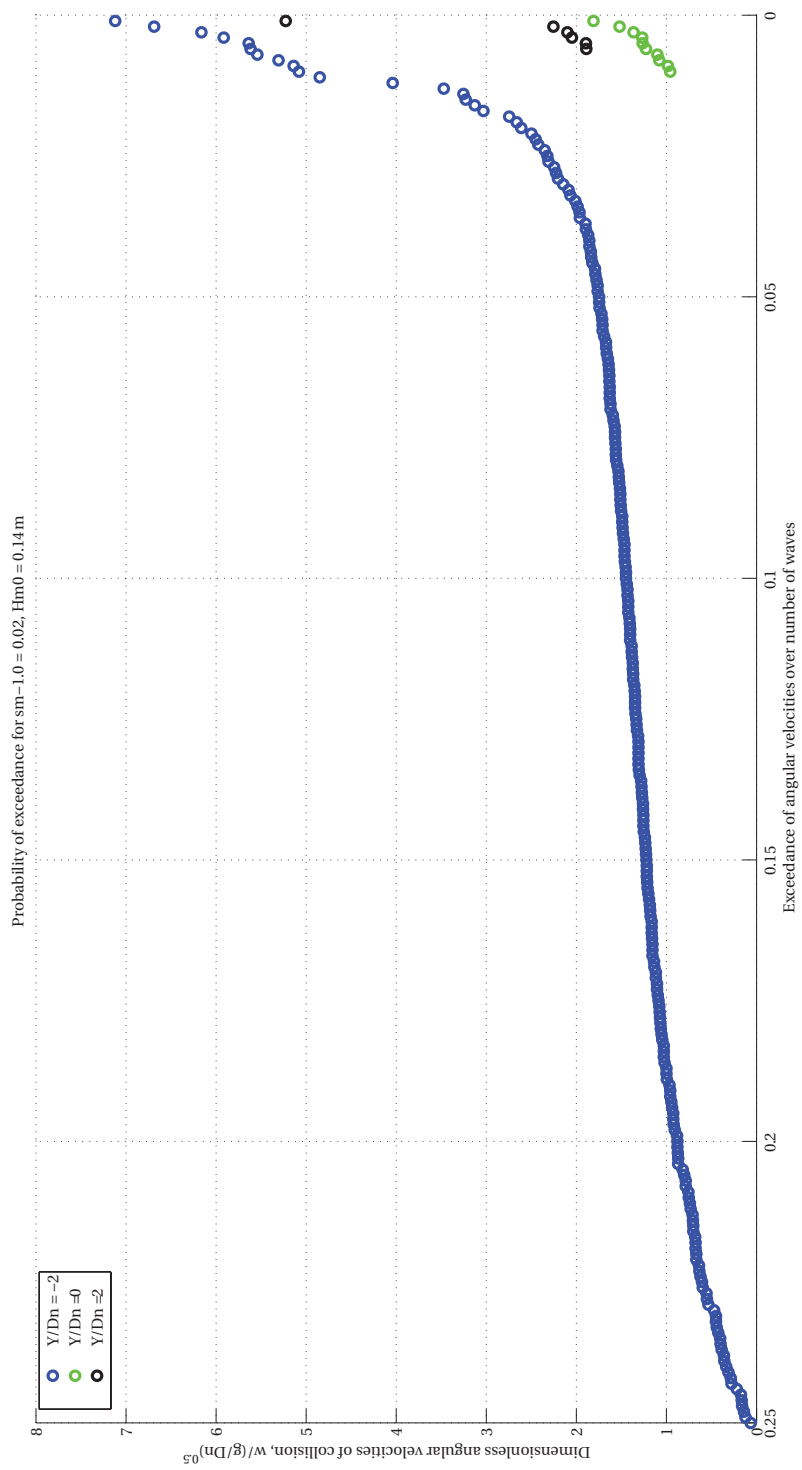


Figure H.49: General distribution - Probability of exceedance over number of waves for position on slope.  $s_{m-1.0} = 0.02$ ,  $H_{m0} = 0.14\text{ m}$

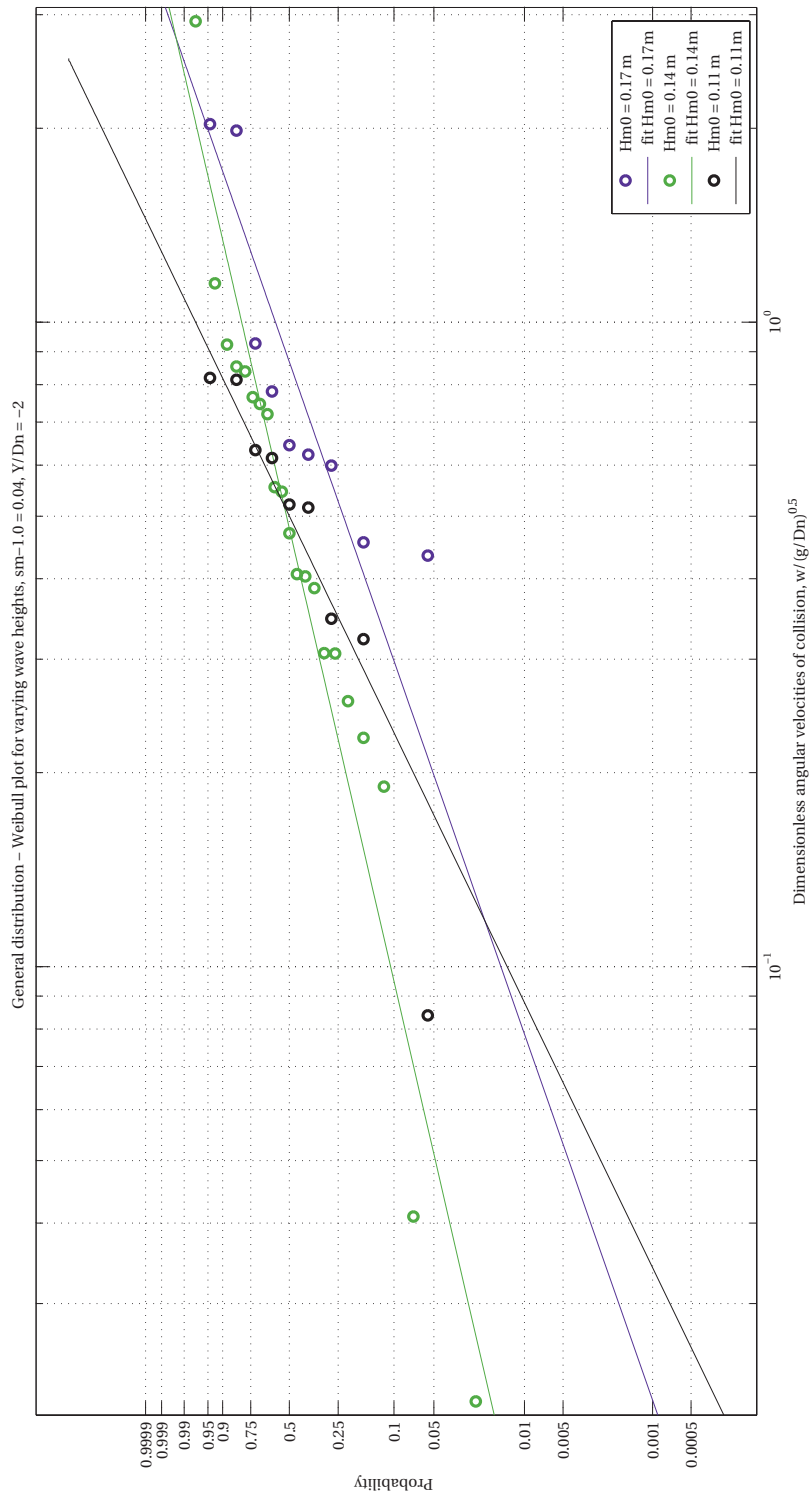


Figure H.50: General distribution - Distribution angular velocities for the embedded cube, variation in significant wave height.  $s_{m-1.0} = 0.04$ ,  $Y/D_n = -2$

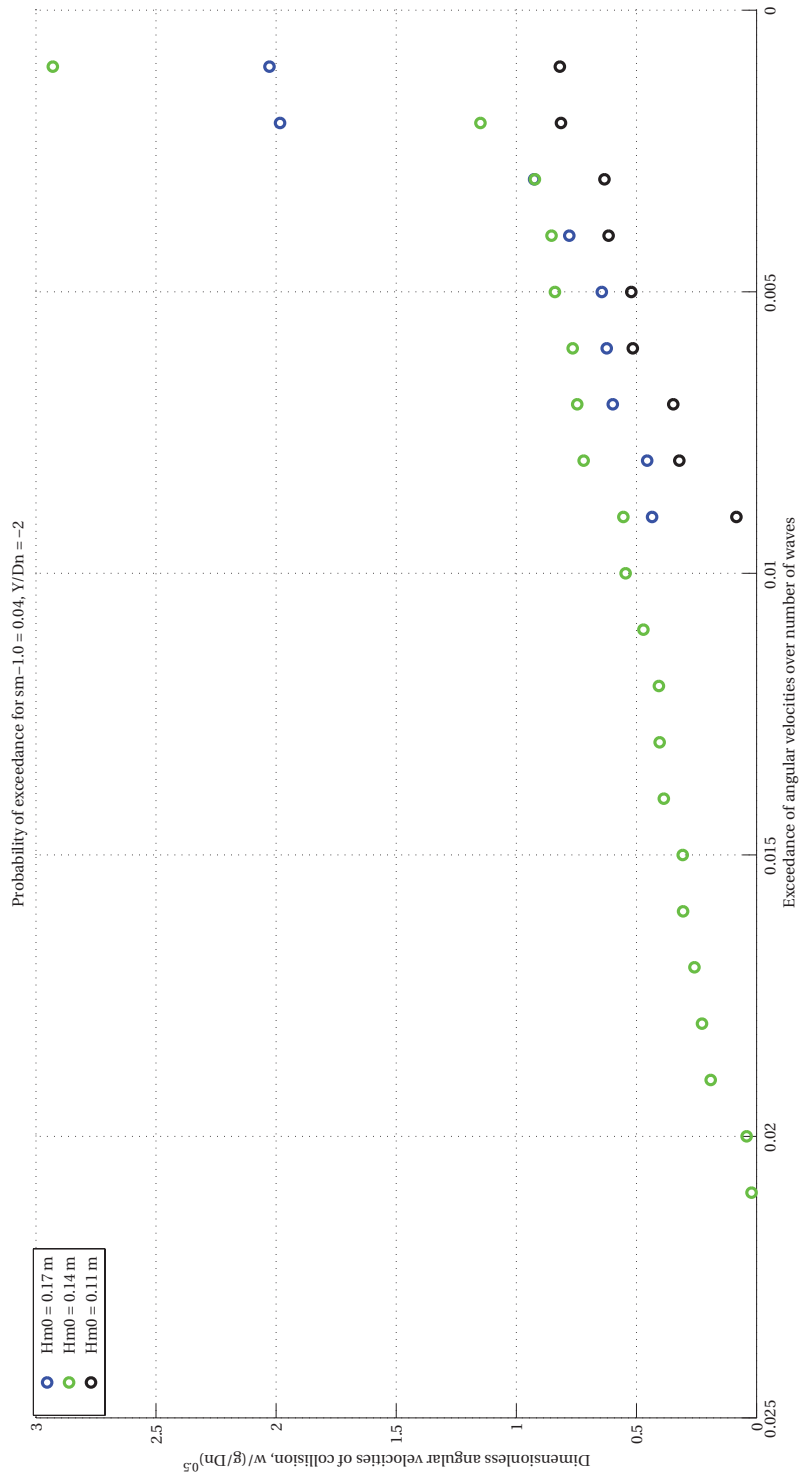


Figure H.51: General distribution - Probability of exceedance over number of waves for the embedded cube, variation in significant wave height.  $sm-1.0 = 0.04, Y/Dn = -2$



# HEXAPOD

## I.1. DESIGN

Breakage of Xblocs and Accropodes are observed in practice. These type of armour unit are often applied to new construction projects. It is therefore interesting to test the behaviour under wave attack of these types of blocks.

It is chosen to design a type of block that represents the movements of both types of blocks. A simple Hexapod is developed, consisting of a cubical core with 6 similar cubes attached to it. In Figure I.1 the Accropode and Xbloc are compared to the newly designed cube. Since the Hexapod consists of a more or less same weight distribution, the moments of inertia are more or less the same. The Hexapod also has approximately the same shape. With a similar placing pattern, similar movements are expected. It is also expected that the order of magnitude of impacts is equal due to its weight distribution. Thus the Hexapod is expected to have sufficient similarity in physical behaviour under wave attack. In addition, the design allows an easy placement of measurement equipment due to its concave squared core. Furthermore, the Hexapod can be disassembled into three parts as shown in Figure I.2. This makes it convenient to insert weights and measurement equipment according to the user's needs. A modification in the layout of the Hexapod might be due to the need of a wired output. For this purpose, a water tight exit of the cable therefore needs to be designed.

Possible differences with in performance of the Hexapod in comparison with Xbloc and Accropodes are the degree of interlocking, the maximum tensile strength and the convenience in concrete casting. It is expected that the Hexapod is inferior to the other armour units because of its simple shape. These aspects are however less relevant in this research, since in this research the way of moving and its magnitude are research. Therefore, the mentioned differences play a less important role.

It is chosen to print the Hexapod in 3D, using PLA (polylactide) as print material. An advantage is the relatively cheap and fast production. A disadvantage is the brittleness and softness of the material.

## I.2. BEHAVIOUR OF HEXAPODS UNDER WAVE ATTACK

The expectations on the behaviour of Hexapods are verified with a theoretical analysis in this section. First, a discussion of the stability of the armour unit is given. Discussed are the loads that lead to movement of an armour unit. Next to that, the possible modes of movement are discussed together with the governing driving forces. Furthermore, the forces due to the collisions are discussed, which are needed to calculate the stresses inside the concrete armour units. Lastly the resulting characteristics of the Hexapod are compared with the tetrapode and Xbloc.

### I.2.1. STABILITY BASED ON SIMILAR ARMOUR UNIT TYPES

The wave structure interaction creates forces on the armour units. Considered are wave forces on a single Hexapod. In summary, the following forces work on the armour unit:

1. Impact forces
2. Drag forces due to the velocity and acceleration of wave run-up and run-down

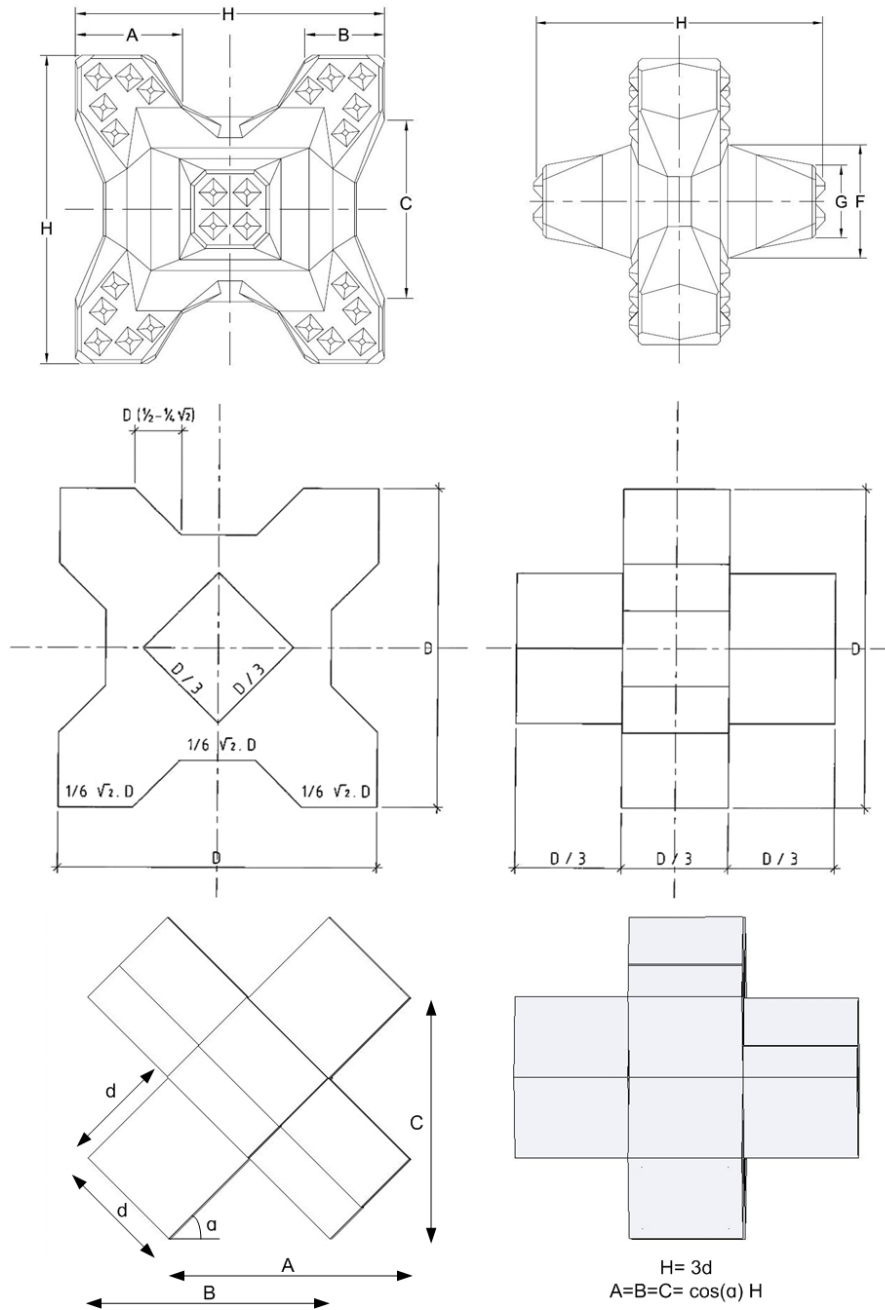


Figure I.1: Front and side view of the Accropode 2 (top) (CLI , 2011), Xbloc (middle) (Zwanenburg , 2012) and Hexapod (bottom)

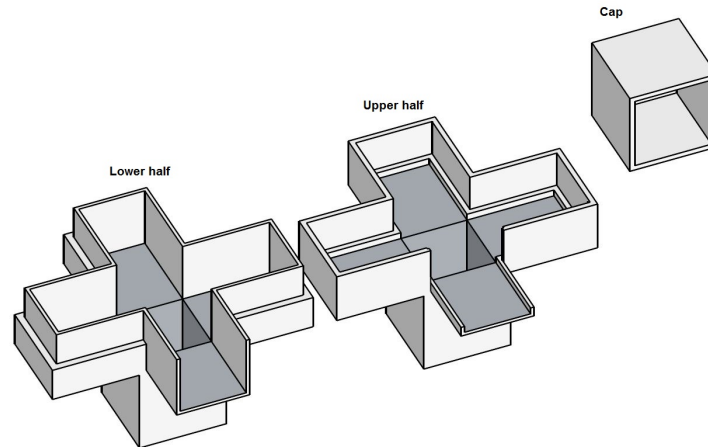


Figure I.2: Open view of the Hexapod

3. Shear forces due to run-up and run-down
4. Lift forces due to pressure differences and reflection
5. Forces due to turbulence

In which impact forces are not taken into account when a surging breaker is considered, since the water level just moves up and down. Lift forces due to reflection might be created due to the wave reflection against the breakwater core. The resulting water flow might create drag forces on the armour stones, resulting into lift.

The magnitude of the forcing is influenced by:

1. Wave height
2. Wave steepness
3. Wave groupiness
4. Wave shape
5. Breakwater configuration: crest height, permeability, slope angle

The resisting forces of an armour unit against movement can be summed up as following:

1. Weight
2. Interlocking
3. Packing density
4. Placing pattern

The mentioned aspects incorporated in empirical formulas for the armour units available on the market. The formulas are based on a stability criterion: a percentage of the armour units that are moved out of the layer. For instance, the formula describing the stability Xblocs is based on the criterion of the start of damage: one or more units is displaced. The formula can be described as following (Zwanenburg , 2012):

$$H_s / \Delta D_n \leq 2.77 \quad (I.1)$$

In which the significant wave height  $H_s$ , nominal diameter  $D_n$  and relative density  $\Delta$  are the only variable parameters. The other parameters are accounted for as a constant or considered of negligible influence. In addition, the stability formula for the Accropode is almost identical (Zwanenburg , 2012):

$$H_s / \Delta D_n \leq 2.5 \quad (I.2)$$

Considering the stability of the Hexapod, it is expected that the stability range is in the same order of magnitude as the Xbloc and Accropode.

### I.2.2. STABILITY BASED ON THEORY

We are interested in the (schematised) movements to get an understanding of the physical processes between the waves and the movements. Therefore a prediction for the minimum wave forcing is done to create rotation and translation of the Hexapod. Whether the Hexapod translates or rotates is dependent on for instance the friction of the underground. Furthermore, a combination of both mechanisms is also possible. To keep it simple, the two modes of movement are separated in this theoretical analysis.

For translation Equation I.3 is used.  $F_{wave}$  is considered to be the minimum driving force of a Hexapod on a slope with angle  $\alpha$ . In this elaboration an upwards translation (against gravity) is considered. Other forces considered are the friction ( $\mu$ ), gravity force ( $F_G$ ) and buoyancy force ( $F_B$ ). A similar elaboration can be done for a translation downwards and parallel to the slope. It is assumed that this wave force is acting as a point load on the Hexapod with orientation parallel to the slope. Furthermore, the influence of neighbouring units is neglected.

$$F_{wave} = (F_G - F_B) \sin \alpha + \mu(F_G - F_B) \cos \alpha \quad (I.3)$$

For rotation a few of the many modes of movement are shown in Figures I.3, I.4 and I.5. The influence of the neighboring units is neglected. The considered mechanisms are Hexapods that are lifted on one or two legs by the wave force. The wave force is considered to be short; the lifted Hexapod falls again to its original position. The other forces that are taken into account are the forces due to the weight ( $F_G$ ) and the forces due to the buoyancy ( $F_b$ ). The minimum force due to the waves is calculated by means of a moment of force balance.

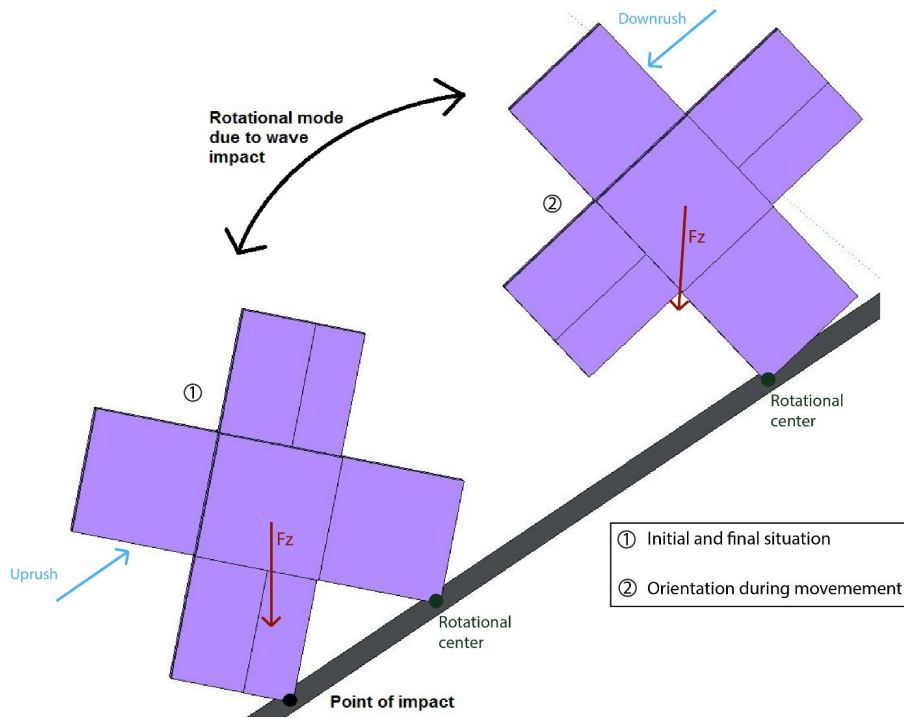


Figure I.3: Rotation Mode 1

The minimum force needed for rotation mode 1 is:

$$F_{wave} = 0.5(F_G - F_B) \quad (I.4)$$

For rotational mode 2 the following relationship is derived:

$$F_{wave} = 0.47(F_G - F_B) \quad (I.5)$$

Lastly, for rotation mode 3 the resulting equation is:

$$F_{wave} = 0.31(F_G - F_B) \quad (I.6)$$

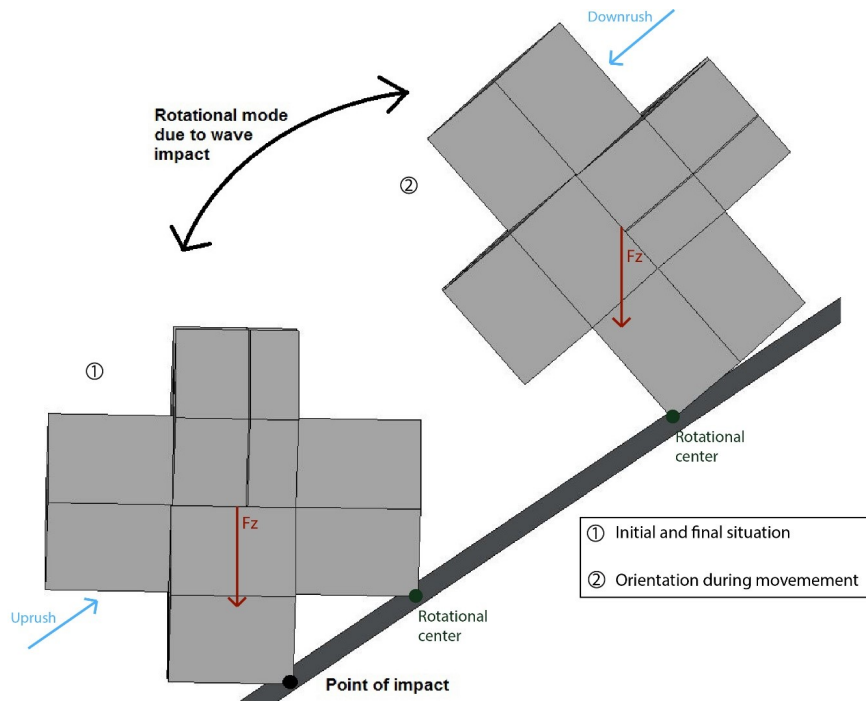


Figure I.4: Rotation Mode 2

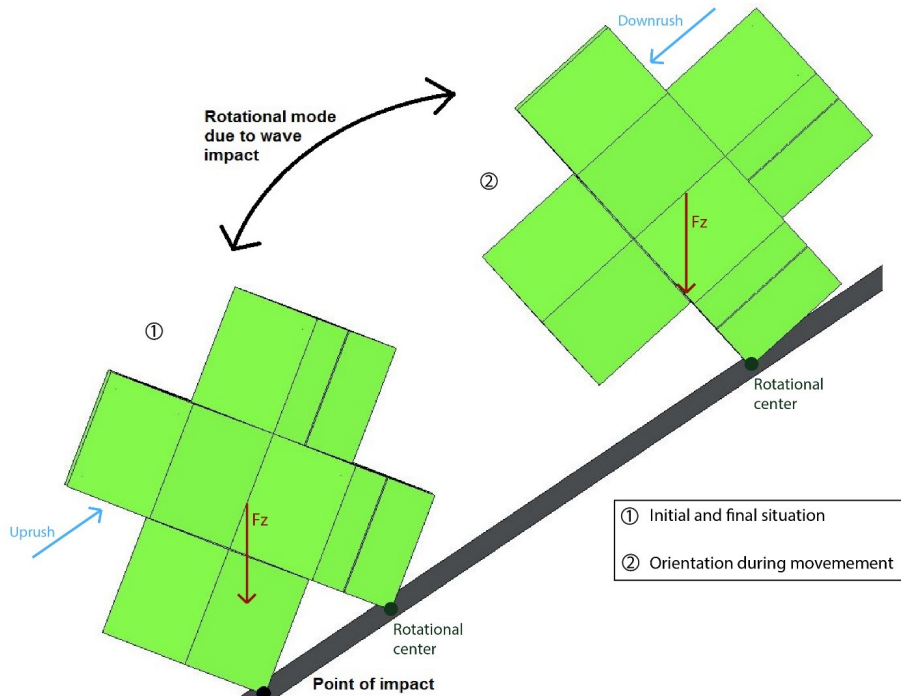


Figure I.5: Rotation Mode 3

Comparing the minimum forces due to waves it seems that rotation mode 3 is the most unstable position for the Hexapod. However, due to the simplified assessment, the results obtained might differ considerably from reality. For instance, the slope on which the Hexapods are deployed is not taken into account to keep the analysis simple. Considering the wave forcing of a collapsing breaker, the impact of the breaker and run-up and run-down may act as the point load described in the assessment. For a surging breaker, this impact must however not be taken into account. A situation in which the surrounding water is not of influence might be correct for a situation during run-up, since there is no water initially in between the pores of the breakwater, provided that all the water from previous run-up has flown out of the breakwater. It is certain that the assessment is too simplified for the situation just after the initial state of run-up or during run-down. The water in between the pores acts as extra inertia, and therefore the forces on the armour unit have to be larger to make the unit move. Furthermore, porous flow and turbulence may contribute or counteract the movements. Also the influence of the wave period, wave trains and interaction with neighbouring armour units should not be forgotten. The minimum wave force for movement of an armour unit is therefore hard to predict analytically.

### I.2.3. MAGNITUDE OF MOVEMENTS

An quantitative estimation is conducted for the magnitude of movements expressed in accelerations and velocities, measured in the center of the armour unit. The moving unit is assumed to return to its original position. An example is worked out for rotation mode 1 on a slope of 1/1.5 (Figure I.3). Rotations during both run-up and run-down are considered.

The following details are considered in the calculation: The width  $D$  of one leg is 0.5 m. Consequently the total height of the Hexapod is 1.5 m. Similar to the wave flume experiments, a low density of  $1500 \text{ kg/m}^3$  is chosen. The density of water is chosen equal to  $1000 \text{ kg/m}^3$ . Regular waves ranging from 2.8 m to 4 m and wave period of 4.5 s act as a force on the Hexapod. In addition, the Hexapod can rotate until an angle of 40 degrees relative to the horizontal axis (74 degrees relative to the slope).

With this wave configuration a range of Iribarren numbers in between 1.9 and 3.7 are obtained (Equation 3.7), indicating a breaking regime in between plunging and collapsing breakers. The Cd-coefficient in the Morison equation is therefore taken to be equal to 2.5 during run-up, to account for the wave impact. Since wave breaking does not act as a force on the armour unit during run-down, the Cd-coefficient is kept equal to 1 during downwards movement of the unit. The area over which the wave force acts is equal to one Hexapod's leg. The force acts on the left upper leg during run-up and the right upper leg during run-down, see Figure I.3.

Sufficient information is obtained to estimate the velocity  $V$  of the water layer on the slope with Equation 3.4. The resulting velocity of the water layer has a range between 2.5 m/s for the lowest waves and 5 m/s for the highest waves. The acceleration of the water motion acts over a time step of a quarter of the wave period. Consequently the torque around the rotational center is calculated with goniometrical modifications of Equation 3.2 and the lever of each force.

The gravitational force on the x and y axis parallel and perpendicular to the slope is determined as following:

$$F_{z_{y1}} = (\rho_s \cos(\alpha) - \rho_w) g V \quad (\text{I.7})$$

$$F_{z_{x1}} = \rho_s g V \cos(90 - \alpha) \quad (\text{I.8})$$

In which  $\alpha$  is the slope angle in degrees,  $V$  is volume of the Hexapod and  $g$  is the gravitational constant. The lever of the forcing around the rotational point is described for run-up as following:

$$\text{arm}_{F_{z_{y1}}} = \text{arm}_{F_{z_{x1}}} = \text{arm}_{F_1} = (\sqrt{2}/2) D \quad (\text{I.9})$$

This results in the torque around the rotational point during run-up in which  $F$  is calculated with *equation2*:

$$\text{Torque} = \text{arm}_{F_{z_{y1}}} F_{z_{y1}} + \text{arm}_{F_{z_{x1}}} F_{z_{x1}} - F \text{arm}_F \quad (\text{I.10})$$

For run-down the following relations apply, in which  $\theta$  represents the turning angle equal to 40 degrees relative to the horizontal axis:

$$F_{z_{y2}} = (\rho_s \cos(90 - \alpha - \theta) - \rho_w) g V \quad (I.11)$$

$$F_{z_{x2}} = \rho_s g V \cos(\alpha + \theta) \quad (I.12)$$

$$arm_{F_{z_{y2}}} = (\sqrt{2}/2) D \cos(90 - \alpha - \theta) \quad (I.13)$$

$$arm_{F_{z_{x2}}} = (\sqrt{2}/2) D (\tan(45) + \sin(90 - \alpha - \theta)) \quad (I.14)$$

$$arm_{F_2} = 2.5 D \cos(\theta) \quad (I.15)$$

$$Torque = -arm_{F_{z_{y2}}} F_{z_{y2}} + arm_{F_{z_{x2}}} F_{z_{x2}} + F arm_{F_2} \quad (I.16)$$

To work to a solution for the angular acceleration the moment of inertia is calculated. First the moment of inertia of a leg is calculated:

$$I_{gk} = (1/24) b^3 h \rho_s D \quad (I.17)$$

In which  $b$  represents the width of the Hexapod's leg parallel to the slope equal to  $\sqrt{2} D$ .  $h$  represents the height of the leg parallel to the slope equal to  $(\sqrt{2}/2) D$ . Consequently the total element's moment of inertia is calculated:

$$I_{gs} = (I_{gk} + (D \cos(\alpha) \cos(33))^2 M) 4 + 3 I_{gk} \quad (I.18)$$

In which  $M$  represents the mass of the unit's leg, equal to  $\rho_s D^3$ . Next the moment of inertia around the rotational point is established:

$$I_0 = I_{gs} + (0.5 D \cos(\alpha) \cos(33))^2 M_u \quad (I.19)$$

In which  $M_u$  represents the mass of the unit, equal to  $7M$ . Consequently the angular acceleration  $\alpha_u$  is estimated with Equation 3.10. The acceleration in the unit's center is obtained with:

$$a = \alpha_u \sqrt{(1.5 D)^2 + (0.5 D)^2} \quad (I.20)$$

Consequently the velocities are found by integration in time. The time over which the unit rotates is found with a simple relation ( $s = 0.5at^2$ ). The results of the accelerations and velocities are shown in Figure I.6.

The same calculation is done for a variation in wave period, shown in Figure I.7. The differences in acceleration and between collapsing and surging breakers is large since the Cd-coefficient is 2.5 times larger for collapsing breakers. It is expected that the differences are smaller in reality, as the water jet caused by breaking and the Cd-coefficient become smaller with larger wave period.

The movements of orientation 2 and 3 are elaborated qualitatively. It is expected that variations in the Cd and Cm-coefficients vary with orientation. After all, the shape changes relative to the wave direction, causing a different flow pattern around the unit. Next to that, the angles relative to the slope are different, changing the torque and moment of inertia. If the wave motion is assumed to act as a point load on the unit (no influence of Cd and Cm), then it is reasonable to expect orientation 3 to be the most unstable orientation. However in terms of collisions, the travel distance of orientation 3 is small and therefore it gains less velocity compared to orientation 1 and 2. Therefore the conclusion is that the movement of orientation 1 and 2 result in the highest velocities, but motion will be initiated first with orientation 3. The inclusion of the flow pattern around the unit may lead to different observations in the wave flume. In addition, due to the random placement it is expected that many other rotating mechanisms occur. Therefore these three rotational modes are considered to be a few options out of many.

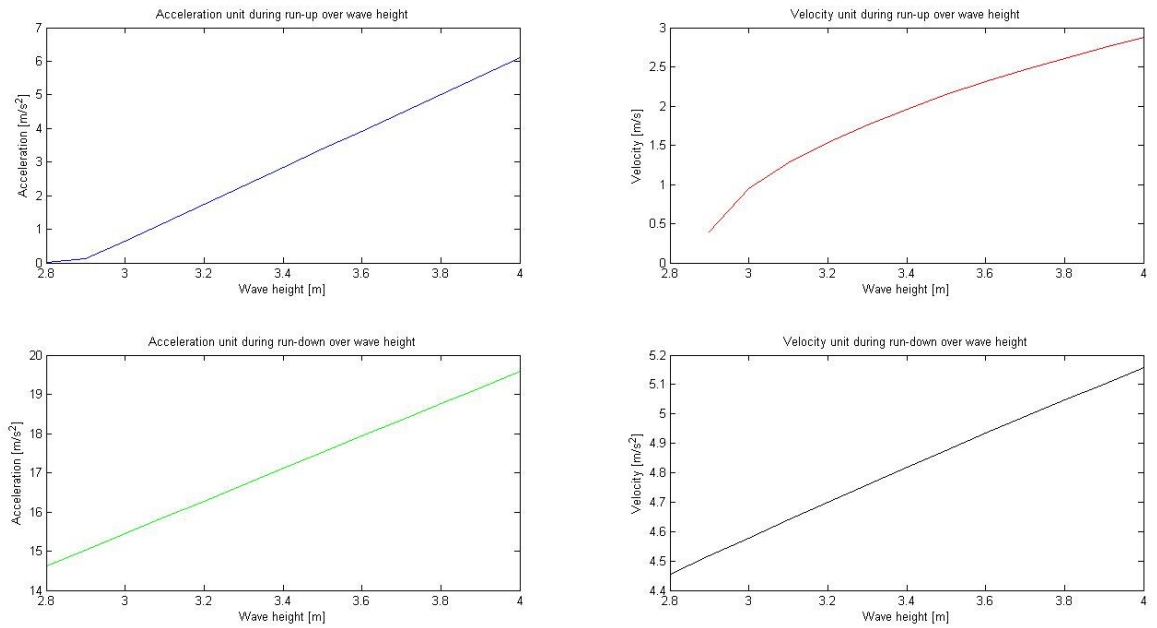


Figure I.6: Resulting accelerations and velocities varying over wave height of prototype Hexapod with orientation 1

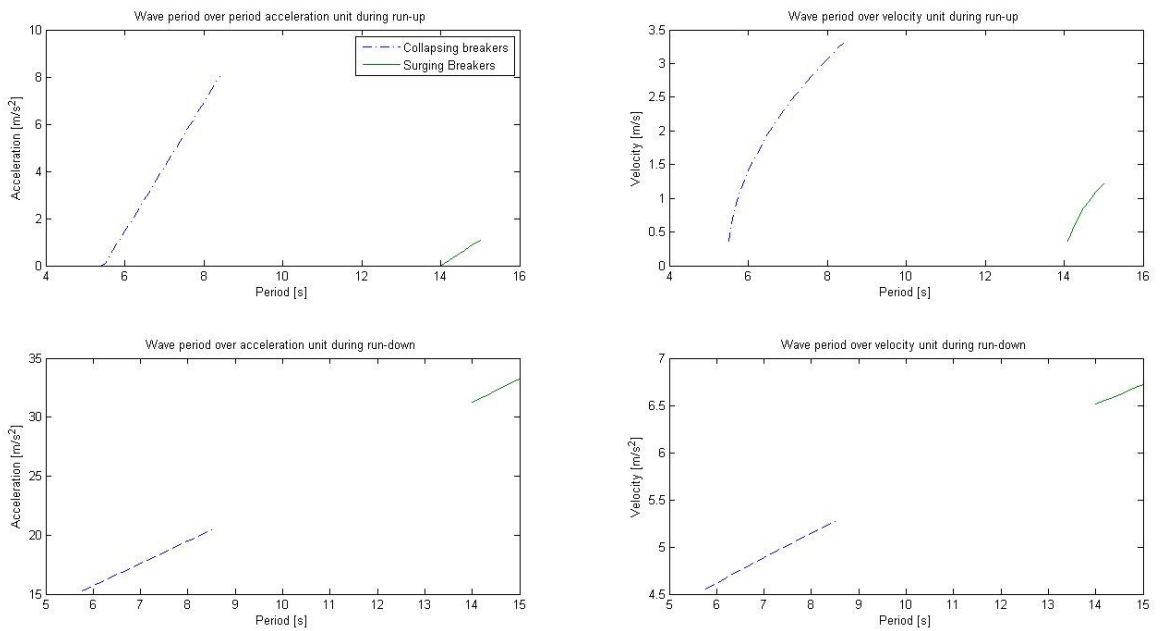


Figure I.7: Resulting accelerations and velocities varying over wave period of prototype Hexapod with orientation 1